

Synthesis of *bis*(oxamato) transition metal complexes and Ni nanoparticles and their structural, magnetic, optical, and magneto-optical characterization

von der Fakultät für Naturwissenschaften der Technischen Universität Chemnitz
genehmigte Dissertation zur Erlangung des akademischen Grades

doctor rerum naturalium

(Dr. rer. nat.)

vorgelegt von Dipl.-Chem. Dipl.-Phys. Björn Bräuer
geboren am 14. Januar 1981 in Marienberg

eingereicht am 14. April 2008

Gutachter: Prof. Dr. Heinrich Lang
Juniorprof. Dr. Georgeta Salvan
Prof. Dr. Annie K. Powell

Tag der Verteidigung: 02. Juli 2008

**„Es gibt kein größeres Hindernis
des Fortgangs in den Wissenschaften
als das Verlangen,
den Erfolg davon zu früh verspüren zu wollen.“¹**

G. C. Lichtenberg (1742 – 1799)
Schriftsteller und erster deutscher Professor für Experimentalphysik

¹ There is no bigger obstacle in science than a premature craving for success.

Bibliografische Beschreibung

Dipl.-Chem. Dipl.-Phys. Björn Bräuer

Synthesis of *bis*(oxamato) transition metal complexes and Ni nanoparticles and their structural, magnetic, optical, and magneto-optical characterization

Technische Universität Chemnitz, Dissertation (in englischer Sprache), 2008

Im Rahmen dieser Arbeit werden ein- und mehrkernige Cu(II)- und Ni(II)-*bis*-(oxamato)-Komplexe im Hinblick auf ihre magneto-optischen Eigenschaften gezielt hergestellt und strukturell charakterisiert. Über ladungs- und übergangsmetallinduzierte Abweichungen vom allgemeinen in der Literatur beschriebenen Reaktionsverhalten wird berichtet.

Aus Elektronenspinresonanz-Untersuchungen wird die Spindichtevertellung in den einkernigen Cu(II)-Komplexen abgeleitet. Die Beeinflussung dieser durch die Koordinationsgeometrie sowie die Auswirkungen auf die Superaustausch-Wechselwirkung werden diskutiert und mit Ergebnissen der Dichtefunktionaltheorie (DFT) verglichen. Dreikernige *bis*(oxamato)-Komplexe werden erstmals durch Spin-Coating auf Si(111)-Substraten aufgebracht und mit Hilfe der spektroskopischen Ellipsometrie sowie der Ramanspektroskopie untersucht und mittels DFT-Berechnungen ausgewertet. Magneto-optische Kerr-Effekt-Untersuchungen werden an dünnen Schichten dieser Komplexe sowie Phthalocyaninen durchgeführt.

Zum Vergleich werden die magnetischen und magneto-optischen Eigenschaften von Ni-Nanopartikeln in verschiedenen organischen Matrizen untersucht. Mit Hilfe der Photoelektronenspektroskopie wird das Oxidationsverhalten dieser studiert und es werden Rückschlüsse auf Ladungstransferprozesse zwischen den Matrizen und den Nanopartikeln gezogen.

Schlagwörter

Bis(oxamato)-Komplexe, Nanopartikel, Phthalocyanin, organische Halbleiter, Elektronenspinresonanz, Magnetismus, Einkristallröntgenstrukturanalyse, Magneto-optischer Kerr-Effekt, Raman-Spektroskopie, Ellipsometrie, Dichtefunktionaltheorie.

Preamble

This PhD thesis has been supervised by Prof. Dr. Heinrich Lang, chair of Inorganic Chemistry, and Juniorprof. Dr. Georgeta Salvan, chair of Organic Semiconductor Physics, in close cooperation with Prof. Dr. Dr. h. c. Dietrich R. T. Zahn and Dr. Tobias Rüffer. During two research stays of 6 months in total the thesis was supervised by Prof. Dr. Dante Gatteschi (Florence/Italy) and Prof. Dr. Antoine Kahn (Princeton/USA).

Table of Contents

Bibliografische Beschreibung	3
Table of Contents	5
List of abbreviations	9
1 Introduction	11
2 Synthesis and structure of Cu(II)- and Ni(II)-bis(oxamato) complexes	15
2.1 Introduction	15
2.2 Theoretical background	17
2.3 Experimental	19
2.4 Synthesis of Diethyl- <i>N,N'</i> -bis(oxamates)	20
2.5 Mononuclear Cu(II)- <i>bis</i> (oxamato) complexes with $\eta^4(\kappa^2N:\kappa^2O)$ coordination geometry	23
2.5.1 Synthesis of mononuclear $\eta^4(\kappa^2N:\kappa^2O)$ coordinated Cu(II)- and Ni(II)- <i>bis</i> (oxamato) complexes	23
2.5.2 Solid state structure of $(^n\text{Bu}_4\text{N})_2[\text{M}(2,3\text{-nabo})]$ (M = Cu (2), Ni (9))	24
2.5.3 Solid state structure of $(^n\text{Bu}_4\text{N})_2[\text{M}(2,3\text{-acbo})]$ (M = Cu (3), Ni (10))	25
2.5.4 Solid state structure of $(^n\text{Bu}_4\text{N})_2[\text{Cu}(\text{obbo})]$ (5)	27
2.5.5 Solid state structure of $(^n\text{Bu}_4\text{N})_2[\text{Cu}(\text{R-bnbo})]$ (7)	28
2.5.6 Solid state structure of $(^n\text{Bu}_4\text{N})_2[\text{Ni}(1,2\text{-acbo})] \cdot 1/4\text{CH}_2\text{Cl}_2$ (17)	30
2.5.7 Solid state structure of $(^n\text{Bu}_4\text{N})_2[\text{Ni}(\text{nibo})]$ (18)	31
2.6 Mononuclear Cu(II)- <i>bis</i> (oxamato) complexes deviating from $\eta^4(\kappa^2N:\kappa^2O)$ coordination geometry	33
2.6.1 Synthesis of $(^n\text{Bu}_4\text{N})_2[\text{Cu}(\text{aibo})_2]$ (15) and $(^n\text{Bu}_4\text{N})_2[\text{Cu}(\text{niqo})_2]$ (16)	33
2.6.2 Solid state structure of $(^n\text{Bu}_4\text{N})_2[\text{Cu}(\text{aibo})_2]$ (15)	35
2.6.3 Solid state structure of $(^n\text{Bu}_4\text{N})_2[\text{Cu}(\text{niqo})_2]$ (16)	36
2.7 Dinuclear Cu(II)- <i>bis</i> (oxamato) complexes	37
2.7.1 Synthesis of dinuclear Cu(II)- <i>bis</i> (oxamato) complexes	37
2.7.2 Solid state structure of $[\text{Cu}_2(\text{opba})(\text{pmdta})(\text{MeOH})]$ (19)	38

2.7.3	Solid state structure of $[\text{Cu}_2(2,3\text{-nabo})(\text{pmdta})(\text{MeOH})]$ (20)	40
2.8	Trinuclear Cu(II)- <i>bis</i> (oxamato) complexes	42
2.8.1	Synthesis of trinuclear Cu(II)- <i>bis</i> (oxamato) complexes	42
2.8.2	Solid state structure of $[\text{Cu}_3(\text{opba})(\text{pmdta})_2(\text{NO}_3)](\text{NO}_3) \cdot 2\text{MeCN}$ (21) and $[\text{Cu}_3(2,3\text{-nabo})(\text{pmdta})_2(\text{BF}_4)](\text{BF}_4) \cdot \text{MeCN} \cdot \text{Et}_2\text{O}$ (22)	43
2.8.3	Solid state structure of $[\text{Cu}_3(\text{obbo})(\text{pmdta})_2(\text{NO}_3)](\text{NO}_3) \cdot \text{CH}_2\text{Cl}_2 \cdot \text{H}_2\text{O}$ (23) and $[\text{Cu}_3(\text{obbo})(\text{tmeda})_2(\text{NO}_3)_2(\text{dmf})]$ (24)	46
2.9	Summary and Conclusions	49
3	Magnetic properties of Cu(II)-<i>bis</i>(oxamato) complexes	52
3.1	Introduction	52
3.2	Theoretical background	55
3.2.1	The spin Hamilton formalism of paramagnets	55
3.2.2	Experimental and theoretical studies of spin population	56
3.2.3	Electron paramagnetic resonance	57
3.2.4	Pulse electron nuclear double resonance	59
3.2.5	Magnetic investigations of exchange coupled systems	60
3.3	Quantum chemical calculations	61
3.3.1	Density functional theory	61
3.3.2	Basis sets	62
3.3.3	Calculation of vibrational frequencies	63
3.3.4	Calculation of EPR parameters	63
3.3.5	Calculation of magnetic super-exchange parameters	64
3.3.6	Time dependent density functional theory	65
3.4	Experimental details	66
3.4.1	EPR investigations	66
3.4.2	Magnetic susceptibility studies	67
3.4.3	Absorption measurements	68
3.4.4	Quantum chemical studies	68
3.5	Results and discussion	69
3.5.1	Absorption spectroscopy investigations	69
3.5.2	EPR investigations	71
3.5.3	Experimental and theoretical studies of spin population	77
3.5.4	Investigation of the magnetic super-exchange parameters	79

3.5.5	DFT calculations of the magnetic super-exchange parameters ..	81
3.5.6	Correlation of spin population with structural and magnetic properties	84
3.6	Summary and Conclusions	87
4	Thin films of Cu(II)-bis(oxamato) complexes	89
4.1	Introduction	89
4.2	Theoretical background	90
4.2.1	Raman effect	90
4.2.2	Resonance Raman effect	91
4.2.3	Infrared absorption	92
4.2.4	The dielectric tensor	92
4.2.5	Spectroscopic ellipsometry	93
4.3	Experimental details	96
4.3.1	Measuring setup for Raman spectroscopy	96
4.3.2	Measuring setup for infrared spectroscopy	97
4.3.3	Spectroscopic ellipsometry and UV/VIS spectroscopy	98
4.3.4	Sample preparation	99
4.3.5	DFT calculations of vibrational frequencies	99
4.4	Results and discussion	100
4.4.1	Preparation of thin films	100
4.4.2	UV/VIS and spectroscopic ellipsometry studies	102
4.4.3	IR and Raman studies for 2 and 9	104
4.4.4	IR and Raman studies for 21	109
4.4.5	Comparison of the Raman spectra of 2 , 21 , and 22	112
4.5	Summary and conclusions	114
5	Magneto-optical investigations	116
5.1	Introduction	116
5.2	Theoretical background	117
5.2.1	Magneto-optical effects	117
5.2.2	Calculation of the Voigt constant	118
5.3	Experimental details	120
5.3.1	Measurement setup for magneto-optical investigations	120

5.3.2	Crystalline structure of H ₂ Pc and PTCDA	122
5.3.3	Sample preparation	123
5.4	Results and discussion.....	124
5.4.1	Spectroscopic ellipsometry investigations	124
5.4.2	Magneto-optical Kerr effect investigations	127
5.4.3	Magneto-optical Kerr effect studies of <i>bis</i> (oxamato) complexes	129
5.5	Summary and Conclusions	130
6	Electronic and magnetic properties of Ni nanoparticles in organic matrices	132
6.1	Introduction	132
6.2	Theoretical background	133
6.2.1	Photoelectron spectroscopy	133
6.2.2	Magnetic nanoparticles.....	135
6.3	Experimental details	135
6.3.1	Sample preparation	135
6.3.2	Experimental techniques	136
6.4	Results and discussion	137
6.4.1	HR-TEM investigations	137
6.4.2	Raman spectroscopic investigations.....	138
6.4.3	Photoelectron spectroscopy studies	139
6.4.4	Magnetic susceptibility studies.....	143
6.4.5	Magneto-optical studies.....	146
6.5	Summary and Conclusions.....	147
7	Summary and Conclusions	148
	Appendix	153
	References.....	166
	Erklärung.....	174
	Curriculum Vitae.....	175
	List of Publications and attended conferences	177
	Acknowledgements	181

List of abbreviations

1,2-acbo	<i>N,N'</i> -anthra-9,10-chinone-1,2- <i>bis</i> (oxamato)
2,3-acbo	<i>N,N'</i> -anthra-9,10-chinone-2,3- <i>bis</i> (oxamato)
aibo	<i>N,N'</i> -anthra[1,2-d]-(imidazole-2-carboxylato)-6,11-dione
av.	average
BS	broken symmetry
Bu	butyl
calc.	calculated
CCD	charge coupled device
cf.	confer
COSMO	conductor-like screening model
CT	charge transfer
cw	continuous wave
DFT	density functional theory
dmf	dimethylformamide
EB	exchange bias
e.g.	exempli gratia (= for example)
ENDOR	electron nuclear double resonance
EPR	electron paramagnetic resonance
Et	ethyl
et al.	et alii (= and others)
FC	magnetic field cooled
HF	high frequency
HOMO	highest occupied molecular orbital
HR-TEM	high resolution transmission electron microscopy
HS	high spin
i.e.	id est (= that is)
IR	infrared
iso	isotropic
LCAO	linear combination of atomic orbitals
LS	low spin
LUMO	lowest unoccupied molecular orbital
M	metal
MCD	magnetic circular dichroism

Me	methyl
MOKE	magneto-optical Kerr effect
MSE	mean square error
MW	microwave
1,8-nabo	<i>N,N'</i> -1,8-naphthalene- <i>bis</i> (oxamato)
2,3-nabo	<i>N,N'</i> -2,3-naphthalene- <i>bis</i> (oxamato)
nibo	<i>N,N'</i> -4,5-dinitro- <i>o</i> -phenylene- <i>bis</i> (oxamato)
niqo	<i>N,N'</i> -7,8-dinitro-2,3-quinoxalinedionato
NMR	nuclear magnetic resonance
NPA	natural population analysis
obbo	<i>N,N'</i> - <i>o</i> -benzyl- <i>bis</i> (oxamato)
pba	1,3-propylene- <i>bis</i> (oxamato)
Pc	phthalocyanine
phen	1,10-phenanthroline
PES	photoelectron spectroscopy
pmdta	<i>N,N,N',N'',N''</i> -pentamethyldiethylenetriamine
Pr	propyl
PTCDA	3,4,9,10-perylenetetracarboxylic-dianhydride
r.m.s.	root mean square
R-bnbo	<i>N,N'</i> -(R)-1,1'-binaphthalene-2,2'- <i>bis</i> (oxamato)
RF	radiofrequency
rpm	rotations per minute
RT	room temperature
SE	spectroscopic ellipsometry
SQUID	super conducting quantum interference device
TDDFT	time dependent DFT
THF	tetrahydrofuran
tmeda	<i>N,N,N',N'</i> -tetramethylethylenediamine
TZV	triple zeta valence
UPS	ultraviolet photoelectron spectroscopy
UV	ultraviolet
VIS	visible
vs.	versus
XPS	x-ray photoelectron spectroscopy
ZFC	zero magnetic field cooled

1 Introduction

The synthesis of new materials and their characterization with respect to their application potential is one of the challenges of chemists, physicists, and material scientists. New developments in the field of nanoscience and nanotechnology in the last decades have impressively shown the tremendous overlap in interest of these scientific communities. Molecule- and nanoparticle-based magnetism are examples of growing modern interdisciplinary research fields where both new material systems [Gatteschi06] and new investigation techniques were developed [Wernsdorfer01]. Magnetic nanomaterials have several unique properties that exhibit novel phenomena. For example, mesoscopic quantum phenomena and strong magnetic exchange interactions were observed in molecular systems [Gatteschi03]. On the other hand, magnetic nanoparticles become single domain with decreasing size [Dormann97]. The variety of interesting properties gave rise to numerous application ideas ranging from biological and medical uses [Pankhurst03], magnetic refrigeration [Tejada01, Shir03], magnetic imaging [Rasing97], and magnetic recording media [Terris05].

A great advantage of dealing with molecular systems is that their properties can be altered thanks to the large flexibility arising from the carbon chemistry. Cu(II)-*bis*(oxamato) complexes are one example of prominent representatives in this research field and were already used for basic research studies of magnetic exchange phenomena [Costa93].

In this context, the possibility of probing the magnetic properties with light becomes a challenging topic in material science, in view of the possible implementation in high density storage devices [Gütlich01]. In fact, optical methods can provide a highly sensitive and rapid way to read and write information [Jenkins03, Milster04]. These promising applications have driven our interest to magneto-optical investigations in reflection on thin films of multinuclear transition metal complexes.

Magneto-optical studies in the ultraviolet and visible (UV/VIS) spectral range of molecular magnetic thin films were so far only performed in transmission, e.g., on $M_{1.5}[Cr^{III}(CN)_6] \cdot (H_2O)_n$ ($M = Co(II), Ni(II), Cu(II)$) [Tozawa03] and V(II/III)-containing hexacyanochromate(III) complexes [Ohkoshi00] embedded in an organic matrix. Measurements in reflection, however, have never been performed on molecular systems at all, even though this method was already successfully used for studies of inorganic ferromagnetic layers [Antonov01, Ohkoshi01, You05], magnetic semiconductors [Iikawa02], magnetic nanostructures [Wahl03, Cowburn00, Allwood02], and is even applied for reading magneto-optical (MO) disks [Keneko00]. There are two possible reasons why, on the one hand, ferromagnetic inorganic materials are already used in MO disks but, on the other hand, the magneto-optical response of carbon-containing thin films of, e.g. molecular magnets, have never been investigated:

1.) First, the magneto-optical signal intensity in reflection of the molecular magnets, paramagnets, or organic compounds is expected to be more than three orders of magnitude smaller compared to that of, e.g., a ferromagnetic Ni film which has a much higher magnetization. The signal intensity might be increased using compounds that exhibit high magnetization and that possess strongly absorbing functional groups with intensive $\pi-\pi^*$ and charge transfer transitions in the spectral range relevant for applications, i.e. visible to near ultraviolet, e.g. aromatic systems and phthalocyanine-like systems. As in the MO data storage the reading light incidents in normal direction on the disk, a maximum signal is to be expected when the electric field of the light is parallel to the optical transition dipole moments of the molecules. Therefore, the transition dipole moment of the molecules has to be aligned in the disk surface plane. This condition may be achieved for compounds with extended aromatic ring systems that are laying flat on the substrate.

2.) Second, it is difficult to prepare homogeneous thin films of transition metal complexes with a controlled thickness if they cannot be sublimed in vacuum without decomposition, which is the case for most of the known molecular magnets or paramagnetic transition metal complexes. If the compounds are soluble, simple dipping of the substrate in a solution of the complex could be used to prepare films, however, the surface roughness is then too high and

strong depolarization effects would make the reading of the MO signal impossible. One alternative is the Langmuir-Blodgett method which was applied to, e.g. $\text{Cu}_3[\text{Fe}(\text{CN})_6]_2$ containing compounds [Lafuente99]. However, in many cases the transition metal complexes have to be modified with hydrophobic ligands like alkyl chains [Seip97, Soyer99] which is sometimes challenging and it makes the alignment of the optical transition dipole moment within the substrate plane difficult. Another promising way to obtain thin films with controlled thickness and good homogeneity may be provided by spin coating. This method was previously reported for Ni(II) complexes [Chen06], but without analyzing the roughness and thickness of such films. The homogeneity might be improved by optimizing the rotation speed, the concentration, the solvent, and the solubility of the complexes.

This dissertation contributes to the literature by preparing and investigating molecule based systems which exhibit as many as possible of the desired physical and chemical properties like, e.g., high solubility and intensive absorption bands. On the example of *bis*(oxamato) type transition metal complexes general trends regarding the influence of a specific structural modification on the complex properties will be derived in the trial to extrapolate this trends also to other compounds. For this purpose many of such *bis*(oxamato) complexes have to be synthesized. Obviously, it would be highly desirable to predict theoretically the material properties by means of quantum chemical calculations like density functional theory (DFT) before a time-consuming synthesis is performed. Although great improvements for reliable predictions of the experimental trends have been made during the last decades [Neese03, Ahlrichs89], there is still a lack of detailed studies regarding the reliability of certain methods. This PhD thesis strongly focuses on an experimental approach, however, most of the results were also reproduced by means of DFT calculations and the reliability of the methods used was tested.

This work is structured in the following way. Since many different investigation methods were used in order to study the compounds herein, each chapter consists of a separate introduction and a short description of the methods used and theoretical approaches. After presenting the results, each chapter closes with a summary. Although each chapter is in a way self-contained they are all motivated by producing suitable model systems of magnetically exchange

coupled molecules which can be deposited by means of spin coating as thin films on Si/SiO₂ surfaces for magneto-optical studies in reflection. In the process of reaching this goal several results were obtained which are also important.

Starting with chapter two, the synthesis and structural characterization of new mono-, di-, and trinuclear Cu(II)-*bis*(oxamato) complexes are presented. Therein the *N,N'*-bridge is varied in order to improve the solubility and the spatial extension of the molecules and thus control the homogeneity of the thin films later on. The magnetic properties of these complexes were investigated by means of electron paramagnetic resonance (EPR) and magnetic susceptibility studies, *cf.* chapter 3, contributing to a better understanding of the magneto-optical results in chapter five. Chapter four describes the preparation of thin films of such complexes. The preservation of the molecular structure through the deposition process was studied by means of vibrational spectroscopy and the film thickness was determined by means of spectroscopic ellipsometry. Chapter five discusses the magneto-optical properties of the films in reflection. The chapter presents a model, necessary to extract the Voigt magneto-optical constant from the measured magneto-optical Kerr effect spectra. The validity of this approach is checked by applying it to metal-free phthalocyanine thin films that can also be used as model systems to prove the sensitivity of the magneto-optical constants with respect to the molecular orientation.

Chapter six turns to comparative studies of the formation of magnetic nanoparticles in organic matrices. Ni nanoparticles are prepared by co-deposition with the organic molecules in a vacuum. The structural and magnetic properties of such mixed thin films are characterized by means of vibrational and photoelectron spectroscopy as well as magnetic susceptibility studies. Finally, these films were magneto-optically investigated and the results compared to those obtained for the complexes in chapter five.

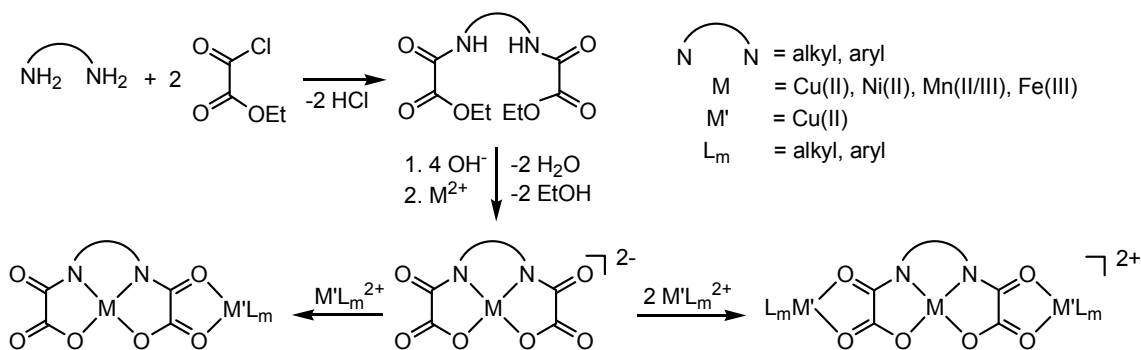
Chapter seven summarizes the whole work. Additional details related to this work, that have been omitted in the thesis due to space limitations, can be found in the scientific publications generated while undertaking this PhD work.

2 Synthesis and structure of Cu(II)- and Ni(II)-bis(oxamato)-complexes

2.1 Introduction

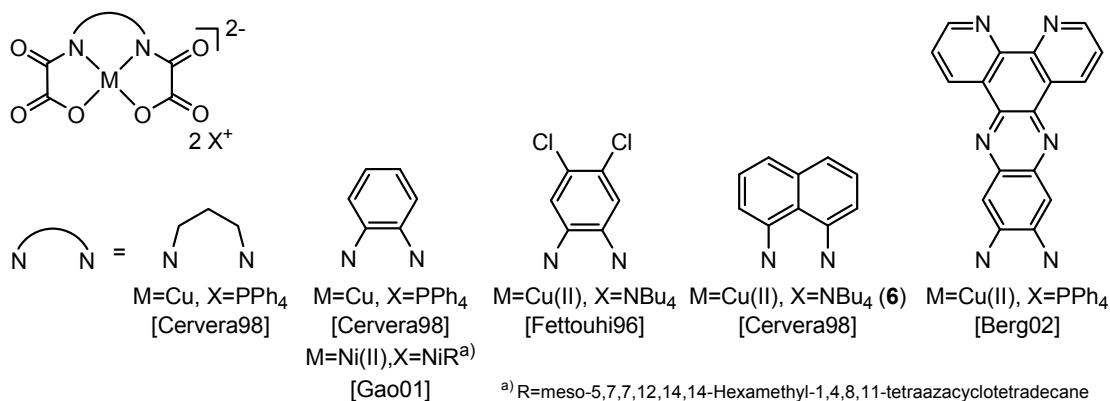
Thanks to their large structural variability, mononuclear Cu(II)-bis(oxamato) complexes have been used as precursors for the synthesis of multimetallic complexes, see e.g. [Kahn93, Costa93], as building blocks for two and three dimensional magnetic networks [Stumpf93a, Kahn96, Aukaloo00], and for single molecule magnets [Dias01, Pereira03]. Their structural variability makes them also excellently suited for basic research studies of magnetic super-exchange phenomena, see e.g. [Costa93].

In 1936 Gaade [Gaade36] synthesized diethyl-*N,N'*-ethylene-1,2-diamino-bis(oxamate) as a first example of a starting material for the preparation of Cu(II)-bis(oxamato) complexes. In general, the treatment of appropriate diamines with ethoxycarbonylchloride leads to diethyl-*N,N'*-diamino-bis(oxamates), cf. scheme 2.1. The following addition of four equivalents of base and a transition metal salt leads to mononuclear bis(oxamato) complexes which can be used as starting materials for the synthesis of di- and trinuclear transition metal complexes, cf. scheme 2.1.



Scheme 2.1. Synthesis of different types of bis(oxamato) complexes starting from diethyl-bis(oxamates).

Several different mononuclear Cu(II)- and Ni(II)-bis(oxamato) complexes have been prepared so far and are summarized in scheme 2.2. Only two complexes are known in which other transition metal ions than Cu(II) and Ni(II) are coordinated, namely Fe(III) [Ruiz87] and Mn(II/III) [Fettouhi96].



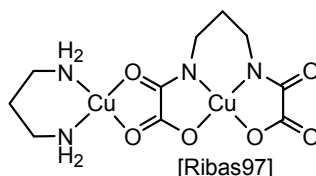
Scheme 2.2. Structurally characterized discrete mononuclear Cu(II)- and Ni(II)-bis(oxamato) complexes.

All these complexes possess a $\eta^4(\kappa^2N:\kappa^2O)$ coordination of the transition metal ion with a close to square planar geometry. The up to date structurally characterized di- and trinuclear transition metal complexes that have been reported are shown in scheme 2.3 and 2.4, respectively. The multinuclear transition metal complexes were used for basic research studies of magnetic exchange phenomena which will be discussed in detail in chapter 3.

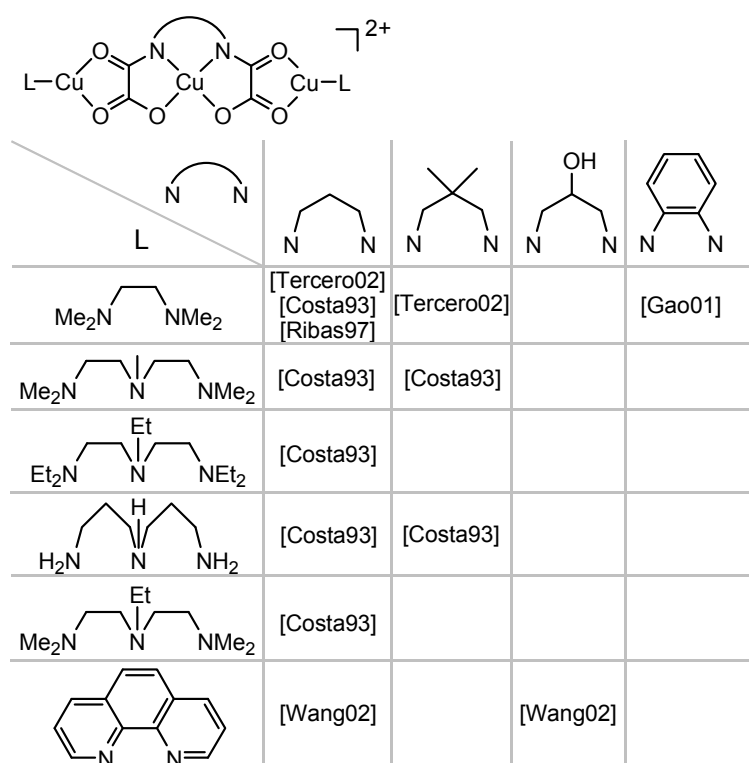
In this chapter the molecular structures of the synthesized bis(oxamato) type molecules will be discussed. A more detailed description of the packing, of further structural details, and of the structure refinements can be found in the published papers generated while undertaking this PhD work. The crystallographic data and the experimental part for all the molecules are outlined in the appendix.

In the following paragraph the synthesis and solid state structures of the nBu_4N^+ salts of new mononuclear bis(oxamato) complexes prepared in the context of this work will be described: $[M(2,3-nabo)]^{2-}$ ($M=Cu$ (2), $M=Ni$ (9), 2,3-nabo= N,N' -2,3-naphthalene-bis(oxamato)), $[M(2,3-acbo)]^{2-}$ ($M=Cu$ (3), $M=Ni$ (10), 2,3-acbo= N,N' -anthra-9,10-chinone-2,3-bis(oxamato)), $[M(obbo)]^{2-}$ ($M=Cu$ (5), $M=Ni$ (12), obbo= N,N' -o-benzyl-bis(oxamato)), $[Cu(R-bnbo)]^{2-} \cdot 2H_2O$ (7, R-bnbo= N,N' -(R)-1,1'-binaphthalene-2,2'-bis(oxamato)), $[Cu(niqo)_2]^{2-}$ (15, niqo= N,N' -7,8-dinitro-2,3-quinoxalinedionato), $[Cu(aibo)_2]^{2-}$ (16, aibo= N,N' -anthra-

[1,2-d]-(imidazole-2-carboxylato)-6,11-dione), $[\text{Ni}(1,2\text{-acbo})]^{2-}$ (**17**, 1,2-acbo = *N,N'*-anthra-9,10-chinone-1,2-bis(oxamato)), and $[\text{Ni}(\text{nibo})]^{2-}$ (**18**, nibo = *N,N'*-4,5-Dinitro-*o*-phenylene-bis(oxamato)). For **1** and **2** the respective dinuclear (**19** and **20**) and for **1**, **2**, and **5** the respective trinuclear Cu(II)-bis(oxamato) complexes were also prepared and characterized.



Scheme 2.3. Structurally characterized discrete dinuclear Cu(II)-bis(oxamato) complex.



Scheme 2.4. Structurally characterized discrete trinuclear Cu(II)-bis(oxamato) complexes.

2.2 Theoretical background

X-ray crystallography is a common technique for determining the arrangement of atoms within a crystal. The technique analyses the scattering of X-rays by the electrons within the crystal. By applying a Fourier transformation to the collected data, $F(\mathbf{q})$, a three dimensional picture of the electron density $f(\mathbf{r})$ in the real space is obtained by

$$f(\mathbf{r}) = \frac{1}{4\pi} \int d\mathbf{q} F(\mathbf{q}) e^{i\mathbf{q}\cdot\mathbf{r}} . \quad (2.1)$$

From this, for instance, the mean atomic positions, chemical bonds, and atomic disorder can be derived.

The terminal point of the vector \mathbf{q} in the reciprocal space corresponds to a particular oscillation in the electron density as one moves in the direction in which \mathbf{q} points. $F(\mathbf{q})$ is a complex number, *i.e.* it can be described by the amplitude $|F(\mathbf{q})|$ and a phase $\phi(\mathbf{q})$ related by the equation

$$F(\mathbf{q}) = |F(\mathbf{q})| e^{i\phi(\mathbf{q})} . \quad (2.2)$$

In the ideal case of perfect periodicity in the crystals the atoms are positioned on a perfect lattice, the electron density is perfectly periodic, and $F(\mathbf{q})$ is non-zero, the so-called Bragg peaks, only when \mathbf{q} is a vector of the reciprocal lattice. In reality, however, the crystals are not perfectly periodic. Atoms vibrate about their mean position and there may be disorder of various types, such as dislocations, point defects, and heterogeneity in the conformation of the crystallized molecules.

In the Bragg model, a given reflection is associated with a set of equally spaced planes running through the crystal. The orientation of a particular set of planes is identified by its Miller indices (h,k,l) and their lattice spacing d . The X-rays are scattered by each plane and combine constructively when the angle θ between the plane and the X-ray results in a path-length difference that is an integer multiple n of the X-ray wavelength λ described as

$$2d \sin \theta = n\lambda . \quad (2.3)$$

When the Miller indices have been identified, the lengths and angles of the unit-cell as well as its space group can be derived. The intensity of the reflections, which is not considered in the Bragg equation, contains information about the kind and spatial distribution of atoms in the unit cell, and is proportional to the square of the structure factor amplitude. In order to obtain an interpretable electron density map, both the amplitude $|F(\mathbf{q})|$ and the phase $\phi(\mathbf{q})$ must be known. The phase cannot be directly recorded during the diffraction experiment,

which is known as the “phase problem”. Initial phase estimates can be obtained in a variety of ways [Massa02]. One method is the so-called direct method, a statistic method based on the over determination of structural parameters by taking into account an excess of reflections. The phase values are then refined, until the match between the diffraction data (F_o) and the model (F_c) is maximized. The goodness of the model is measured by the R factor defined as

$$R = \frac{\sum_{hkl} ||F_o| - |F_c||}{\sum_{hkl} |F_o|} \quad (2.4)$$

and the statistically weighted R values wR and wR_2 defined as

$$wR = \sqrt{\frac{\sum_{hkl} w (|F_o| - |F_c|)^2}{\sum_{hkl} w F_o^2}} \quad \text{and} \quad wR_2 = \sqrt{\frac{\sum_{hkl} w (F_o^2 - F_c^2)^2}{\sum_{hkl} w (F_o^2)^2}} \quad (2.5)$$

where the weighting factor w is related to the standard deviation σ , e.g. by $w = 1/\sigma^2$. Variations in wR and wR_2 are a sensitive indication to whether changes in the structure model were useful or not. In a good data set the values for wR and R should be below 0.05 and for wR_2 below 0.15.

Since the atoms in single crystals execute vibrations around their centre or are structurally disordered it leads to an apparent increase of the atom volume which can be described by isotropic and anisotropic displacement parameters represented by ellipsoids, cf. Ortep plots.

2.3 Experimental

Single crystal X-ray structure analysis measurements were performed on an Oxford Gemini S 4-circle diffractometer, cf. figure 2.1. The X-rays are generated by a sealed tube, which is mounted on the goniometer and powered by the high voltage X-ray generator for Mo K_α radiation ($\lambda = 0.71073 \text{ \AA}$) and Cu K_α radiation ($\lambda = 1.54184 \text{ \AA}$).

The X-ray optics consist of a high speed shutter located next to the tube shield, a monochromator for selecting a specific bandwidth from the tube spectrum and a collimator for limiting the divergence. The detector system consists of a

charge coupled device (CCD) area detector with a Beryllium window to the vacuum sealed detector unit. A scintillation screen transforms the X-ray photons to visible light which is conducted via a fibre to the CCD chip.

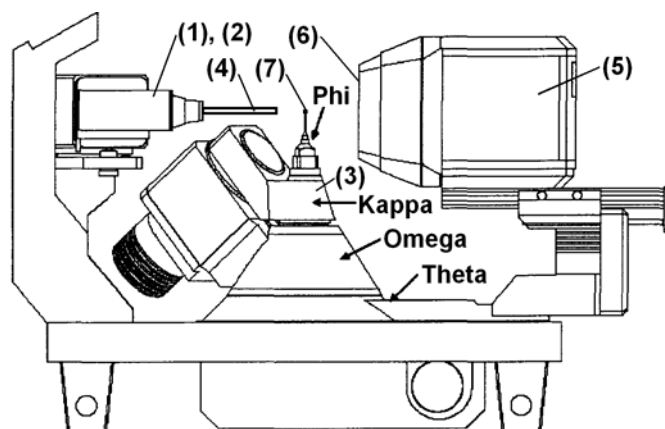


Figure 2.1. Schematic of the kappa geometry 4-circle diffractometer. (1) X-ray tube, (2) X-ray shutter, (3) 4-circle kappa goniometer, (4) Collimator, (5) CCD area detector, (6) Beryllium window, and (7) single crystal.

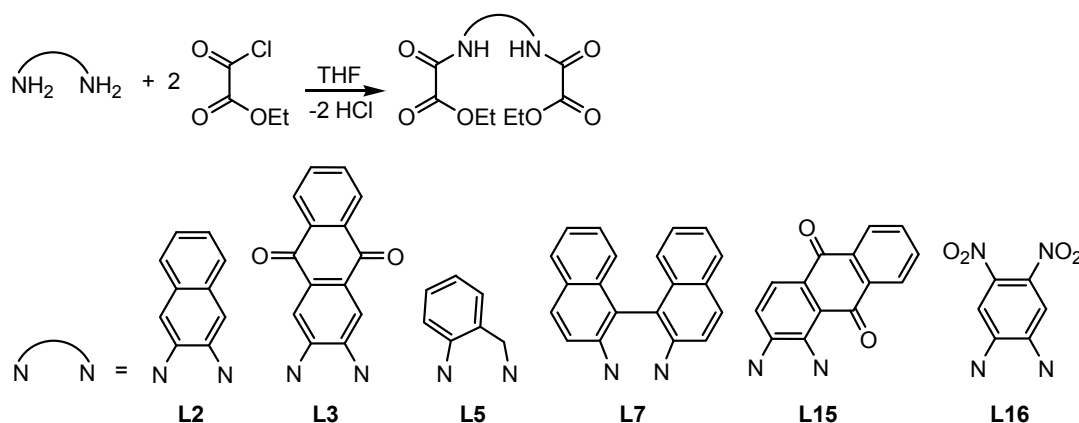
The software CrysAlis CCD [Crys06] was used for the collection of data frames, for indexing reflections, and to determine lattice parameters; CrysAlis Red [Crys06] was used for the integration of the intensity of the reflections and for scaling as well as for empirical absorption correction.

For the space group and structure determination, refinements, graphics, and structure reporting the computer program SHELXTL [Sheldrick96] was used. All structures were solved by direct methods and refined by full-matrix least squares on F^2 with anisotropic thermal parameters for non-hydrogen atoms. Hydrogen atoms bounded to carbon atoms were included and their positions were refined using a riding model.

2.4 Synthesis of Diethyl-*N,N'*-*bis*(oxamates)

Diethyl-*N,N'*-*bis*(oxamate) precursors for the synthesis of *bis*(oxamato) type transition metal complexes were prepared according to scheme 2.5. For this purpose a diamine in THF is treated with ethoxyalylchloride in the presence of triethylamine as a HCl scavenger. Single crystals suitable for X-ray structure analysis can be obtained by slow diffusion of diethyl ether into a dichloromethane solution. Herein, only the molecular structure of **L7** will be discussed.

Impressively, (*R*)- or (*S*)-2,2'-bis(diphenylphosphino)-1,1'-binaphthyl was in several cases, the ligand of choice for preparing optically active transition-metal complexes for asymmetric catalysis [Miyashita80, Noyori02]. Using *bis*(oxamato) type transition metal complexes with an optically active *N,N'*-bridge as catalysts for oxidation reactions therefore might give optically active reaction products. For this purpose the (*R*)-[1,1'-binaphthalene]-2,2'-diamine was treated with two equivalents of ethoxyalylchloride in THF in the presence of triethylamine as a HCl scavenger. The resulting (*R*)-diethyl-*N,N'*-[1,1'-binaphthalene]-2,2'-*bis*(oxamate) (**L7**) was enantiopure. The molecular structure of **L7** is shown in figure 2.2. Selected bond lengths as well as bond angles are listed in table 2.1.



Scheme 2.5. Preparation of Diethyl-*N,N'*-bis(oxamate) precursors.

Related bond lengths of **L7a** and **L7b** are identical, whereas related bond angles show marginal differences. Usually, for 2,2'-substituted-[1,1'-binaphthyl] compounds, a nearly cross-arrangement of the two substituted binaphthyl groups is observed in the solid state [Takaya86]. For the two ethyl[*N*-1-naphthyl]-2-oxamate groups of **L7a** and **L7b**, respectively, the same cross-arrangement is observed. The interplanar angle from calculations of the mean planes of the non-hydrogen atoms of these groups is 81.52(4)° for **L7a** and 83.84(2)° for **L7b**, respectively. Most probably due to this cross-arrangement, no intermolecular formation of hydrogen bonds are observed for **L7'**, whereas for related compounds, like diethyl *N,N'*-*o*-phenylene-*bis*(oxamate) [Martin02] and diethyl *N,N'*-(naphthalene-1,8-diyl)-*bis*(oxamate) [Francesco98], the formations of intermolecular hydrogen bonds were observed in the solid state. The oxamato group of **L7a** containing atoms N1, O1, C1, C2, O2, O3 (oxamato group I) and the oxamato group of **L7b** containing atoms N3, O7, C29, C30, O8,

O9 (oxamato group III), respectively, are nearly planar, as shown by their torsion angles (I: e.g. O3–C2–C1–N1 = 175.4(2)°; III: e.g. O9–C30–C29–N3 = 178.3(2)°). For I and III an antiperiplanar conformation is observed. The oxamato group of **L7a** containing atoms N2, O4, C5, C6, O5, O6 (oxamato group II) and the oxamato group of **L7b** containing atoms N4, O10, C33, C34, O11, O12 (oxamato group IV), respectively, are only roughly planar, since their torsion angles deviate significantly from 180° (II: e.g. N2–C5–C6–O5 = 156.6(2)°; IV: e.g. N4–C33–C34–O11 = 160.1(2)°). Considering, however, II and IV as being planar, these oxamato groups adopt an idealized synperiplanar conformation. The different ideal conformations of the oxamato groups I – IV indicate a free rotatability, without the formation of a π -conjugated system, along their C–C bonds. Indeed, the respective C–C-bond lengths of I – IV, ranging from 1.529(3) Å (IV) to 1.541(3) Å (III), are in the expected range for C–C single bonds [Huheey93]. All carbon atoms of the oxamato groups I – IV are perfectly sp^2 -hybridized.

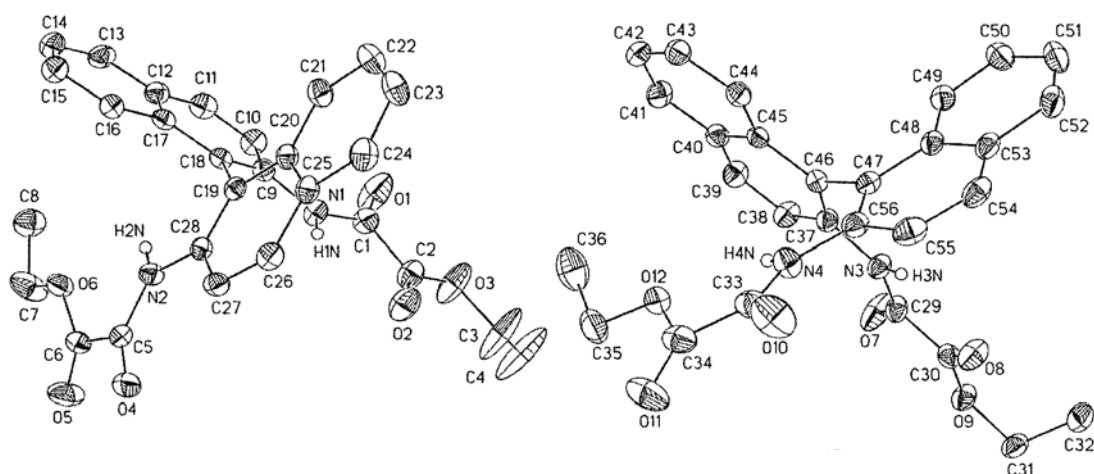


Figure 2.2. ORTEP plot (50% probability level) of the molecular structure of **L7'** with the two crystallographically independent molecules of **L7** (left: **L7a**, right: **L7b**). Hydrogen atoms, except those from NH-groups, as well as one CH₂Cl₂ molecule as packing solvent, are omitted for clarity. Only one position of the disordered atom C4 is shown.

Table 2.1. Selected bond lengths and angles for **L7**.

Bond lengths / Å				Bond angles / °			
C1–C2	1.534(3)	C29–C30	1.541(3)	N1–C1–O1	126.3(2)	N3–C29–O7	128.2(2)
C1–N1	1.345(2)	C29–N3	1.349(2)	N1–C1–C2	111.4(2)	N3–C29–C30	109.6(2)
C1–O1	1.196(2)	C29–O7	1.212(2)	O1–C1–C2	122.4(2)	O7–C29–C30	122.3(2)
C2–O2	1.208(2)	C30–O8	1.207(2)	C1–C2–O2	122.9(2)	C29–C30–O8	122.5(2)
C2–O3	1.313(2)	C30–O9	1.321(2)	C1–C2–O3	110.3(2)	C29–C30–O9	111.3(2)
C5–C6	1.534(3)	C33–C34	1.529(3)	O2–C2–O3	126.8(2)	O8–C30–O9	126.2(2)
C5–N2	1.357(2)	C33–N4	1.348(2)	N2–C5–O4	127.1(2)	N4–C33–O10	126.6(2)
C5–O4	1.214(2)	C33–O10	1.216(2)	N2–C5–C6	112.7(2)	N4–C33–O34	113.0(2)
C6–O5	1.202(2)	C34–O11	1.195(2)	O4–C5–C6	120.2(2)	O10–C33–C34	120.4(2)
C6–O6	1.331(2)	C34–O12	1.340(2)	C5–C6–O5	122.3(2)	C33–C34–O11	123.7(2)
				C5–C6–O6	111.7(1)	C33–C34–O12	110.6(2)
				O5–C6–O6	126.0(2)	O11–C34–O12	125.6(2)

2.5 Mononuclear Cu(II)-*bis*(oxamato) complexes with $\eta^4(\kappa^2N:\kappa^2O)$ coordination geometry

2.5.1 Synthesis of mononuclear $\eta^4(\kappa^2N:\kappa^2O)$ coordinated Cu(II)- and Ni(II)-*bis*(oxamato) complexes

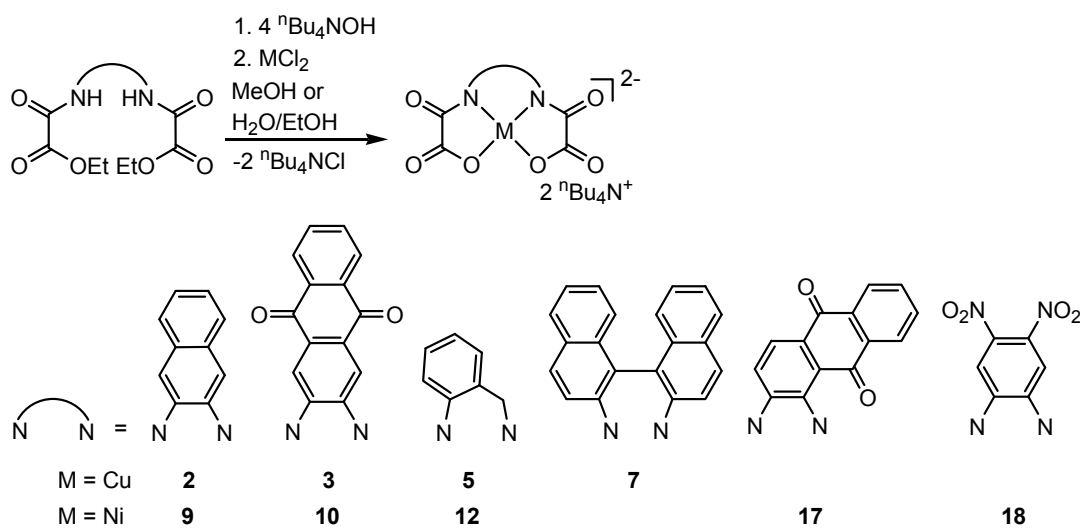
The $\eta^4(\kappa^2N:\kappa^2O)$ coordinated Cu(II)-*bis*(oxamato) complexes, shown in scheme 2.1, are usually prepared by using diethyl-*N,N'*-*bis*(oxamates) which are treated with four equivalents of OH^- [Nonoyama76, Cervera98]. The reaction mixtures are then gently heated until complete dissolution, cooled down to room temperature and subsequently solutions of transition metal salts are added. The formation of Cu(II)-*bis*(oxamato) complexes proceeds thereby at once, accompanied by a colour change. The nature of the intermediate compounds, obtained by the addition of four equivalents of OH^- to diethyl *N,N'*-*bis*(oxamates) has not yet been investigated, although in selected cases the formation of tetraanionic species - due to a twofold deprotonation as well as saponification - has been assumed [Berg02]. Recently, the synthesis of $(^n\text{Bu}_4\text{N})_4[\text{Cu}(\text{endaH})_2]$ (enda = *N,N'*-1,2-ethanediyl-*bis*(oxamato)) showed strong evidence that upon treatment of $\text{endaH}_2\text{Et}_2$ with four equivalents of $(^n\text{Bu}_4\text{N})\text{OH}$ the dianionic species $(^n\text{Bu}_4\text{N})_2[\text{endaH}_2]$ is formed [Rüffer06].

In order to obtain *bis*(oxamato) transition metal complexes possessing largely extended and planar *N,N'*-bridges diethyl *N,N'*-*bis*(oxamates) with anthra-9,10-chinone entities were prepared. As expected, the addition of four equivalents of $(^n\text{Bu}_4\text{N})\text{OH}$ to 2,3-acboH₂Et₂ followed by addition of solutions of Cu(II) and Ni(II) salts, respectively, gave rise to the formation of the *bis*(oxamato) complexes **3** and **10**, as shown in scheme 2.6.

The transition metal ions of **3** and **10** are $\eta^4(\kappa^2N:\kappa^2O)$ coordinated by the $[2,3\text{-acbo}]^{4-}$ ligands as usually observed for $[\textit{bis}(\text{oxamato})]^{4-}$ ligands. Furthermore, upon treatment of 1,2-acboH₂Et₂ with four equivalents of $(^n\text{Bu}_4\text{N})\text{OH}$ followed by the addition of a methanolic solution of $[\text{Ni}(\text{H}_2\text{O})_6]\text{Cl}_2$, complex **17** was obtained as depicted in the scheme 2.6. The Ni(II) ions of **17** are $\eta^4(\kappa^2N:\kappa^2O)$ coordinated by the $[1,2\text{-acbo}]^{4-}$ ligands.

In the following sections the molecular structures of **2**, **3**, **5**, **7**, **9**, **10**, **17**, and **18** will be described. All complexes have been crystallized as $(^n\text{Bu}_4\text{N})^+$ salts, in which the complex anions are more or less spatially extended and π -conjugated. Therefore, intermolecular π - π stacking interactions can be expected. However,

among the solid state structures of all complexes, such interactions are only observed for **17**.



Scheme 2.6. Synthesis strategy.

2.5.2 Solid state structure of $({}^n\text{Bu}_4\text{N})_2[\text{M}(\text{2,3-nabo})]$ (M = Cu(**2**), Ni (**9**))

The molecular structures of **2** and **9** are shown in figure 2.3. Selected bond lengths and bond angles are listed in table 2.2.

The crystal structures of **2** and **9** consist of discrete $({}^n\text{Bu}_4\text{N})^+$ cations and $[\text{M}(\text{nabo})]^{2-}$ anions, respectively. The anionic entities possess crystallographically imposed C_2 symmetry and have an almost planar structure with maximum deviations from the mean molecular planes of 0.065(3) Å (C7 for **2**) and 0.054(2) Å (C4 for **9**), respectively, *cf.* figure 2.3. The metal atoms of **2** and **9** are coordinated to two deprotonated amido nitrogens and two carboxylate oxygens resulting in a $\eta^4(\kappa^2\text{N}:\kappa^2\text{O})$ planar-trapezoidal coordination of the $[\text{nabo}]^{4-}$ ligands. This coordination type is usually observed for related complexes of bis(oxamato) ligands [Tuner95], although exceptions can be observed [Rüffer07, Zhu00]. In agreement with related Cu(II) complexes [Fettouhi96, Cervera98] the Cu1–N1 (amide) bond length (1.887(2) Å) of **2** is significantly shorter compared to the Cu1–O3 (carboxylate) bond length (1.927(2) Å). The same tendency is observed for **9** ($d(\text{Ni1–N1}) = 1.816(2)$ Å vs. $d(\text{Ni1–O3}) = 1.876(2)$ Å). As discussed by Cervera *et al.* [Cervera98] this is due to the greater basicity of the amido nitrogens. Related M–N and M–O distances of **9** are significantly shorter compared to **2**. This fact is also observed for related pairs of bis(oxamato) type complexes [Fettouhi96, Aukauloo99].

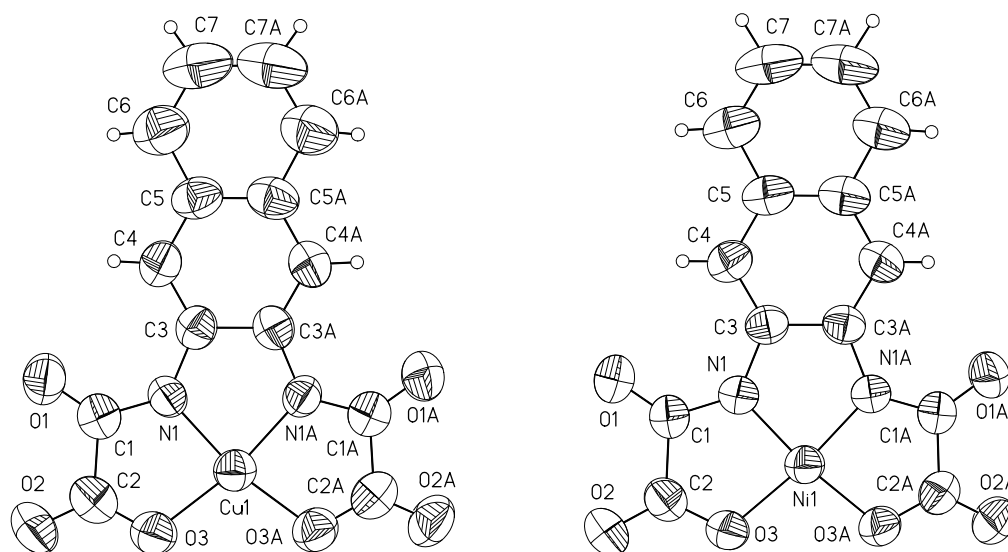


Figure 2.3. ORTEP-plot (50 % probability level) of the molecular structures of **2** (left) and **9** (right). The $n\text{Bu}_4\text{N}^+$ cations have been omitted for clarity.

Table 2.2. Selected bond lengths and angles for **2** and **9**.

Bond lengths / Å				Bond angles / °			
2		9		2		9	
Cu1–N1	1.887(2)	Ni1–N1	1.816(2)	N1–Cu1–N1A	84.1(2)	N1–Ni1–N1A	86.3(1)
Cu1–O3	1.927(2)	Ni1–O3	1.876(2)	N1–Cu1–O3	85.3(1)	N1–Ni1–O3	86.8(8)
N1–C3	1.403(4)	N1–C3	1.408(3)	O3–Cu1–O3A	105.4(2)	O3–Ni1–O3A	100.2(1)
N1–C1	1.326(4)	N1–C1	1.336(3)	N1–Cu1–O3A	169.0(1)	N1–Ni1–O3A	173.0(7)
C1–C2	1.568(5)	C1–C2	1.539(4)	C1–N1–C3	128.3(3)	C1–N1–C3	128.4(2)
O1–C1	1.237(3)	O1–C1	1.232(3)	O1–C1–N1	129.2(3)	O1–C1–N1	128.1(2)
O2–C2	1.220(4)	O2–C2	1.224(3)	O1–C1–C2	121.0(3)	O1–C1–C2	122.7(2)
O3–C2	1.295(4)	O3–C2	1.301(3)	N1–C1–C2	109.8(3)	N1–C1–C2	109.1(2)
				C1–C2–O2	119.2(3)	C1–C2–O2	120.3(2)
				C1–C2–O3	115.9(3)	C1–C2–O3	115.4(2)
				O2–C2–O3	124.8(4)	O2–C2–O3	124.3(2)

Interestingly, the C–C distances of the oxamato groups of **9** and **2** are significantly different (**9**: $d(\text{C1}–\text{C2}) = 1.539(4)$ Å vs. **2**: $d(\text{C1}–\text{C2}) = 1.568(5)$ Å). Together with the different O,N-bite angles of the oxamato groups towards the central metals (**9**: $\text{N1}–\text{Ni1}–\text{O3} = 86.8(8)^\circ$ vs. **2**: $\text{N1}–\text{Cu1}–\text{O3} = 85.3(1)^\circ$) this indicates the structural flexibility of oxamato groups in their coordination of variable metal centres.

2.5.3 Solid state structure of $(n\text{Bu}_4\text{N})_2[\text{M}(\text{2,3-acbo})]$ ($\text{M} = \text{Cu}(\text{3})$, $\text{Ni}(\text{10})$)

The molecular structures of **3** and **10** are shown in figure 2.4. Selected bond lengths and bond angles are listed in table 2.3.

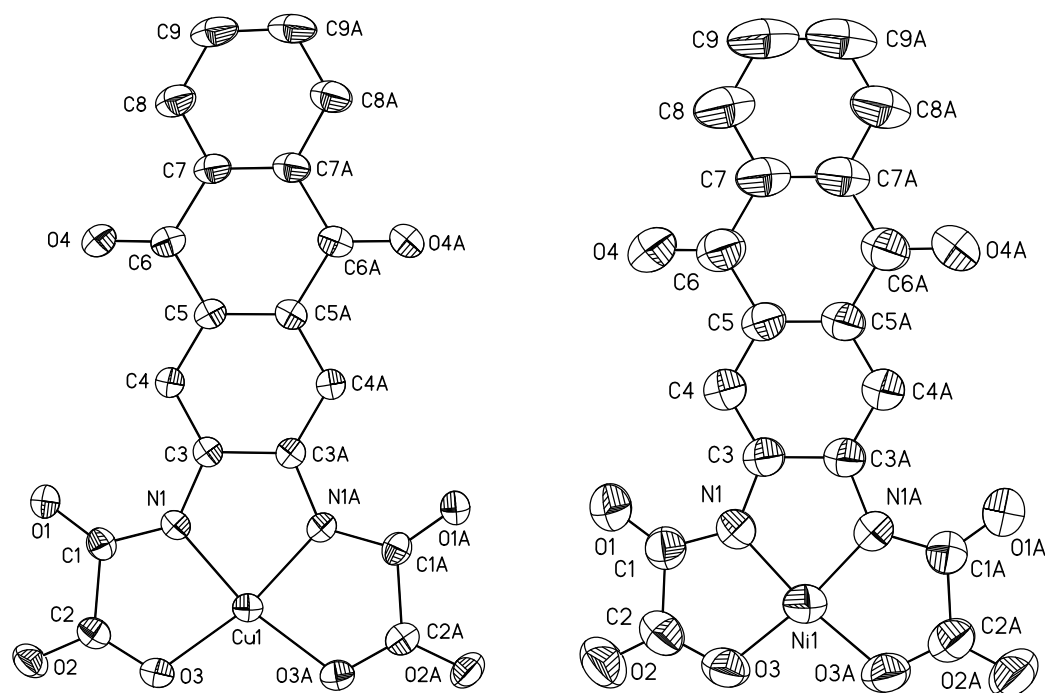


Figure 2.4. Ortep plots (50 % probability level) of the molecular structure of **3** (left) and **10** (right). Hydrogen atoms have been omitted for clarity.

Table 2.3. Selected bond lengths and angles for **3** and **10**.

Bond lengths / Å				Bond angles / °			
3		10		3^{a)}		10^{b)}	
Cu1–N1	1.900(1)	Ni1–N1	1.803(3)	N1–Cu1–N1A	83.56(8)	N1–Ni1–N1A	86.1(2)
Cu1–O3	1.938(1)	Ni1–O3	1.871(3)	N1–Cu1–O3	84.75(5)	N1–Ni1–O3	86.4(1)
N1–C3	1.391(2)	N1–C3	1.393(5)	O3–Cu1–O3A	107.02(7)	O3–Ni1–O3A	101.1(2)
N1–C1	1.341(2)	N1–C1	1.337(5)	N1–Cu1–O3A	168.10(5)	N1–Ni1–O3A	172.4(1)
C1–C2	1.561(2)	C1–C2	1.545(6)	C1–N1–C3	128.3(2)	C1–N1–C3	127.3(3)
O1–C1	1.230(2)	O1–C1	1.231(5)	O1–C1–N1	128.7(2)	O1–C1–N1	128.2(4)
O2–C2	1.228(2)	O2–C2	1.219(5)	O1–C1–C2	122.0(1)	O1–C1–C2	123.0(4)
O3–C2	1.297(2)	O3–C2	1.305(5)	N1–C1–C2	109.3(1)	N1–C1–C2	108.8(4)
C6–O4	1.220(2)	C6–O4	1.228(6)	C1–C2–O2	118.8(2)	C1–C2–O2	120.4(4)
				C1–C2–O3	116.5(1)	C1–C2–O3	114.3(4)
				O2–C2–O3	124.7(2)	O2–C2–O3	125.3(4)

^{a)} Symmetry transformations used to generate equivalent atoms: $-x+2, y, -z+3/2$.

^{b)} Symmetry transformations used to generate equivalent atoms: $-x+1, y, -z+3/2$.

The crystal structure of **3** and **10** consists of discrete ${}^n\text{Bu}_4\text{N}^+$ cations and $[\text{M}(\text{2,3-acbo})]^{2-}$ anions, respectively. The anionic entities possess crystallographically imposed C_2 symmetry and have an almost planar structure with maximum deviations from the mean molecular planes of $-0.069(2)$ Å (C8 for **3**) and $0.057(5)$ Å (C8 for **10**).

The metal ions of **3** and **10** are coordinated to two deprotonated amido nitrogens and two carboxylate oxygens, respectively, resulting in a $\eta^4(\kappa^2\text{N}:\kappa^2\text{O})$ planar-trapezoidal coordination of the $[\text{2,3-acbo}]^{4-}$ ligands. The Cu1–N1 (amide) bond length ($1.900(1)$ Å) of **3** is significantly shorter compared to the Cu1–O3 (carboxylate) bond length ($1.938(1)$ Å). The same tendency is observed for **10**

($d(\text{Ni1-N1}) = 1.803(3) \text{ \AA}$ vs. $d(\text{Ni1-O3}) = 1.871(3) \text{ \AA}$). Related M–N and M–O distances of **10** are significantly shorter compared to **3**. The reasons were already discussed in 2.5.2.

The comparison of structural data of **3** and **10** with a related pair of *bis*(oxamato) complexes, e.g. **2** and **9** (see structural discussion above) reveals very minor differences of related bond lengths and angles. Thus, replacing the central 2,3-naphthalene *N,N'*-bridge of **2** and **9** to the more extended 9,10-anthrachinone *N,N'*-bridge of **3** and **10** and thereby changing its electronic properties does not result in a significantly changed bonding situation of the central metal ions. This was also confirmed by the results of EPR measurements which will be discussed in chapter 3.

2.5.4 Solid state structure of $(^n\text{Bu}_4\text{N})_2[\text{Cu}(\text{obbo})]$ (**5**)

The molecular structure of **5** is shown in figure 2.5. Selected bond lengths and bond angles are listed in table 2.4.

Compound **5** crystallizes in the monoclinic space group C2/c. The crystal structure of **5** consists of discrete $[\text{Cu}(\text{obbo})]^{2-}$ anions and $(^n\text{Bu}_4\text{N})^+$ cations, without any unusual short intermolecular interactions. Along a crystallographically imposed C_2 symmetry, which intersects Cu1, two structurally identical molecules of $[\text{Cu}(\text{obbo})]^{2-}$ anions (**5a** and **5b**, cf. figure 2.5) are statistically disordered.

The two statistically disordered $[\text{Cu}(\text{obbo})]^{2-}$ anions **5a** and **5b**, exhibit analogous bond lengths and angles and therefore only the structure of **5a** will be discussed further. The Cu(II) ion is coordinated to two deprotonated amido nitrogens and two carboxylate oxygens, respectively, resulting in a $\eta^4(\kappa^2\text{N}:\kappa^2\text{O})$ distorted square-planar coordination of the $[\text{obbo}]^{4-}$ ligands. The Cu1 ion deviates by 0.030 Å from a calculated mean plane by the atoms N3A, N2, O4A, and O1 [Zhu00]. Due to the asymmetric *N,N'*-bridge two different Cu–N (amide) ($d(\text{Cu1-N3A}) = 1.889(19) \text{ \AA}$ vs. $d(\text{Cu1-N2A}) = 1.921(19) \text{ \AA}$) and Cu–O (carboxylate) ($d(\text{Cu1-O4A}) = 1.983(16) \text{ \AA}$ vs. $d(\text{Cu1-O1}) = 1.869(17) \text{ \AA}$) bond lengths are observed for **5a**. In analogy to related Cu(II)-*bis*(oxamato) complexes, cf. scheme 2.2, Cu–N (amide) bond lengths are expected to be significantly shorter compared to Cu–O (carboxylate) bond lengths as discussed in 2.5.2. However, in the case of **5a** the expected trend is only observed for the

N–C_{aryl} bonded oxamato unit ($d(\text{Cu1–N3A}) = 1.889(19) \text{ \AA}$ vs. $d(\text{Cu1–O4A}) = 1.983(16) \text{ \AA}$), whereas for the N–C_{alkyl} bonded oxamato unit no significant difference is observed ($d(\text{Cu1–N2}) = 1.921(19) \text{ \AA}$ vs. $d(\text{Cu1–O1}) = 1.869(17) \text{ \AA}$). Similarly to the already discussed Cu(II)-bis(oxamato) complexes the N–C_{aryl} bond distance of **5a** ($d(\text{N3A–C19A}) = 1.38(2) \text{ \AA}$) is significantly shorter compared to the N–C_{alkyl} bond distance ($d(\text{N2–C27}) = 1.461(19) \text{ \AA}$).

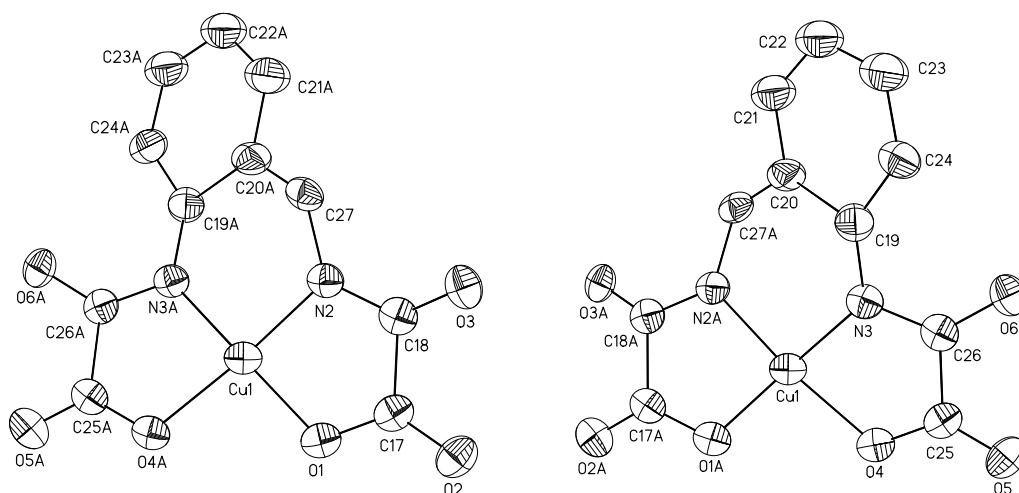


Figure 2.5. ORTEP-plots (25 % probability level) of the two statistically disordered molecules of **5** (left: **5a**, right: **5b**). The $n\text{Bu}_4\text{N}^+$ cations and the hydrogen atoms have been omitted for clarity. Label 'A' refers to symmetry generated atoms of the respective disordered molecule.

Table 2.4. Selected bond lengths and angles for **5a**.^{a)}

Bond lengths ^{b)} / \AA		Bond angles ^{b)} / $^\circ$	
Cu1–N3A	1.889(19)	N3A–Cu1–O1	170.5(6)
Cu1–N2	1.921(19)	N2–Cu1–O4A	166.4(6)
Cu1–O4A	1.983(16)	N3A–Cu1–O4A	84.3(6)
Cu1–O1	1.869(17)	N3A–Cu1–N2	95.2(3)
C25A–C26A	1.562(13)	N2–Cu1–O1	87.1(6)
C18–C17	1.566(13)	O1–Cu1–O4A	95.6(2)
N3A–C26A	1.328(11)	Cu1–N3A–C26A	116.0(10)
O4A–C25A	1.297(11)	Cu1–O4A–C25A	113.0(9)
C25A–O5A	1.205(11)	Cu1–N2–C18	112.5(10)
N3A–C19	1.38(2)	Cu1–O1–C17	113.3(10)
N2–C18	1.323(11)		
C18–O3	1.276(16)		
O1–C17	1.300(11)		
C17–O2	1.212(11)		
N2–C27	1.461(19)		

^{a)} Data for **5b** are analogous to **5a** with respect to the statistical disorder and crystallographical symmetry.

^{b)} Symmetry transformation used to generate equivalent atoms: A: $-x, y, -z+3/2$.

2.5.5 Solid state structure of $(n\text{Bu}_4\text{N})_2[\text{Cu}(\text{R-bnbo})]$ (**7**)

The molecular structure of **7** is shown in figure 2.6. Selected bond lengths as well as bond angles are listed in table 2.5.

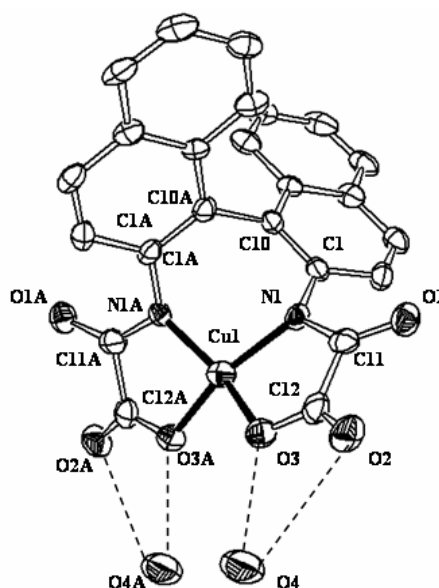


Figure 2.6. ORTEP-plot (50 % probability level) of the molecular structure of **7a**·2H₂O. The H atoms have been omitted for clarity.

Table 2.5. Selected bond lengths and angles.

Bond lengths / Å		Bond angles / °			
Cu1–N1	1.915(3)	N1–Cu1–N1A	99.9(1)	C1–N1–Cu1	120.2(2)
Cu1–O3	1.932(2)	N1–Cu1–O3	85.2(1)	O1–C11–N1	128.9(4)
N1–C1	1.409(5)	N1–Cu1–O3A	158.8(1)	O1–C11–C12	119.4(4)
N1–C11	1.338(5)	O3–Cu1–O3A	97.6(1)	N1–C11–C12	111.7(4)
C11–C12	1.563(6)	C12–O3–Cu1	113.7(3)	C10–C1–N1	121.0(3)
O1–C11	1.248(5)	C1–C10–C10A	122.4(3)	O2–C12–C11	120.0(4)
O2–C12	1.220(5)	C11–N1–C1	121.3(3)	C11–C12–O3	114.2(4)
O3–C12	1.291(5)	C11–N1–Cu1	113.9(2)	O2–C12–O3	125.8(4)
O2···O4 ^{a)}	3.291(4)				
O3···O4 ^{a)}	2.773(4)				

^{a)}O4A is reported by the symmetry operation $y, x, -z$.

The crystal structure of **7** consists of discrete ⁿBu₄N⁺ cations and [Cu(R-bnbo)]²⁻ anions (**7a**), to which two water molecules are connected via hydrogen bonds. Complex **7** crystallizes in the tetragonal chiral space group P4₁2₁2. The [Cu(R-bnbo)]²⁻ anion (**7a**) possesses a crystallographically induced C₂ symmetry with the C₂ axis along Cu1 ion and the centre of the C10–C10A bond. The Cu(II) ion of **7a** is coordinated by two deprotonated amido nitrogens and two carboxylate oxygens resulting in a $\eta^4(\kappa^2N:\kappa^2O)$ coordination. This coordination type is usually observed for related complexes of bis(oxamato) ligands.

The CuN₂O₂ set of the structurally characterized bis(oxamato) type complexes with a $\eta^4(\kappa^2N:\kappa^2O)$ coordination of the central metal ion has been detected so far as almost planar, *cf. e.g.* [Cervera98]. The highest deviation from planarity of

the CuN₂O₂ set has been observed for **6**. The deviation from the N₂O₂ mean plane to which the metal atom belongs to is ± 0.177 Å for the N and ± 0.180 Å for the O atoms resulting in a slight tetrahedral distortion of the Cu(II) environment [Cervera98]. This is furthermore confirmed by the calculation of interplanar angles of the mean planes of the oxamato groups [C11, C12, O1 - O3, N1 (group I); C11A, C12A, O1A - O3A, N1A (group II)] with I : II = 13.5° for **6**.

For **7a** the related interplanar angle was calculated to be $43.8(3)^\circ$ (r.m.s. deviation: 0.091 Å, highest deviation from mean plane: ± 0.144 Å for O3). Thus, the tetrahedral distortion of **7a** is larger compared to **6** and due to steric hindrance of the 2,2'-substituted-[1,1'-binaphthyl] ligand.

Usually, for 2,2'-substituted-[1,1'-binaphthyl] compounds, a nearly cross-arrangement of the two substituted binaphthyl groups is observed in the solid state. For the two ethyl[*N*-1-naphthyl]-2-oxamate groups of **7** and **L7**, such a cross-arrangement is also observed. The interplanar angle from calculations of the mean planes of the non-hydrogen atoms of these groups is $81.52(4)^\circ$ and $83.84(2)^\circ$ for the two crystallographically independent molecules of **L7**. The complexation of Cu decreases this angle to $74.1(3)^\circ$ for **7**.

2.5.6 Solid state structure of ⁿBu₄N₂[Ni(1,2-acbo)]·1/4CH₂Cl₂ (**17**)

The molecular structure of **17** is shown in figure 2.7. Selected bond lengths as well as bond angles are listed in table 2.6.

The crystal structure of **17** consists of discrete ⁿBu₄N⁺ cations, [Ni(1,2-acbo)]²⁻ anions and CH₂Cl₂ molecules as packing solvent. The anionic entity possesses C₁ symmetry and deviate significantly from planarity due to the steric repulsion of the O1 and O8/O8' atoms, *cf.* figure 2.5, with a distance of O1 and O8/O8' of 2.533 and 2.817 Å, respectively.

The Ni(II) ion of **17** is coordinated by two deprotonated amido nitrogens and two carboxylate oxygens, resulting in a $\eta^4(\kappa^2N:\kappa^2O)$ planar-trapezoidal coordination of the [1,2-acbo]⁴⁻ ligands. This coordination type is usually observed for related complexes of *bis*(oxamato) ligands [Tuner95]. In agreement with related Cu(II) complexes [Cervera98, Fettouhi96, Berg02] the bond lengths Ni1–N1 ($d(\text{Ni1–N1}) = 1.826(3)$ Å) and Ni1–N2 ($d(\text{Ni1–N2}) = 1.816(3)$ Å) (amide) of **17** are significantly shorter compared to the Ni1–O3 ($d(\text{Ni1–O3}) = 1.866(3)$ Å) and Ni1–

O6 ($d(\text{Ni1}-\text{O6}) = 1.880(3) \text{ \AA}$) (carboxylate) bond length. The reason was already discussed in 2.5.2.

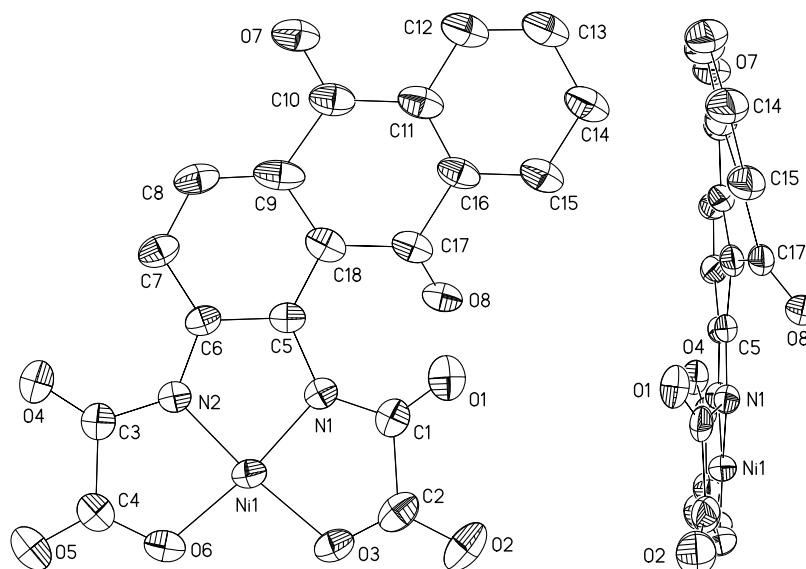


Figure 2.7. Ortep plots (30 % probability level) of the molecular structure of **17** in two different views (left: top view with labels of all atoms, right: side view with labels of selected atoms). Hydrogen atoms as well as disordered atoms have been omitted for clarity.

Table 2.6. Selected bond lengths and angles for **17**.

Bond lengths / \AA				Bond angles / $^\circ$			
Ni1–N1	1.826(3)	Ni1–N2	1.816(3)	N1–Ni1–N2	86.0(1)	O3–Ni1–O6	99.9(1)
Ni1–O3	1.866(3)	Ni1–O6	1.880(3)	N1–Ni1–O6	172.2(1)	N2–Ni1–O3	172.2(1)
N1–C1	1.352(5)	N2–C3	1.341(5)	N1–Ni1–O3	87.8(1)	N2–Ni1–O6	86.2(1)
N1–C5	1.402(4)	N2–C6	1.381(4)	Ni1–N1–C5	114.1(2)	Ni1–N2–C6	115.3(2)
C1–C2	1.582(6)	C3–C4	1.532(6)	Ni1–N1–C1	112.5(2)	Ni1–N2–C3	116.3(2)
C1–O1	1.210(5)	C3–O4	1.232(5)	C1–N1–C5	127.6(3)	C3–N2–C6	127.8(3)
C2–O3	1.264(6)	C4–O6	1.298(5)	N1–C1–O1	129.3(4)	N2–C3–O4	129.0(4)
C2–O2	1.238(5)	C4–O5	1.235(5)	N1–C1–C2	107.8(3)	N2–C3–C4	109.3(3)
C17–O8	1.22(1)	C10–O7	1.24(1)	O1–C1–C2	122.9(4)	O4–C3–C4	121.8(4)
C17'–O8'	1.21(1)	C10'–O7'	1.26(1)	C1–C2–O2	118.2(5)	C3–C4–O5	120.6(4)
				C1–C2–O3	115.7(3)	C3–C4–O6	115.0(4)
				O2–C2–O3	126.1(5)	O5–C4–O6	124.4(4)

2.5.7 Solid state structure of $(^n\text{Bu}_4\text{N})_2[\text{Ni}(\text{nibo})]$ (**18**)

The molecular structure of **18** is shown in figure 2.8. Selected bond lengths and bond angles are listed in table 2.7.

The crystal structure of **18** consists of discrete $^n\text{Bu}_4\text{N}^+$ cations and $[\text{Ni}(\text{nibo})]^{2-}$ anions. Apart from the two NO_2 groups, the $[\text{Ni}(\text{nibo})]^{2-}$ anion possesses a nearly planar structure with the maximum deviation from the mean molecular plane (atoms C1 - C10, N1, N2, Ni1, O1 - O6) of $0.147(3) \text{ \AA}$ observed for O2. The atoms O8 and O9 of the two NO_2 groups exhibit the largest deviation from

the mean molecular plane: they are located 0.845(6) Å and -0.987 (5) Å above and below the molecule plane, respectively.

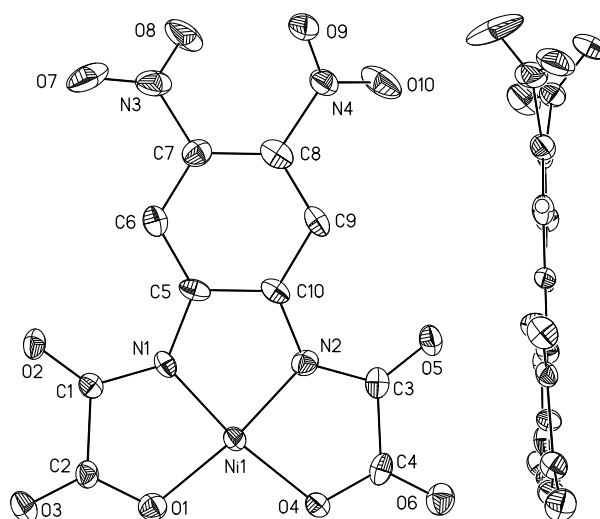


Fig. 2.8. Ortep plots (50 % probability level) of the molecular structure of **18** in two different views (left: top view, right: side view). Hydrogen atoms have been omitted.

Table 2.7. Selected bond lengths and angles for **18**.

Bond lengths / Å				Bond angles / °			
Ni1–N1	1.797(5)	Ni1–N2	1.822(5)	N1–Ni1–N2	85.7(2)	O1–Ni1–O4	101.8(2)
Ni1–O1	1.874(4)	Ni1–O4	1.897(4)	N1–Ni1–O4	171.6(2)	N2–Ni1–O1	172.3(2)
N1–C5	1.399(6)	N2–C10	1.371(7)	N1–Ni1–O1	86.6(2)	N2–Ni1–O4	85.9(2)
N1–C1	1.357(7)	N2–C3	1.357(7)	Ni1–N1–C5	115.6(4)	Ni1–N2–C10	114.4(4)
C1–C2	1.548(7)	C3–C4	1.541(8)	Ni1–N1–C1	116.8(3)	Ni1–N2–C3	116.9(4)
O1–C2	1.289(7)	O4–C4	1.302(6)	Ni1–O1–C2	113.3(3)	Ni1–O4–C4	113.0(3)
O3–C2	1.226(6)	O6–C4	1.224(7)	C1–N1–C5	127.6(5)	C3–N2–C10	128.5(5)
O2–C1	1.228(6)	O5–C3	1.226(6)	N1–C1–O2	127.7(5)	N2–C3–O5	126.8(5)
				N1–C1–C2	108.4(4)	N2–C3–C4	108.9(4)
				O2–C1–C2	123.8(5)	O5–C3–C4	124.3(5)
				O1–C2–C1	114.6(4)	O6–C4–C3	120.4(5)
				O1–C2–O3	126.3(5)	O4–C4–O6	124.5(5)
				O3–C2–C1	119.1(5)	O4–C4–C3	120.4(5)

The Ni(II) ion of **18** is coordinated to two deprotonated amido nitrogens and two carboxylate oxygens, respectively. Thus, the usual $\eta^4(\kappa^2N:\kappa^2O)$ planar-trapezoidal coordination of *bis*(oxamato) ligands is here also observed for the [nibo]⁴⁻ ligands.

The [Ni(nibo)]²⁻ anion possess *C*₁ molecular symmetry, compared to the often observed crystallographically induced *C*₂ molecular symmetry for *bis*(oxamato) complexes [Cervera98]. Due to the *C*₁ molecular symmetry two different Ni–N (1.797(5) Å and 1.822(5) Å) and two different Ni–O (1.874(4) Å and 1.897(4) Å) distances are observed for the NiN₂O₂ fragment. Thus, the Ni(II) ion is

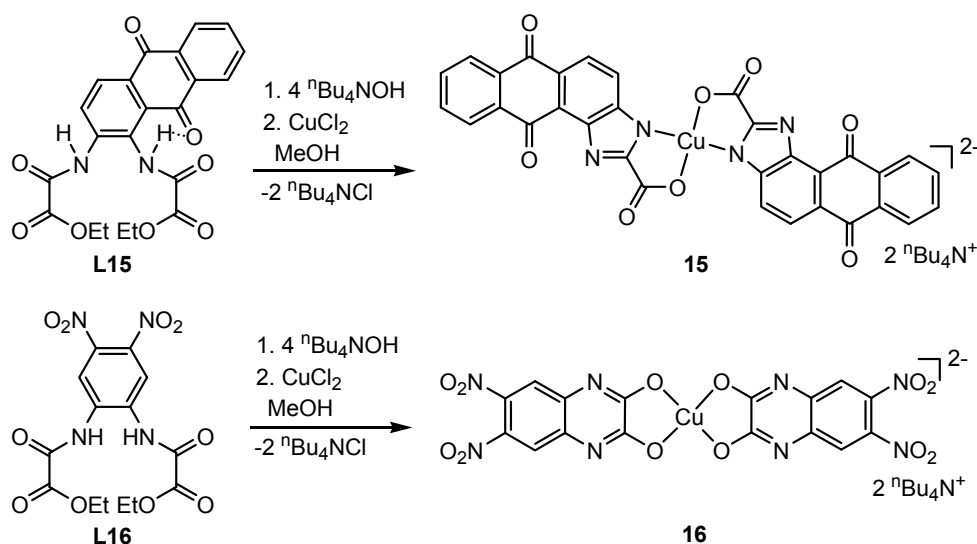
coordinated more strongly by the oxamato group consisting of the atoms C1, C2, N1, O1 - O3, a situation which has been already discussed in 2.5.2.

Compared to related structurally characterized Ni(II)-bis(oxamato) complexes such as **9**, analogous bond lengths and angles show, if at all, very minor differences. This clearly demonstrates, that varying the central *N,N'*-bridge of diethyl *N,N'*-bis(oxamates) can change their reactivity dramatically, without changing the bonding situation of transition metal ions coordinated by the [bis(oxamato)]⁴⁻ ligands.

2.6 Mononuclear Cu(II)-bis(oxamato) complexes deviating from $\eta^4(\kappa^2N:\kappa^2O)$ coordination geometry

2.6.1 Synthesis of (ⁿBu₄N)₂[Cu(aibo)₂] (**15**) and (ⁿBu₄N)₂[Cu(niqo)₂] (**16**)

Surprisingly, the addition of [CuCl₂(H₂O)₂], dissolved in methanol, does not result in the formation of the expected Cu(II) analogue of **17**, but the complex **15** has been formed, *cf.* scheme 2.7. Thus, the addition of Cu(II) ions leads to a transition metal induced derivatisation of the intermediate compound obtained by reacting 1,2-acboH₂Et₂ with four equivalents of (ⁿBu₄N)OH. Such a derivatisation reaction of diethyl *N,N'*-bis(oxamates) during the formation of transition metal complexes has never been described.



Scheme 2.7. Synthesis of **15** and **16**. In **L15** the possible orientations of the hydrogen atoms are illustrated indicating the possible formation of intramolecular hydrogen bonds between the NH group and the O atom of the chinone systeme.

It is reasonable to assume that the addition of four equivalents of OH^- to a solution of 1,2-acboH₂Et₂ results in the formation of the trianionic intermediate compound $[1,2\text{-acboH}]^{3-}$. One NH-bonded proton is most probably involved in an intramolecular $\text{NH}\cdots\text{O}$ hydrogen bond, *cf.* scheme 2.7, and is therefore easy to separate. While Ni(II) ions are insensitive to the formation of hypothetical $[1,2\text{-acboH}]^{3-}$, Cu(II) ions recognize their presence, leading to their derivatisation by formation of an imidazole-2-carboxylate.

As the formation of a hypothetical trianionic intermediate compound already results in a transition metal induced derivatisation of diethyl-*N,N'*-bis(oxamates), we tried to force the formation of a tetraanionic intermediate compound by reacting niboH₂Et₂ with four equivalents of OH^- . The electron withdrawing properties of the two NO_2 -groups of niboH₂Et₂ should therefore be suitable for that purpose. Actually, the addition of four equivalents of (ⁿBu₄N)OH to the slightly yellow solutions of niboH₂Et₂ results in a colour change to orange. Gentle heating of this solution reversibly results in a colour change to dark-red. For ¹H and ¹³C NMR measurements niboH₂Et₂ was treated with four equivalents of NaOH in D₂O giving a clear orange reaction mixture. NMR measurements at room temperature reveals the presence of $[\text{niboH}_2]^{2-}$, $[\text{niboH}]^{3-}$, and $[\text{nibo}]^{4-}$ species and at elevated temperatures, the preferred formation of the $[\text{nibo}]^{4-}$ species. Upon cooling down to room temperature once again a mixture of the di-, tri-, and tetraanionic intermediate compound has been observed. Thus, by using niboH₂Et₂ as starting material, tetraanionic intermediate compounds are accessible, especially at elevated temperatures.

The addition of solutions of Ni(II) and Cu(II) salts, respectively, to heated reaction mixtures of niboH₂Et₂ and four equivalents of (ⁿBu₄N)OH results in the formation of unidentifiable reaction products. At room temperature, however, the addition of Ni(II) salts gave rise to the formation of complex **18**, *cf.* scheme 2.6, in which the Ni(II) ions are $\eta^4(\kappa^2\text{N}:\kappa^2\text{O})$ coordinated by the $[\text{nibo}]^{4-}$ ligands. Intriguingly, the addition of Cu(II) salts at room temperature results in the formation of complex **16**, *cf.* scheme 2.7. Consequently, a further transition metal induced derivatisation reaction of diethyl *N,N'*-bis(oxamates) took place, resulting in a cyclization leading to a Cu(II)-2,3-quinoxalinediolato complex. In analogy to observations made for **4**, Ni(II) ions are insensitive to the formation of either $[\text{niboH}]^{3-}$ or $[\text{nibo}]^{4-}$ intermediate compounds, whereas Cu(II) ions seem

to recognize their formation, leading to derivatisation. An analogous transition metal induced derivatisation reaction has been already reported [Munoz98]. Starting from basic solutions of $\text{opbaH}_2\text{Et}_2$ ($\text{opba} = N,N'$ -*o*-phenylene-bis(oxamato)), the addition of Cu(II) salts results in the formation of the bis(oxamato) type complex $[\text{Cu}(\text{opba})]^{2-}$ [Cervera98], whereas the addition of Fe(III) salts results in the formation of an Fe(III)-2,3-quinoxalinediolato complex [Munoz98].

2.6.2 Solid state structure of $(^n\text{Bu}_4\text{N})_2[\text{Cu}(\text{aibo})_2]$ (**15**)

The molecular structure of **15** is shown in figure 2.9. Bond lengths and bond angles cannot be discussed due to the low completeness of the data obtained from single crystal x-ray analysis. The identity of **15** and the chemical connectivity is, however, verified without doubt.

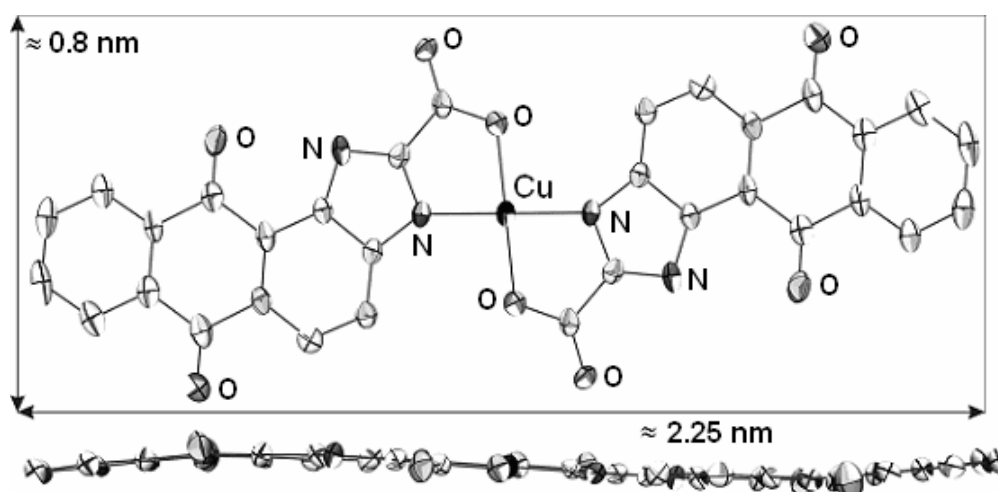


Figure 2.9. ORTEP plot (50 % probability level) of the molecular structure of **15** in two different views (above: top view, below: side view) giving its approximate dimensions. Non-labeled atoms are carbon atoms. Hydrogen atoms and the $^n\text{Bu}_4\text{N}^+$ cations have been omitted for clarity.

The crystal structure of **15** consists of discrete $^n\text{Bu}_4\text{N}^+$ cations and $[\text{Cu}(\text{aibo})_2]^{2-}$ anions. The asymmetric unit comprises two crystallographically independent anionic entities, both possessing a crystallographically imposed inversion symmetry.

The Cu(II) ions of both $[\text{Cu}(\text{aibo})_2]^{2-}$ anions are coordinated by two deprotonated imidazole nitrogens and two carboxylate oxygens, respectively, resulting in a *trans*-bis(aibo-*N,O*) approximately square planar coordination. Thus, the Cu(II)-induced derivatisation leads here to the formation of an imidazole derivate. An

analogous derivatisation of diethyl *N,N'*-bis(oxamates) has never been described. Due to the imidazole formation, however, a novel and potential flexidendate ligand has been obtained. Describing the $[\text{Cu}(\text{aibo})_2]^{2-}$ anions by a rectangular frame, its dimensions reach up to the nanometer range, cf. figure 2.9.

2.6.3 Solid state structure of $(^n\text{Bu}_4\text{N})_2[\text{Cu}(\text{niqu})_2]$ (**16**)

The molecular structure of **16** is shown in figure 2.10. Selected bond lengths and bond angles are listed in table 2.8.

The crystal structure of **16** consists of discrete $^n\text{Bu}_4\text{N}^+$ cations and $[\text{Cu}(\text{niqu})_2]^{2-}$ anions, respectively, whereby the complex anions possess crystallographically imposed inversion symmetry. The Cu(II) ion of **16** is coordinated by four oxygen atoms of the $[\text{niqu}]^{2-}$ anions resulting in an approximately square-planar $\kappa^4\text{O}$ coordination geometry. From a calculated mean plane of the CuO_4 set, the Cu1 ion shows with 0.0516(6) Å the highest deviation from planarity. As observed for a series of closely related $[\text{Cu}(\text{tdpd})]^{2-}$ complexes (tdpd = 1,4,5,6-tetrahydro-5,6-dioxo-2,3-pyrazinedicarbonitrile) [Adachi05], two different Cu–O bond lengths ($d(\text{Cu1–O1}) = 1.904(1)$ Å, $d(\text{Cu1–O2}) = 1.929(1)$ Å) are found for the CuO_4 set. Thus, the Cu–O bond lengths of **16** are in the range of the $[\text{Cu}(\text{tdpd})]^{2-}$ complexes. Furthermore, with respect to the structurally related complex $[\text{FeL}_3]^{3-}$ (L = 2,3-quinoxalinediolate) [Munoz98], the metal–O distances are comparable to those of Cu(II)-catecholates (1.9303(3) and 1.9165(4) Å) [Tapodi06], verifying the description of L within $[\text{FeL}_3]^{3-}$ and of the $[\text{niqu}]^{2-}$ ligands within $[\text{Cu}(\text{niqu})_2]^{2-}$ as 2,3-quinoxalinediolates.

A structural comparison of related bond lengths of **16** with those of 1,4-dihydro-6,7-dinitro-2,3-quinoxalinedione (niquH_2), [Kubicki96] the protonated precursor of the $[\text{niqu}]^{2-}$ ligands, shows that the C–O distances of niquH_2 (1.211(2) and 1.213(2) Å) are explicitly shorter compared to **16** ($d(\text{O1–C1}) = 1.293(2)$ Å, $d(\text{O2–C2}) = 1.294(2)$ Å). Additionally, the central C–C bond (1.522(2) Å) and the C–N bonds (1.362(2) Å and 1.357(2) Å) of the pyrazine-2,3(1*H*,4*H*)-dione entity of niquH_2 are longer than the related bond distances of **16** ($d(\text{C1–C2}) = 1.487(2)$ Å; $d(\text{C1–N1}) = 1.310(2)$ Å and $d(\text{C2–N2}) = 1.312(2)$ Å). A similar observation has been made for the structural comparison of $[\text{FeL}_3]^{3-}$ with 1,4-dihydro-2,3-quinoxalinedione [Munoz98, Svensson76], and shows that the

excess electron density of the $[\text{niqu}]^{2-}$ anions is partially delocalized over their pyrazine-2,3-dionate entity. In contrast to observations made for $[\text{FeL}_3]^{3-}$, the N–C_{aryl} distances of **16** are significantly shorter compared to the related distances of niquH_2 ($d(\text{N1}–\text{C3}) = 1.369(2) \text{ \AA}$, $d(\text{N2}–\text{C8}) = 1.374(2) \text{ \AA}$ vs. $1.392(2)$ and $1.391(2) \text{ \AA}$). This shows that excess electron density, in case of $[\text{niqu}]^{2-}$ anions, is additionally partially delocalized over the dinitro-benzene entity and is evidence for the electron withdrawing properties of the nitro groups.

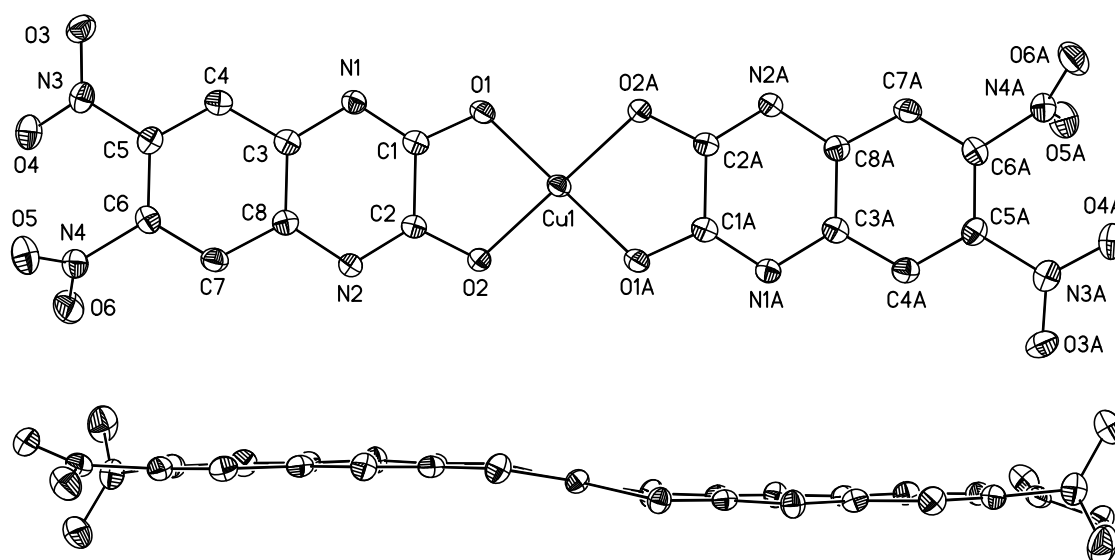


Figure 2.10. ORTEP plots (50 % probability level) of the molecular structure of **16** in two different views (above: top view with labels of all atoms, below: side view with labels of selected atoms). Hydrogen atoms and $^n\text{Bu}_4\text{N}^+$ cations have been omitted.

Table 2.8. Selected bond lengths and angles for **16**.

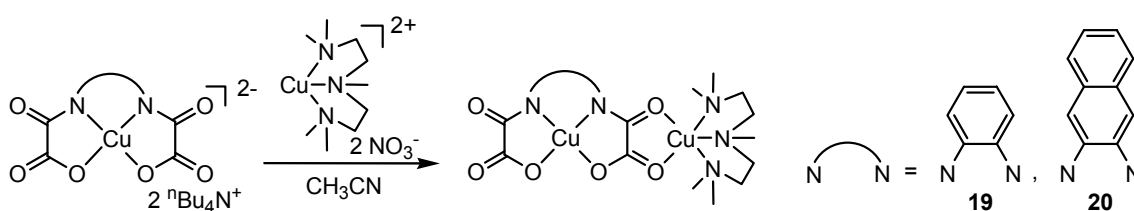
Bond lengths / \AA				Bond angles / $^\circ$			
Cu1–O1	1.904(1)	Cu1–O2	1.929(1)	O1–Cu1–O2	85.98(4)	O1–Cu1–O1A	180.0(1)
O1–C1	1.293(2)	O2–C2	1.294(2)	O1–Cu1–O2A	94.02(4)	O2–Cu1–O2A	180.0(1)
C1–N1	1.310(2)	C2–N2	1.312(2)	Cu1–O1–C1	110.91(9)	Cu1–O2–C2	110.1(1)
N1–C3	1.369(2)	N2–C8	1.374(2)	O1–C1–N1	122.1(1)	O2–C2–N2	121.5(1)
C1–C2	1.487(2)			O1–C1–C2	115.8(1)	O2–C2–C1	115.8(1)

2.7 Dinuclear Cu(II)-bis(oxamato) complexes

2.7.1 Synthesis of dinuclear Cu(II)-bis(oxamato) complexes

The complexes **1** and **2** were used as starting materials for the preparation of binuclear Cu(II)-bis(oxamato) complexes having the formula $[\text{Cu}_2(\text{opba})(\text{pmdta})(\text{MeOH})] \cdot \frac{1}{2}\text{MeOH} \cdot \text{dmf}$ (**19**) and $[\text{Cu}_2(\text{nabo})(\text{pmdta})(\text{MeOH})]$ (**20**, $\text{pmdta} = N,N,N',N'',N''$ -pentamethyldiethylenetriamine, and $\text{dmf} = \text{dimethylformamide}$),

respectively according to the synthesis procedure shown in scheme 2.8. Pure samples of **19** and **20** were only obtained after crystallization of the green powders. It must be emphasized that **19'** and **20'** were never obtained analytically pure. This may be attributed to varying amounts of solvents, based on elemental analysis measurements. However, after crystallization, **19** and **20** can be separated in crystalline form in nearly quantitative yields. The new complexes **19** and **20** were characterized by X-ray crystallography studies, in order to determine possible structural differences induced by their different *N,N'*-bridges.



Scheme 2.8. Synthesis of **19** and **20**.

2.7.2 Solid state structure of [Cu₂(opba)(pmdta)(MeOH)] (**19**)

The molecular structure of **19a** is shown in figure 2.11. Selected bond lengths and bond angles are listed in table 2.9. The structure of **19** consists of neutral, binuclear [Cu₂(opba)(pmdta)(MeOH)] complexes (denoted as **19a**) with the MeOH molecule bonded *via* hydrogen bonds, together with dmf and MeOH molecules as packing solvents. Two molecules of **19a** are connected to each other by the formation of a mutual Cu^{II}...O contact ($d(\text{Cu1}\cdots\text{O1A}) = 2.722 \text{ \AA}$), as shown in figure 2.11. Further unusual short intermolecular distances within the solid state structure of **19** were not observed.

The Cu1 ion of **19a** is coordinated by two deprotonated amido nitrogens (N1 and N2) and two carboxylate oxygens (O1 and O4) of the [opba]⁴⁻ ligand, resulting in an approximately square-planar environment. The Cu1 ion is placed 0.118(2) Å out of a calculated least-square plane of its surrounding N- and O-atoms N1, N2, O1, O4 (r.m.s. deviation from planarity: 0.082 Å) into the direction of one carboxylate oxygen (O1A) from a second complex entity **19a**. As outlined for the mononuclear Cu(II)-bis(oxamato) complexes, *cf.* discussion above, the Cu1–N (amide) bond distances (av. 1.919(6) Å) are significantly shorter compared to the Cu1–O (carboxylate) bond distances (av. 1.973(6) Å). The Cu1 ion is, however, significantly more weakly bonded to the bridging

oxamato group containing the atoms C3, C4, O1 - O3, N2, as shown by the differences in the Cu1–O ($d(\text{Cu1–O1}) = 1.998(4) \text{ \AA}$ vs. $d(\text{Cu1–O4}) = 1.947(4) \text{ \AA}$) as well as Cu1–N ($d(\text{Cu1–N2}) = 1.936(4) \text{ \AA}$ vs. $d(\text{Cu1–N1}) = 1.902(5) \text{ \AA}$) bond distances. The related tendency has been observed for related binuclear Cu(II)-bis(oxamato) complexes [Ribas91].

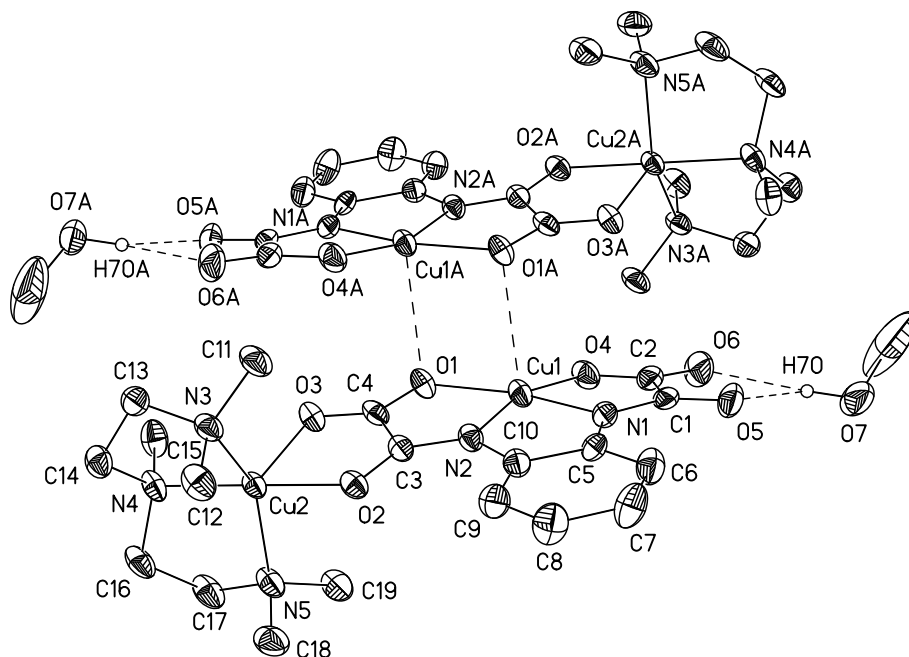


Figure 2.11. Drawing of the dimeric entity of two molecules of **19a** in the solid state together with two MeOH molecules joined by hydrogen bridges. Ellipsoids are drawn at the 50 % probability level. Further packing solvents as well as carbon bonded hydrogen atoms have been omitted.

The terminal Cu2 ion of **19a** is coordinated by three N-donor atoms of the terminal ligand and two O-donor atoms of the oxamato bridge. The τ -parameter has been used as an index to define whether the coordination geometry around fivefold coordinated metal atoms is closer to the ideal square pyramidal ($\tau = 0$) or to the ideal trigonal bipyramidal ($\tau = 1$) type [Addison84]. With $\tau = 0.510$, the coordination geometry around Cu2 can be considered as intermediate between the two possible ideal coordination geometries.

The whole $[\text{Cu}(\text{opba})]^{2-}$ moiety is not flat, as expressed e.g. by the interplanar angle of $15.7(2)^\circ$ of the two oxamato groups I and II (group I: C1, C2, O4-O6, N1; r.m.s. deviation from planarity: 0.04 \AA . group II: C3, C4, O1-O3, N2; r.m.s. deviation from planarity: 0.03 \AA). This is obviously due to the interaction of the molecules of **19a** via intermolecular $\text{Cu}\cdots\text{O}$ contacts, cf. figure 2.11. The $\text{Cu1}\cdots\text{Cu2}$ distance amounts to $5.3275(9) \text{ \AA}$.

2.7.3 Solid state structure of [Cu₂(2,3-nabo)(pmdta)(MeOH)] (20)

The molecular structure of **20** is shown in figure 2.12. Selected bond lengths as well as bond angles are listed in table 2.9.

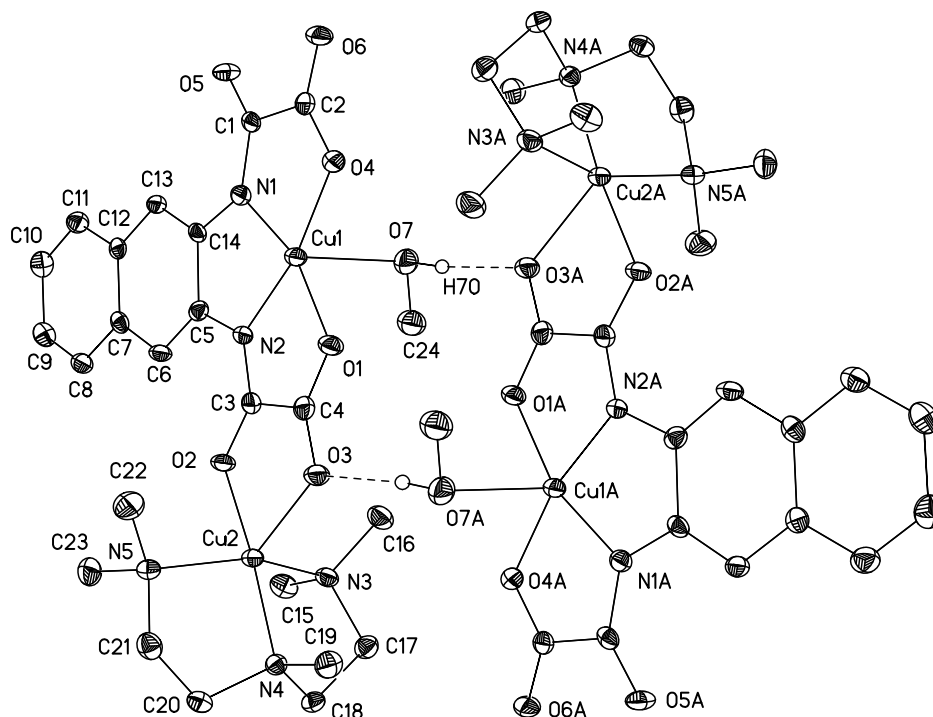


Figure 2.12. Drawing of the dimeric entity of two molecules of **20** in the solid state joined together by hydrogen bridges. Ellipsoids are drawn at the 50 % probability level. Carbon bonded hydrogen atoms have been omitted.

Table 2.9. Selected bond distances and angles for **19a** and **20**.

Bond lengths / Å			Bond angles / °		
	19a	20		19a	20
Cu1–N1	1.902(5)	1.912(2)	N1–Cu1–O1	165.9(2)	163.99(8)
Cu1–N2	1.936(4)	1.921(2)	N1–Cu1–N2	82.4(2)	83.15(8)
Cu1–O1	1.998(4)	2.0345(17)	N1–Cu1–O4	84.6(2)	85.41(8)
Cu1–O4	1.947(4)	1.9335(17)	N2–Cu1–O4	162.6(2)	167.86(8)
Cu1···O1A	2.722	2.4223(19) ¹⁾	N2–Cu1–O1	83.5(2)	82.73(8)
N1–C5	1.405(7)	1.399(3) ²⁾	O1–Cu1–O4	109.0(2)	108.01(7)
N2–C10	1.394(7)	1.410(3) ³⁾	O2–Cu2–N4	178.4(2)	173.51(8)
N1–C1	1.329(7)	1.338(3)	O2–Cu2–N5	93.4(2)	92.32(8)
C1–C2	1.532(9)	1.564(4)	O2–Cu2–N3	91.5(2)	92.41(8)
C1–O5	1.256(7)	1.240(3)	O2–Cu2–O3	80.7(1)	79.73(7)
C2–O4	1.291(7)	1.290(3)	O3–Cu2–N4	100.7(2)	106.76(7)
C2–O6	1.225(7)	1.231(3)	O3–Cu2–N5	97.7(2)	100.85(7)
N2–C3	1.303(7)	1.303(3)	O3–Cu2–N3	114.5(2)	103.21(7)
C3–C4	1.546(8)	1.543(4)	N3–Cu2–N5	147.8(2)	155.94(8)
C3–O2	1.267(6)	1.277(3)	N3–Cu2–N4	87.2(2)	86.31(8)
C4–O1	1.279(6)	1.263(3)	N4–Cu2–N5	87.2(2)	86.35(8)
C4–O3	1.232(7)	1.255(3)	O5···H7O–O7	140(9)	174(3) ⁵⁾
Cu2–O2	1.963(4)	1.9573(17)	O6···H7O–O7	143(8)	
Cu2–O3	2.234(4)	2.2519(17)			
Cu2–N3	2.045(4)	2.047(2)			
Cu2–N4	2.007(5)	2.001(2)			
Cu2–N5	2.055(5)	2.053(2)			
O5···O7	2.765(6)	2.749(3) ⁴⁾			
O6···O7	3.258(7)				

¹⁾ Cu1–O7. ²⁾ N1–C14. ³⁾ N2–C5. ⁴⁾ O3···O7A. ⁵⁾ O3···H7O–O7.

The structure of **20** consists of neutral, binuclear $[\text{Cu}_2(2,3\text{-nabo})(\text{pmdta})(\text{MeOH})]$ complexes. The MeOH molecule is bonded with its oxygen atom O7 to the Cu1 ion of **20** ($d(\text{Cu1-O7}) = 2.4223(19) \text{ \AA}$) and bridges two complexes of **20** via the formation of an intermolecular hydrogen bond ($d(\text{O7}\cdots\text{O3A}) = 2.749(3) \text{ \AA}$), cf. figure 2.12.

The Cu1 ion of **20** is coordinated by two deprotonated amido nitrogens (N1 and N2) and two carboxylate oxygens (O1 and O4) of the $[\text{opba}]^{4-}$ ligand, resulting in an approximately square-planar environment. The Cu1 ion is placed $0.111(1) \text{ \AA}$ out of a calculated least-square plane of its surrounding N- and O-atoms N1, N2, O1, O4 (r.m.s. deviation from planarity: 0.028 \AA) into the direction of the coordinated oxygen atom O7 of the MeOH molecule. As discussed for **19a**, the Cu1–N (amide) bond distances (av. $1.916(3) \text{ \AA}$) are significantly shorter compared to the Cu1–O (carboxylate) bond distances (av. $1.984(2) \text{ \AA}$), attributed to the greater basicity of the amido nitrogens [Cervera98]. The Cu1 ion of **20** is, as observed for **19a**, significantly more weakly bonded to the bridging oxamato group (cf. $d(\text{Cu1-O1}) = 2.0345(17) \text{ \AA}$ vs. $d(\text{Cu1-O4}) = 1.9335(17) \text{ \AA}$) and Cu1–N ($d(\text{Cu1-N2}) = 1.921(2) \text{ \AA}$ vs. $d(\text{Cu1-N1}) = 1.912(2) \text{ \AA}$). In contrast to **19a**, however, all related bond lengths of the two different oxamato groups of **20** (bridging group: C3, C4, N2, O1-O3; non-bridging group: C1, C2, N1, O4-O6) are significantly different. This demonstrates the structural flexibility of oxamato groups when coordinating a transition metal complex. A possible electronic influence of the different *N,N'*-bridges of **20** vs. **19a** cannot be deduced from this structural difference, most probably due to the different bonding of MeOH molecules to the neutral, binuclear complex entities.

The terminal Cu2 ion of **20** is coordinated by three N-donor atoms of the terminal ligand and two O-donor atoms of the oxamato bridge. The τ parameter [Addison84] for Cu2 with $\tau = 0.293$ indicates the coordination geometry around Cu2 is closer to the ideal square pyramidal geometry and significantly different to the τ parameter of Cu2 of **19a** ($\tau = 0.510$).

Whereas the $[\text{Cu}(\text{opba})]^{2-}$ moiety of **19a** was non-planar, the whole $[\text{Cu}(\text{nabo})]^{2-}$ moiety of **20** is quite flat. The calculation of a least-square plane of all non-hydrogen atoms belonging to this moiety gives a r.m.s. deviation from planarity of 0.068 \AA , with the highest deviation observed for O3 with $\pm 0.116(2) \text{ \AA}$. The Cu1 \cdots Cu2 distance amounts to $5.3793(5) \text{ \AA}$.

Furthermore, the analysis of the solid state structure of **20** reveals that the dimeric entities of **20**, *cf.* figure 2.13, are connected via π - π interactions to each other. The interplanar distance of adjacent $[\text{Cu}(\text{nabo})]^{2-}$ complex fragments, related by crystallographically imposed inversion symmetry, amounts to approximately 3.45 Å. In the case of **20** an additional overlap of the phenyl rings is observed. With a distance of ca. 3.45 Å the interaction of neighbored phenyl rings, containing the atoms C5-C7, C12-C14 and symmetry related atoms, can be considered as very strong. Repeating π - π interactions of dimeric entities of **20** results in the formation of an 1D-chain. This situation is depicted in figure 2.13.

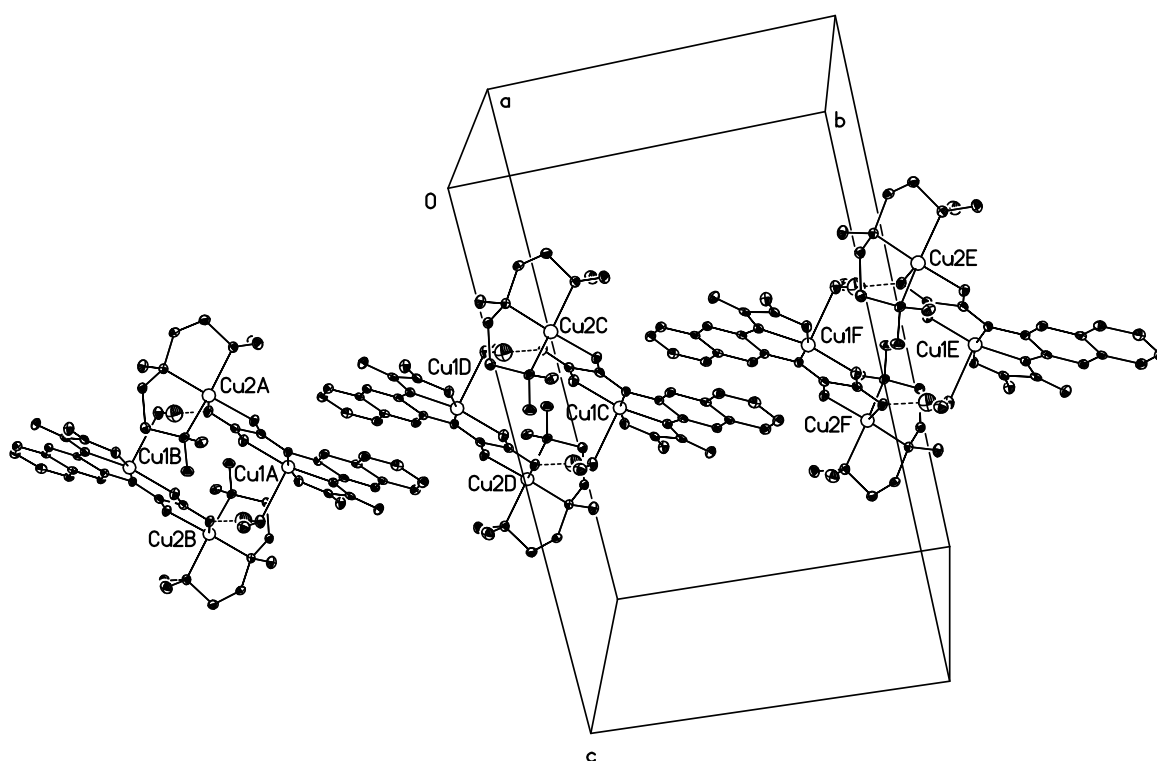


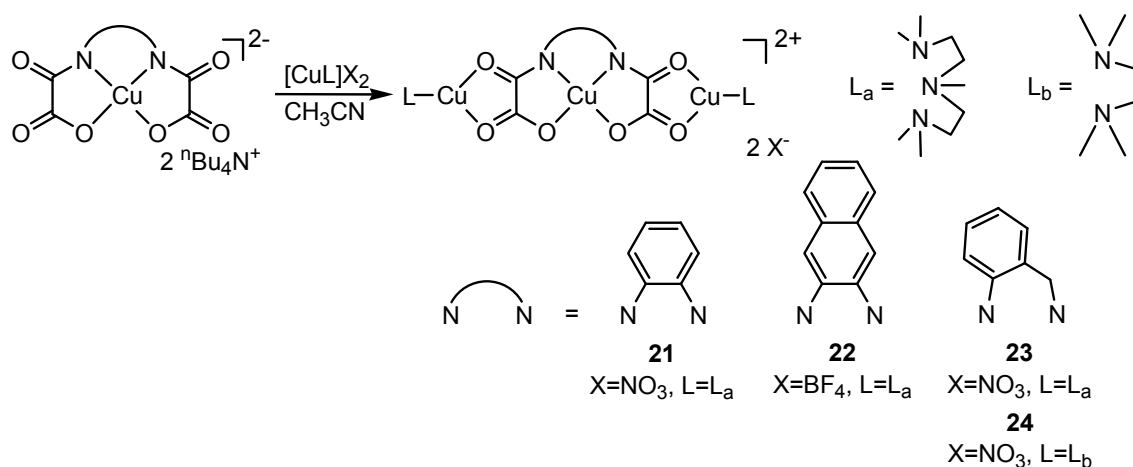
Figure 2.13. Part of the 1D-chain formed by **20** in the solid state. All carbon bonded hydrogen atoms have been omitted for clarity.

2.8 Trinuclear Cu(II)-bis(oxamato) complexes

2.8.1 Synthesis of trinuclear Cu(II)-bis(oxamato) complexes

The complexes **1**, **2**, and **5** were used as starting materials for the preparation of trinuclear Cu(II)-bis(oxamato) complexes shown in scheme 2.9. The new complexes were characterized by X-ray crystallography studies, in order to determine possible structural differences induced by their different N,N' -bridges.

In chapter 3 conclusions will be made regarding how the magnetic properties of the complexes are influenced by their *N,N'*-bridges.



2.8.2 Solid state structure of $[\text{Cu}_3(\text{opba})(\text{pmdta})_2(\text{NO}_3)](\text{NO}_3) \cdot 2\text{MeCN}$ (**21**) and $[\text{Cu}_3(2,3\text{-nabo})(\text{pmdta})_2(\text{BF}_4)](\text{BF}_4) \cdot \text{MeCN} \cdot \text{Et}_2\text{O}$ (**22**)

The structure of **21** consists of cationic trinuclear entities $[\text{Cu}_3(\text{opba})(\text{pmdta})_2(\text{NO}_3)]^+$ (denoted as **21a**), non-coordinated nitrate anions and acetonitrile molecules as packing solvent. The structure of **22** consists of cationic trinuclear entities $[\text{Cu}_3(\text{nabo})(\text{pmdta})_2(\text{BF}_4)]^+$ (denoted as **22a**), non-coordinated tetrafluoroborate anions together with acetonitrile and diethyl ether molecules as packing solvent. For both **21** and **22** no unusual short intermolecular distances were observed. Perspective views of **21a** and **22a** are given in figure 2.14 and 2.15, respectively, selected bond lengths and angles are listed in Table 2.10.

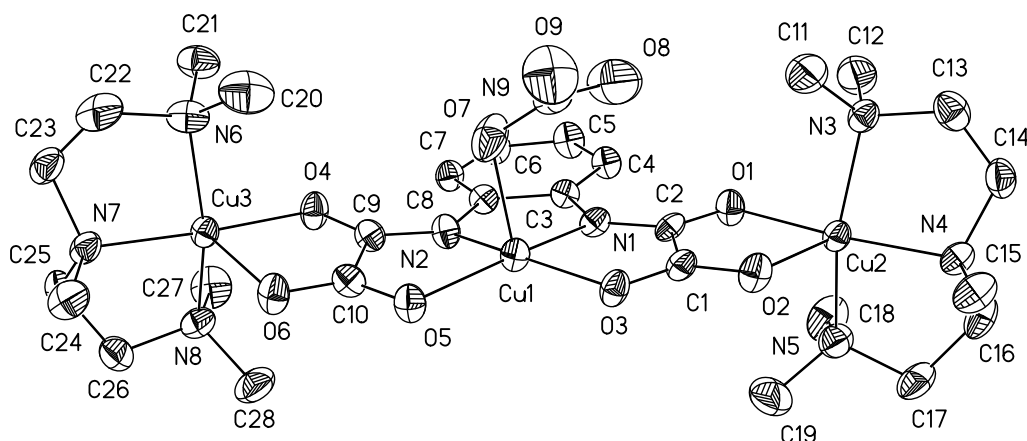


Figure 2.14. ORTEP-plot (50% probability level) of the molecular structure of **21a**. Hydrogen atoms have been omitted for clarity.

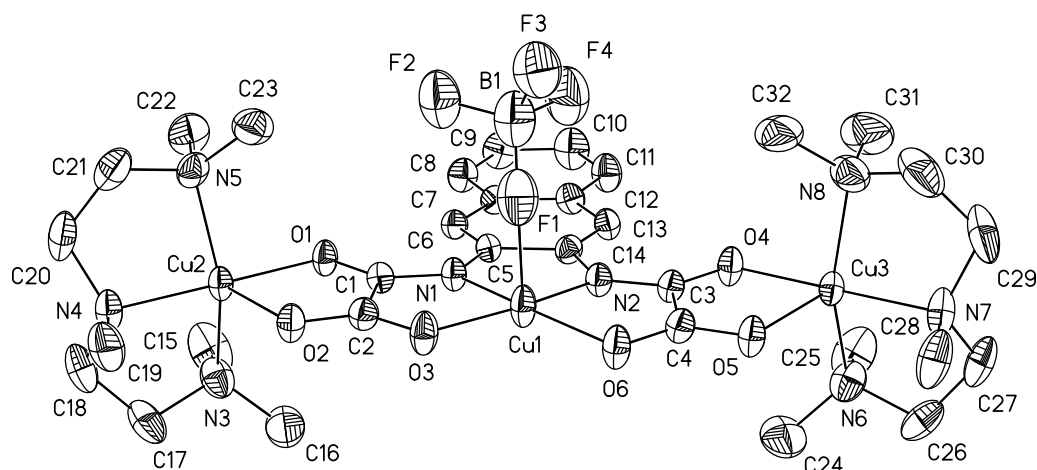


Figure 2.15. ORTEP-plot (50% probability level) of the molecular structure of **22a**. Hydrogen atoms have been omitted for clarity.

Table 2.10. Selected bond lengths and angles for **21** and **22**.

Bond lengths / Å				Bond angles / °			
21		22		21		22	
Cu1–N1	1.930(5)	Cu1–N1	1.914(3)	N2–Cu1–N1	81.6(2)	N2–Cu1–N1	82.5(1)
Cu1–N2	1.927(5)	Cu1–N2	1.924(3)	N1–Cu1–O3	83.8(2)	N1–Cu1–O3	85.1(1)
Cu1–O3	1.991(4)	Cu1–O3	1.967(3)	O5–Cu1–O3	109.7(2)	O6–Cu1–O3	107.1(1)
Cu1–O5	2.006(5)	Cu1–O6	1.966(3)	O5–Cu1–N2	83.1(2)	O6–Cu1–N2	84.9(1)
Cu1–O7	2.298(5)	Cu1–F1	2.42(3)	N2–Cu1–O3	163.4(2)	N2–Cu1–O3	167.2(1)
Cu2–O1	1.966(5)	Cu2–O1	1.973(3)	N1–Cu1–O5	162.0(2)	N1–Cu1–O6	165.9(1)
Cu2–O2	2.258(4)	Cu2–O2	2.219(3)	O1–Cu2–O2	79.7(2)	O1–Cu2–O2	80.6(1)
Cu2–N3	2.040(6)	Cu2–N3	2.040(4)	O1–Cu2–N3	91.4(2)	O1–Cu2–N3	92.2(1)
Cu2–N4	2.006(6)	Cu2–N4	2.005(3)	O1–Cu2–N4	169.2(2)	O1–Cu2–N4	177.9(1)
Cu2–N5	2.047(6)	Cu2–N5	2.039(4)	O1–Cu2–N5	91.7(2)	O1–Cu2–N5	93.3(1)
Cu3–O4	1.960(5)	Cu3–O4	1.984(3)	N3–Cu2–O2	102.6(2)	N3–Cu2–O2	103.3(2)
Cu3–O6	2.262(5)	Cu3–O5	2.187(3)	N4–Cu2–O2	111.0(2)	N4–Cu2–O2	101.4(1)
Cu3–N6	2.073(6)	Cu3–N6	2.034(4)	N5–Cu2–O2	99.5(2)	N5–Cu2–O2	103.7(1)
Cu3–N7	1.987(6)	Cu3–N7	2.000(4)	N4–Cu2–N3	86.3(2)	N4–Cu2–N3	86.7(2)
Cu3–N8	2.059(6)	Cu3–N8	2.041(4)	N3–Cu2–N5	158.0(2)	N3–Cu2–N5	152.9(2)
C1–C2	1.544(8)	C1–C2	1.548(5)	N4–Cu2–N5	86.5(2)	N4–Cu2–N5	86.8(2)
C9–C10	1.550(9)	C3–C4	1.541(5)	O4–Cu3–O6	80.2(2)	O4–Cu3–O5	81.2(1)
C1–O3	1.267(8)	C2–O3	1.267(5)	O4–Cu3–N6	93.6(2)	O4–Cu3–N6	92.1(1)
C1–O2	1.236(8)	C2–O2	1.242(5)	O4–Cu3–N7	172.1(2)	O4–Cu3–N7	177.7(2)
C10–O5	1.267(8)	C4–O6	1.265(5)	O4–Cu3–N8	91.1(2)	O4–Cu3–N8	93.8(2)
C10–O6	1.246(8)	C4–O5	1.250(5)	N6–Cu3–O6	99.6(2)	N6–Cu3–O5	102.2(1)
				N7–Cu3–O6	107.6(2)	N7–Cu3–O5	100.9(1)
				N8–Cu3–O6	100.5(2)	N8–Cu3–O5	103.3(1)
				N7–Cu3–N6	86.1(2)	N7–Cu3–N6	86.5(2)
				N6–Cu3–N8	159.9(2)	N6–Cu3–N8	154.4(2)
				N7–Cu3–N8	86.6(2)	N7–Cu3–N8	86.7(2)

The central Cu1 atoms of **21a** and **22a**, respectively, are coordinated by two deprotonated amido nitrogens and two carboxylate oxygens of their [opba]⁴⁻ (**21a**) and [nabo]⁴⁻ (**22a**) ligands. Furthermore, in the case of **21a** one nitrate anion and in case of **22a** one tetrafluoroborate anion is weakly bound to the central Cu1 atoms, resulting in approximately square-pyramidal coordinations. The Cu1 atoms of **21a** and **22a** are located 0.173(2) Å and 0.089(2) Å, respectively, above a calculated mean plane of their coordinating N₂O₂ frag-

ments. For the central CuN_2O_2 complex fragments of **21a** and **22a**, respectively, no significant difference between the averaged Cu1–N distances is observed. However, the averaged Cu1–O distance of **21a** (1.998(6) Å) is significantly shorter compared to the averaged Cu1–O distance of **22a** (1.966(4) Å). As discussed for the mononuclear precursors **1** and **2** of **21a** and **22a**, respectively, the different Cu1–O distances might indicate an influence of the different central *N,N'*-bridges of **21a** and **22a**. It is, however, also possible that this difference is due to the different, weakly coordinating anions towards Cu1 in **21a** and **22a**.

The terminal Cu atoms of **21a** and **22a**, respectively, are coordinated by three *N*-donor atoms of the terminal ligands and two *O*-donor atoms of the oxamato bridges. Two parameters, Δ [Galy79] and τ [Addison84], have been frequently used as an index to define whether the coordination geometry around five-coordinated metal atoms is closer to the ideal square pyramidal ($\Delta = 1$, $\tau = 0$) or to the ideal trigonal bipyramidal ($\Delta = 0$, $\tau = 1$) type. The τ parameter was calculated by subtracting the second largest from the largest bond angle and dividing the difference by 60° . Table 2.11 shows that the coordination type of the terminal Cu atoms of **21a** and **22a**, respectively, is closer to trigonal bipyramidal. However, noticeable differences exist between **21a** and **22a**. Most probably, the different Δ and τ parameters of **21a** and **22a** are due to packing effects within the solid state structures of **21** and **22**, respectively.

Table 2.11. Experimental values of the geometric Δ and τ parameters for terminal Cu(II) ions in **21** and **22**.

21			22		
	Cu2	Cu3	Cu2	Cu3	
Δ	0.439	0.434	0.241	0.284	
$\langle\Delta\rangle^{\text{a)}$	0.436		0.262		
τ	0.187	0.203	0.417	0.388	
$\langle\tau\rangle^{\text{a)}$	0.195		0.402		

^{a)} The averaged values $\langle\Delta\rangle$ and $\langle\tau\rangle$ are additionally given.

Figure 2.16 shows the superimposition of the molecular structures of **21a** and **22a**, respectively, without their weakly coordinating anions. The variable bonding situation around the terminal Cu atoms can be clearly seen together with, for example, the different orientations of the two oxamato bridges of **21a** and **22a**, respectively, to each other. This is confirmed by the calculation of the interplanar angles of the mean planes of the oxamato groups of **21a** (C1, C2,

O1 - O3, N1 (group I); C9, C10, O4 - O6, N2 (group II); I : II = 7.4(3)°) and **22a** (C1, C2, O1 - O3, N1 (group I); C3, C4, O4 - O6, N2 (group II); I : II = 6.0(2)°).

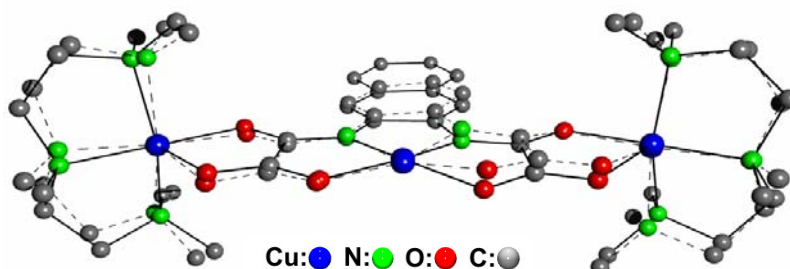


Figure 2.16. Superimposition of the molecular structures of **21a** (dotted line) and **22a** (full line), without their weakly coordinating anions and hydrogen atoms.

Related bond lengths of the Cu2 and Cu3 atoms in either **21a** or **22a** do not show significant differences, except the Cu–O bonds to the carboxylate group of the [nabo]⁴⁻ ligand in **22a** ($d(\text{Cu2}–\text{O2}) = 2.219(3) \text{ \AA}$ vs. $d(\text{Cu2}–\text{O5}) = 2.187(3) \text{ \AA}$). The average of these C–O bond lengths of **22a** is significantly shorter in comparison with the related bond lengths of **21a** (**22a**: $\bar{d}(\text{C}–\text{O}) = 2.203(4) \text{ \AA}$ vs. **21a**: $\bar{d}(\text{C}–\text{O}) = 2.260(6) \text{ \AA}$). This difference could be induced by the different bonding of the carboxylate groups of the [opba]⁴⁻ and [nabo]⁴⁻ ligands in **21a** and **22a**, respectively, to the central Cu2 atoms. Related bond lengths of the carboxylate groups of **21a** and **22a** are, however, identical within the standard deviations. Thus, based on related structural parameters an electronic influence of the different *N,N'*-bridges of **21a** and **22a**, respectively, cannot be clearly inferred. The intermolecular Cu···Cu distances across the oxamato bridges are noticeably longer for **21a** ($d(\text{Cu1} \cdots \text{Cu2}) = 5.336(1) \text{ \AA}$, $d(\text{Cu1} \cdots \text{Cu3}) = 5.318(1) \text{ \AA}$) compared with **22a** ($d(\text{Cu1} \cdots \text{Cu2}) = 5.2969(7) \text{ \AA}$, $d(\text{Cu1} \cdots \text{Cu3}) = 5.2772(7) \text{ \AA}$).

2.8.3 Solid state structure of [Cu₃(obbo)(pmdta)₂(NO₃)](NO₃)·CH₂Cl₂·H₂O (**23**) and [Cu₃(obbo)(tmeda)₂(NO₃)₂(dmf)] (**24**)

The structure of **23** consists of cationic trinuclear entities [Cu₃(obbo)(pmdta)₂-(NO₃)]⁺ (denoted as **23a**), non-coordinated nitrate anions, dichloromethane, and water molecules as packing solvents. The structure of **24** consists of neutral trinuclear entities [Cu₃(obbo)(tmeda)₂(NO₃)₂(dmf)] (**24**, tmeda = *N,N,N',N'*-tetramethylethylenediamine). For both **23a** and **24** no unusual short intermolecular distances were observed. Perspective views of **23a** and **24**,

showing the atomic labelling are given in Figure 2.17 and 2.18, respectively, selected bond lengths and angles are listed in Table 2.12.

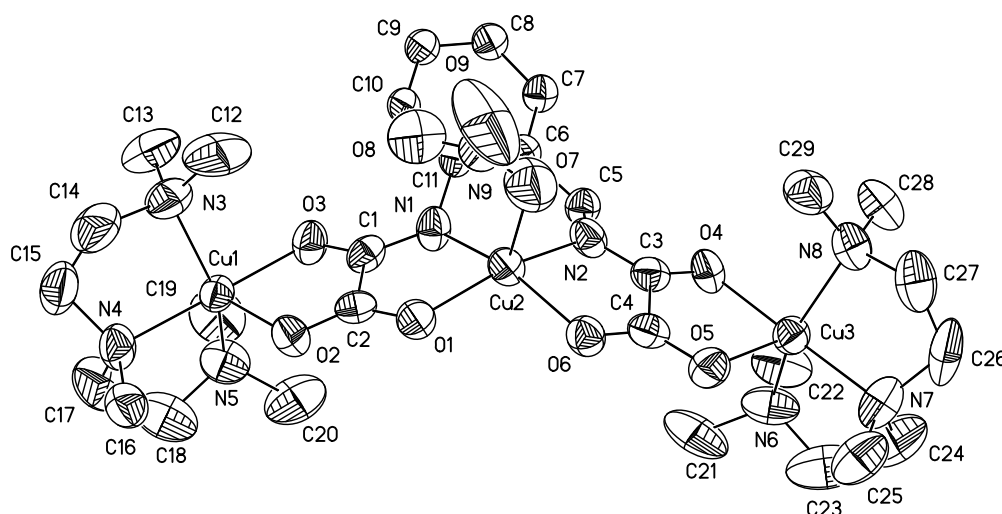


Figure 2.17. ORTEP-Plot (50 % probability level) of the molecular structure of **23a**. Hydrogen atoms as well as disordered atoms (C5' – C11') have been omitted for clarity.

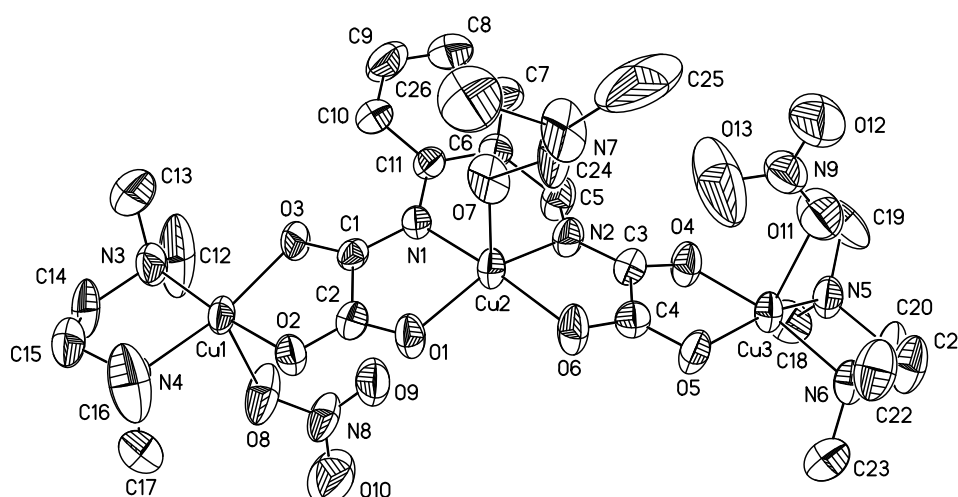


Figure 2.18. ORTEP-Plot (50 % probability level) of the molecular structure of **24**. Hydrogen atoms as well as disordered atoms (C20' and C21', O7', N7', C24' – C26') have been omitted for clarity.

Homotrinnuclear Cu(II)-bis(oxamato) type complexes consisting of discrete trinuclear entities in the solid state have so far only been synthesized with symmetric *N,N'*-bridges. As outlined for **21** and **22**, in the latter class of complex the oxamato units have near-planar orientation to each other, introduced by the planar and non-flexible *N,N'*-*o*-phenylene bridge. Calculated interplanar angles (δ_p) between their $\text{Cu}^{\text{II}}(\text{O}_3\text{C}_2\text{N})\text{Cu}^{\text{II}}$ vs. $\text{Cu}^{\text{II}}(\text{N}'\text{C}'_2\text{O}'_3)\text{Cu}^{\text{II}}$ units are therefore relatively small, ranging from $\delta_p = 4.4^\circ$ ($[\text{Cu}_3(\text{opba})(\text{tmeda})_2(\text{H}_2\text{O})_2]^{2+}$) [Gao01] to

$\delta_p = 7.9^\circ$ ($[\text{Cu}_3(\text{opba})(\text{tmeda})_2(\text{H}_2\text{O})_2]^{2+}$) [Tercero01]. In the case of *N,N'*-1,3-propylene bridged complexes, analogous interplanar angles range from $\delta_p = 0.8^\circ$ ($[\text{Cu}_3(\text{pba})(\text{phen})_2(\text{H}_2\text{O})(\text{dmsO})_2]^{2+}$, pba = 1,3-propylene-bis(oxamato), phen = 1,10-phenanthroline) [Wang02] up to $\delta_p = 36.8^\circ$ ($[\text{Cu}_3(\text{pba})(\text{bapa})_2(\text{H}_2\text{O})]^{2+}$, bapa = bis(3-aminopropyl)amine) [Costa93]. Thus, *N,N'*-1,3-propylene bridged complexes do already show distinctive deviations from planarity. Due to the non-planar molecular structure of **5a**, significant deviations from planarity were expected for **23a** and **24**. Indeed, analogous calculations of the interplanar angles described above yielded the values of $\delta_p = 27.7(1)^\circ$ (**23a**) and $\delta_p = 29.4(1)^\circ$ (**24**), respectively. These angles fall in the range reported for *N,N'*-1,3-propylene bridged complexes.

Table 2.12. Selected bond lengths and angles for **23a** and **24**.

Bond lengths / Å				Bond angles / °			
23a		24		23a		24	
Cu1–N3	2.050(7)	Cu1–N3	2.004(5)	O3–Cu1–N3	93.7(3)	O3–Cu1–N3	92.5(2)
Cu1–N4	2.014(7)	Cu1–N4	2.029(5)	O3–Cu1–N4	177.9(3)	O3–Cu1–N4	164.4(2)
Cu1–N5	2.045(7)	Cu1–O8	2.292(5)	O3–Cu1–N5	92.4(3)	O3–Cu1–O2	84.55(16)
Cu1–O3	1.975(6)	Cu1–O3	1.967(4)	O3–Cu1–O2	80.7(2)	O2–Cu1–N3	170.9(2)
Cu1–O2	2.177(5)	Cu1–O2	1.966(4)	O2–Cu1–N3	101.5(3)	O2–Cu1–N4	93.48(19)
Cu2–N1	1.925(6)	Cu2–N1	1.951(5)	O2–Cu1–N4	101.2(2)	N3–Cu1–N4	87.0(2)
Cu2–N2	1.949(6)	Cu2–N2	1.935(5)	O2–Cu1–N5	109.1(3)	O1–Cu2–N2	155.3(2)
Cu2–O1	1.976(5)	Cu2–O1	1.979(4)	N3–Cu1–N4	86.6(3)	O1–Cu2–N1	85.36(18)
Cu2–O6	1.989(5)	Cu2–O6	1.992(4)	N3–Cu1–N5	149.3(4)	O1–Cu2–O6	93.92(17)
Cu2–O7	2.288(7)	Cu2–O7	2.43(3)	N4–Cu1–N5	86.2(3)	O6–Cu2–N1	170.4(2)
		Cu2–O7'	2.13(3)				
Cu3–O4	1.963(6)	Cu3–O4	1.945(4)	N1–Cu2–N2	92.3(3)	O6–Cu2–N2	83.23(18)
Cu3–O5	2.196(6)	Cu3–O5	1.969(4)	N1–Cu2–O1	84.3(2)	N1–Cu2–N2	93.4(2)
Cu3–N6	2.057(7)	Cu3–N6	2.018(5)	N1–Cu2–O6	161.5(3)	N1–Cu2–O7	97.8(10)
						N1–Cu2–O7'	99.9(9)
Cu3–N7	2.001(8)	Cu3–N5	2.018(5)	N2–Cu2–O1	165.2(3)	O1–Cu2–O7	97.5(12)
						O1–Cu2–O7'	90.5(9)
Cu3–N8	2.061(7)	Cu3–O11	2.281(5)	N2–Cu2–O6	84.1(2)	O6–Cu2–O7	91.8(10)
						O6–Cu2–O7'	89.7(9)
C1–C2	1.535(10)	C1–C2	1.534(8)	O1–Cu2–O6	94.5(2)	O7'–Cu2–O7	7.5(19)
C3–C4	1.560(10)	C3–C4	1.515(9)	N1–Cu2–O7	114.1(3)	O4–Cu3–N5	92.29(19)
C1–O3	1.265(9)	C1–O3	1.257(6)	N2–Cu2–O7	100.2(3)	O4–Cu3–N6	168.6(2)
C1–N1	1.306(10)	C1–N1	1.323(7)	O1–Cu2–O7	94.3(3)	O4–Cu3–O5	84.56(17)
C2–O2	1.236(9)	C2–O2	1.260(7)	O6–Cu2–O7	84.4(3)	O5–Cu3–N5	162.8(2)
C2–O1	1.264(9)	C2–O1	1.245(7)	O4–Cu3–N6	92.3(3)	O5–Cu3–N6	92.46(19)
C3–N2	1.298(10)	C3–N2	1.288(7)	O4–Cu3–N7	178.4(3)	N5–Cu3–N6	87.3(2)
C3–O4	1.258(9)	C3–O4	1.274(7)	O4–Cu3–N8	92.7(3)		
C4–O5	1.237(9)	C4–O5	1.258(7)	O4–Cu3–O5	81.1(2)		
C4–O6	1.254(10)	C4–O6	1.245(7)	O5–Cu3–N6	105.3(3)		
N1–C11	1.545(11)	N1–C11	1.422(8)	O5–Cu3–N7	100.5(3)		
N2–C5	1.47(2)	N2–C5	1.469(8)	O5–Cu3–N8	102.3(3)		
				N6–Cu3–N7	86.9(4)		
				N6–Cu3–N8	152.4(3)		
				N7–Cu3–N8	87.3(3)		

The central Cu2 ions of **23a** and **24**, respectively, are coordinated by two deprotonated amido nitrogens and two carboxylate oxygens of the [obbo]⁴⁻

ligands. In the case of **23a**, one nitrate anion and for **24**, one disordered dmf molecule, is bonded through its oxygen atom to the central Cu₂ atom (**23a**: $d(\text{Cu}_2\text{-O}7) = 2.288(7) \text{ \AA}$; **24**: $d(\text{Cu}_2\text{-O}7) = 2.43(3) \text{ \AA}$, $d(\text{Cu}_2\text{-O}7') = 2.13(3) \text{ \AA}$). Thus, the coordination number of the Cu₂ atoms of both **23a** and **24** is five with a coordination geometry close to the ideal trigonal bipyramidal type, as expressed by the τ parameter (**23a**: $\tau = 0.062$; **24**: $\tau = 0.252$. $\tau = 0$: ideal square pyramidal, $\tau = 1$: ideal trigonal bipyramidal coordination geometry). The coordination of the nitrate anion (**23a**) and the dmf molecule (**24**), respectively, results in a significant delocalization of the central metal ions from an ideal square-planar N₂O₂ environment of their donor atoms. The metal ions are located 0.289(3) Å (**23a**) and 0.291 Å (**24**), respectively, above a calculated mean plane of their N1, N2, O1, O6 donor atoms compared to 0.030 Å for **5**.

The terminal copper(II) ions of **23a** (Cu1 and Cu3) are coordinated by three N-donor atoms of the terminal ligands and two O-donor atoms of the oxamato bridges. This results in five-coordinated metal ions with a coordination geometry intermediate between the ideal square pyramidal and ideal trigonal bipyramidal type (Cu1: $\tau = 0.477$. Cu3: $\tau = 0.455$). In complex **24** the terminal copper(II) ions (Cu1 and Cu3) are coordinated by two N-donor atoms of the terminal ligands and two O-donor atoms of the oxamato bridges. Furthermore, each of the Cu1 and Cu3 metal ions coordinate one nitrate anion, resulting in five-fold coordinated metal ions with a coordination geometry very close to the ideal square pyramidal type (Cu1: $\tau = 0.097$. Cu3: $\tau = 0.108$).

The intermolecular Cu...Cu distances across the oxamato bridges are noticeably longer for **23a** ($d(\text{Cu}1\cdots\text{Cu}2) = 5.2960(14) \text{ \AA}$, $d(\text{Cu}2\cdots\text{Cu}3) = 5.3007(14) \text{ \AA}$) in comparison with **24** ($d(\text{Cu}1\cdots\text{Cu}2) = 5.1708(10) \text{ \AA}$, $d(\text{Cu}2\cdots\text{Cu}3) = 5.1708(10) \text{ \AA}$).

2.9 Summary and Conclusions

The molecules **L2**, **L3**, **L5**, **L7**, **L15**, and **L16** were synthesized. Moreover, the mononuclear Cu(II)- and Ni(II)-bis(oxamato) complexes **2**, **3**, **5**, **7**, **9**, **10**, **15**, **16**, **17**, and **18** were synthesized and structurally characterized. Most of them show a $\eta^4(\kappa^2\text{N}:\kappa^2\text{O})$ coordination. Exceptions were observed for the reaction of **L7** with a base and a Ni(II) salt. Due to the strong deviation of **L7** from the square planar coordination geometry resulting in a distorted tetrahedral one, the

chelating effect is too weak for coordinating Ni(II). The treatment of **L15** and **L16** with a base and a transition metal salt leads to the expected product for Ni(II) which is then square planar coordinated. In contrast, the Cu(II) salt leads to the formation of the novel quinoxalinedionato derivative **15** and the formation of an imidazole derivative **16** which indicates the influence of the transition metals and the electronic properties of the *N,N'*-bridge on the reaction products. Consequently, it was shown that selective variations of the central *N,N'*-bridge of diethyl *N,N'*-*bis*(oxamates) can lead to a transition metal induced derivatisation in the course of the formation of transition metal complexes. On the one hand, the observed derivatisation reactions depend most likely on the nature of intermediate compounds obtained after addition of four equivalents of OH⁻ to diethyl *N,N'*-*bis*(oxamates). On the other hand, they clearly depend on the kind of transition metal ions added to such reaction mixtures. Our results strongly suggests that Ni(II) ions are insensitive to the presence of either di-, tri- and/or tetraanionic intermediate compounds, whereas Cu(II) ions delicately recognize their presence.

With the synthesis of complex **3** and **15** we have already achieved mononuclear *bis*(oxamato) complexes for the synthesis of multinuclear *bis*(oxamato) complexes. They possess a largely extended and planar central *N,N'*-bridge which is one requirement for the formation of preferentially oriented thin films by spin-coating.

With **7** the first enantiopure Cu(II)-*bis*(oxamato) complex has been synthesized. Due to the extremely high tetrahedral distortion induced by the *N,N'*-bridge, **7** is a valuable system for bench-marking theoretical studies. The obtained structural parameters of **1** to **7**, see figure 2.19, necessary for the discussion in chapter 3, are summarized in table 2.13.

Furthermore, di- and trinuclear Cu(II)-*bis*(oxamato) complexes (**19** to **24**) were synthesized and structurally characterized, cf. figure 2.20. The Cu(II) ions of **21** and **22** are aligned in one plane, while for **23** and **24** they are tilted by around 28°. **21** and **22** have a different bonding situation, especially in the terminal ligand system, which is due to packing effects. The differences in geometry were quantified by the geometry parameter τ , see section 2.8.2 and table 2.14.

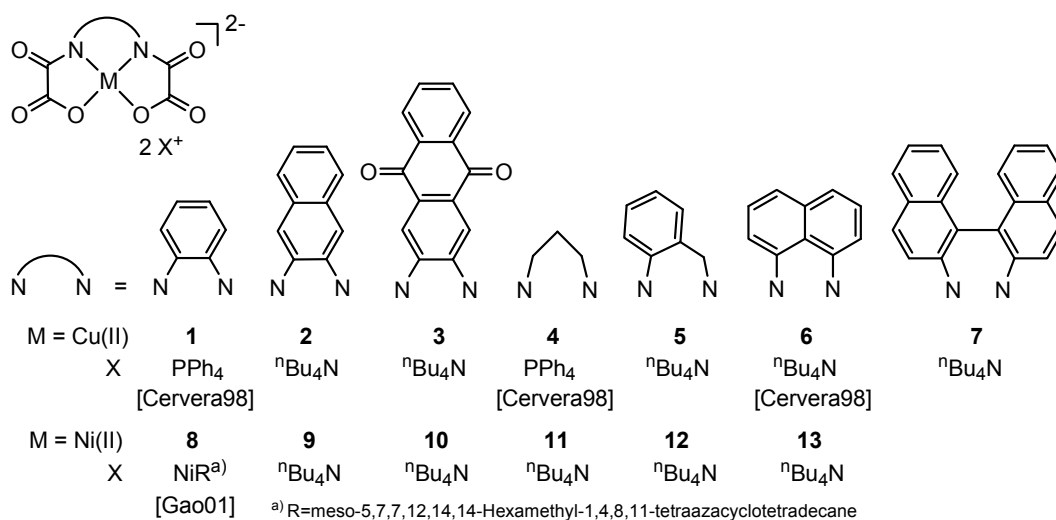


Figure 2.19. Synthesized mononuclear Cu(II)-bis(oxamato) complexes.

Table 2.13. Structural properties of different Cu(II)-bis(oxamato) complexes.

Complex	1	2	3	4	5	6	7
$d(\text{Cu}-\text{N})/\text{\AA}^{(c)}$	1.886(2)	1.887(2)	1.902(2)	1.904(3)	1.889(2) ^{a)} 1.921(2) ^{b)}	1.912(5)	1.915(3)
$d(\text{Cu}-\text{O})/\text{\AA}^{(c)}$	1.922(3)	1.927(2)	1.940(2)	1.939(3)	1.98(2) ^{a)} 1.87(2) ^{b)}	1.925(5)	1.932(2)
$\alpha(\text{N}-\text{Cu}-\text{N})/^{\circ(d)}$	83.8(2)	84.1(2)	83.6(1)	97.0(2)	95.2(3)	95.6	99.9(1)
$\delta(\text{C}-\text{N}-\text{Cu}-\text{N})/^{\circ(e)}$	0.3(2)	0.3(2)	0.6(1)	0.2(2)	7.2(1)	12.3	27.1(3)
Crystal system ^{f)}	m	m	m	m	m	m	t
Space group	C2/c	C2/c	C2/c	C2/c	C2/c	C2/c	P4 ₁ 2 ₁ 2
Cu chelate rings ^{g)}	5-5-5	5-5-5	5-5-5	5-6-5	5-6-5	5-6-5	5-7-5

^{a)} aryl-*N*(oxamato) entity, ^{b)} alkyl-*N*(oxamato) entity, ^{c)} bond length, ^{d)} bond angle, ^{e)} dihedral angle with respect to the amido carbon, ^{f)} m: monoclinic, t: tetragonal, ^{g)} the ligand forms three chelate rings around the Cu(II) ion involving a certain number of atoms

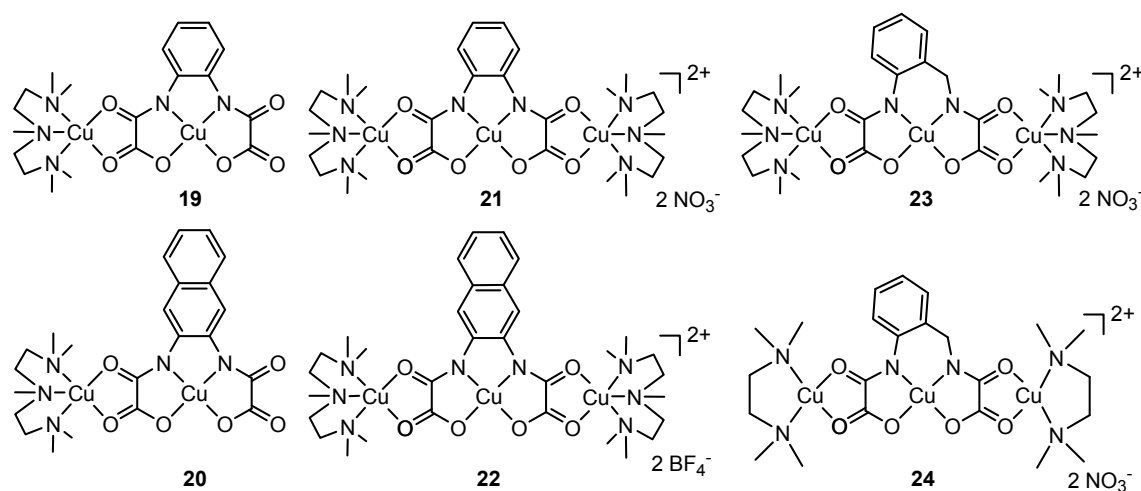


Figure 2.20. Synthesized mononuclear Cu(II)-bis(oxamato) complexes.

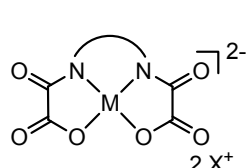
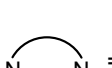
Table 2.14. τ -parameters of the terminal Cu(II) ions in different trinuclear Cu(II)-bis(oxamato) complexes.

	$\tau(\text{Cu2})$	$\tau(\text{Cu2}')$	average
21	0.187	0.203	0.195
22	0.417	0.388	0.403
23	0.477	0.455	0.466

3 Magnetic properties of Cu(II)-bis(oxamato) complexes

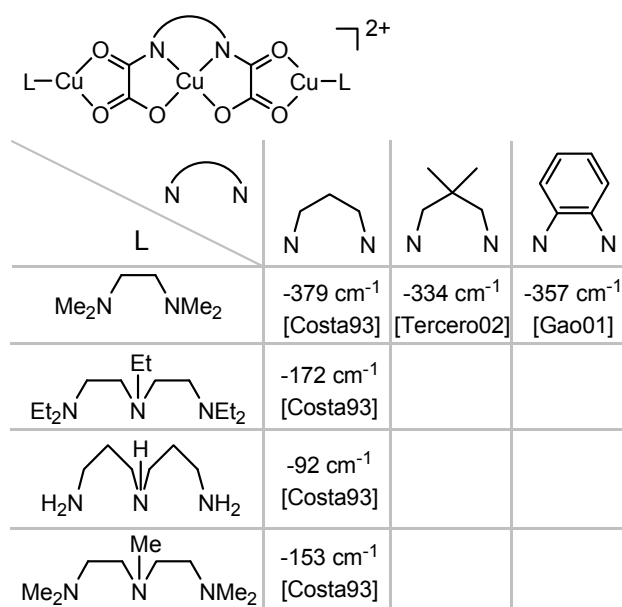
3.1 Introduction

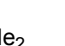
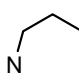
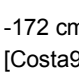
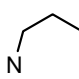
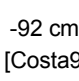
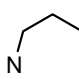
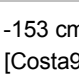
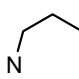
This chapter deals with the EPR and magnetic susceptibility studies of mono-, di-, and trinuclear Cu(II)-bis(oxamato) complexes. Scheme 3.1 shows the mononuclear Cu(II)-bis(oxamato) complexes investigated so far in the literature by means of EPR and the derived parameters. Up to now only measurements in liquid and frozen solutions have been performed; media that limit the spectral resolution and thus allows in most cases only the determination of the isotropic and anisotropic g values, respectively [Cervera98, Berg02]. In two cases, *cf.* scheme 3.1, the anisotropic hyperfine coupling values, A , of copper were derived. The anisotropic A values of nitrogen, however, were never determined for Cu(II)-bis(oxamato) complexes, since highly resolved measurements on diamagnetic diluted powders have never been performed. Due to the lack of information about the A values of nitrogen, a detailed analysis of the spin population distribution within the complexes cannot be performed by means of EPR.

				
				
	M=Cu, X=PPh ₄ [Cervera98]	M=Cu, X=PPh ₄ [Cervera98]	M=Cu(II), X=NBu ₄ (6) [Cervera98]	M=Cu(II), X=PPh ₄ [Berg02]
g_{iso}	2.096	-	-	-
$g_x=g_y$	-	2.049	2.04	2.04
g_z	-	2.178	2.191	2.191
$A_{iso}(Cu)$	270 MHz	-	-	-
$A_x(Cu)=A_y(Cu)$	-	-	95 MHz	95 MHz
$A_z(Cu)$	-	-	658 MHz	658 MHz
$A_{iso}(N)$	45.6 MHz	-	-	-

Scheme 3.1. EPR parameters of Cu(II)-bis(oxamato) complexes.

Starting with the mononuclear Cu(II) complexes di- and trinuclear Cu(II) complexes can be prepared as shown in chapter 2. By varying the N,N' -bridge and the terminal ligands the magnetic super exchange interaction J between the adjacent Cu(II) ions within the molecule can be influenced as shown for the structurally and magnetically characterized multinuclear Cu(II)-bis(oxamato) complexes reported in scheme 3.2. This dependency was explained by different overlaps of the magnetic orbitals and the magnetic super-exchange interaction was shown to be mediated mainly by the N–C–O entity of the oxamato bridge [Costa93].



L	N,N' -bridge	J (cm ⁻¹)	Reference
Me_2N  NMe_2		-379 cm ⁻¹	[Costa93]
		-172 cm ⁻¹	[Costa93]
		-92 cm ⁻¹	[Costa93]
		-153 cm ⁻¹	[Costa93]

Scheme 3.2. Magnetically and structurally characterized trinuclear Cu(II)-bis(oxamato) complexes under variation of the N,N' -bridge and the terminal ligand.

A correlation between the magnitude of the J parameter and the coordination geometry of the terminal Cu(II) ion was derived for a series of propylene bridged Cu(II)-bis(oxamato) complexes [Costa93]. For this purpose the τ parameter, which was introduced in section 2.8.2, was used. The resulting linear dependency of J vs. τ is shown in figure 3.1. Again, the different overlaps of the magnetic orbitals can explain the different antiferromagnetic interactions. One can presume that the spin population distribution should also vary when different magnetic couplings are obtained. However, up to now, no detailed experimental study about such a dependency has been performed. Moreover, no detailed analysis regarding the influence of the N,N' -bridge on the spin population distribution and thus the magnetic coupling can be found in literature.

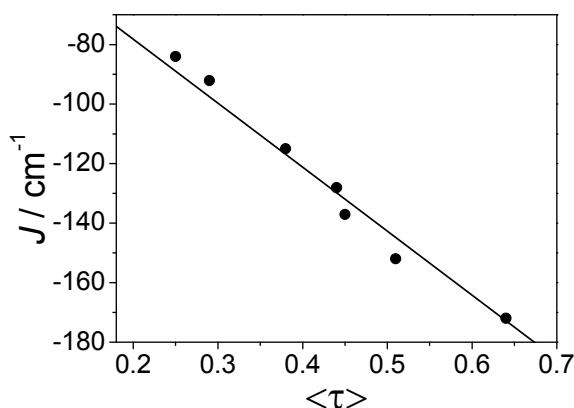


Figure 3.1. Representation of the J values vs. their averaged τ parameter for the terminal Cu(II) ions [Costa93].

So far the spin population was determined by means of high resolution X-ray and polarized neutron diffraction measurements. In the case of *bis*(oxamato) type transition metal complexes, the combination of these two methods has been successfully applied for studying the ferrimagnetic chain compound $\text{MnCu(pba)(H}_2\text{O)}_3 \cdot 2\text{H}_2\text{O}$ with $\text{pba} = 1,3\text{-propylene-bis(oxamato)}$ [Pillet04, Baron97]. The measurements are rather time consuming and large single crystals are necessary for these studies which limits the applicability to only a few selected compounds.

Recently, Sun *et al.* [Sun05] published a theoretical study on the magneto-structural correlation in linear trinuclear Cu(II) complexes bridged by oxamato groups. The calculations were performed using the broken symmetry approach with the framework of DFT. The coupling interaction difference among these compounds was explained by the overlap between magnetic orbitals. It was indicated that the geometry change of terminal Cu(II) ions plays a key role in determining the magnitude of the J parameter. In comparison to experimental values the J parameters were overestimated by a factor of 3 to 4.

In the first part of this chapter it will be shown that continuous wave (cw) EPR in X, Q, and W band and pulse electron nuclear double resonance (ENDOR) techniques in the Q band at various temperatures can be applied to extract detailed information about the spin population distribution of mononuclear Cu(II)-*bis*(oxamato) complexes. In the second part, the magnetic super exchange interaction of the corresponding multinuclear transition metal complexes will be determined from measurements of the magnetization as a function of the temperature. The obtained parameters will be compared to those predicted by means of DFT calculations.

3.2 Theoretical background

3.2.1 The spin Hamilton formalism of paramagnets

In quantum theory, molecular systems can be described using the spin Hamilton operator. It describes the interactions of an unpaired electron with the nuclei having a nuclear spin $I \neq 0$ in its surrounding. Cu(II)-bis(oxamato) complexes consist of Cu ($I = 3/2$) and the coordinated atoms N ($I = 1$) and O ($I = 0$). Since the O nucleus is EPR silent only the CuN₂ fragment has to be considered in the spin Hamiltonian as follows:

$$H_{sp} = \mu_B \mathbf{B}_0 \cdot \mathbf{g} \cdot \mathbf{S} + \mathbf{S} \cdot \mathbf{A} \cdot \mathbf{I}^{Cu} + \sum_{i=1}^2 \mathbf{S} \cdot \mathbf{A}^{N_i} \cdot \mathbf{I}^{N_i} + \mathbf{I} \cdot \mathbf{Q} \cdot \mathbf{I} - \mu_N \mathbf{B}_0 \cdot \mathbf{g}_N \cdot \mathbf{I} \quad (3.1)$$

The first term represents the electron Zeeman interaction with the Bohr magneton μ_B , the external magnetic field \mathbf{B}_0 , and the g tensor \mathbf{g} . The second term stands for the hyperfine interaction between the electron spin \mathbf{S} and the nuclear spin \mathbf{I} of the copper nucleus (^{63}Cu , ^{65}Cu). The third term describes the hyperfine interaction of the electron spin with the two nitrogens. The forth term takes into account the nuclear quadrupole interaction with the nuclear quadrupole tensor \mathbf{Q} which occurs for $I > 1/2$. The last term is the so-called nuclear Zeeman term with the nuclear magneton μ_N and the nuclear g tensor \mathbf{g}_N . The continuous wave EPR spectra are dominated by the first three terms. The nuclear quadrupole tensors of the nitrogens can be determined by means of pulse ENDOR using the Davies sequence. \mathbf{A} is the hyperfine tensor and can be written as the sum of:

- the isotropic or Fermi contact contribution A_{iso} , given by the sum of the unpaired spin population determined by the unpaired electron in a s orbital and the spin polarization of the inner s orbitals [McGarvy67],
- the spin dipolar contribution A_{dip} , which is determined by the dipolar interaction between the electron and the nuclear spin,
- and the orbit dipolar contribution A_L [Bencini83] which will be neglected herein.

The spin dipolar contribution depends on the orientation of the external magnetic field with respect to the molecular plane, resulting in an anisotropic

character of the EPR spectra. The EPR spectrum becomes isotropic, *i.e.* orientation independent, when statistic rotations of the molecules occur. This is the case in solutions where the dipolar contributions average to zero.

The hyperfine interaction of the unpaired electron with the nuclear spin of $|I|$ leads to a $2|I|+1$ multiplet since only transitions with $\Delta m_I = 0$ are allowed. The coupling with n non-equivalent and h_k equivalent nuclei having a nuclear spin of $I > 0$ lead to a number of

$$N = \prod_{k=1}^n (2I_k \cdot h_k + 1) \quad (3.2)$$

EPR signals.

3.2.2 Experimental and theoretical studies of spin population

In order to get insights into the delocalization of the spin density on the Cu complex, and how this depends on the molecular structure of the complex, simplified models are used to extract the spin population from the experimentally determined hyperfine tensors.

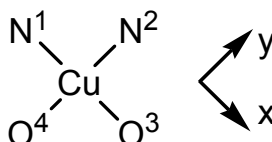


Figure 3.2. Coordinate system for the investigated complexes.

Using the definition of the x and y axes given for Cu in figure 3.2, the relevant molecular orbital for the unpaired electron is

$$\Psi_{MO} = \alpha |d_{x^2-y^2}\rangle - \frac{\alpha_N}{\sqrt{2}} (-\sigma_1^x + \sigma_2^y) - \frac{\alpha_O}{\sqrt{2}} (+\sigma_3^x - \sigma_4^y). \quad (3.3)$$

for which the subscripts 1, 2, 3, and 4 denote the hybrid orbitals σ of the coordinated nitrogens and oxygens, respectively. The parameter α^2 is the covalency parameter which describes the in-plane metal-ligand σ bonding and results in $\alpha^2 = 1$ for a pure ionic bonding and $\alpha^2 < 1$ when a covalent part contributes to the bonding. The normalization of the Ψ_{MO} orbital yields

$$\alpha^2 + \alpha_N^2 + \alpha_O^2 - 2\alpha\alpha_N S_{Cu-N} - 2\alpha\alpha_O S_{Cu-O} = 1. \quad (3.4)$$

In the literature, the overlap integrals S were calculated for a ligand-to-metal distance of 1.92 Å leading to overlap integrals $S_{Cu-N} = 0.093$ and $S_{Cu-O} = 0.076$ for nitrogen and oxygen, respectively [Kivelson61]. The distance differs slightly for different compounds but the influence on the calculated overlap integrals is negligible.

The copper hyperfine values can be expressed as

$$\begin{aligned} A_{\parallel} &= P \left(-\kappa - \frac{4}{7} \alpha^2 + \Delta g_{\parallel} + \frac{3}{7} \Delta g_{\perp} \right) \\ A_{\perp} &= P \left(-\kappa + \frac{2}{7} \alpha^2 + \frac{11}{14} \Delta g_{\perp} \right) \end{aligned} \quad (3.5)$$

where $-P\kappa$ is the Fermi contact term, $P(^{63}\text{Cu}) = \mu_B g_e \mu_n g_n \langle r^{-3} \rangle = 1164$ MHz is the dipolar hyperfine coupling parameter of the unpaired electron, and $\Delta g_{\parallel,\perp} = g_{\parallel,\perp} - 2.0023$.

Furthermore, the values obtained for the spin population on the Cu(II) ion are compared with those deduced by the procedure of Morton and Preston [Morton78]. These authors used the basic approach that the spin populations in the s and p orbitals (d orbitals for copper) are proportional to the isotropic (A_{iso}) and the dipolar ($A_{\text{dip}} = A_{\text{iso}} - A_{\perp}$) hyperfine coupling constants, respectively. In literature [Morton78] the proportional constants were calculated for many abundant nuclei from Hartree-Fock-Slater atomic orbitals using the Hermann-Skillman wavefunction.

3.2.3 Electron paramagnetic resonance

When an atom, having a nonzero magnetic moment μ , is exposed to a magnetic field B , the interaction of the magnetic moment with the field is known as Zeeman effect. The magnetic moment is related to the total spin (\mathbf{S}) and the orbital angular momentum (\mathbf{L}):

$$\mu = -\frac{e}{2m} (\mathbf{L} + g_e \mathbf{S}). \quad (3.6)$$

where e and m is the charge and mass of the electron, respectively. The g_e is the free electron g value ($g_e = 2.002319$). The appropriate Hamiltonian for B parallel to the z axis is

$$H = -\mu_z B_z. \quad (3.7)$$

The corresponding eigenvalues can be found in the Russell-Saunders coupling scheme by using the z component of $\mathbf{J} = \mathbf{L} + \mathbf{S}$ to label the states as

$$E_{m_J} = g_J \mu_B m_J B. \quad (3.8)$$

where the Landé splitting factor, g_J , is given by

$$g_J = 1 + \frac{S(S+1) + J(J+1) - L(L+1)}{2J(J+1)} \quad (3.9)$$

and μ_B is the Bohr magneton ($\mu_B = 9.27401 \cdot 10^{-24} \text{ JT}^{-1}$).

By applying an oscillating magnetic field with the frequency ν , for instance in the microwave range for EPR, perpendicular to static magnetic field B_0 a transition between two J states can be induced when ν meets the resonance condition

$$h\nu = g_e \mu_B B_0 \quad (3.10)$$

where h is the Planck constant ($h = 6.626 \cdot 10^{-34} \text{ Js}$). The selection rule $|\Delta m_J| = \pm 1$, sketched in figure 3.3, holds in general for any paramagnetic species with one unpaired electron and g_e can be substituted by g , a constant which is different from 2.002319 and depends on the orientation of \mathbf{B} .

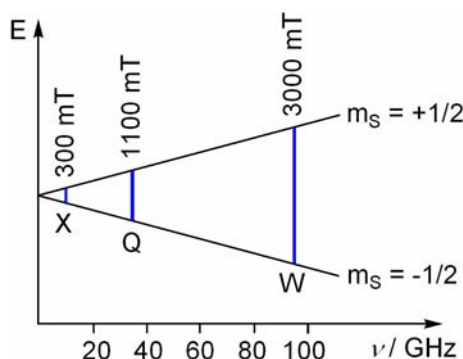


Figure 3.3. Schematic of the EPR resonance excitation. The degeneracy of electronic states is lifted in an external magnetic field. Depending on the frequency of the microwave field the bands are called X, Q, and W. The corresponding strength of the static magnetic field for selected resonance conditions are given in the figure for the case of a system with $g = 2.00$.

Depending on the frequency of the oscillating magnetic field one distinguishes between S- (≈ 3 GHz), X- (≈ 9.5 GHz), K- (≈ 23 GHz), Q- (≈ 35 GHz), and W-band (≈ 95 GHz) EPR measurements. Only the X-, Q-, and W-band resonances will be used for the investigations herein, *cf.* figure 3.3.

3.2.4 Pulse electron nuclear double resonance

The electron nuclear double resonance (ENDOR) effect is based on a polarization transfer between electron and nuclear transitions. The advantage of pulse ENDOR, used for the investigations presented in this work, compared to continuous wave ENDOR is that the entire pulse sequence can be made short enough to exclude unwanted relaxation effects like spin-spin and spin-lattice relaxation [Schweiger01]. The pulse ENDOR scheme introduced by Davies [Davies74] is based on selective microwave pulses, *cf.* figure 3.4. The polarization of a particular EPR transition is inverted by a microwave π pulse flipping the electron spin, *cf.* figure 3.4 (b) and (c). During the mixing period, a selective resonant radio frequency pulse is applied, changing the nuclear polarization as illustrated in figure 3.4 (d). This change also alters the polarization of the electron spin observer transition. The resonance is then measured via the detection sequence $\pi/2 - \tau - \pi - \tau$ -echo.

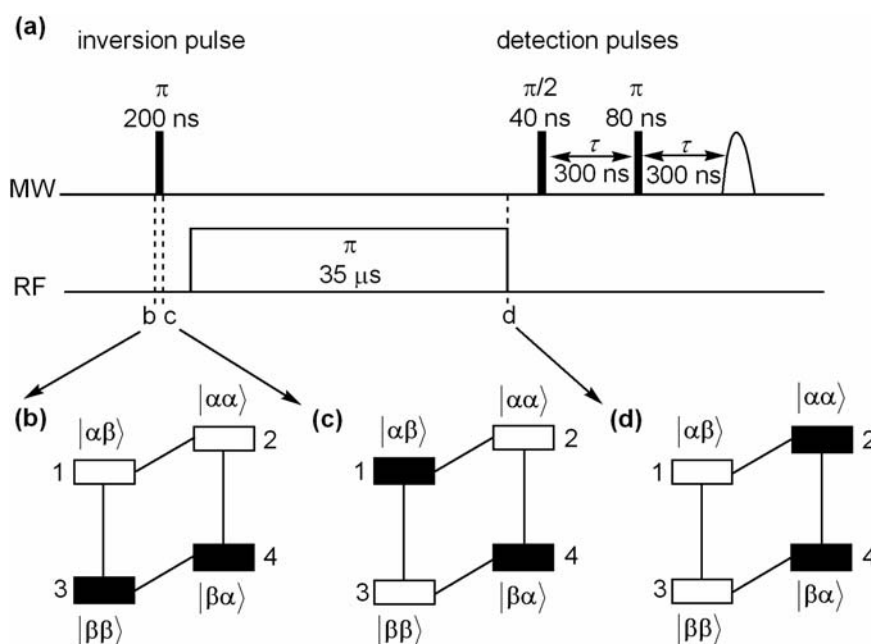


Figure 3.4. (a) Pulse sequence for the Davies-ENDOR experiment. (b) - (d) Corresponding inversion of polarization for $|m_S m_I\rangle$.

3.2.5 Magnetic investigations of exchange coupled systems

The relevant magnetic interactions between two spin carrying centres, linked by one or more atoms, can arise from either magnetic dipole-dipole interactions or super-exchange interactions. The former is dominated by the latter for temperatures higher than $T = 1$ K and is not taken into consideration herein. The Hamilton operator for n spin centres of a super-exchange coupled system is defined as

$$\hat{H}_{ex} = - \sum_{\substack{i,j=1 \\ i \neq j}}^n J_{ij} \mathbf{S}_i \mathbf{S}_j . \quad (3.11)$$

and is often called the Heisenberg operator where J is the super-exchange coupling parameter and \mathbf{S} the spin operator. Using this definition $J < 0$ implies an antiferromagnetic and $J > 0$ a ferromagnetic ground state, *i.e.* an antiparallel and parallel spin alignment, respectively.

In describing the magnetic properties of di- and trinuclear Cu(II)-bis(oxamato) complexes investigated in this work the atom numbering as shown in figure 3.5 will be used.

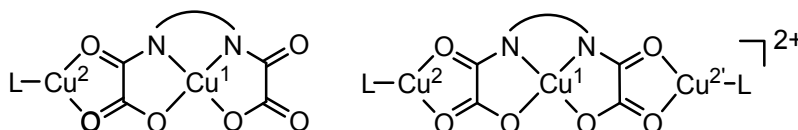


Figure 3.5. Numbering scheme of the Cu(II) centres in the Cu(II)-bis(oxamato) complexes investigated in this work.

The Heisenberg operator is defined as

$$\hat{H}_{ex} = -J_1 \hat{S}_{Cu1} \hat{S}_{Cu2} \quad \text{and} \quad (3.12)$$

$$\hat{H}_{ex} = -J_1 (\hat{S}_{Cu1} \hat{S}_{Cu2} + \hat{S}_{Cu1} \hat{S}_{Cu2'}) - J_2 \hat{S}_{Cu2} \hat{S}_{Cu2'} \quad (3.13)$$

for the dinuclear and trinuclear complex, respectively, where J_1 denotes the exchange coupling parameter between the central and the terminal Cu(II) ions, and J_2 the coupling parameter between the two terminal Cu(II) ions. It has been assumed that $J_{Cu1Cu2} = J_{Cu1Cu2'} = J_1$. This assumption is based on the presence of a reflection symmetry plane that contains the Cu1 atom provided by the same

nature of the terminal ligand L bridged to Cu1 and Cu2. The magnetic susceptibility derived from the Heisenberg operator is

$$\chi = \frac{2N_A g^2 \mu_B^2}{kT} \left(\frac{1-\rho}{3 + \exp(-J_1/kT)} + \frac{\rho}{4} \right) \text{ and} \quad (3.14)$$

$$\chi = \frac{N_A \mu_B^2 g^2}{4k(T-\Theta)} \cdot \frac{\exp(-J_2/kT) + \exp(-J_1/kT) + 10 \exp(J_1/2kT)}{\exp(-J_2/kT) + \exp(-J_1/kT) + 2 \exp(J_1/2kT)} \quad (3.15)$$

for the dinuclear and trinuclear complex, respectively, where k is the Boltzman constant, N_A the Avogadro number, and ρ the contribution of paramagnetic impurities [Kahn93]. The parameter Θ is introduced to take into account the intermolecular interaction and is deduced from the molecular-field approximation

$$\Theta = 2zJ' \frac{\chi_m}{N_A \mu_B^2 g^2} \quad (3.16)$$

where zJ' denotes the intermolecular exchange parameter. The fit of the calculated, $(\chi_m T)^{\text{calc}}$, to the experimental $(\chi_m T)^{\text{obs}}$ product was performed by minimizing the parameter R in

$$R = \frac{\sum [(\chi_m T)^{\text{obs}} - (\chi_m T)^{\text{calc}}]^2}{\sum [(\chi_m T)^{\text{obs}}]^2} \quad (3.17)$$

using the OriginPro7.5G software.

3.3 Quantum chemical calculations

3.3.1 Density functional theory

The density functional approach is based on a strategy of modeling the electron correlation via general functionals of the electron density published by Kohn and Sham [Szabo89]. The approximate functionals employed by current DFT methods separate the electronic energy into several terms

$$E = E_J + E_{Ne} + E_{ee} + E_{XC} \quad (3.18)$$

where E_{ee} is the kinetic energy term, E_{Ne} includes terms describing the potential energy of the nuclear-electron attraction and of the repulsion between pairs of nuclei, E_J is the electron-electron repulsion term, and E_{XC} is the exchange-correlation term and includes the remaining part of the electron-electron interactions. The first three terms correspond to the classical energy of the charge distribution ρ . The last term, *i.e.* the E_{XC} term, is entirely determined by the electron density

$$E_{XC}(\rho) = \int f(\rho_\alpha(r), \rho_\beta(r), \nabla\rho_\alpha(r), \nabla\rho_\beta(r)) d^3r \quad (3.19)$$

where ρ_α and ρ_β refer to the corresponding α and β spin densities [Hohenberg64]. The E_{XC} term can be subdivided into

$$E_{XC}(\rho) = E_X(\rho) + E_C(\rho) \quad (3.20)$$

referred to as the exchange and correlation parts. Pure DFT methods like the BLYP functional [Becke88] pair the Becke's gradient-corrected exchange functional (B88) with the gradient-corrected correlation functional of Lee, Yang, and Parr (LYP) [Lee88] and of Vosko, Wilk, and Nusair (VWN) [Vosko80]. One of the most famous functionals is B3LYP which includes a mixture of Hartree-Fock (HF) and DFT exchange along with DFT correlation, conceptually defining E_{XC} as:

$$E_{XC} = 0.8E_X^{LDA} + 0.2E_X^{HF} + 0.72E_X^{B88} + 0.81E_C^{LYP} + 0.19E_C^{VWN} \quad (3.21)$$

where LDA stands for local density approximation [Kohn65].

3.3.2 Basis sets

Molecular orbitals can be described as a linear combination of atomic orbitals (LCAO). These molecular orbitals are the sum of the basis functions ϕ_μ :

$$\psi_i = \sum_{\mu=1}^N C_{\mu,i} \phi_\mu \quad (3.22)$$

weighted with molecular expansion coefficients C_μ . Essentially, two general classes of basis sets are used. The more accurate, but also more time

consuming in the computation of the integrals, is the one based on the atomic orbitals proposed by Slater [Slater30]. A very successful compromise between computational cost and accuracy is offered when contracted Gaussians are used:

$$\psi_i = \sum_{\mu=1}^N c_{\mu,i} \left(\sum_p d_{\mu,p} g_p \right). \quad (3.23)$$

The contraction coefficients $d_{\mu,p}$ are fixed constants within a basis set and g_p are primitive Gaussian functions having different forms and used to approximate the molecular orbitals. The number of primitive Gaussians per basis set can be varied depending on the degree of precision which is needed. In addition, split-valence sets can be used, meaning that a number of differently sized basis sets are used to describe the valence orbitals. Within this work triple zeta valence (TZV) basis sets with polarization (P) functions are used. Their characteristics are as outlined in table 3.1.

Table 3.1. Used basis sets [Weigend05, Schaefer92, Neese01].

atom	basis set	uncontracted	contracted
Cu	CP(PPP)	17s11p5d1f	17s7p3d1f
Cu	TZVP	17s11p6d	6s4p3d
N, O, C	Def2-TZVP	11s6p2d1f	5s3p2d1f
N, O, C	TZVP	11s6p1d	5s3p1d
H	TZVP	5s1p	3s1p

3.3.3 Calculation of vibrational frequencies

Vibrational frequencies are computed by determining the second derivatives of the energy with respect to the Cartesian nuclear coordinates and then transforming to mass-weighted coordinates. DFT methods often overestimate the vibrational frequencies [Kobitski03, Ong99]. Therefore, scaling factors for the frequencies are often used in order to decrease the root-mean-square (rms) error between the frequencies of the calculated and experimental modes.

3.3.4 Calculation of EPR parameters

The theoretical calculation of EPR parameters is a very new field. Its implementation is based on DFT and the use of gauge-including atomic orbitals (GIAO) [Schreckenbach97]. Experimental trends are generally reproduced fairly

accurately; however, severe problems occur for heavier elements. To overcome this, the spin-orbit-coupling is taken into account variationally including zeroth-order regular approximation (ZORA) in the Dirac equation. A detailed explanation is given in [Lenthe97].

For the calculation of the hyperfine coupling, basis sets with high flexibility are essential. The crucial requirements for obtaining accurate results for isotropic hyperfine coupling constants is the availability of reliable spin densities at the nuclear positions, which is known to be difficult to achieve. Standard TZP sets are generally too small. Several basis sets were employed like IGLO-III [Eriksson94] and EPR-III [Barone95]. For the first and second row transition metals the CP basis was developed [Neese01]. General purpose HF-limit basis sets are the uncontracted Partridge basis sets which are in most cases too time consuming but are useful for calibration purposes. There are too few systematic studies on the determination of (isotropic) hyperfine couplings to allow for a solid evaluation of the correlation between expected accuracy and employed technique. However, it seems clear that density functional methods are capable of providing reasonable predictions for these properties, even though they are not able to rival the accuracy obtained from highly correlated wave function based methods, as shown in a comprehensive recent study [Gauld97]. The choice of the functional and/or the one-particle basis set to expand the Kohn-Sham orbitals is of crucial importance, since the isotropic coupling depends only on the spin density at the nuclear positions. Hence, the performances of the different functionals are directly related to their abilities to generate good spin densities, not on average but at these exact positions.

3.3.5 Calculation of magnetic super-exchange parameters

The broken-symmetry (BS) approach developed by Noodleman [Noodleman81] was used to calculate the coupling parameters for the magnetic super-exchange. The BS determinant is built from spin orbitals localized on two spin centres. Therefore, the magnetic properties of insulating molecular magnetic materials are investigated by partitioning the magnetic interaction in spin-spin interactions of pairs of paramagnetic centres on which the unpaired electrons are localized leading to a spin Hamiltonian of the type

$$\begin{aligned}
 H &= -\sum_{i<j} J_{ij} \mathbf{S}_i \cdot \mathbf{S}_j \\
 &= -J_{12} (\mathbf{S}_{Cu1} \cdot \mathbf{S}_{Cu2}) - J_{12'} (\mathbf{S}_{Cu1} \cdot \mathbf{S}_{Cu2'}) - J_{22'} (\mathbf{S}_{Cu2} \cdot \mathbf{S}_{Cu2'})
 \end{aligned}
 \tag{3.24}$$

where \mathbf{S}_{Cu} are the spins associated with the different paramagnetic Cu(II) centres with Cu1 in the middle and Cu2/Cu2' in the terminal positions of the complex. J_{ij} are the respective isotropic magnetic exchange coupling constants. The following eigenvalues E result from the four eigenstates $|(\mathbf{S}_{Cu2})(\mathbf{S}_{Cu1})(\mathbf{S}_{Cu2'})\rangle$:

$$\begin{aligned}
 \text{HS: } M_S = \pm 3/2 \text{ and } |(1/2)(1/2)(1/2)\rangle &\rightarrow E_{HS} = -\frac{J_{12}}{4} - \frac{J_{12'}}{4} - \frac{J_{22'}}{4} \\
 \text{LS1: } M_S = \pm 1/2 \text{ and } |(1/2)\overline{(1/2)}(1/2)\rangle &\rightarrow E_{LS1} = +\frac{J_{12}}{4} + \frac{J_{12'}}{4} - \frac{J_{22'}}{4} \\
 \text{LS2: } M_S = \pm 1/2 \text{ and } |\overline{(1/2)}(1/2)(1/2)\rangle &\rightarrow E_{LS2} = +\frac{J_{12}}{4} - \frac{J_{12'}}{4} + \frac{J_{22'}}{4} \\
 \text{LS2': } M_S = \pm 1/2 \text{ and } |(1/2)(1/2)\overline{(1/2)}\rangle &\rightarrow E_{LS2'} = -\frac{J_{12}}{4} + \frac{J_{12'}}{4} + \frac{J_{22'}}{4}
 \end{aligned}
 \tag{3.25}$$

where HS means high spin with three parallel oriented spins and LS stands for the remaining low spin configurations. In order to determine the J parameters the total energy of each spin configuration is calculated. The values of J can then be calculated by building sums and differences of the four equations in the system (3.25).

This approach is often used in order to obtain a meaningful set of exchange coupling parameters in systems with several different coupling parameters [Bencini05]. However, the quantitative accuracy of the current DFT approaches for transition metal complexes is not always satisfactory. Numerous functionals were investigated for several transition metal complexes as well as for main group radicals [Arbuznikov02] and were shown not to improve substantially the accuracy of the popular B3LYP functional. This method is also the most consistent with total energy calculations and thus the method of choice for the following calculations performed in this work.

3.3.6 Time dependent density functional theory

Time dependent DFT (TDDFT) was used in this work to study the absorption spectra, *i.e.* the excitation energies, oscillator strengths, and transition moment

directions of Cu(II)-bis(oxamato) complexes. The method is based on an extension of the time-independent Hohenberg–Kohn–Sham DFT. In short, the system, initially in a ground stationary state, is exposed to a time-dependent perturbation by modifying its external potential. A detailed theoretical description of this method is given in [Marques04] and an evaluation of the performance of TDDFT for the calculation of high-lying bound electronic excitation energies of molecules is described in detail by Casida *et al.* [Casida98]. Generally, DFT over estimates the covalent interaction between the metal d-orbitals and the ligands. This causes an over estimation of the energy gap between the highest occupied molecular orbital (HOMO) and the lowest unoccupied molecular orbital (LUMO) in 3d metal complexes of up to 0.5 eV [Autschbach03].

3.4 Experimental details

3.4.1 EPR investigations

In continuous wave EPR experiments, as shown in figure 3.6 (a), the microwave source, a klystron, emits monochromatic radiation at a fixed frequency. It is then guided through a cavity which operates as a resonator. A circulator separates the microwaves going to and coming from the sample. Two coils generate an external magnetic field which lifts the spin degeneracy in the material under investigation. The applied fields and the corresponding microwave frequencies are summarized in figure 3.3. Two small coils close to the cavity generate a sinusoidal modulation of the resonance signal. The amplitude of the generated signal is proportional to the first derivative of the absorption signal.

For ENDOR experiments, see figure 3.6 (b), the spectrometer has to be supplemented with a radio frequency unit and the corresponding control devices. The radio frequency is generated by a sweep generator which is controlled by a pulse sequence generator. The pulse pattern is then amplified by a radio frequency amplifier up to the kilowatt range. Pulse EPR investigations have to be carried out at low temperature to achieve sufficiently long relaxation times.

The EPR spectra were recorded in the X-, Q-, and W-band using a Bruker E600 EPR spectrometer at various temperatures. If not otherwise stated, a modulation amplitude of 4 Gauss was used. The spectral simulations were performed using the program packages EasySpin [Stoll06] and Xsophe from

Bruker [Wang95]. Line broadening effects were included by convoluting the calculated line spectrum with a Gaussian lineshape. The line broadening which mainly originates from the unresolved hyperfine couplings was assumed to be 0.5 mT for powder measurements. The Davies ENDOR investigations were performed at a temperature of 16 K using a Bruker Elexsys E700 FT-EPR spectrometer operating at Q-band frequencies and an ENI 300 RF amplifier.

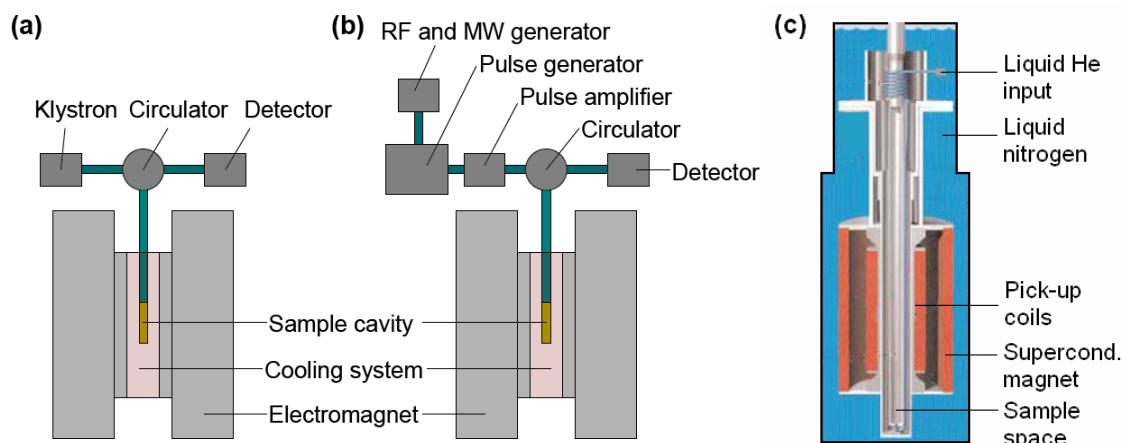


Figure 3.6. Schematic of (a) continuous wave EPR, (b) pulse ENDOR, and (c) SQUID magnetometer setups.

The isotropic EPR parameters were obtained from room temperature measurements of the *bis*(oxamato) type complexes in CH_2Cl_2 with a concentration of 0.5 mg/ml. The anisotropic part of the EPR parameters was extracted from measurements of the paramagnetic complexes in frozen solution of 0.5 mg/ml CH_2Cl_2 in case of **7** and from measurements on diamagnetically diluted powder measurements in cases **1** – **6** in order to decrease the broadening of the EPR lines. Such powders were produced by solving 0.5 % of the Cu(II) complex and 99.5 % of the structurally isomorphous Ni(II) complex in MeCN. The solid was obtained by following precipitation with Et_2O .

3.4.2 Magnetic susceptibility studies

The magnetic susceptibility studies were carried out in the 1.9 to 300 K temperature range using a Quantum Design MPMS SQUID (Superconducting QUantum Interference Device) magnetometer, *cf.* figure 3.6. A SQUID is one of the most sensitive instruments for magnetization measurements and can detect magnetizations up to 10^{-14} T. It consists, among others, of a superconducting coil equipped with Josephson contacts. The detection is based on the fact that

the magnetic field in the middle of the coil is influenced by the sample magnetization, yielding to a change in the current flow.

3.4.3 Absorption measurements

UV/VIS absorption and circular dichroism spectra at room temperature were recorded in CH_2Cl_2 (2×10^{-5} mol/l and 3×10^{-3} mol/l). For the absorption spectra the Thermo Spectronics UV/VIS spectrometer of the type “Genesys 6” was used. The circular dichroism investigations were performed on a homebuilt instrument based on a JASCO J-715 spectropolarimeter at the Max Planck institute in Mülheim.

3.4.4 Quantum chemical studies

Quantum chemical calculations were performed with the program packages TURBOMOLE [Ahlrichs89, Turbo05] and ORCA [Neese03] using methods of the density functional theory by applying the B3LYP hybrid functional [Lee88] with def2-TZVP [Weigend05, Schaefer92] basis sets for all atom types. The two $^n\text{Bu}_4\text{N}^+$ counter ions were neglected. The charge of the dianion was compensated by the conductor-like screening model (COSMO) [Klamt93, Zimmer05], *i.e.* by placing the molecule in a cavity defined by the molecular shape and to impose a constant electrostatic potential on the cavity surface. This leads to negative energies for all occupied orbitals. All calculations were done with default settings for convergence criteria and with default parameters for the COSMO model. The EPR parameters were obtained using the flexible CP(PPP) basis set of ORCA [Neese03] for Cu in order to get a good estimation for the g tensor components and def2-TZVP [Weigend05, Schaefer92] for all the other atoms.

The analysis of the spin population, $\rho_s(\mathbf{r})$, *i.e.* the difference of populations of alpha and beta electrons, was done for the optimized geometry using the Mulliken population analysis [Mulliken55], the Loewdin analysis, and the natural population analysis (NPA) [Reed85] in order to obtain the number of unpaired electrons per atom, n_A ($A = \text{Cu}, \text{N}, \text{O}$). As an additional check, $\rho_s(\mathbf{r})$ was also integrated numerically within spheres of radius R centred at these atoms. This leads to $n_s(R)$, the number of unpaired electrons contained in a sphere of radius R around the respective atom. The radius for which $n_s(R)$ may be identified with

n_A is defined by $n_s(R)$ being stationary with respect to variation of R . For an isotropic spin population this would correspond to $\rho_s(R)=0$. For the present case showing an anisotropic distribution this is only an approximation. Nevertheless, from the shape of the spin population, this definition appears to be reasonable and will be discussed in chapter 3.5.3.

For the calculation of the magnetic coupling parameters the BS approach was used in the program package TURBOMOLE. For more details see chapter 3.3.5. The calculations were performed for the corresponding trinuclear complex of **7** which was constructed by adding two $[\text{Cu}(\text{pmdta})]^{2-}$ fragments in the terminal positions of the $[\text{Cu}(\text{R-bnbo})]^{2-}$ entity. The bond distances and angles of the $[\text{Cu}(\text{pmdta})]^{2-}$ fragments, and thus the τ -parameter, were exactly the same as used for $[\text{Cu}_3(\text{nabo})(\text{pmdta})_2](\text{BF}_4)_2$ (**16**) in order to compare the effect of the central N,N' -bridge on the calculated J .

3.5 Results and discussion

3.5.1 Absorption spectroscopy investigations

The electronic ground state of the Cu(II) and Ni(II) complexes can be derived from absorption spectroscopy investigations in the visible to ultraviolet range. In the following section the absorption properties of systems which include one or more naphthyl units as an N,N' -bridge will be discussed. The absorption properties of **6** were taken from literature [Cervera98] for comparison. The absorption spectra of **2**, **6**, and **7** are shown together in figure 3.7. They are characterized by low-energy transitions arising from d-d transitions of Cu(II) with a d^9 electronic configuration with $d_{x^2-y^2}$ as highest occupied molecular orbital. For **2** and **6** a square planar environment (*i.e.* ${}^2B_{1g} - {}^2A_{1g}$, ${}^2B_{1g} - {}^2B_{2g}$, and ${}^2B_{1g} - {}^2E_{1g}$ in ideal D_{4h} symmetry) can be assumed, *cf.* figure 3.8. The most intensive absorption can be found at 17900 cm^{-1} ($\epsilon \approx 250\text{ M}^{-1}\text{ cm}^{-1}$), 18400 cm^{-1} ($\epsilon \approx 250\text{ M}^{-1}\text{ cm}^{-1}$), and 16500 cm^{-1} ($\epsilon \approx 230\text{ M}^{-1}\text{ cm}^{-1}$) for **2**, **6**, and **7**, respectively. The significant red shift of the absorption maximum for **7** in comparison to **2** and **6** is due to strong deviations from the square planar coordination geometry in the case of **7**. Since **7** has a chirality axis, its circular dichroism spectrum allows to distinguish the existence of several d-d transitions. It was, however, not possible to perform unequivocally the assignment of the transitions since the

energy order of the respective orbitals is unknown. The same is valid for the transitions at higher energies arising mainly from the $\sigma\text{--}\sigma^*$ and $\pi\text{--}\pi^*$ transitions. The corresponding bands vary strongly in intensity and energy position due to the different N,N' -bridges.

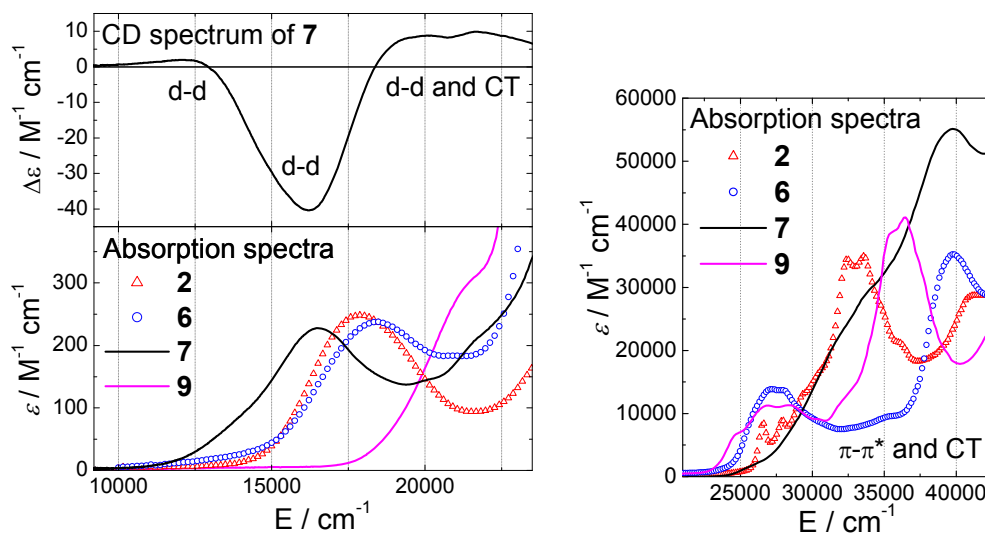


Figure 3.7. Circular dichroism (CD) spectrum of **7** and absorption spectra of **2**, **6**, **7**, and **9** (left panel). The right panel shows the high energy range of the absorption spectra.

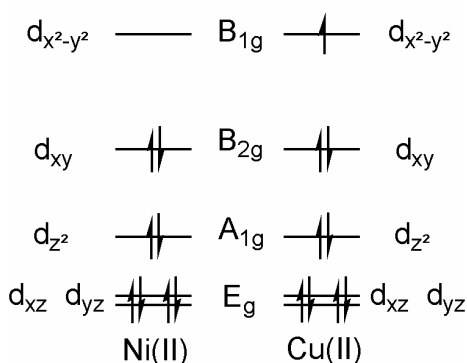


Figure 3.8. Schematic energy level diagram of square planar Ni(II) and Cu(II) complexes.

In the case of Ni(II) the energy gap between the highest occupied (B_{2g}) and the lowest unoccupied molecular orbital (B_{1g}) is larger compared to the respective Cu(II) complex which can be clearly seen from the blue shift for the Ni(II) complex **9** compared to the Cu(II) analogue **2**. This confirms the existence of a square planar coordination geometry [Huheey93] leading to a singlet ground state for the Ni(II) and a doublet for the Cu(II) complexes. Since the Ni(II) complexes are EPR silent but structurally isomorphous to the Cu(II) complexes, see chapter 2, they are excellently suited as diamagnetic host lattice for the paramagnetic Cu(II) complexes in order to avoid intermolecular magnetic interactions and thus allows the recording of highly resolved EPR spectra.

3.5.2 EPR investigations

For the investigated complexes the g and A^{Cu} matrices are assumed to be coaxial and axially symmetric with

$$|A_x^{\text{Cu}}| \approx |A_y^{\text{Cu}}| \approx |A_{\perp}^{\text{Cu}}| < |A_z^{\text{Cu}}| = |A_{\parallel}^{\text{Cu}}|. \quad (3.26)$$

Figure 3.9 shows the measured and simulated Q-band EPR spectra on the example of complex **6**. For all the other compounds the EPR spectra look rather similar and are not shown here. The features labelled with x, y, and z consist of a quartet ($I(^{63,65}\text{Cu})=3/2$) of quintets ($I(^{14}\text{N})=1$) for B_0 field orientations for which both N donor atoms are magnetically equivalent. The individual ^{63}Cu and ^{65}Cu signals are different in intensity because of their different natural abundances (^{63}Cu (69%), ^{65}Cu (31%), $g_{\text{N}}(^{63}\text{Cu})=1.4804$, $g_{\text{N}}(^{65}\text{Cu})=1.5860$). For B_0 orientations in the molecular xy-plane of the Cu g-ellipsoid the spectra become more complicated since the ^{14}N quintets overlap each other due to the small $^{63,65}\text{Cu}$ hyperfine coupling.

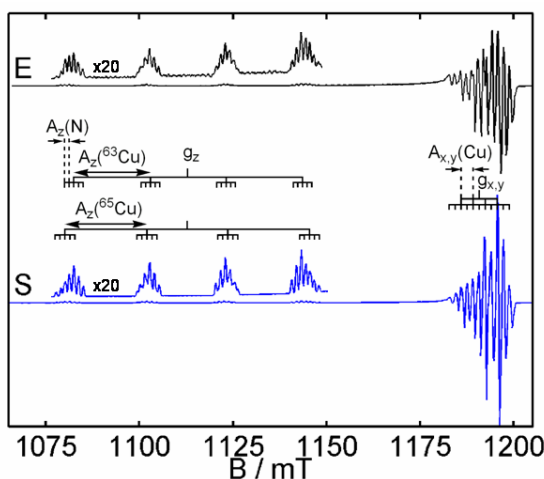


Figure 3.9. Experimental (E) and simulated (S) EPR spectrum of **6** at $f = 34.031$ GHz (Q-band) and $T = 298$ K. For B_0 orientations along the z axis of the g tensor, the EPR spectra are zoomed in. The assignment of the EPR bands is schematically given.

For **6**, the orientation of the tensor principal axis system of Cu and N was investigated in detail performing Davies ENDOR studies in the Q-band. Furthermore, this method was used in order to determine the hyperfine and nuclear quadrupole principal values of the nitrogens. The Davies ENDOR spectra were collected at different observer positions which are highlighted in figure 3.10 as red vertical lines. The respective Davies ENDOR spectra are

shown in figure 3.11 and the obtained EPR parameters, *i.e.* the principal values of g , A^{Cu} , A^N , Q^N , and the Euler angles, are reported in table 3.2.

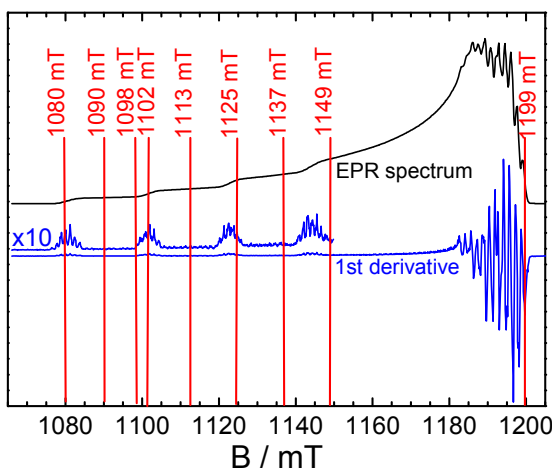


Figure 3.10. Experimental free induction decay detected EPR spectrum ($\pi/2$ -pulse of 200 ns) of **6** and its first derivative at $f = 34.031$ GHz (Q-band) and $T = 16$ K. The vertical lines represent the different observer positions for the respective pulse ENDOR measurements.

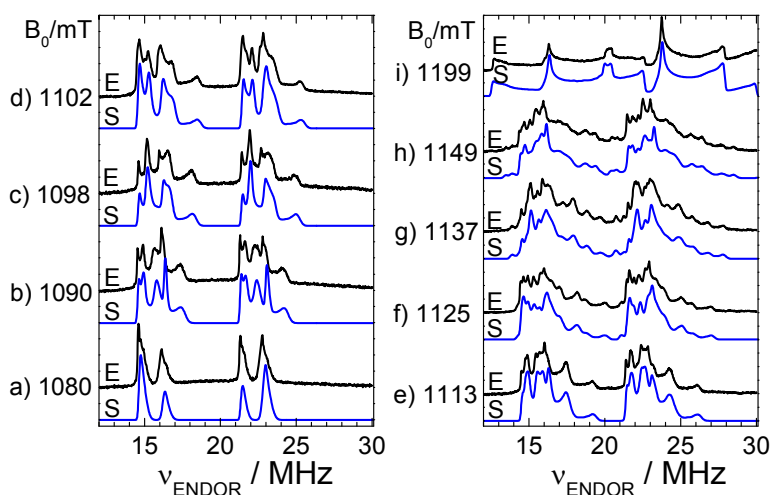


Figure 3.11. Experimental (E) and simulated (S) nitrogen Davies ENDOR spectra of **6** at $f = 34.031$ GHz (Q-band) and $T = 16$ K using an RF pulse length of 35 μ s. The MW pulse lengths were 200 ns for the (soft, selective) inversion pulse and 40-80 ns for the two pulse detection sequence which had a waiting time (τ) of 300 ns. The respective observer positions are shown in figure 3.10.

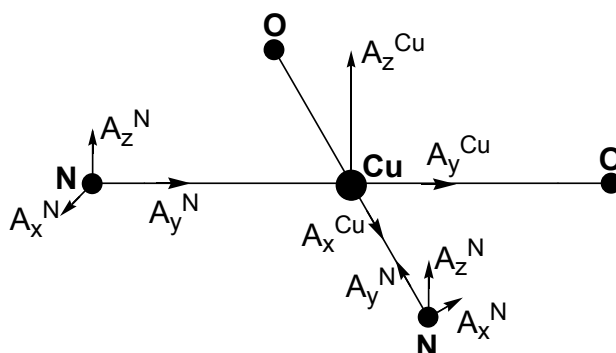
The Euler angles describe the orientations of the nitrogen hyperfine and nuclear quadrupole tensors in the g tensor frame. The resulting geometry of the principal axis system is illustrated in figure 3.12. The same orientation of the A tensor was derived from W-band EPR measurements which have a better spectral resolution and thus improve the accuracy of the spectral analysis.

Table 3.2. The g , A , and Q principal values and the respective Euler angles for **6**.

	g	A^{Cu}/MHz	A^{N}/MHz	Q^{N}/MHz	$Q^{\text{N}}/\text{MHz}(\text{calc.})^{\text{a)}$	Euler angle/ $^\circ$
x	2.041	95	36.3	1.28	1.21	$\alpha = 35$
y	2.041	95	50.5	-0.70	-0.70	$\beta = 14$
z	2.186	632	37.5	-0.58	-0.51	$\gamma = 0$

^{a)} B3LYP, COSMO model, basis: CP(PPP) for Cu, def2-TZVP for all the other atoms using the Orca program. Experimental error bars: $g(\pm 0.002)$, $A^{\text{Cu}}(\pm 3 \text{ MHz})$, $A^{\text{N}}(\pm 0.4 \text{ MHz})$, $Q(\pm 0.03 \text{ MHz})$, Euler angles ($\pm 2^\circ$).

It was assumed that the A^{N} and Q tensors are collinear to each other but they are not collinear with the g and A^{Cu} tensors. The Euler angles, derived from the simulations of the Davies ENDOR spectra using the program Xsophe from Bruker [Wang95], between the z-axes of A^{Cu} and A^{N} amounts to 14° and between the xy planes to 35° . Although the angle β is quite small, it is a very sensitive parameter in the low field part ($B = 1075 - 1150 \text{ mT}$) of the Q-band EPR spectrum. The difference in the EPR parameters of the two coordinating nitrogens is almost negligible. The EPR parameters are qualitatively reproduced by means of DFT calculations (see Table 3.2 and 3.3).

**Figure 3.12.** Schematic representation of the principal axis system for all investigated compounds.

For all the investigated complexes, the following assumption was made in the analysis of the data

$$|A_x^{\text{N}}| \approx |A_z^{\text{N}}| \approx |A_{\perp}^{\text{N}}| < |A_y^{\text{N}}| = |A_{\parallel}^{\text{N}}| \quad (3.27)$$

and the two coordinating nitrogens were considered to be equivalent. Nevertheless, these assumptions are rather rough, since the DFT results (table 3.3) predict the rhombicity of A^{N} . A good agreement between the X-band EPR spectra and the simulations is obtained, as shown for **3** (see figure 3.13).

In figure 3.13, the quintets arising from the coupling of the unpaired electron with the nuclear spin of two nitrogens are clearly resolved in the parallel region

of the spectrum. The peaks marked with “x” in the left hand side diagram result from the coupling between nitrogen and the ^{65}Cu isotope.

Table 3.3. g and A values for **1** to **7**.

compound	Experimentally obtained values ^{f)}					Calculated values using DFT ^{e)}			
	g_x	g_y	g_z	g_{iso}	g_{av}	g_x	g_y	g_z	g_{iso}
1	2.042 ^{b)}	2.042 ^{b)}	2.184 ^{b)}	2.092	2.089	2.033	2.035	2.116	2.061
2	2.041	2.041	2.180	2.092	2.087	2.034	2.037	2.115	2.062
3	2.042	2.042	2.186	2.093	2.090	2.038	2.039	2.131	2.069
4	2.045	2.045	2.185	2.096 ^{a)}	2.092	2.034	2.036	2.119	2.063
5	2.042	2.042	2.193	2.096	2.092	2.038	2.040	2.133	2.070
6	2.040	2.040	2.185	2.092	2.088	2.031	2.032	2.105	2.056
7	2.048	2.048	2.223	2.108	2.106	2.043	2.043	2.151	2.079

compound	$A_x(^{63}\text{Cu})$	$A_y(^{63}\text{Cu})$	$A_z(^{63}\text{Cu})$	$A_{\text{iso}}(^{63}\text{Cu})$	$A_{\text{av}}(^{63}\text{Cu})$	$A_x(^{63}\text{Cu})$	$A_y(^{63}\text{Cu})$	$A_z(^{63}\text{Cu})$	$A_{\text{iso}}(^{63}\text{Cu})$
1	-104	-104	-617	-275	-275	-35	-40	-634	-237
2	-104	-104	-617	-275	-275	-21	-27	-637	-228
3	-99	-99	-618	-267	-270	-31	-34	-616	-227
4	-100	-100	-614	-270 ^{a)}	-271	-25	-34	-634	-231
5	-92	-92	-596	-257	-259	-11	-26	-600	-212
6	-95	-95	-632	-269	-269	-20	-25	-651	-232
7	-55	-55	-555	-220	-220	-5	-13	-564	-194

compound	$A_x(^{14}\text{N})$	$A_y(^{14}\text{N})$	$A_z(^{14}\text{N})$	$A_{\text{iso}}(^{14}\text{N})$	$A_{\text{av}}(^{14}\text{N})$	$A_x(^{14}\text{N})$	$A_y(^{14}\text{N})$	$A_z(^{14}\text{N})$	$A_{\text{iso}}(^{14}\text{N})$
1	40	59.5	40	46.2	46.5	43	62	42	49
2	40	59.5	40	46.5	46.5	49	67	50	55
3	40	59.5	40	46.0	46.5	44	61	42	49
4	40	59	40	45.6 ^{a)}	45.3	45	60	44	50
5	39	51	39	43.0	43.0	39 ^{c)}	55 ^{c)}	37 ^{c)}	43 ^{c)}
6	38	54	38	42.7	43.3	40 ^{d)}	56 ^{d)}	39 ^{d)}	45 ^{d)}
7	33	44	33	37.6	36.7	43	59	45	49

^{a)} in agreement with literature [Wang03] and ^{b)} [Unamuno98]. ^{c)} aromatic amine, ^{d)} aliphatic amine, ^{e)} B3LYP, COSMO model, basis: CP(PPP) for Cu, def2-TZVP for all the other atoms using the Orca program. ^{f)} Experimental error bars: $g(\pm 0.003)$, $A^{\text{Cu}}(\pm 3)$, $A^{\text{N}}(\pm 2)$. A in MHz.

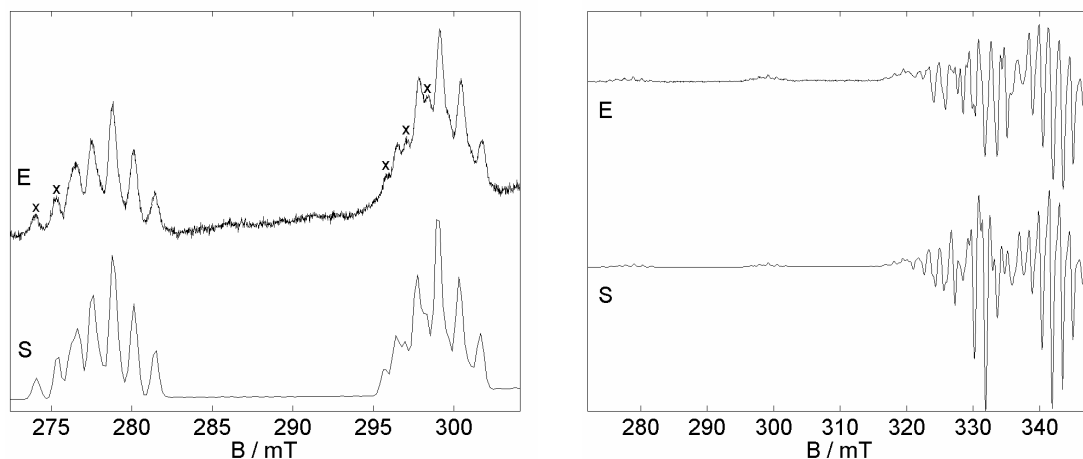


Figure 3.13. Experimental (E) and simulated (S) EPR powder spectrum of **3** at $f = 9.437$ GHz (X-Band) and $T = 298$ K. On the left side the low field range is zoomed in and the clearly seen isotope peaks are highlighted with “x”.

The better resolution of the W-band EPR spectra compared to those recorded in X-band reconfirms the limits of the assumptions made. The simulated (S) and the experimental (E) W-band spectra of **3** are shown in figure 3.14. The signals corresponding to g_z are clearly separated from the signals corresponding to g_{\perp} .

The values of g_x and g_y are assumed to be equal since simulations have shown that these parameters differ less than 0.05 % from each other.

The differences between the experimental and simulated spectrum in the right panel of figure 3.14 could not be minimized with the assumptions taken; the equivalence of the two nitrogens and the axial symmetry of the Cu and N hyperfine tensors.

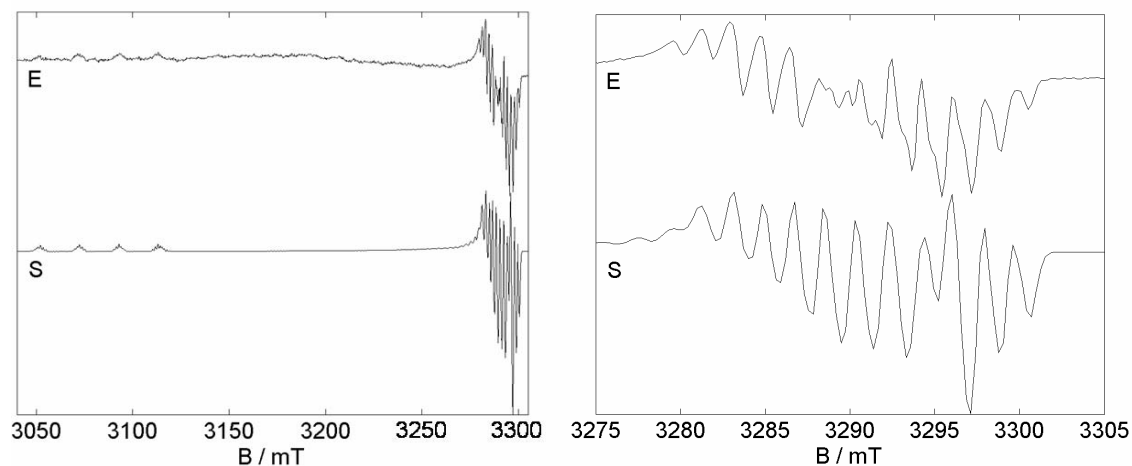


Figure 3.14. Experimental (E) and simulated (S) EPR powder spectrum of **3** at $f = 93.897$ GHz (W-Band) and $T = 10$ K. The right panel shows a zoom in the high field spectral range of the left panel.

The tensor principal values of the investigated complexes are reported in table 3.3. The average values were calculated according to

$$A_{av} = \frac{1}{3}(A_x + A_y + A_z) \quad \text{and} \quad (3.28)$$

$$g_{av} = \frac{1}{3}(g_x + g_y + g_z). \quad (3.29)$$

They correspond very well to the values determined from the solution spectra, *cf.* isotropic values (iso) in table 3.3.

The X-band EPR spectrum of the solution of **6** in CH_2Cl_2 recorded at room temperature is shown in figure 3.15. It shows a well-resolved four line pattern as expected for the coupling of an electron spin with the nucleus of Cu. At lower m_I values the peak-to-peak line width Γ becomes larger. In 1966 Wilson and Kivelson [Wilson66] extensively studied EPR linewidths in liquids considering the Brownian tumbling in solution. According to this theory the line broadening, described by the peak-to-peak line width Γ , is a function of the magnetic

nuclear spin quantum number m_I and can be approximated by the expression $\Gamma = A + Bm_I + Cm_I^2 + Dm_I^3$ where the parameters A , B , C , and D depend on the temperature. The spectrum in figure 3.15 was simulated using line width parameters $A = 1.625$ mT, $B = 0.65$ mT, and $C = D = 0$.

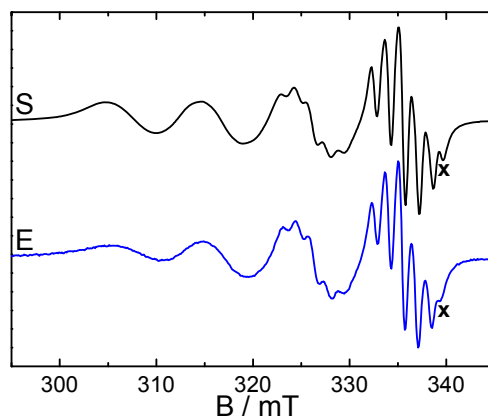


Figure 3.15. Experimental (E) and simulated (S) EPR spectrum of **6** in CH_2Cl_2 at $f = 9.438$ GHz (X-Band) and $T = 298$ K. The band resulting from the interaction with ^{65}Cu is highlighted with “x”.

The signs of the hyperfine eigenvalues, listed in table 3.3, which could not be obtained experimentally, were taken from the predictions of DFT calculations. As expected, the parameters determined for compound **7** differ significantly from those of the other compounds. This clearly demonstrates that the structural parameters, summarized in table 2.13, have a huge influence on the EPR parameters. The g_x , g_y , and g_z values are smaller in the approximately square planar compounds **1** - **4** compared to the tetrahedrally distorted complex **7**. In contrast, the respective hyperfine values A for Cu(II) and N are larger for the square planar complexes compared to the tetrahedrally distorted one.

The qualitative trends in g arise from a decrease in the energy separation of the electronic levels when going from square planar to tetrahedrally distorted structures. The same effect is expected to cause the decrease in A .

The EPR parameters resulting from quantum chemical calculations are reported in table 3.3. They reproduce well the experimental trends of the EPR parameters. The calculated g values are smaller than those experimentally determined, but differ from the experimental values by less than 0.01 in the case of g_x and g_y and by less than 0.07 for g_z . The absolute values of A^{N} are up to 20 % too high, while A_z^{Cu} meets the experimental values with deviations smaller than 5 %. The highest deviations arise for A_x and A_y of Cu for which the experiment leads to values which are four or five times higher. Such high

deviations have already been reported for other Cu(II) transition metal complexes [Finazzo06]. Reasons for this behaviour are given in e.g. [Szilagyi02, Deeth01] and some new approaches are reported in [Deeth01, Atanasov06]. Therein it is reported that DFT intrinsically overestimates the covalency of the bonds between the transition metal and the ligand. Conventional DFT programs, based on perturbation theory, do not predict e.g. the g -tensor properly since the spin-orbit coupling constant has the same order of magnitude as the ${}^2E-{}^2A_1$ energy separation. The mismatch between experiment and theoretical predictions becomes increasingly pronounced from left to right of the 3d-transition metal series. This can be improved by using localized orbitals obtained via a modification of the Cu(II) nuclear charge. A reduction of nuclear charge by 0.8 for Cu(II) has led to a good agreement with optical and EPR data for a wide range of Cu(II) amine complexes [Deeth01].

3.5.3 Experimental and theoretical studies of spin population

For the complexes **1** - **4**, with an almost ideal square planar coordinated Cu(II) ion, a spin population on Cu(II) from 70.5 to 71.8 % was found. For **5** - **7**, the spin population on the Cu(II) ion ranged from 71.4 to 73.9 %; the increase is due to the deviation from square planar coordination geometry and has its maximum for the distorted tetrahedral coordinated Cu(II) ion in **7**. The values of the spin populations agree well with the values measured by polarized neutron diffraction for similar Cu(II)-bis(oxamato) complexes [Baron97] as well as with those of Cu(II)-phthalocyanines investigated by means of EPR [Finazzo06]. The opposite trend was calculated for the spin population on the coordinated heteroatoms which is obvious since the normalization condition given in equation 3.4 was used. The obtained spin population for the tetrahedrally distorted complex **7** (9.2 %) is smaller compared to the almost ideal square planar complexes **1** - **4** (10.3 %), cf. table 3.4. Similar results were obtained for Cu(II)-phthalocyanines [Finazzo06].

The model of Morton and Preston [Morton78] seems to overestimate the spin delocalisation from Cu(II) to the coordinated heteroatoms, i.e. the degree of covalency of the bonding is too high. Following this model the values for the spin population on Cu(II) in the range of 52.6 to 57.6 % are much smaller than expected and give no clear trend. In the case of N the expected trend can be

verified, *i.e.* a higher spin population on N when the coordination geometry is closer to square planar. Using the approach of Morton and Preston the spin population on N can be derived from the hyperfine coupling parameters of N, *i.e.* independently of the spin population on the Cu(II) ion and consequently no D_{4h} symmetry has to be assumed in this case.

Table 3.4. Spin population (in %) for Cu (α^2) and N ($(\alpha'/2)^2$) for 1-7.

compound	atom	α^2 ^{a)}	α^2 ^{b)}	atom	$(\alpha'/2)^2$ ^{a)}	ρ^N (s orbital) ^{a)}	$(\alpha'/2)^2$ ^{b)}
1	Cu	71.0	54.6	N	10.3	3.0	14.5
2	Cu	70.5	54.6	N	10.4	3.0	14.3
3	Cu	71.8	55.8	N	10.1	3.0	14.7
4	Cu	71.1	54.8	N	10.3	3.0	14.6
5	Cu	73.0	53.8	N	10.1	2.8	9.6
6	Cu	72.9	57.6	N	9.6	3.2	12.3
7	Cu	74.0	52.6	N	9.2	2.4	7.8

^{a)} according to equations 3.4 and 3.5; ^{b)} according to [53]

The spin populations of **2**, **5**, and **7** were calculated with the quantum chemical methods specified in the experimental section and are given in table 3.5. Qualitatively, all the theoretical methods used show the same trends of the spin population, in agreement with those experimentally obtained. The unpaired electron is mainly localized at the Cu(II) ion. The highest relative contribution from the Cu(II) ion was obtained with the NPA (73 - 75 %), the lowest for the Mulliken analysis (55 - 57 %), the other methods under study yield values in between. The spin population calculated on N is higher than on O due to the stronger N–Cu bond, which correlates with the smaller Cu–N distances compared to the Cu–O distances, *cf.* table 2.13.

Table 3.5. Spin population (given in %) for **2**, **5**, and **7** obtained from DFT studies.

	Mulliken			Loewdin			NPA			Integrated spin population		
	Cu	N	O	Cu	N	O	Cu	N	O	Cu	N	O
2	55	15	7	62	10	6	74	8	4	64	12	6
5 ^{a)}	57	12	7	63	8	6	75	7	4	65	10	6
5 ^{b)}		14	8		10	7		7	5		11	7
7	57	11	8	63	8	6	73	6	5	64	9	7

^{a)} aryl-*N*(oxamato) entity, ^{b)} alkyl-*N*(oxamato) entity; B3LYP, COSMO model, basis: CP(PPP) for Cu, def2-TZVP for all the other atoms using the Turbomole program

The spin population, ρ_s , for **7** is plotted in figure 3.16 and iso-density surfaces are shown for $\rho_s = 0.1(0.01)$ electrons/Bohr³. A clear localization of the spin population on the Cu, N, and O atoms is observed. The unpaired electrons occupy the d-orbital pointing to the surrounding N and O atoms and p orbitals of the latter pointing to the central Cu(II) ion.

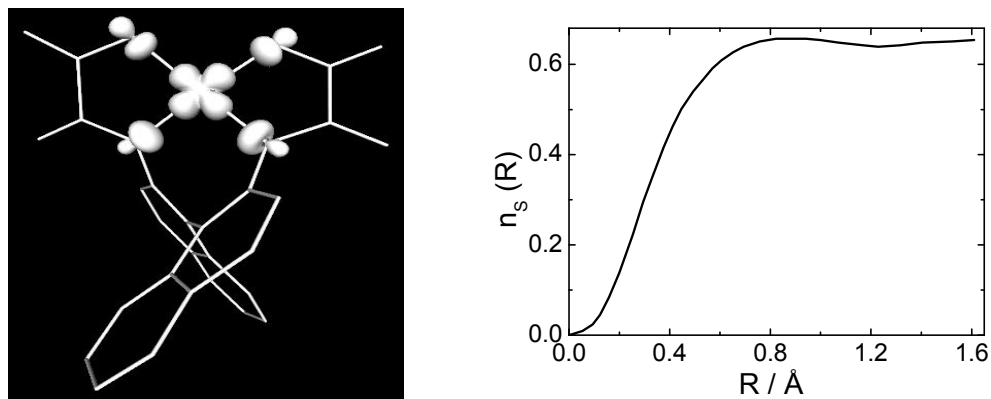


Figure 3.16. Spin population of **7**. Iso-surfaces are drawn at 0.01 electrons/Bohr³ (left). Dependence of the number of unpaired electrons $n_s(R)$ on Cu within a sphere of radius R on R (right).

3.5.4 Investigation of the magnetic super-exchange parameters

The evolution of the magnetic susceptibility, χ_m , and $\chi_m T$ with the temperature for **19** - **24** is reported in figures 3.17 - 3.19. The concentration of the paramagnetic impurities ρ , and the parameter R (cf. equation 3.17) along with the g factors, measured by means of EPR, for **19** - **24**, are summarized in table 3.6.

The $\chi_m T$ product of the dinuclear Cu(II) complexes **19** and **20** amounts to almost zero at 2.7 K, see figure 3.17, indicating an antiferromagnetically coupled spin zero ground state of the two Cu(II) ions. Especially in the χ_m versus T plot the paramagnetic impurities show a strong influence on the line shape, leading to an increase in the magnetic susceptibility with decreasing temperatures below 25 K. Upon heating to 300 K the $\chi_m T$ product increases to 0.72 cm³ K mol⁻¹ which is close to the calculated value for two uncoupled Cu(II) ions (0.83 cm³ K mol⁻¹) [Kahn93]. The fit to the experimental data was performed using the definition of the magnetic susceptibility in equation 3.14. The best match of the calculated to the experimental curve was obtained for the J values given in table 3.6. For **19** and **20** the paramagnetic impurities were fitted to about 1 %.

The $\chi_m T$ product of the trinuclear Cu(II) complexes **21** - **24** vs. the temperature is shown in figures 3.18 and 3.19. At 300 K it amounts to about 1.03 cm³ K mol⁻¹ for **21** - **23** and 0.67 cm³ K mol⁻¹ for **24**. The values are smaller than expected for a system of three uncoupled Cu(II) ions (1.2 cm³ K mol⁻¹ for an average g value of 2.09). This difference is much more pronounced for **24** than for **21** - **23** due to the strong antiferromagnetic superexchange interaction among the terminal and the central Cu(II) ions in **24**. Thus, the Cu(II) ions cannot be

treated as independent in the temperature range of the measurement, *i.e.* up to 300 K.

The adjacent Cu(II) ions are antiferromagnetically coupled with absolute J values ranging from -89 to -114 cm^{-1} for $[\text{Cu}(\text{pmdta})]^{2+}$ as terminal ligand system, *cf.* **19** - **23**. For **24** the antiferromagnetic interaction is strongly increased to -363 cm^{-1} because of the square planar coordination geometry of the $[\text{Cu}(\text{tmeda})]^{2+}$ entity as terminal ligand system, which induces a higher overlap of the magnetic orbitals and thus a much stronger antiferromagnetic interaction compared to the $[\text{Cu}(\text{pmdta})]^{2+}$ entity. The influence on the magnetic properties resulting from intermolecular exchange interactions, see zJ' in table 3.6, is almost negligible for **21** - **23** and only slightly higher for **24**. This may also be related to the square planar coordination geometry of the terminal Cu(II) ions in **24** which allows stronger intermolecular interactions.

Whereas the difference in J of the dinuclear Cu(II) complexes **19** ($J = -114 \text{ cm}^{-1}$) and **20** ($J = -112 \text{ cm}^{-1}$) is negligible, the difference in J of the corresponding trinuclear complexes **21** ($J = -89 \text{ cm}^{-1}$) and **22** ($J = -113 \text{ cm}^{-1}$) is significant. The reason for this behaviour will be discussed in the following sections.

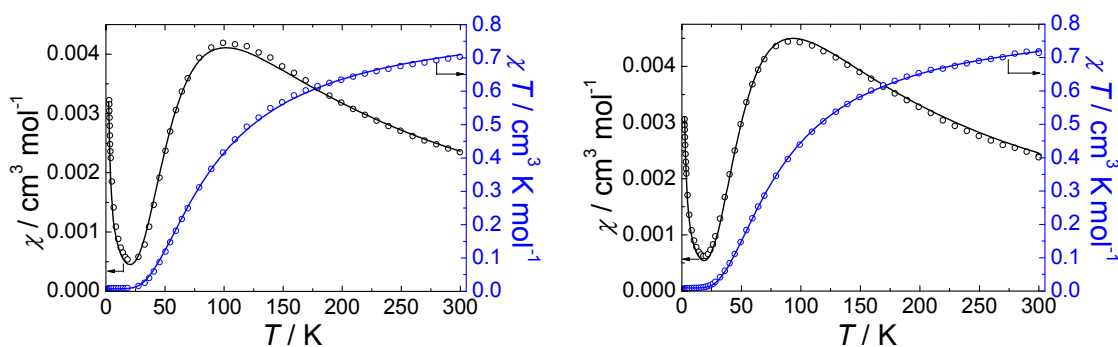


Figure 3.17. χ_m and $\chi_m T$ versus T plot for **19** (left) and **20** (right).

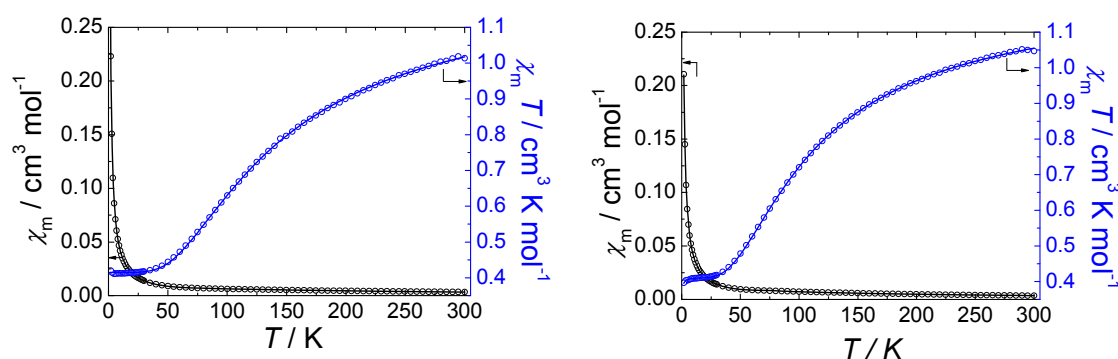


Figure 3.18. χ_m and $\chi_m T$ versus T plot for **21** (left) and **22** (right).

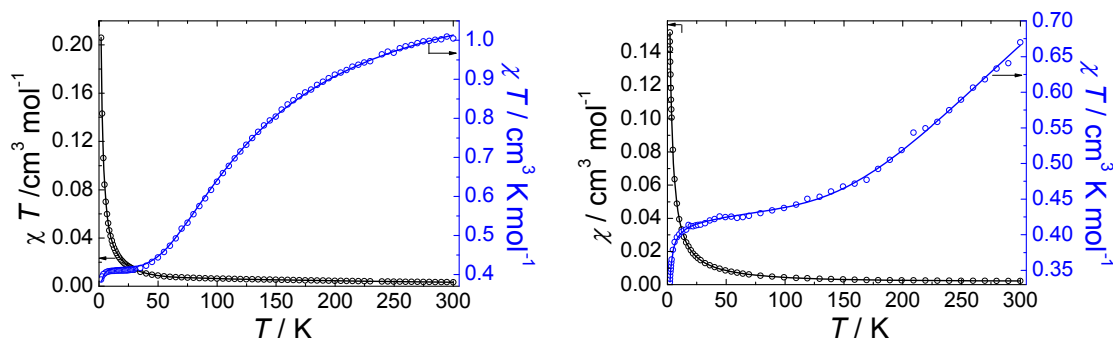


Figure 3.19. χ_m and $\chi_m T$ versus T plot for **23** (left) and **24** (right).

Table 3.6. Values of J determined from the fitting of the experimental data along with the corresponding values of the R parameter. The zJ' term results from intermolecular interactions.

complex	J_1 / cm^{-1}	$\rho / \%$	zJ' / cm^{-1}	g	R
19	-114 ± 2	0.9 ± 0.1	-	2.10 ± 0.01	$2 \cdot 10^{-4}$
20	-112 ± 2	1.0 ± 0.1	-	2.10 ± 0.01	$5 \cdot 10^{-4}$
21	-89 ± 2	-	-0.02 ± 0.01	2.09 ± 0.01	$3 \cdot 10^{-5}$
22	-113 ± 2	-	-0.02 ± 0.01	2.09 ± 0.01	$5 \cdot 10^{-6}$
23	-111 ± 2	-	-0.04 ± 0.01	2.09 ± 0.01	$5 \cdot 10^{-4}$
24	-363 ± 4	-	-0.06 ± 0.01	2.09 ± 0.01	$1 \cdot 10^{-3}$

3.5.5 DFT calculations of the magnetic super-exchange parameters

Calculated and measured values for magnetic coupling parameters of **21** and **22** are collected in table 3.7. Both compounds were treated firstly by omitting (**21'** and **22'**) and secondly by including (**21'NO₃⁻** and **22'BF₄⁻**) the respective counter ions which are weakly coordinated to the central Cu(II) ion. For each case the eigenenergies for the four different magnetic states were calculated using the COSMO model. In addition, calculations without the COSMO model were carried out for **21'**, **21'NO₃⁻**, and **22'BF₄⁻**. The coupling parameters were obtained by inserting the respective energies into the equation system 3.25 and solving it.

In all cases the calculated coupling parameters are significantly larger than the measured ones, which is not untypical. Coupling parameters are usually largely overestimated by pure DFT methods and underestimated by Hartree-Fock. The hybrid functional B3LYP, which contains 20 % Hartree-Fock exchange, still tends to overestimate these quantities [Sun05, Ruiz05]. Moreover, the calculated coupling parameters correspond to energy differences between the magnetic states of ca. 10 meV, which in terms of DFT is very small. The values calculated within the COSMO model are ca. 1.5 times larger than those

experimentally determined, independently of whether the counter ions are considered or neglected. Without COSMO the differences to the experimental values are larger; for **21'** one obtains a factor of 1.7, whereby the explicit consideration of the counter ion leads to even larger discrepancies; the values for **21'**NO₃⁻ (without COSMO) are more than twice as large as the experimental data. The trends are very similar for **22**, **22'** and **22'**BF₄⁻.

Table 3.7. *J* parameters measured for **21** (a) and **22** (f) and calculated without considering the counter ions for **21'** (b, c) and **22'** (g), as well as calculated taking into consideration the counter ions coordinating to the central Cu(II) ion for **21'**NO₃⁻ (d,e) and **22'**BF₄⁻ (h). The structural parameters were taken from the X-ray diffraction analysis.

	compound	Method	J_{12}/cm^{-1}	$J_{12'}/\text{cm}^{-1}$	$J_{22'}/\text{cm}^{-1}$
(a)	21	Measured	-89 ± 2	-89 ± 2	0
(b)	21'	Calc., with COSMO	-135	-135	0
(c)	21'	Calc., without COSMO	-152	-154	-1
(d)	21' NO ₃ ⁻	Calc., with COSMO	-134	-136	0
(e)	21' NO ₃ ⁻	Calc., without COSMO	-215	-210	+26
(f)	22	Measured	-113 ± 2	-113 ± 2	-
(g)	22'	Calc., with COSMO	-166	-169	0
(h)	22' BF ₄ ⁻	Calc., with COSMO	-166	-170	-1
(i)	22' BF ₄ ⁻	Calc., without COSMO	-244	-260	0

Even though the calculated values for *J* deviate significantly from the experiment, the experimentally observed differences between **21** and **22** are reproduced very well by **21'** and **22'**. According to the experimental results, the coupling parameter J_{12} is larger by 27 % for **22** as compared to **21**, while the values calculated for **22'** (or **22'**BF₄⁻) are larger than those calculated for **21'** (or **21'**NO₃⁻) by ca. 25 %, when the results obtained with the same method are compared. The difference in the coupling constants of **21** and **22** thus obviously cannot be traced back to different counter ions, but rather to the structural differences of the two molecules themselves. On one hand these can be differences in stoichiometry (opba vs. nabo), on the other hand different structure parameters due to packing effects can play a role.

In order to find out which of these two factors brings the larger contribution, the coupling parameters of an artificial species were calculated, which is of the composition of **21'**, but of the geometric structure of **22'**. This molecule was obtained by removing four C and four H atoms of the terminal phenyl ring in **22'** and adding two H instead without any further structural modifications. For this structure we found (using the COSMO model and neglecting the counter ion) $J_{12} = -167 \text{ cm}^{-1}$, $J_{12'} = -164 \text{ cm}^{-1}$, and $J_{22'} = 1 \text{ cm}^{-1}$, which is practically identical with the values obtained for **22'**. Thus we may conclude that the difference in

coupling parameters of **21** and **22** mainly arise from differences in the geometric structure for instance introduced by packing effects. The choice of the counter ion (NO_3^- or BF_4^-) or of the organic bridge (opba or nabo) is of much less significant influence. The latter conclusion is further supported by the previous experimental observation that the spin density distribution of the respective mononuclear precursor molecules **1** and **2** does not significantly vary with replacing the aromatic systems.

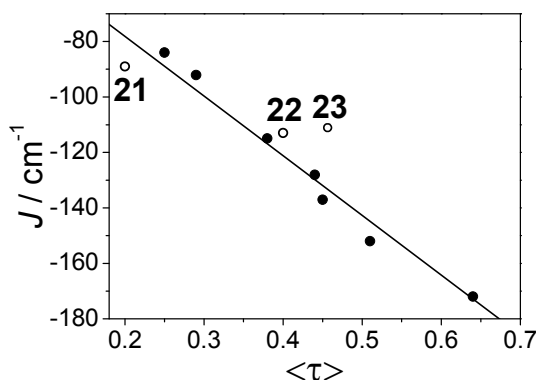
Packing effects, which are generally understood as effects caused by the arrangement of molecules with respect to each other in the solid state, lead to different local geometry for the Cu(II) ions in **21** and **22** and hence to differences in the overlap of magnetic orbitals which is finally reflected in different coupling parameters. The differences between the molecular structures of **21** and **22** determined from x-ray diffraction studies were discussed in section 2.8 and were compared in figure 2.16. Since the coordination geometries of the terminal Cu(II) ions of **21** are closer to the ideal trigonal bipyramidal one for which the overlap of the magnetic orbitals is more reduced in comparison to **22**, the magnetic super-exchange interaction for **21** is weaker.

For fivefold coordinated transition metal ions the variation of J values depending on the coordination type has already been observed and intensively discussed [Stumpf93]. The τ parameter, which was introduced in section 2.6, is a measure of the distortion from the ideal trigonal-bipyramidal coordination. A linear dependence of J on τ was confirmed by several reports [Costa93]. The τ and the corresponding J parameters are given in table 3.8. Figure 3.20 shows the J versus τ values for **21** and **22** superimposed on the plot already reported by Costa *et al.* [Costa93]. It can be seen that the J versus τ values for **21** and **22** follow the linear tendency. This is a further proof that the differences in the J parameters of **21** and **22** are due to the different coordination geometry of their terminal Cu(II) ions which is induced by packing effects in the solid state as described in chapter 2.

The deviation of the J value of **23** from the linear dependency in figure 3.20 is most probably due to the deviation of the three Cu(II) ions from the molecular plane which reduces the overlap of the magnetic orbitals and thus the antiferromagnetic interaction.

Table 3.8. Experimental values of the τ parameter for terminal Cu(II) ions in **21** - **23**.

	$\tau(\text{Cu2})$	$\tau(\text{Cu2}')$	average	J
21	0.187	0.203	0.195	-89±2
22	0.417	0.388	0.403	-113±2
23	0.477	0.455	0.466	-111±2

**Figure 3.20.** Representation of the J values of **21** - **23** vs. their averaged τ parameter for the terminal Cu(II) ions (open symbols) in comparison with values of similar complexes (full symbols) [Costa93].

3.5.6 Correlation of spin population with structural and magnetic properties

In the following section some conclusions regarding the influence of the spin population distribution in the mononuclear complexes as starting materials for the corresponding trinuclear complexes, *cf.* figure 3.21, will be derived. DFT calculations of the spin population were performed for **1** and **15** using the same method and basis set, *cf.* experimental section. The numbering scheme of the Cu(II) ions in figure 3.22 will be used for all the other trinuclear complexes. The calculations indicate that the spin population on the central Cu(II) ion and the coordinated nitrogens remains almost unchanged when going from the mononuclear to the trinuclear complexes, *cf.* table 3.6. This fact is a prerequisite for the following discussion.

In order to study the relation between the molecular structure, the spin population on the heteroatoms, and the corresponding J parameter, the J of $[\text{Cu}_3(\text{R-bnbo})(\text{pmdta})_2]^{2+}$ (**25**) was predicted using the bond lengths and angles of the $[\text{Cu}(\text{pmdta})]^{2-}$ fragments of **22**. For **25** the obtained values are $J_{12} = -141 \text{ cm}^{-1}$ and $J_{12'} = -150 \text{ cm}^{-1}$. The average J value is given in table 3.9. Above it was shown that the trends in J can be predicted with high accuracy for Cu(II)-bis(oxamato) complexes using the broken-symmetry approach. It can thus be

reliably stated that the values $J_{12} = -166 \text{ cm}^{-1}$ and $J_{12'} = -169 \text{ cm}^{-1}$ calculated for $[\text{Cu}_3(\text{nabo})(\text{pmdta})_2]^{2+}$ are significantly larger than that of **25**, the relative difference being well above the accuracy of the calculations. Since the coordination geometry of the terminal ligands was the same for the two considered complexes, only the distortion from the square planar coordination geometry and its effect on the spin population distribution can be responsible for the predicted trend. For the used method and basis set the theoretical values are larger than the experimental values of *bis*(oxamato) complexes by a factor of 1.49 as stated above. This factor will also be used for correcting the predicted J value of **25**.

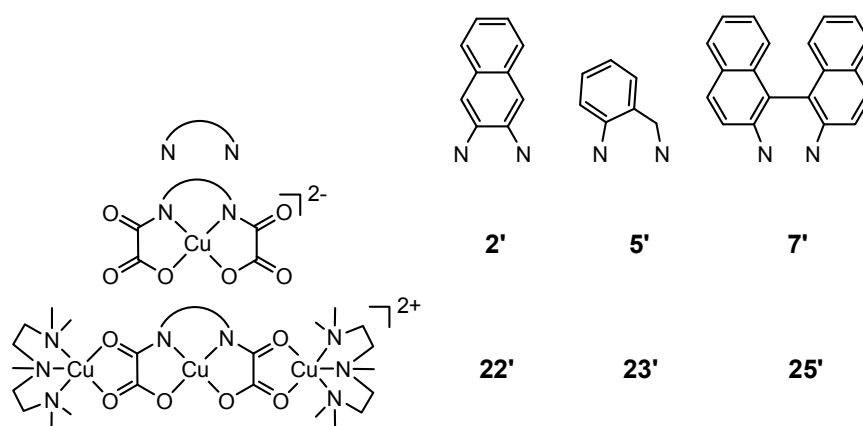


Figure 3.21. Investigated mono- and corresponding trinuclear Cu(II)-*bis*(oxamato) complexes.

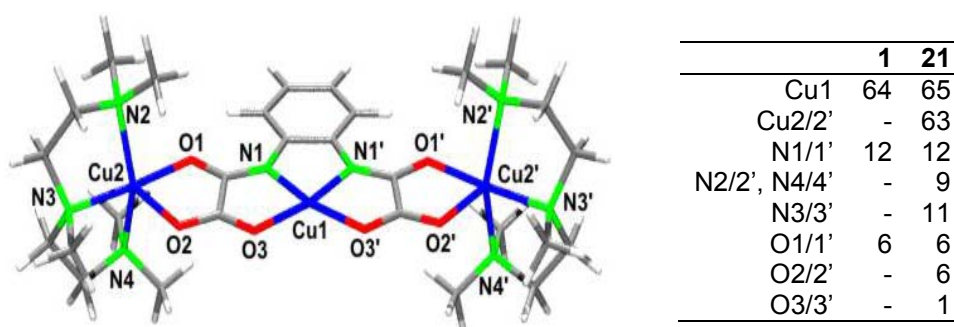


Figure 3.22. Geometry optimized molecular structure of **21** without counter ions. The spin populations (in %) of **1** and the corresponding trinuclear complex **21** are given in the right table.

Only when the coordination geometry of the terminal ligands and thus its τ parameter remains unchanged the structural influences on the spin population of the N atoms, coordinated to Cu(1), can be studied. For this purpose a linear dependency " $\Delta J = -(120 \pm 20) \text{ cm}^{-1} \cdot \Delta \tau$ " found for **21** and **22**

was used to normalize the experimental J values of **21**, **22**, and **23** at $\tau = 0.4$. The extracted J values are given in table 3.9 and are plotted in figure 3.23.

Table 3.9. Calculated and experimental J values of **21** - **23** and **25**.

	experiment J/cm^{-1}	τ parameter	normalized J $J(\tau = 0.4)/\text{cm}^{-1}$	DFT calculated $J_{\text{calc}}/\text{cm}^{-1}$	$J_{\text{calc}}/1.49\text{ cm}^{-1}$
21	-89	0.2	-113	-135 ^{a)}	-91
22	-113	0.40	-113	-168 ^{a)}	-113
23	-111	0.47	-104	-	-
25	-	-	-	-146 ^{b)}	-98

Single point energy calculation of ^{a)} the X-ray structures and ^{b)} the structure of **7** assembled with the $[\text{Cu}(\text{pmdta})]^{2+}$ entities of **22**.

The N–Cu–N bond angle was found to be the best parameter for visualizing the correlation between the spin population on N, the J parameter, and the structural variations in the complexes under study, as shown in figure 3.23.

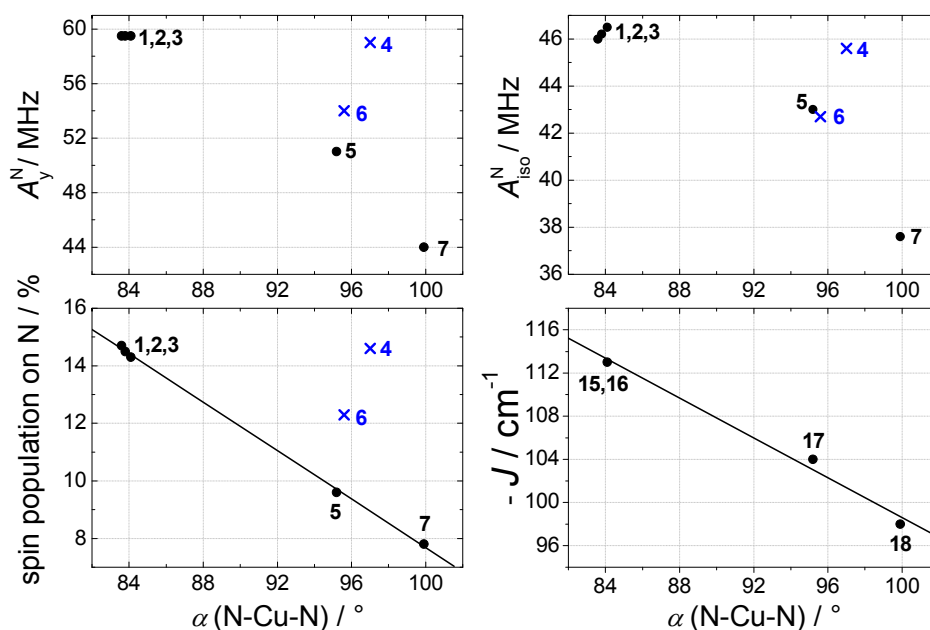


Figure 3.23. Dependence of the hyperfine coupling parameter of N, the spin population on N (calculated according to [Morton78]), and the J parameter over the N–Cu–N angle.

This statement holds for the complexes **1**, **2**, **3**, **5**, and **7**, whereas for **4** and **6** deviations were observed. To recall, **1**, **2**, and **3** consist of fused 5-5-5 chelate rings, whereas **4**, **5**, and **6** of 5-6-5 chelate rings, and **7** of 5-7-5 chelate rings. Cervera *et al.* [Cervera98] reported that a stronger ligand field, *i.e.* a stronger metal-ligand- σ -bonding destabilization of the singly occupied molecular orbital (SOMO) of Cu(II), associated with the six- compared to the five-membered chelate rings leads to differences in the absorption spectra. The EPR parameters are associated with the absorption behaviour by the spin-orbit

coupling. The deviations from the trends, shown in figure 3.23, for the complexes **4** and **6** are most probably related to such effects. An influence of the atom number in coordinated chelate rings on the spin population distribution in such systems has already been reported [Kirmse85]. The spin population in figure 3.23 was derived according to [Morton78] and is outlined in table 3.5. Since the A_y and A_{iso} of N are included in the equation for the spin population calculation on N, these plots are also shown. Deviations from the linear dependence on the N–Cu–N bond angle for **4** and **6** can also be found for g and A^{Cu} but are not shown here.

The absolute values of the spin population on N of the precursor and the corresponding J parameter of the trinuclear complexes increase when the bond angle decreases, clearly reflecting the correlation of these parameters.

3.6 Summary and Conclusions

The excellent resolution in cw EPR as well as in pulse ENDOR for diamagnetically diluted powders of the investigated Cu(II) complexes allows the determination of all tensor components of g , A , and Q leading to a valuable insight into the magnetic properties of such complexes. The principal values of the g tensor are smaller for the almost ideal square planar compounds **1** - **4** compared to the tetrahedrally distorted complex **7**, while the opposite case holds for the A tensor principal values. This effect arises from the decrease in the energy separation of the electronic levels when going from square planar to tetrahedrally distorted structures.

Knowledge about these parameters enables the determination of the spin population distribution in the mononuclear complexes **1** - **7**. Extrapolation of this information on the multimetallic complexes enables to gain insight into the main mechanisms responsible for the magnetic coupling of the respective multimetallic compounds. The comparison of the EPR and DFT results, for the complexes **1** - **7**, shows that the spin delocalisation decreases when going from the square planar to the tetrahedral coordination geometry.

The results of this work suggest similar coupling parameters for multimetallic complexes in which **1** and **2** are used as building blocks. Indeed, the different antiferromagnetic couplings observed for the trinuclear complexes **21** and **22** based on **1** and **2**, respectively, have now been indirectly proved to originate

from packing induced structural effects. Experimental as well as theoretical studies by means of DFT of **21** - **23** and **25** have shown a linear dependence of the J parameter on the N–Cu–N bond angle. The studies of their precursors **1**, **2**, **5**, and **7** lead to the conclusion that an increase in the spin population on N increases the antiferromagnetic super-exchange interaction in the corresponding trinuclear complexes.

4 Thin films of Cu(II)-*bis*(oxamato) complexes

4.1 Introduction

The structural variety of Cu(II)-*bis*(oxamato) complexes makes them excellently suited for basic research studies of magnetic super-exchange phenomena as shown in chapter 3. However, especially in the case of polymeric structures of such complexes, the structural characterisation is rather difficult because in many cases no suitable crystals for single crystal X-ray analysis are available. This limits the structural characterization of several interesting compounds in the field of molecular magnetism, like *e.g.* many Co complexes. Due to their sensitivity to the vibrations of groups of atoms in one molecule, vibrational spectroscopies represent alternative methods in order to obtain structural information about new synthesized compounds by comparing similar complexes where *e.g.* only the metals differ from each other. Due to their high sensitivity to changes in the structural parameters, such as bond lengths, the temperature dependent studies using vibrational spectroscopies can be used to monitor the correlation between the molecular structure and magnetic properties. Moreover, due to the surface sensitivity of vibrational spectroscopy, this technique is suited for investigations on thin films of such complexes on *e.g.* Si substrates.

In this chapter the optical and vibrational properties of the complexes **1**, **2**, **21**, and **22** are characterized by means of UV/Vis, ellipsometry, infrared (IR) and Raman spectroscopic measurements of solution, powders, and thin films. The assignment of the vibrational modes and the absorption bands is supported by theoretical calculations with DFT, and TDDFT methods, respectively.

All the compounds under investigation in this chapter contain aromatic ring systems leading to intensive absorption features. Strong absorbing properties are important prerequisites, *e.g.*, for obtaining highly effective magneto-optically media which will be discussed in chapter 5. For this purpose thin films of such complexes deposited on Si(111) will be prepared by means of spin

coating with thickness ranging from 20 nm to several hundreds of nanometres thickness.

4.2 Theoretical background

4.2.1 Raman effect

In the classical description the Raman scattering is treated as a radiation of light by a time-dependent dipole $\mu(t)$ which is induced in a molecule by the incident electromagnetic light and is modulated by molecular vibrations. The incidental coherent light of frequency ν_L is generated by a laser. The induced dipole moment in a molecule can be expressed by

$$\mu = \alpha E + \frac{1}{2} \beta E^2 + \dots \quad (4.1)$$

Here $E = E_L \cos(2\pi \nu_L t)$ is the electric field component of the incident light with the amplitude E_L , α is the electronic polarizability of the molecule and β is the hyper-polarizability which is responsible for the hyper-Raman effect. The polarizability depends on the electronic charge distribution ρ . If the atomic configuration changes during a vibration ρ and hence α will change. For sufficiently small displacements of the nuclei from the equilibrium position, α will change linearly with the normal coordinates q and can be written as

$$\alpha = \alpha_0 + \left(\frac{\partial \alpha}{\partial q} \right)_0 q + \frac{1}{2} \left(\frac{\partial^2 \alpha}{\partial q^2} \right)_0 q^2 + \dots \quad (4.2)$$

Thus a vibrational mode is Raman active when

$$\left(\frac{\partial \alpha}{\partial q} \right) \neq 0 \quad (4.3)$$

is valid. Hereby $q = q_{0,j} \cos(2\pi \nu_j t)$ describes the nuclear displacement during the vibration with the amplitude $q_{0,j}$ and the frequency ν_j of the incident light. The constant α_0 represents the polarizability at the equilibrium position. The expression of the induced dipole moment is

$$\begin{aligned}
\mu(t) &= \alpha E_L \cos(2\pi\nu_L t) \\
&= \alpha_0 E_L \cos(2\pi\nu_L t) + \left(\frac{\partial\alpha}{\partial q}\right)_0 q_{0,j} E_L \cos(2\pi\nu_L t) \cos(2\pi\nu_j t) \\
&= \alpha_0 E_L \cos(2\pi\nu_L t) \\
&\quad + \frac{1}{2} \left(\frac{\partial\alpha}{\partial q}\right)_0 q_{0,j} E_L \{ \cos[2\pi(\nu_L + \nu_j)t] + \cos[2\pi(\nu_L - \nu_j)t] \}
\end{aligned} \tag{4.4}$$

The first term represents an oscillating dipole that radiates light with the same frequency ν_L as the incident light. The corresponding process is known as elastic scattering or Rayleigh scattering. The second and the third terms describe the inelastic scattering or Raman scattering at the Stokes frequency $\nu_L - \nu_j$ and Anti-Stokes frequency $\nu_L + \nu_j$, respectively.

4.2.2 Resonance Raman effect

According to Mingardi and Hamaguchi [Mingardi75, Hamaguchi77] the connection between the scattering tensor and the quantum interaction between the matter and radiation is given by

$$(\alpha_{\eta\sigma})_{fg} = \frac{1}{h} \sum_e \left[\frac{\langle f | R_\sigma | e \rangle \langle e | R_\eta | g \rangle}{\nu_e - \nu_g - \nu_L + i\Gamma_e} + \frac{\langle f | R_\eta | e \rangle \langle e | R_\sigma | g \rangle}{\nu_e - \nu_f + \nu_L + i\Gamma_e} \right]. \tag{4.5}$$

Here g, e, and f stand for the ground, excited, and final state of the molecule, respectively. R_σ and R_η are the vector components of the transition dipole moment operators with $\sigma, \eta = x, y, z$. The transition processes are illustrated in figure 4.1 in comparison to IR spectroscopy [Silaghi05, Salvan03].

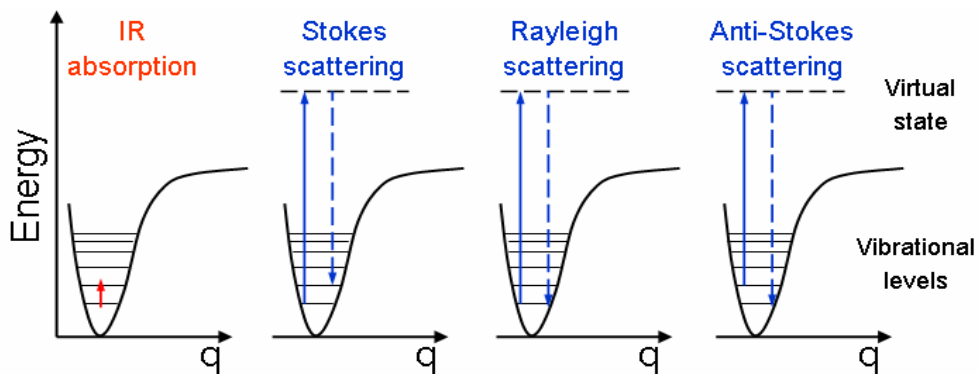


Figure 4.1. Comparison of the energy diagrams of IR absorption, and scattering processes plotted versus the normal coordinate q . The energy of the exciting and the emitting photon is indicated by a full and by a broken line, respectively.

If the incident photon energy $h\nu_L$ is in the range of $h\nu_e - h\nu_g$ the first term of the equation becomes large and the corresponding Raman band increases enormously. This phenomenon is called resonance Raman effect.

4.2.3 Infrared absorption

In contrast to Raman scattering the absorption of IR radiation occurs without participation of intermediate virtual electronic states. A dynamic dipole with

$$\left(\frac{\partial\mu}{\partial q}\right) \neq 0 \quad (4.6)$$

can absorb a photon when the frequencies of the light and of the oscillation are the same, *cf.* figure 4.2, and the electric field of the photon is parallel to the charge oscillation. The process can be quantified by measuring the ratio T between the intensity of the light transmitted through a sample and the intensity of the light incident on it. Absorbance is a dimensionless quantity related to the transmittance via $A = -\ln(T)$. If a molecule contains inversion symmetry the IR active modes are forbidden in Raman and vice versa.

4.2.4 The dielectric tensor

The dielectric tensor describes the connection between the electric displacement field (**D**) in a medium and the electric field strength (**E**). The polarization (**P**) of the medium is defined as

$$\mathbf{P} = \mathbf{D} - \varepsilon_0 \mathbf{E} = \varepsilon_0 (\boldsymbol{\varepsilon} - \mathbf{1}) \mathbf{E}. \quad (4.7)$$

P can be interpreted as a response function of the medium to the external electric field. In the general case the dielectric function ε is described by a tensor

$$\boldsymbol{\varepsilon}(\omega) = \begin{pmatrix} \varepsilon_{xx} & \varepsilon_{xy} & \varepsilon_{xz} \\ \varepsilon_{yx} & \varepsilon_{yy} & \varepsilon_{yz} \\ \varepsilon_{zx} & \varepsilon_{zy} & \varepsilon_{zz} \end{pmatrix}. \quad (4.8)$$

In the absence of a magnetic field and for a suitable choice of the coordinate system the tensor can be diagonalised:

$$\boldsymbol{\varepsilon}(\omega) = \begin{pmatrix} \varepsilon_{xx} & 0 & 0 \\ 0 & \varepsilon_{yy} & 0 \\ 0 & 0 & \varepsilon_{zz} \end{pmatrix}. \quad (4.9)$$

Depending on the symmetry of the material three cases can be distinguished:

- $\varepsilon_{xx} = \varepsilon_{yy} = \varepsilon_{zz}$ arises in the case of optically isotropic materials
- $\varepsilon_{xx} = \varepsilon_{yy} \neq \varepsilon_{zz}$ is characteristic for materials with uniaxial anisotropy,
- $\varepsilon_{xx} \neq \varepsilon_{yy} \neq \varepsilon_{zz} \neq \varepsilon_{xx}$ describes materials with biaxial anisotropy

If an external magnetic field is switched on, the change in the dielectric properties of the material can be described by the material parameter Q , the so-called Voigt constant. This is contained in the off-diagonal components of the macroscopic dielectric tensor written in the sample eigen coordinate system. When the magnetic field direction is parallel to the sample normal, defined as the z -axis, the dielectric tensor of a material with uniaxial symmetry has the following shape [91Zak], [Bauer00]:

$$\boldsymbol{\varepsilon} = \begin{pmatrix} \varepsilon_{xx} & iQ\varepsilon_{xx} & 0 \\ -iQ\varepsilon_{xx} & \varepsilon_{xx} & 0 \\ 0 & 0 & \varepsilon_{zz} \end{pmatrix}. \quad (4.10)$$

Q can be treated as linearly dependent on the magnetization in the present investigations that were performed in the range of low magnetic fields (0.35 T) provided that the materials have small Q values. This will be discussed in chapter 5. However, for metallic films deviations from this linear behaviour are reported [Oppeneer92].

4.2.5 Spectroscopic ellipsometry

Spectroscopic ellipsometry (SE) is a non-destructive optical method sensitive to both surface and bulk properties depending on the penetration depth of the light for the wavelength used. Currently, this method is used for the determination of the optical properties of materials *i. e.* refractive index, extinction coefficient and

dielectric function. In addition, information concerning the surface roughness, film thickness, anisotropy, crystallinity, composition, uniformity, *etc.* can be extracted [Azzam92, Azzam99].

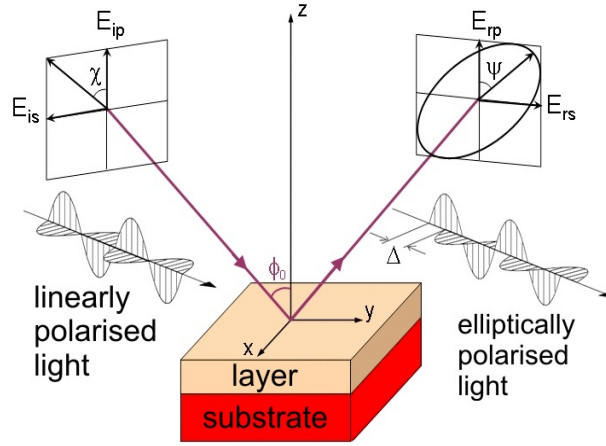


Figure 4.2. Principle of a spectroscopic ellipsometry (SE) measurement. After reflection under an angle ϕ_0 from the sample the change in polarisation is measured via the ellipsometric angles ψ and Δ .

The principle of a SE measurement is shown in figure 4.2. A linearly polarised light beam, described by the electrical field vectors E_{ip} and E_{is} for the field components parallel (index p) and perpendicular (index s) to the plane of incidence, respectively, is incident on the sample under an angle ϕ_0 . The beam is reflected (index r) from the sample as elliptically polarised light, described by the electrical field vectors E_{rp} and E_{rs} . The resulting change in the state of polarisation is quantified via the ellipsometric angles ψ and Δ representing the shape and orientation of the ellipse and the phase relation of the electromagnetic wave, respectively.

From the measured parameters using the ratio

$$\rho = \frac{r_p}{r_s} = \left| \frac{r_p}{r_s} \right| e^{i\Delta} = \tan \psi \cdot e^{i\Delta} \quad (4.11)$$

of the Fresnel reflection coefficients r_p and r_s defined as

$$r_p = \frac{E_{rp}}{E_{ip}} \quad \text{and} \quad r_s = \frac{E_{rs}}{E_{is}} \quad (4.12)$$

the effective dielectric function which contains information about the whole sample can be calculated by

$$\langle \tilde{\varepsilon} \rangle = \langle \varepsilon_1 \rangle + i \langle \varepsilon_2 \rangle = (\langle n \rangle + i \langle k \rangle)^2 = \sin^2 \phi \left[1 + \tan^2 \phi \left(\frac{1 - \rho}{1 + \rho} \right)^2 \right] \quad (4.13)$$

The unknown dielectric functions are described by Cauchy's equation in the transparent part of the spectrum in order to extract the layer thickness. This model is a dispersion function described by the refractive index

$$n(\lambda) = A + \frac{B}{\lambda^2} + \frac{C}{\lambda^4} + \dots \quad (4.14)$$

where A , B , and C are fit parameters. Commonly, it is enough to consider only A and B parameters. Their values are directly connected with the physical meaning of the refractive index. In general the refractive index should not exhibit strong dispersion and should decrease monotonically with increasing wavelength. In the absorbing part of the spectrum the Gauss-oscillator model can be used. This model describes the dielectric function of a film as a linear summation of real or complex terms, *i. e.* oscillators, as described by

$$\varepsilon = \varepsilon_1 + i\varepsilon_2 = \text{Offset} + \frac{A_1}{E_1^2 - E^2} + \frac{A_2}{E_1^2 - E^2 - iB_2E} + \text{Gaussian term} \quad (4.15)$$

where A_i , B_i , and E_i are the amplitude, broadening and energy position, respectively corresponding to the oscillator “*i*”, the “Offset” term is a real constant corresponding to $\varepsilon \rightarrow \infty$, the second term consists of Pole or Sellmeier oscillators with zero broadening, and the third term is based on Lorentz oscillators. The Gaussian term is a complex function in which the imaginary part models a Gaussian absorption and the real part is its Kramers-Kronig transform. The Kramers-Kronig relation

$$\begin{aligned} \text{Re } \varepsilon(\omega) - 1 &= \frac{2}{\pi} p.v. \int_0^\infty \frac{\omega' \text{Im } \varepsilon(\omega')}{\omega'^2 - \omega^2} d\omega' \\ \text{Im } \varepsilon(\omega) &= -\frac{2\omega}{\pi} p.v. \int_0^\infty \frac{\omega' \text{Re } \varepsilon(\omega')}{\omega'^2 - \omega^2} d\omega' \end{aligned} \quad (4.16)$$

links the real and imaginary part of the complex dielectric function if the dielectric function is analytical and $\varepsilon(\omega) \rightarrow 0$ for $|\omega| \rightarrow \infty$. The Kramers-Kronig relation allows the calculation of the real part of the dielectric function when the imaginary part is known in the whole definition range and vice versa.

In order to determine the sample thickness, surface roughness and the dielectric function from ellipsometric data, a model which describes the interaction of light with matter has to be employed. An iterative procedure is used to find the thicknesses and the dielectric functions. In this way the ellipsometric data are simulated and compared to the experimental data. The iterative cycle minimizes the differences between the simulated and experimental data. In the Woollam WVASE software the mean-square error (MSE) gives the differences between the model and the experimental points according to

$$MSE = \frac{1}{2N - M} \sum_{i=1}^N \left[\left(\frac{\psi_i^{\text{mod}} - \psi_i^{\text{exp}}}{\sigma_{\psi,i}^{\text{exp}}} \right)^2 - \left(\frac{\Delta_i^{\text{mod}} - \Delta_i^{\text{exp}}}{\sigma_{\Delta,i}^{\text{exp}}} \right)^2 \right] \quad (4.17)$$

where N is the number of the experimental points, M is the number of fit parameters and σ is the standard deviation for each point. The standard deviation is used to weigh the contributions of each data point to the mean-square error during the fitting process, such that very noisy data points are effectively excluded from the fit [Woollam99]. A MSE of 1 means that the simulated data pass through experimental data within the experimental error.

4.3 Experimental details

4.3.1 Measuring setup for Raman spectroscopy

A schematic of the experimental Raman setup is shown figure 4.3. A He cooled cryostat attached to a Raman spectrometer allows temperature dependent measurements in the range from 15 to 300 K to be performed. During the measurements the sample chamber is evacuated to achieve a pressure of ca. 10^{-5} mbar. The spectra presented in this work were recorded in a macro-configuration at 15 K unless otherwise specified.

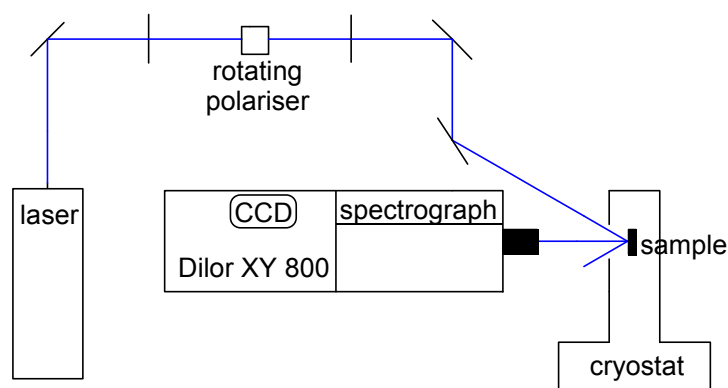


Figure 4.3. Schematic of the experimental setup for Raman spectroscopic investigations.

The Raman spectra were excited with the 21839 cm^{-1} (457.9 nm) line of an Ar^+ laser and with the 15454 cm^{-1} (647.1 nm) line of a Kr^+ laser. The 647.1 nm line lies in the lower energy tail of the HOMO-LUMO optical transition of all compounds, while the 457.9 nm line is located at the onset of the next higher energy optical transition. The scattered light is collected by a Dilor XY 800 triple monochromator with a multichannel charge coupled device detector. The spectral resolution was $\sim 4\text{ cm}^{-1}$ as determined from the full-width at half-maximum (FWHM) of the laser line. Typical values of the incident laser power were in the range from 5 to 10 mW and the size of the laser spot on the sample was about $300\text{ }\mu\text{m}$. The angle of incidence of the laser light was approximately 20° . The polarization of the scattered light was not analyzed in this work.

4.3.2 Measuring setup for infrared spectroscopy

The IR experiments were carried out using a Fourier transform infrared (FTIR) spectrometer Bruker IFS 66 (see figure 4.4).

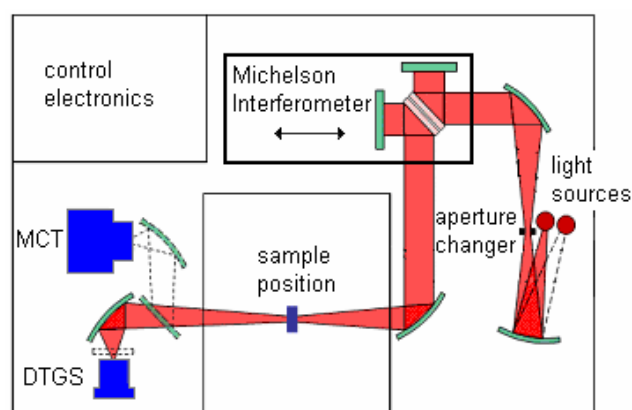


Figure 4.4. Schematic of the Fourier transform IR spectrometer Bruker IFS 66.

It is equipped with a Globar source, KBr beamsplitter and MCT (Mercury Cadmium Telluride) and DTGS (Deuterated Triglycine Sulphate) detectors. Transmission measurements were performed on the transition metal complexes in KBr pellets using a mass ratio of 1:100. The spectral resolution was about 2 cm^{-1} .

4.3.3 Spectroscopic ellipsometry and UV/VIS spectroscopy

The Woollam VASE ellipsometer is shown in figure 4.5. It consists of two goniometers for rotating the sample stage and the analyzer arm separately. The precision in measuring the incidence angle ϕ_0 is 0.01° which is useful in increasing the sensitivity of the ellipsometric measurements as it depends on the magnitude of changes in Ψ and Δ . The samples are measured near to the Brewster angle where the biggest changes in Ψ and Δ are expected. The VASE measurements were performed in the range of 0.8-5 eV under different angles of incidence, *i.e.* $60^\circ - 75^\circ$ using an energy step size of 0.02 eV.

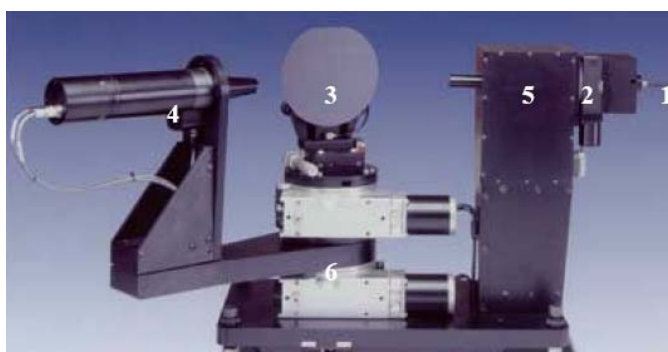


Figure. 4.5. Woollam VASE ellipsometer. (1) optical fiber, (2) polarizer, (3) compensator, (4) sample stage, (5) analyzer, (6) goniometers.

The ellipsometer consists of a Xe arc lamp as light source, a Czerny-Turner scanning monochromator, and calcite Glan-Taylor prisms as polariser and analyzer. The light is guided from the source to the monochromator using a standard optical fiber. The measurements presented in this work were performed with autoretarder. This generates a phase shift between the s and p components of the polarized light which allows to detect Δ in an interval from 0° to 360° .

Absorption measurements in solution were performed using 10^{-5} M and 10^{-3} M CH_3CN solutions. The spectra were measured in the range from 11000 to

42000 cm^{-1} at room temperature using a Thermo Spectronics UV/VIS spectrometer “Genesys 6”. Polarized optical microscopy investigations were performed with a Zeiss Axioscop 40 device.

4.3.4 Sample preparation

The films of **21** and **22** were deposited on Si wafers (8x8 mm) covered with 2 nm thick natural SiO_2 using spin coating. For this purpose **21** and **22** were dissolved in acetonitrile. The film thickness was controlled by the variation of two parameters: the concentration of the solution and the rotation speed, *cf.* table 4.1. The error bars in the third column were obtained from several experiments with the respective concentration and rotation speed. For comparison a film of approximately 100 nm was spin coated on a quartz substrate.

Table 4.1. Layer thicknesses of spin coated films determined using SE.

concentration	rotation speed	layer thickness
mg / ml	rpm	nm
3	1000	30 ± 10
5	600	100 ± 20

4.3.5 DFT calculations of vibrational frequencies

Calculation of vibrational spectra as well as previous optimization of structure parameters were carried out for **1**, **2**, and **21** at DFT level with the B3LYP hybrid functional [Lee88, Becke88]. The counter ions were neglected, leading to the dianionic species $[\text{M}(\text{opba})]^{2-}$ ($\text{M} = \text{Cu}(\text{II})$ (**1'**) and $\text{Ni}(\text{II})$ (**2'**)) and the dicationic species $[\text{Cu}_3(\text{opba})(\text{pmdta})_2]^{2+}$ (**21'**). **1'** and **2'** were treated with the program package Gaussian 03 [Frisch04] employing 6-311G basis sets, **21'** was calculated with TURBOMOLE [Turbomole05] taking advantage of the RI-J approximation [Eichkorn95] using def2-TZVP [Weigend05] basis sets and corresponding auxiliary basis sets [Weigend06].

For charged molecules it seems reasonable to compensate the excess charge, *e.g.*, with COSMO as outlined in chapter 3. However, this was not done for the calculation of vibrational frequencies, as calculation of these quantities within the COSMO model is not implemented in TURBOMOLE for conceptual reasons (a vibrational mode would change the shape of the cavity which is not accounted for, as frequencies are calculated from the second derivatives of the

energy for a fixed geometric structure). As effects of COSMO on vibrational frequencies are expected to be small, the calculation of frequencies without the COSMO model is sufficient to allow for an assignment of the modes. TDDFT calculations have been performed with the Orca program package [Neese01, Neese03] using the TZVP basis.

4.4 Results and discussion

4.4.1 Preparation of thin films

In order to optimize the homogeneity of spin coated films with respect to the uniformity in film thickness over the whole sample several solvents were employed. The most important criteria are good solubility and spreading of the solution on the sample surface. **21** exhibits high solubility in dimethylsulfoxide, *N,N*-dimethylformamide, and acetonitrile. The latter is the most suited solvent since it has the best spreading properties on the Si/SiO₂ substrate among the mentioned solvents and a comparatively low boiling point (82 °C).

Different rotation speeds were used for the preparation of the films on Si/SiO₂ ranging from 60 rotations per minute (rpm) up to 1000 rpm in order to vary their thickness. Polarisation microscopy images measured in reflection are displayed in figure 4.6 for the films produced by dipping the substrate into a solution and using spin coating with 1000 rpm rotation speed. Figures 4.6 (a) and (c) were taken in non-polarized, while (b) and (d) were obtained in polarized mode.

For the films produced by dipping into a solution, the formation of preferentially ordered needle shaped crystals with lengths of the order of 200 µm was observed (figure 4.6 (a)). The crystalline nature of these structures is confirmed by their appearance in the polarised microscopy mode (figure 4.6 (b)). The image recorded in non-polarised mode from the sample coated at high rotation speed (figure 4.6 (c)) clearly shows the alternation of bright and dark areas with size in the order of only a few microns. The absence of bright regions in figure 4.6 (d) recorded using polarized light reflects that only a few areas have a crystalline nature at the micrometer scale given by the resolution of the polarisation microscope. It must be noted, however, that on the nanometer scale small crystals without a preferential orientation were observed using scanning electron microscopy.

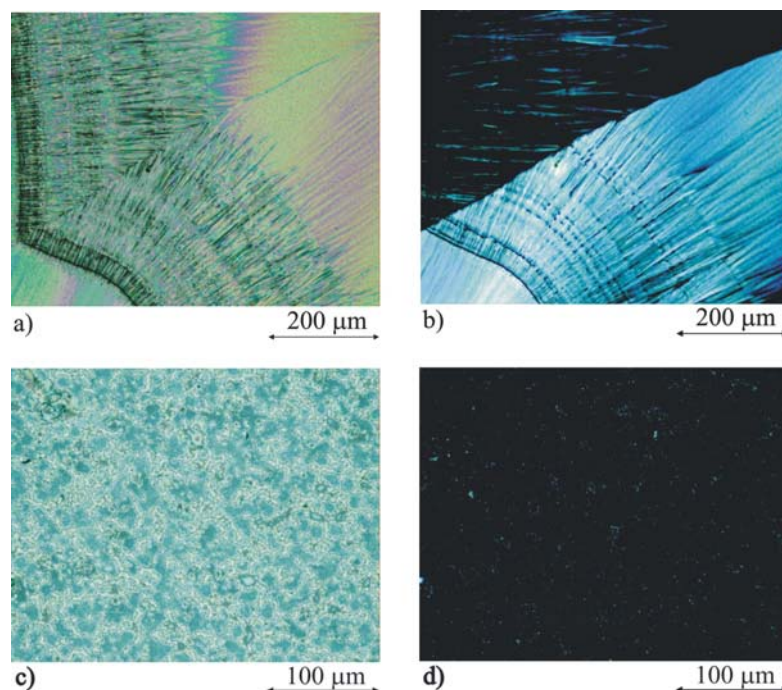


Figure 4.6. Polarization microscopy images of **21** on Si(111)/SiO₂ using unpolarized (a)/(c) and polarized light (b)/(d), respectively, for a film produced by dipping into a solution (a)/(b) and a sample spin coated with 1000 rpm (c)/(d).

The preservation of the molecular structure during the deposition process was proved by the results of Raman spectroscopy measurements on powders and thin films for all investigated complexes. An example is shown for complex **21** in figure 4.7. A close look at the two spectra shows that the band positions as well as their relative intensities are the same, a clear indication for the preservation of the molecular structure. A detailed assignment of the vibrational bands will be provided below.

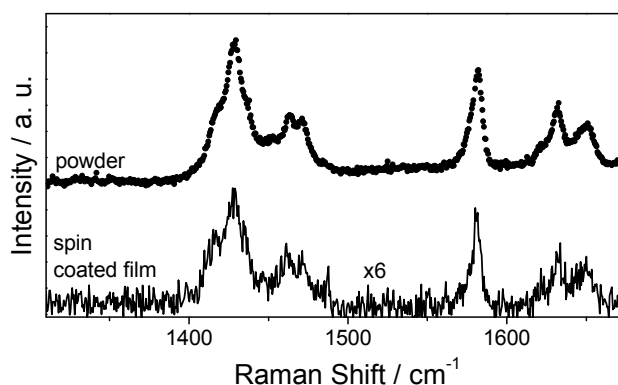


Figure 4.7. Comparison between the Raman spectra of **21** measured on powder (upper spectrum) and on a thin spin coated film on Si(111)/SiO₂ (lower spectrum). The spectra are normalised to the height of the mode at 1580 cm⁻¹.

4.4.2 UV/VIS and spectroscopic ellipsometry studies.

The absorption spectra of **2** and **9** from measurements in CH₃CN solution are shown in figure 4.8. The Laser lines for the Raman investigations are shown as vertical lines.

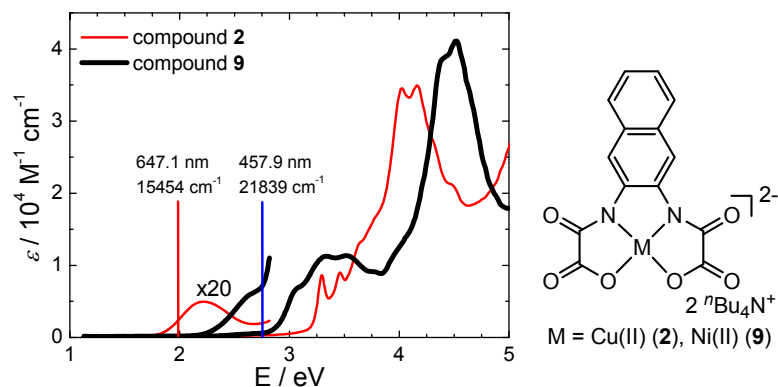


Figure 4.8. Absorption spectrum of **2** and **9**. The Laser lines for the Raman investigations are shown as vertical lines.

In the visible range weak d-d transitions appear at 17800 cm⁻¹ (2.21 eV, $\epsilon = 250 \text{ M}^{-1} \text{ cm}^{-1}$) for **2** and 21600 cm⁻¹ (2.68 eV, $\epsilon = 320 \text{ M}^{-1} \text{ cm}^{-1}$) for **9**. This difference in the energy position is due to the different electronic ground state configurations of Cu(II) with [Ar] 3d⁹ and Ni(II) with [Ar] 3d⁸ as already discussed in chapter 3.

The absorption spectra of **21** and **22** from measurements in solution are shown in figure 4.9 a) and are compared with the TDDFT calculations. The calculated oscillator strengths were broadened by a Gaussian line shape and multiplied by a factor which was the same for **21** and **22**. The calculated spectra were shifted by 0.7 eV to lower energies. The optical transitions were assigned as d-d transitions around 2 eV and π - π^* transitions at around 4 eV. Charge transfer transitions could also contribute to the optical spectra, however, they cannot be reliably predicted by means of TDDFT. The relative differences in total energy, *cf. e.g.* bands at 4 eV for **21** and **22**, are well predicted. On the band shape some deviations occur between the experimental and the theoretically predicted spectra. However, this is expected since the experimental spectra were measured in solution whereas the calculations were performed on a single molecule in the “gas phase” [Zimmer05].

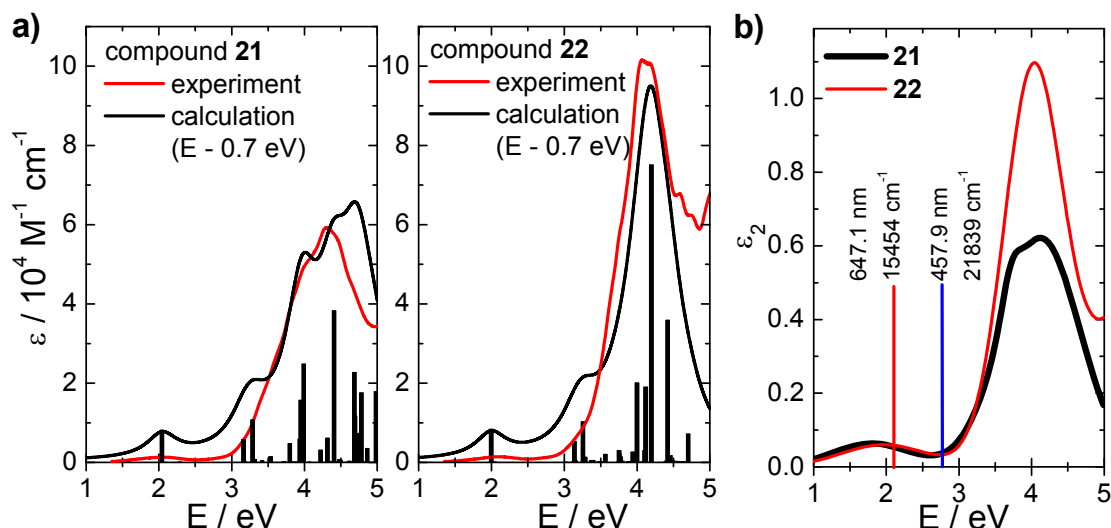


Figure 4.9. (a) Absorption spectra of **21** and **22** in comparison with the TDDFT calculations. The calculated spectra were shifted to lower energies by 0.7 eV. (b) The imaginary part of the dielectric function. The energy positions of the laser lines used for the Raman investigations are shown by vertical lines.

The imaginary part of the dielectric function, ε_2 , obtained from VASE measurements, which describes the absorption behaviour of the molecular thin films, are shown in figure 4.9 b). VASE delivers valuable information concerning the absorption behaviour of the molecules on the substrate. The dielectric function in the range from 0.8 to 5 eV was evaluated considering the layers as isotropic. In a first step a point-by-point fit of the measured ellipsometric angles Ψ and Δ was performed, *i.e.* fitting the calculated ellipsometric parameters to the experimental data at each wavelength separately, *cf.* figure 4.a1 of the appendix, for **21** and **22**. In the next step a sum of Gaussian oscillators was used to simulate the line shape of the imaginary part of the dielectric function ε_2 , while the real part of the dielectric function ε_1 is generated according to the Kramers-Kronig relation. The spectral behaviour of ε_1 , Ψ , and Δ is given in figure 4.a1 and 4.a2 in the appendix.

At energies of 16800 cm⁻¹ (2.08 eV, $\varepsilon = 1300 \text{ M}^{-1} \text{ cm}^{-1}$) for **21** and 17000 cm⁻¹ (2.11 eV, $\varepsilon = 1400 \text{ M}^{-1} \text{ cm}^{-1}$) for **22** charge transfer and d-d transitions of the Cu(II) ions appear and above 20000 cm⁻¹ (2.5 eV) charge transfer and π - π^* transitions dominate the spectrum. The latter are more intensive for **22** due to the larger aromatic system in comparison to **21**. This trend is clearly observable also in the line-shape of ε_2 of films determined from VASE investigations. In contrast, the d-d transitions show almost the same intensity and are only slightly shifted to higher wavenumbers for **22**.

4.4.3 IR and Raman studies for **2** and **9**.

The experimental and calculated IR and Raman spectra of **2** and **9** are shown in figures 4.10 and 4.11 and the proposed mode assignment is presented in table 4.2. The calculated spectra were obtained by broadening the calculated vibrational lines with Lorentz functions having a FWHM of 5 cm^{-1} , a value that corresponds to the typical FWHM of the bands in the experimental spectra. Due to the low symmetry of the molecule, the same modes are both Raman and IR active.

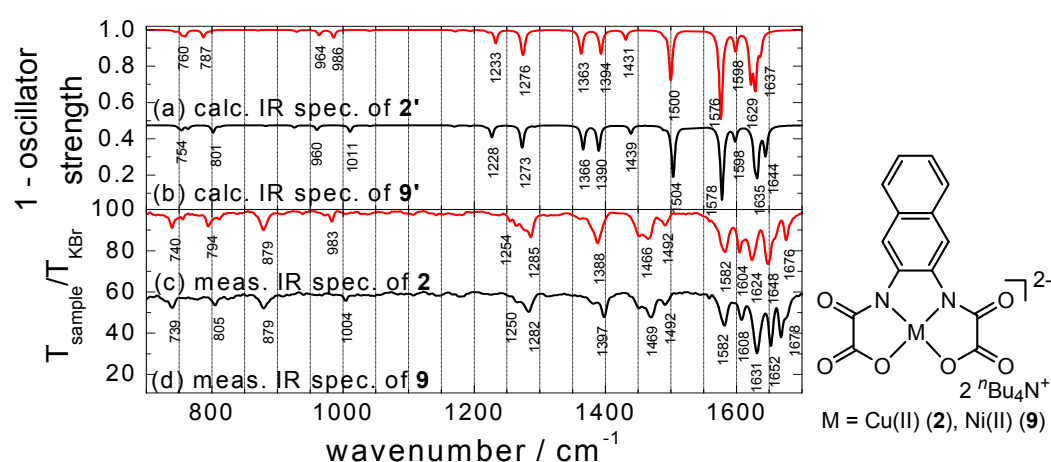


Figure 4.10. Comparison of the calculated IR spectra of **2'** (a) and **9'** (b), which correspond to **2** and **9** when neglecting the counter ions, and the measured IR spectra of **2** (c) and **9** (d). The calculated oscillator strengths were divided by 2000. For clarity the spectra (c) and (d) were vertically shifted.

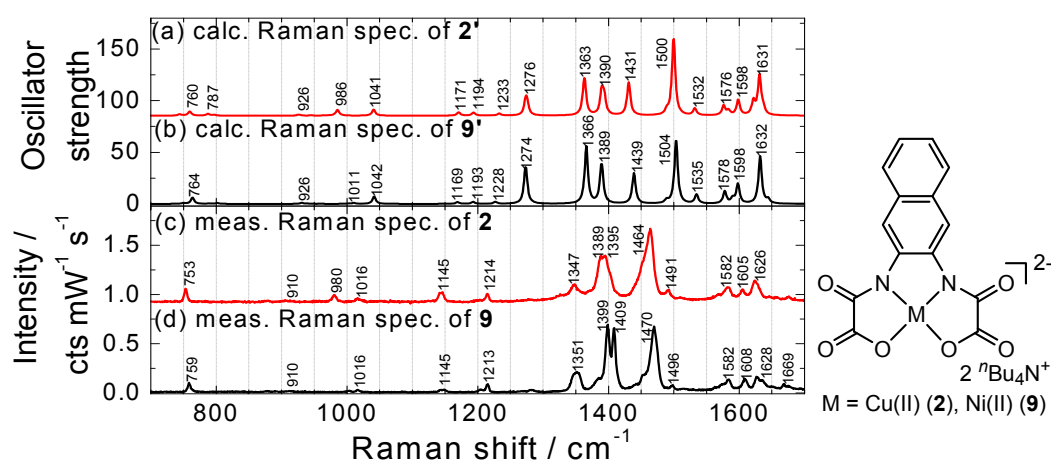


Figure 4.11. Comparison of the calculated Raman spectra of **2'** (a) and **9'** (b), which correspond to **2** and **9** when neglecting the counter ions, and the measured Raman spectra of **2** (c) and **9** (d). For clarity the spectra (c) and (d) were vertically shifted.

Table 4.2. Assignment¹⁾ of Infrared (IR) and Resonance Raman (RR) ($\lambda = 457$ nm, T = 15 K) spectra of **2** and **9**. Frequencies²⁾ are given in cm⁻¹.

Mode	symmetry	Spectroscopic data of 2			Spectroscopic data of 9		
		IR investigations	RR investigations	IR investigations	RR investigations	calc.	meas.
$\delta(\text{CO})$, $\delta(\text{MO})$, $\delta(\text{MN})$	B ₂	calc. 360 w	meas. 360 vw	calc.	meas.	360 vw	
$\delta(\text{CC oop})$	B ₁	364 w				370 vw	
$\delta(\text{OMN})$, $\delta(\text{ring}^1 \text{ rotation})$	B ₂	374 w					
$\delta(\text{OMN})$, $\delta(\text{CC})$ of ring ^{1,2}	B ₁			441 w			
$\delta_{\text{sym}}(\text{CC oop})$	B ₁	461 w		453 w			
$\delta_{\text{sym}}(\text{CC, CH oop})$	B ₁	498 m		496 m			
$\delta_{\text{asym}}(\text{CC})$ of ring ^{1,2} , $\nu_{\text{asym}}(\text{MN})$	B ₂	554 w		564 w			
$\delta_{\text{sym}}(\text{ring}^{1,2} \text{ breathing})$	A ₁	555 w	545 w	568 w	549 w		
$\delta_{\text{sym}}(\text{CC, CH, CN oop})$	B ₁	576 w	558 w	568 w			
$\delta_{\text{sym}}(\text{ring}^{1,2} \text{ breathing})$	A ₁		581 vw				
$\delta_{\text{asym}}(\text{CC})$ of ring ^{1,2} , $\delta(\text{OCuC})$, $\delta(\text{NCC})$	B ₂	587 vw		593 vw	563 vw		
$\delta(\text{ring}^{1,2})$, $\delta(\text{OCO})$	B ₂	744 vw		750 vw			
$\delta_{\text{sym}}(\text{CH oop})$	B ₁	754 w		754 w			
$\delta_{\text{asym}}(\text{CC, CH})$	A ₁	760 w	740 w	764 w	739 w	764 w	759 m
$\delta_{\text{sym}}(\text{OCO, NCO oop})$	B ₁					790 vw	
$\delta_{\text{sym}}(\text{OCO})$, $\delta_{\text{sym}}(\text{ring}^{1,2} \text{ breathing})$	A ₁	787 w	794 w	801 w	805 w		
$\nu_{\text{sym}}(\text{CC})$	A ₁	870 vw	879 m	883 vw	879 m		
$\delta_{\text{asym}}(\text{ring}^{1,2})$	B ₂		926 vw	926 w		926 vw	910 w
$\delta_{\text{sym}}(\text{CH oop})$	B ₁	929 vw		960 w			
$\delta_{\text{sym}}(\text{CH oop})$	B ₁	964 w					
$\delta_{\text{asym}}(\text{CNC})$, $\delta_{\text{asym}}(\text{CH})$	B ₂					1003 vw	
$\nu_{\text{sym}}(\text{MN})$, $\delta_{\text{sym}}(\text{CH})$	A ₁	986 w	983 w	1011 w	1004 w	1011 w	
$\delta_{\text{sym}}(\text{CH})$, $\delta_{\text{sym}}(\text{ring}^2 \text{ breathing})$	A ₁	1041 vw	1041w	1042 vw		1042 w	1016 w
$\delta_{\text{sym}}(\text{CH})$, $\delta_{\text{sym}}(\text{ring}^1 \text{ breathing})$, $\nu_{\text{sym}}(\text{CNC})$	A ₁	1171 vw	1171 vw	1169 vw		1169 vw	1145 w
$\delta_{\text{sym}}(\text{CH})$	A ₁	1194 vw		1193 vw		1193 vw	
$\delta_{\text{asym}}(\text{CH})$, $\nu_{\text{asym}}(\text{CO})$	B ₂	1221 vw		1218 vw			
$\delta_{\text{sym}}(\text{CH})$, $\nu_{\text{sym}}(\text{CO})$	A ₁	1233 w	1254 w	1228 m	1250 w	1228 vw	1213 w

¹⁾oop: out of plane vibration, v: stretching vibration, δ : deformation vibration, ring¹: nitrogen substituted aromatic naphthyl ring, ring²: remaining aromatic naphthyl ring; ²⁾v: very, w: weak, m: medium, s: strong

Continuation of table 4.2.

Mode	symmetry	spectroscopic data of 2			spectroscopic data of 9		
		IR investigations	RR	meas.	IR investigations	RR	meas.
		calc.	calc.		calc.	calc.	
$\nu_{\text{asym}}(\text{CC})$, $\delta_{\text{asym}}(\text{CH})$, $\delta_{\text{asym}}(\text{CC})$ of ring	B ₂	1276 m	1285 m	1276 m	1273 m	1282 m	1273 m
$\delta_{\text{sym}}(\text{CH})$, $\delta_{\text{sym}}(\text{ring}^1 \text{ breathing})$, $\nu_{\text{sym}}(\text{CC})$	B ₂	1274 m		1274 w	1274 m		1274 s
$\delta_{\text{asym}}(\text{CH})$, $\delta_{\text{asym}}(\text{ring}^{1,2})$	B ₂	1360 w	1366 w		1366 w	1382 w	1366 w
$\nu_{\text{sym}}(\text{CC}, \text{CC})$ of ring ^{1,2} , $\delta_{\text{sym}}(\text{CH})$, $\nu_{\text{sym}}(\text{CN})$	A ₁	1363 m		1363 m	1366 s		1366 s
$\nu_{\text{sym}}(\text{CC}, \text{CC})$ of ring ^{1,2} , $\nu_{\text{sym}}(\text{CN})$, $\delta(\text{NCuN scissoring})$	A ₁	1390 vw		1390 m	1389 vw		1389 s
$\delta(\text{NCuN rocking})$, $\delta_{\text{asym}}(\text{CH})$ of ring ²	B ₂	1394 m	1388 m	1394 m	1390 m	1397 m	1390 m
$\delta_{\text{sym}}(\text{CH})$, $\nu_{\text{sym}}(\text{CC})$ of ring ^{1,2}	A ₁	1431 w	1466 m	1431 m	1439 w	1469 m	1439 m
$\delta_{\text{asym}}(\text{CH})$, $\delta_{\text{asym}}(\text{ring}^{1,2})$, $\nu_{\text{sym}}(\text{CN})$	B ₂	1489 w		1489 w	1489 w		1489 w
$\delta_{\text{sym}}(\text{CH})$, $\nu_{\text{sym}}(\text{CC})$ of ring ²	A ₁	1500 s	1492 w	1500 s	1504 s	1492 w	1504 s
$\delta_{\text{sym}}(\text{CH})$, $\nu_{\text{sym}}(\text{CC})$ of ring ²	A ₁	1532 vw		1532 w	1535 w		1535 w
$\delta_{\text{asym}}(\text{CH})$, $\nu_{\text{sym}}(\text{CO})$, $\nu_{\text{asym}}(\text{ring}^1)$	B ₂	1576 vs	1582 s	1576 w	1578 vs	1582 m	1578 w
$\nu_{\text{sym}}(\text{CO})$, $\nu_{\text{sym}}(\text{CC})$ of ring ^{1,2}	A ₁	1584 w		1584 w		1590 w	1590 w
$\nu_{\text{sym}}(\text{CO})$, $\nu_{\text{sym}}(\text{CC})$ of ring ^{1,2}	A ₁	1598 w	1604 m	1598 m	1598 w	1608 m	1598 m
$\nu_{\text{asym}}(\text{CO}, \text{CC})$ of ring ^{1,2}	B ₂	1622 s	1624 s	1622 m	1628 s	1631 s	
$\nu_{\text{asym}}(\text{CO}, \text{CC})$ of ring ^{1,2}	B ₂	1629 s			1632 s		1632 s
$\nu_{\text{asym}}(\text{CO}, \text{CC})$ of ring ^{1,2}	B ₂	1631 vw	1648 s	1631 m	1635 s	1652 s	1635 m
$\nu_{\text{asym}}(\text{CO}, \text{CC})$ of ring ^{1,2}	A ₁	1637 m	1676 m	1637 w	1644 m	1678 s	1644 w
$\nu_{\text{sym}}(\text{OCO})$	B ₂			3114 w			3115 w
$\nu_{\text{asym}}(\text{CH})$ of ring ²	A ₁	3129 w	2873 m	3129 m	3130 w	2874 m	3130 m
$\nu_{\text{asym}}(\text{CH})$ of ring ²	B ₂	3145 m	2930 m	3145 m	3145 m	2932 m	3145 m
$\nu_{\text{sym}}(\text{CH})$ of ring ²	A ₁	3158 m	2961 m	3158 s	3159 m	2962 m	3159 s
$\nu_{\text{sym}}(\text{CH})$ of ring ¹	A ₁			3204 m			3208 m

¹loop: out of plane vibration, ν : stretching vibration, δ : deformation vibration, ring¹: nitrogen substituted aromatic naphthyl ring, ring²: remaining aromatic naphthyl ring, ²v: very, w: weak, m: medium, s: strong

At a first glance the comparison between the experimental and the calculated IR spectra shows some differences concerning the number of modes exhibiting significant intensity. The additional modes observed in the experimental spectra can be attributed to the ${}^n\text{Bu}_4\text{N}^+$ counter ion which was neglected in the calculations. In contrast, the calculated Raman spectra fit much better to the experimental data. ${}^n\text{Bu}_4\text{N}^+$ is a non-coordinating counter ion due to steric reasons. Thus a charge transfer from the $[\text{Cu}(\text{nabo})]^{2-}$ (**2'**) entity to ${}^n\text{Bu}_4\text{N}^+$ is not possible and the energy of its first optical transition lies well above the excitation energy used in this work. Therefore its Raman-active bands cannot be resonantly enhanced by the excitation energy used and should have a Raman cross-section much smaller compared to that of **2**.

For the assignment of the experimental modes to elongations of atom groups within the molecules, the comparison between the experimental vibrational spectra of the Cu (**2**) and the corresponding Ni (**9**) complex with the theoretically predicted spectra was considered. The root mean square (rms) deviation of the calculated from the measured IR frequencies is 20 cm^{-1} for **2** and 23 cm^{-1} for **9**. This rather large rms value could be mainly due to the fact that the IR active counter ion ${}^n\text{Bu}_4\text{N}^+$ was neglected in the theoretical calculations.

In the case of the Raman investigations the rms deviation is only 6 cm^{-1} for **2** and 10 cm^{-1} for **9**. The low rms deviations indicate a very good agreement between the calculations and the experimental spectra which is also due to the lack of Raman activity of the counter ions. The correlation between the calculated and the measured wavenumbers is shown in figure 4.12 a) and b). The red line represents the best fit in the range $500 - 3300\text{ cm}^{-1}$ with a slope of 1.06 and 1.09 for **2** and **9**, respectively. As expected [Ong99], the hybrid-DFT methods slightly overestimate vibrational frequencies.

The blue line represents the best fit in the range $500 - 1700\text{ cm}^{-1}$. The slope of the blue line is 1.00 for **2** and **9** which clearly indicates that the mismatch between the experimental and calculated frequencies strongly depends on which vibrational modes were excited. It should be noted that no clear trend for the mismatch value and size with increasing frequency was observed. That is why the calculated spectra were not shifted here in contrast to the investigations on complex **21**, see below.

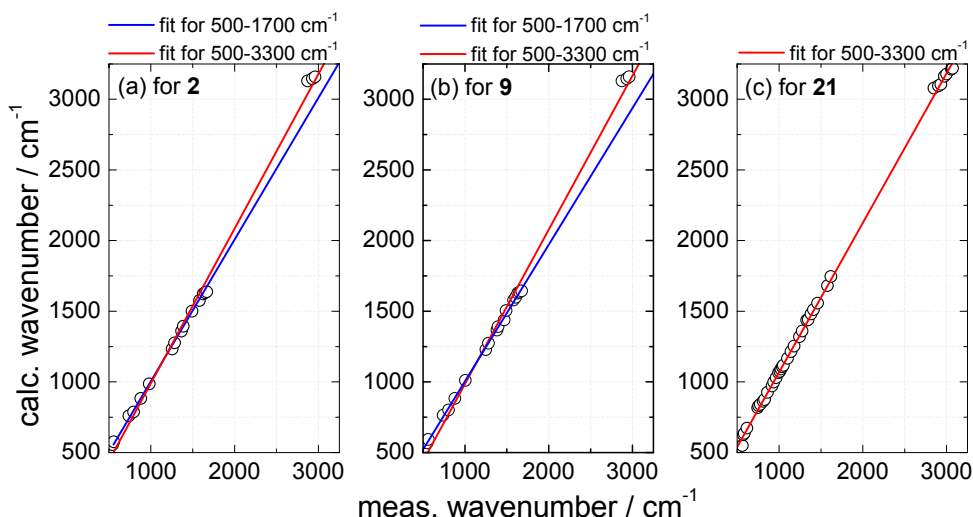


Figure 4.12. Correlation of calculated and measured IR wavenumbers for **2**, **9**, and **21**.

Both IR and Raman spectroscopies are very sensitive to the coordination of the transition metal ion. The Cu(II) ion is stronger coordinated to Nitrogen than the Ni(II) ion leading to a lower electron density in the ligand system of **2**, *cf.* chapter 2 and 3. Thus most of the vibrational modes of the ligand should appear at lower frequencies in the case of **2** compared to **9**. This fact provides an experimental criterion that can be used to support the assignment of the mode characters. Indeed, the breathing modes of the aromatic system appear in the IR spectrum at 545 cm^{-1} (calc. 555 cm^{-1}) and 549 cm^{-1} (calc. 568 cm^{-1}) for **2** and **9**, respectively. Even though localized on the O-M-N skeleton, the change in the electron density when replacing the metal atom (M) also extends over the central bridge, in this case the naphthyl group. Therefore also the ring vibrations $\nu(\text{CC})$ are influenced by the difference in the electron density, but to a lesser extent, *cf.* 1464 cm^{-1} (calc. 1500 cm^{-1}) and 1470 cm^{-1} (calc. 1504 cm^{-1}) for **2** and **9**, respectively. For the CO stretching vibrations the same systematic tendency was observed, *cf.* e.g. 1648 cm^{-1} (calc. 1631 cm^{-1}) and 1652 cm^{-1} (calc. 1635 cm^{-1}) for **2** and **9**, respectively. For a schematic visualization of the elongation patterns of some selected modes see figure 4.13.

Further support for the mode assignment was gained by an inspection of the relative intensities in the IR and Raman spectrum. The most intensive bands in the Raman spectrum are expected to be the CH deformation vibrations while in the IR spectrum the stretching vibrations of CO should dominate. Representative for the former are the modes at 1389 cm^{-1} (calc. 1363 cm^{-1}) and 1464 cm^{-1} (calc. 1500 cm^{-1}) for **2** and those at 1399 cm^{-1} (calc. 1366 cm^{-1}) and

1470 cm^{-1} (calc. 1504 cm^{-1}) for **9**. Exemplary CO modes are located at 1582 cm^{-1} (calc. 1576 cm^{-1}) for **2**, 1582 cm^{-1} (calc. 1578 cm^{-1}) for **9**.

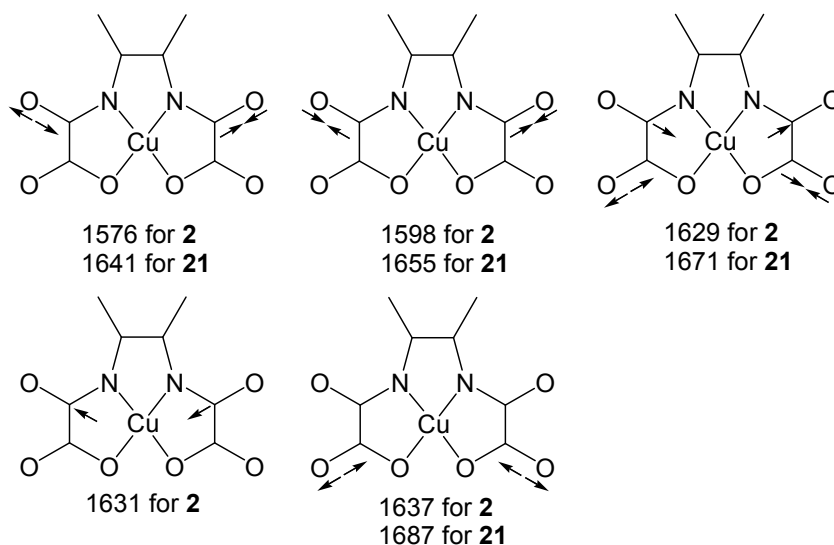


Figure 4.13. Elongation patterns of the CO stretching vibrations of compound **2** and **21** with their calculated frequencies.

4.4.4 IR and Raman studies for **21**

The measured IR and Raman spectra of **21** are shown in figure 4.14 along with the calculated IR spectrum. The mode assignment based on the comparison between the experimental and calculated spectra is provided in table 4.3.

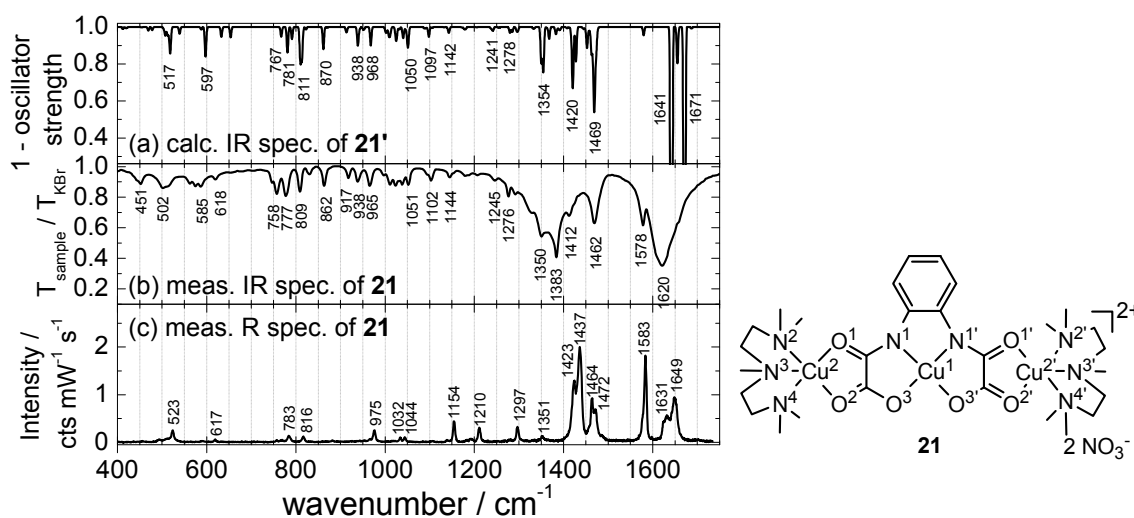


Figure 4.14. Comparison of the calculated IR spectrum of **21'** (a) which corresponds to **21** neglecting the counter ions, the measured IR spectrum of **21** (b) on a KBr pellet, and the measured Raman spectrum of **21** (c) on a 300 nm thick film on Si/SiO₂.

Due to the low symmetry of the molecule, the same modes are both Raman and IR active. The frequencies of the calculated spectrum were divided by 1.06 to get a better match to the experimental frequencies (*cf.* figure 4.12). To recall, in

general DFT methods slightly overestimate vibrational frequencies [Ong99]. After this procedure the calculated and measured IR spectra show very good agreement which is underlined by the small root mean square deviation of only 5 cm^{-1} . The fact that a multiplication by a factor improves the correspondence between the calculated and experimental spectra for **21**, but it would less improve it for the complexes **2** and **9**, is due to the larger root mean square deviation for **2** and **9** in comparison to **21**. The reasons for such differences are not clear at this point, they could for instance arise from slight structural differences of the complex in the solid state and after the geometry optimization or because of neglecting the counter ions resulting in the dianionic species $[\text{M}(\text{opba})]^{2-}$ ($\text{M} = \text{Cu}(\text{II})$ (**2'**) and $\text{Ni}(\text{II})$ (**9'**)) and the dicationic species $[\text{Cu}_3(\text{opba})(\text{pmdta})_2]^{2+}$ (**21'**), respectively.

Table 4.3. Assignment^(a) of IR and Raman (R) ($\lambda = 457.9 \text{ nm}$, $T = 15 \text{ K}$) spectra of **21**. Frequencies are given in cm^{-1} .

mode	calc. IR	meas. IR	meas. R
$\nu(\text{CuN3}), \delta(\text{CH}_3)$	411 vw		
$\nu(\text{CuN2}, \text{CuN4})$	418 vw		
$\delta(\text{CH}_3), \delta(\text{COCu}), \delta(\text{CH ring})$	468 vw	451 w	
$\nu(\text{CuN2}, \text{CuN3}, \text{CuN4})$	477 w		
$\nu(\text{CuN2}, \text{CuN4})$	506 w	502 w	
$\nu(\text{CuN3}), \nu(\text{CuO1})$	517 m	562 w	
$\delta(\text{CC ring oop})$	538 w		523 w
$\delta(\text{CNC})$ of pmdta	587 vw	562, 574 w	
$\delta(\text{Cu1O}, \text{Cu1N})$	597 m	585 w	
$\delta(\text{CC ring})$	632 w	618 vw	617 vw
$\delta(\text{CC oop}), \delta(\text{CH ring oop})$	653 w		
$\nu(\text{CuN2}, \text{CuN3}, \text{CuN4})$	767 w	744 w	
$\nu(\text{CuN2}, \text{CuN4})$	781 m	758 m	
$\delta(\text{CC ring}), \nu(\text{OCu1O}),$ $\delta(\text{NCu1N}), \nu(\text{Cu2O}, \text{Cu2'O})$	791 w	777 m	783 w
$\nu(\text{CuN})$ of pmdta	811 m	809 m	816 w
$\nu(\text{O2CO2}), \nu(\text{O1CN1}), \delta(\text{CC ring})$	822 vw	829 w	
$\delta(\text{CC oop})$	870 m	862 m	
$\nu(\text{CC})$ of pmdta	913 vw	917 w	
$\delta(\text{CH}_2)$ rocking of pmdta, $\nu(\text{NCH}_3)$ of pmdta	938 w	938 w	
$\delta(\text{CH}_2)$ rocking of pmdta, $\nu(\text{NCH}_3)$ of pmdta	968 w	965 m	975 w
$\nu(\text{NCH}_3)$ of pmdta	1001 w	996 w	
$\delta(\text{CH}), \delta(\text{NCu2N}, \text{NCu2'N}),$ $\nu(\text{NCH}_3)$ of pmdta	1009 w	1011 w	
$\delta(\text{CH}_2)$ rocking of pmdta	1025 w	1023 w	1032 vw
$\delta(\text{CH}_2)$ rocking of pmdta	1040 w	1038 w	1044 vw
$\delta(\text{CH}_2)$ twisting of pmdta	1050 m	1051 w	
$\delta(\text{CH}_2)$ twisting of pmdta	1097 w	1102 w	
$\delta(\text{CH}_2)$ twisting of pmdta	1142 vw	1144 w	1154 m

Continuation of table 4.3.

mode	calc. IR	meas. IR	meas. R
δ (CC ring)	1178 vw	1179 vw	
δ (CH ₂) twisting of pmdta	1241 vw	1245 vw	1210 w
δ (CH ring)	1278 w	1276 w	1297 w
δ (CH ₂) twisting of pmdta	1285 w		
δ (CH ₂) twisting of pmdta	1295 w		
δ (CH ₂) wagging of pmdta	1332 vw		
δ (CH ₂) wagging of pmdta	1350 m	1330 s	
ν (CC)	1354 s	1350 s	1351 vw
ν (CC)	1368 w		
δ (CH ₃) scissoring	1383 w		
δ (CH ₃) scissoring	1391 w	1383 s	
δ (CH ₃) scissoring	1420 s	1412 m	1418 s
δ (NCuN, OCuO), ν (CC) of ring and oxamato group	1428 m		1423 s
δ (aliph. CH)	1452 w		1437 vs
δ (aliph. CH)	1463 m	1462 s	1464 s
δ (aliph. CH)	1469 s		1472 m
δ (arom. CH)	1579 w	1578 m	1583 vs
ν (CO), ν (CN) asym.	1641 vs	1620 vs	1631 m
ν (CO), ν (CN) sym	1655 m		1649 s
ν (CO), ν (CN) asym	1671 vs		
ν (CO), ν (CN) sym	1687 w		
ν (aliph. CH)	2894 m	2807, 2849 w	
ν (aliph. CH)	2909 w	2883, 2903 m	
ν (aliph. CH)	2919 m	2931 m	
ν (aliph. CH)	2973 vw	2975 m	
ν (aliph. CH)	2987 m	3000 m	
ν (aliph. CH)	3019 w	3058 w	
ν (aliph. CH)	3026 w	3073 w	
ν (arom. CH)	3055 vw		
ν (arom. CH)	3065 vw		
ν (arom. CH)	3090 vw		

^{a)}oop: out of plane vibration, ν : stretching vibration, δ : deformation vibration, atom labels refer to atom numbering scheme in Figure 4.14; v: very, w: weak, m: medium, s: strong

The spectra of **21** are dominated by the vibrational modes of the aromatic and the terminal pmdta ligand system, *cf.* deformation vibrations in the range of 1000 – 1600 cm⁻¹ and stretching vibrations at 2894 – 3090 cm⁻¹. In the range of 1600 – 1700 cm⁻¹ the stretching vibrations of CO and CN bonds appear. The full width at half maximum of the IR bands around 1400 and 1600 cm⁻¹ is larger compared to the bands in the same region of the mono-nuclear complexes. This broadening effect was also observed for other trinuclear Cu(II)-bis(oxamato) complexes, not shown here, and is most probably due to the asymmetry of the complexes in the solid state where the terminal pmdta ligand systems induce slightly different bond angles with Cu(II) and thus differences in the charge density distribution in the right and the left oxamato groups.

Furthermore, the broadening of the IR bands is higher in comparison with the Raman bands. This observation can be explained by taking into account the presence of the solvent molecules that are embedded between the transition metal complexes during the crystallization procedure from solution. The solvent molecules show almost no absorption in the visible spectral range and thus no high Raman intensities are expected whereas in IR their vibrations can be excited, leading to the observed broadening effects. The smaller number of bands in the DFT calculation is a consequence of the higher symmetry achieved during structure optimization, as symmetry-breaking counter ions are neglected.

As for the mono-nuclear complexes, the relative intensities can be again used to cross-check the band assignment. The largest intensities are observed for the $\delta(\text{CH})$ modes at 1437 cm^{-1} and 1583 cm^{-1} in the Raman spectrum whereas in IR the $\nu(\text{CO})$ are the most intensive bands, *cf.* 1620 cm^{-1} (calc. 1641 cm^{-1} , 1671 cm^{-1}).

Raman spectroscopic measurements were also performed using the red light of a Krypton laser (1.92 eV, 647 nm) as excitation light. Even though its energy is located in the lower energy tail of the HOMO-LUMO absorption band, *cf.* figure 4.9, the intensity of the Raman bands excited using the 647 nm line is two orders of magnitude lower in comparison to the excitation using the 457.9 nm line. Recalling that the 647.1 nm line is located at the onset of the charge transfer and d-d transitions while the 457.9 nm at the onset of the next higher energy transition, the low Raman cross-section for the 647.1 compared to 457.9 nm excitation line is an additional indication that the lowest energy optical excitation is strongly localized on the metal centre whereas the next optical transition involves the ligand skeleton.

4.4.5 Comparison of the Raman spectra of **2**, **21**, and **22**

The measured Raman spectra of **2**, **21**, and **22** are shown in figure 4.15. The spatial extension of the aromatic ring system seems to influence the vibrational properties as reflected by the spectra of **22** (b) and **21** (d) in figure 4.15.

A direct comparison of the spectra of **2** (a) and **22** (b) reveals that the coordination of two $[\text{Cu}(\text{pmdta})]^{2+}$ on **2** influences mainly the Raman shifts and less the relative intensities, an indication that this structural modification keeps

roughly the symmetry of the central skeleton. The main differences between the Raman spectra of **2** and **22** arise primarily from the terminal ligands of the coordinated $[\text{Cu}(\text{pmdta})]^{2+}$ fragments.

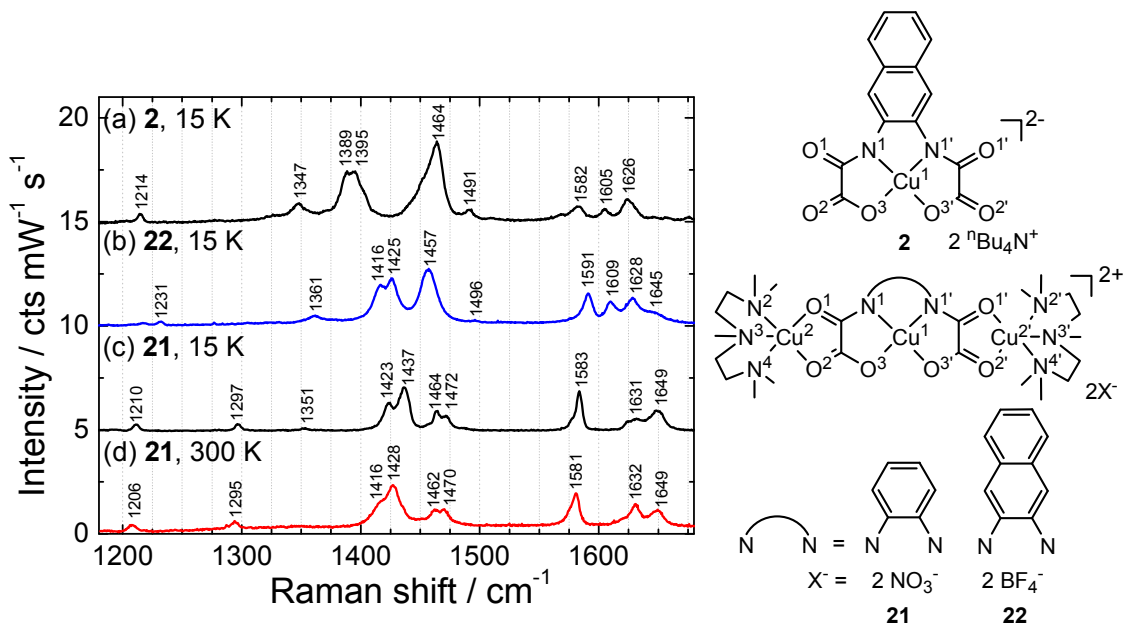


Figure 4.15. Comparison of the measured Raman spectra of **2** (a), **22** (b), and **21** (c) at 15 K, and **21** (d) at 300 K. The spectra were normalized to the intensity of the band at 1395 cm^{-1} (a), 1425 cm^{-1} (b), 1437 cm^{-1} (c), and 1428 cm^{-1} (d).

The bands originating from a stretching vibration of CO are shifted to higher frequencies for **22** compared to **2**. Even though the coordination of $[\text{Cu}(\text{pmdta})]^{2+}$ changes, the electron density distribution in the central $[\text{Cu}(\text{nabo})]^{2-}$ fragment is only marginally affected and thus the bands of $\nu(\text{CO})$ undergo only slight shifts, compare e.g. 1605 cm^{-1} with 1609 cm^{-1} and 1626 cm^{-1} with 1628 cm^{-1} for **2** and **22**, respectively. The same is applicable for $\delta(\text{CH})$ at 1582 cm^{-1} for **2** and 1591 cm^{-1} for **22**. Much stronger shifts towards higher frequencies appear in the region of CN modes, cf. e.g. 1389 and 1395 cm^{-1} for **2** and 1416 and 1425 cm^{-1} for **22**, respectively.

Even though the Raman active entity of **2** is two times negatively charged and that of **22** two times positively charged no general tendency of shifting to higher frequencies in the case of **2** compared to **22** was observed, as one might have expected at a first glance. Moreover, a shift in the opposite direction was observed when comparing the band at 1464 for **2** and 1457 cm^{-1} for **22**. One reason may be the coordination of one nitrate counter ion on the central Cu(II) ion in the case of **22** which increases the negative charge in this complex.

More obvious is the influence of the size of the aromatic system of the compounds **21** and **22** on their Raman spectra. For example, the rotation vibration of the aromatic CH appears at 1583 cm^{-1} for **21** and 1591 cm^{-1} for **22**. Such differences can be also detected for bands above 1600 cm^{-1} , *cf.* figure 4.15.

All the investigated complexes show a similar temperature dependence. An exemplary comparison of the Raman spectra at 15 and 300 K is shown in figure 4.15 for the complex **21**. For most of the bands only minor changes in the intensity and frequency shifts were observed. Remarkable shifts of 9 cm^{-1} were observed for $1416/1428\text{ cm}^{-1}$ for 300 K and $1425/1437\text{ cm}^{-1}$ for 15 K. These bands were assigned to $\delta(\text{NCuN}, \text{OCuO})$, $\nu(\text{CC})$ of the aromatic ring and the oxamato group and the $\delta(\text{CH})$ of the aliphatic hydrogens. The shift to higher wave numbers when decreasing the temperature is caused by decreasing bond lengths in the molecule. The fact that not all bands shift by the same amount indicates that different bonds undergo different length change.

Monitoring the temperature dependent Raman spectra show that the changes described above occur and saturate at temperatures above 100 K. Below 50 K, where the magnetic super-exchange overcomes the thermal energy no more changes were observed in the spectra, clearly indicating that the onset of the magnetic coupling does not imply a significant change in the intramolecular bond angles or bond lengths. The quantum chemical DFT calculations for different spin states will give a rough estimate on the magnitude of such effects, *cf.* discussions in the next section.

4.5 Summary and conclusions

This chapter presents an analysis of the influence of a systematic variation of the molecular structure on the optical and vibrational properties of four Cu(II)-*bis*(oxamato) complexes (**2**, **9**, **21**, and **22**).

Replacing the metal atom in the mono-nuclear complexes was found to yield dramatic shifts in the energy of the optical transitions, as shown by UV/Vis absorption measurements in solution. On the other hand, the extension of the aromatic system of the bridging ligand brings more influence on the intensity of the CT and $\pi\text{-}\pi^*$ optical transitions in the UV range as demonstrated by the optical absorption measurements on the solution, TDDFT calculations, and by

the SE measurements on the films of the trinuclear complexes **21** and **22**. The best match of the SE model to the experimental data was achieved for an isotropic model which means that the molecules orient randomly on the substrate. Thin films of good homogeneity are accessible for molecules with a high solubility.

A first comprehensive assignment of the vibrational bands of the *bis*(oxamato) type transition metal complexes is proposed for **2**, **9**, and **21** by a detailed comparison of the experimental spectra with the vibrational energies as well as IR and Raman intensities calculated using DFT. For example, the replacement of Cu with Ni in the mononuclear complexes was found to induce significant frequency shifts (up to 6 cm^{-1}) of the bands involving vibrations of the coordinating N and O atoms while having less influence on the bands stemming from the terminal ligands. Moreover, temperature dependent Raman spectroscopy investigations show that the onset of super-exchange interactions at low temperatures does not involve a modification of the structural parameters.

5 Magneto-optical investigations

5.1 Introduction

The application potential of magneto-optical effects measured in reflection, *i.e.* of the magneto-optical Kerr effect (MOKE), for inorganic ferromagnets was already outlined in chapter 1. At the same time challenges like the weak signal intensity of this method, when applied to thin films of organic materials and transition metal complexes, were pointed out. In the following sections the MOKE spectroscopy studies of a pure organic compound, namely metal free phthalocyanine (H_2Pc) and of a paramagnetic transition metal complex will be discussed for the first time. Differences in the orientation of H_2Pc molecules were artificially induced by using different substrates following the example of, *e.g.* [Gordan06a] in order to study whether the MOKE spectroscopy is a highly sensitive method for the determination of the molecular orientation. For this purpose the Voigt constant, a material parameter extracted from the MOKE spectra and the optical constants derived from SE, have been determined. The techniques used up to now for the determination of the molecular orientation are spectroscopic methods like ellipsometry, IR, Raman, and angular resolved near x-ray absorption fine structure, see *e.g.* Zahn *et al.* [Zahn07] and the references therein.

Phthalocyanines were used as model systems since they have a good thermal stability and hence are well suited for the controlled deposition of thin films by thermal sublimation in vacuum. On the other hand, the phthalocyanines show semiconducting and photoconducting properties and are often used as active layers in organic based electronic or optoelectronic devices [Pope99]. In the view of possible applications in the emerging field of organic-based spintronic devices, their magneto-optical activity in reflection mode may be of high interest. After a brief description of the investigation methods MOKE and magnetic circular dichroism (MCD) a theoretical model will be introduced for the determination of the Voigt constant of organic thin films. The orientation of the

molecules will be determined and compared with other methods. Finally, *bis(oxamato)* complexes in solution and in form of thin films will be investigated magneto-optically.

5.2 Theoretical background

5.2.1 Magneto-optical effects

Every material influences the polarisation state of light if it is exposed to a magnetic field. Depending on the measuring geometry and the magnetic field orientation with respect to the angle of incidence of the polarized light one has to distinguish between three effects:

- the Voigt effect is measured in transmission and the magnetic field is oriented perpendicular to the propagation direction of light
- the Faraday effect is also measured in transmission, but the magnetic field is oriented parallel to the propagation direction of light
- the Kerr effect is measured in reflection; depending on the orientation of the magnetic field to the propagation of light one distinguishes according to figure 5.1 the following geometries
 - transversal: the magnetic field is applied perpendicular to the sample normal and the plane of incidence of light
 - longitudinal: the magnetic field is applied perpendicular to the sample normal and parallel to the plane of incidence of light
 - polar: the magnetic field is applied parallel to the sample normal and the angle of incidence of the light is close to zero.

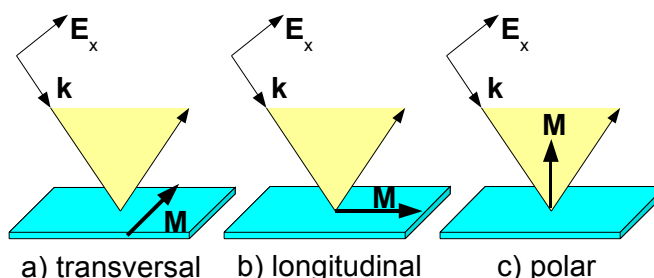


Figure 5.1. Different geometries for the Kerr effect.

After transmission of light through a magnetized sample the changes in the state of polarization is described by the complex rotation

$$\Theta_F = \theta_F + i\eta_F, \quad (5.1)$$

which is illustrated in figure 5.2. It consists of the rotation θ and the ellipticity η which are the real and the imaginary part of the Faraday rotation, respectively. The former is called the magnetic circular birefringence (MCB) and the latter is known as the magnetic circular dichroism (MCD) effect. For thin films of the thickness d the MCD signal can be calculated according to [Bauer00]:

$$\Theta_F = \theta_F + i\eta_F = \frac{\omega}{2c} \tilde{n} Q d, \quad (5.2)$$

with ω being the angular frequency of the light, c the light velocity, and \tilde{n} the complex index of refraction.

The change in the polarization state induced by reflection on a sample in a magnetic field is called the magneto-optical Kerr effect (MOKE) [Zvezdin97, Sugano00] and can be described by θ and η according to figure 5.2.

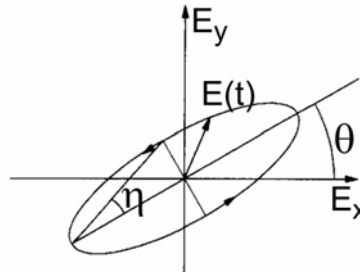


Figure 5.2. State of polarization of the reflected or transmitted light.

5.2.2 Calculation of the Voigt constant

The Voigt constant Q can be obtained from the MOKE spectra recorded in polar MOKE geometry, a method which has already been applied to ferromagnetic films with thicknesses well below the penetration depth of the light where the Voigt constant lies in the order of magnitude of 10^{-2} [Herrmann06]. Since thin films of organic semiconductors are expected to have a very low Voigt constant, in the order of 10^{-5} , the magneto-optical investigations are commonly performed in transmission by means of MCD taking advantage of the higher sensitivity of this method compared to measurements in reflection.

A general model for the determination of the Voigt constant of thin films was proposed by Zak *et al.* [Zak91]. In the present case some simplifications can be done [Fronk08]:

- Since the angle of incidence can be considered to be zero the magnetisation in a paramagnetic medium is always parallel to the magnetic field direction and hence in this case to the propagation direction of the light.
- The samples can be treated as three layer systems consisting of the air with a refractive index $n_A = 1$, the organic film with the thickness d and the optical constants known from SE investigations, and the substrate consisting of Si with 3 nm SiO₂ on top.

A detailed description can be found in literature [Fronk08] closely related to this thesis work. In brief, it takes into account the optical effects occurring at the interfaces shown in figure 5.3.

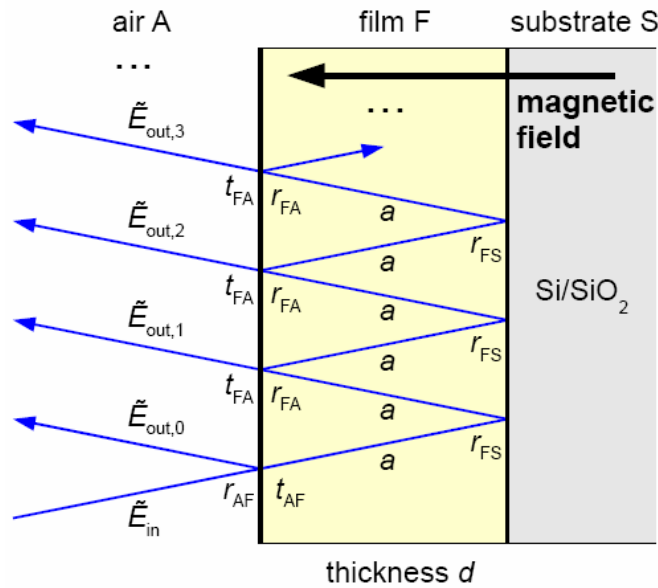


Figure. 5.3. Schematic of the three layer model used to model the MOKE spectra. The Fresnel coefficients of the interfaces (r , t) and the propagation terms (a) in the organic layer are marked. The electric field vectors of the outgoing radiation is \vec{E}_{out} . For a better visualization the angle of incidence is shown to be larger than zero in the sketch, although the model is constructed for the case of normal incidence [Fronk08].

The parameters t and r represent the Fresnel coefficients for the light transmission through and reflection at an interface, respectively. The term denoted with a stands for the exponential attenuation of light passing through the organic layer. Using the Jones formalism [Azzam99] the complex Kerr

rotation Θ_K can be written as a function of the effective reflection coefficients for the two circular polarization modes u_{\pm} :

$$\Theta_K = \arctan \frac{i(u_+ - u_-)}{(u_+ + u_-)} \approx \frac{i(u_+ - u_-)}{(u_+ + u_-)} = f(\tilde{n}_{\text{substrate}}, \tilde{n}_{\text{layer}}, d, Q). \quad (5.3)$$

This equation can be numerically solved for Q if all other parameters are known from SE and MOKE measurements. To account for the sign definition of the Q and the Jones vectors used here, the sign of the MOKE spectra needs to be inverted. The numerical calculations were performed using the Matlab[®] software.

The contribution of the optical anisotropy of the sample which can be measured by means of reflection anisotropy spectroscopy was neglected in equation 5.3 because this part is eliminated by calculating the difference of the effective reflection coefficients.

5.3 Experimental details

5.3.1 Measurement setup for magneto-optical investigations

The MOKE measurements were carried out *ex situ* with a home made setup similar to that described by Herrmann *et al.* [Herrmann06], see figure 5.4. It is constructed to detect very small rotation angles of the polarization of about 10^{-3} or even smaller. A Xe arc lamp is used as a light source. The incident light is linearly polarized by a Rochon prism polarizer perpendicular to the plane of incidence, so-called s-polarized light. The light reflected from the sample, which is mounted inside of an electromagnet, is elliptically polarized. Its polarization state is modulated by the photoelastic modulator (PEM) which generates a time dependent periodic phase shift between the s- and p-polarized light. The frequency of the PEM is $f = 50$ kHz introducing a time dependent phase shift of

$$\Delta\varphi = \delta_0 \sin(2\pi f t) \quad (5.4)$$

and thus a time dependent state of polarization. The main axis of the PEM is aligned parallel to the transmission axis of the polarizer but 45° with respect to the analyzer which also consists of a Rochon prism. The latter together with the

PEM are used to determine the polarization state of the reflected light. Then the light passes a monochromator and a photomultiplier for energy dependent detection. The accessible photon energy range is between 1.5 and 5.5 eV.

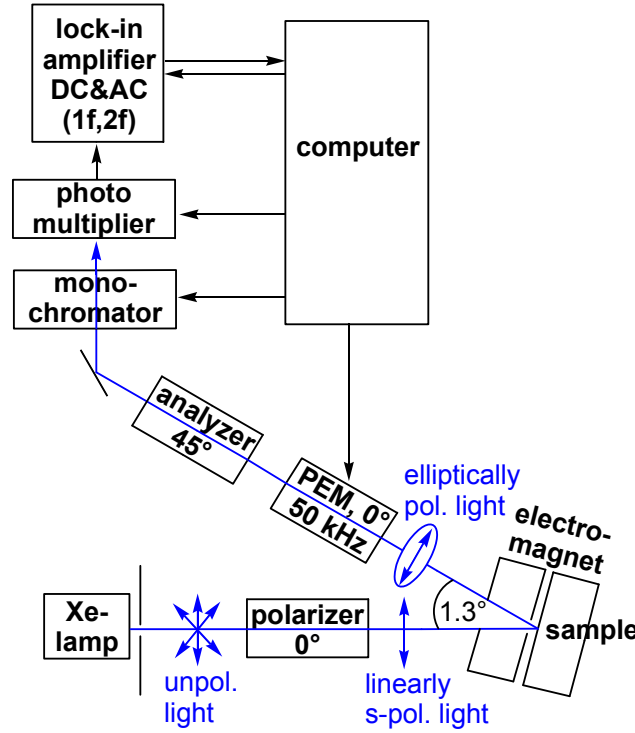


Figure 5.4. Schematic of the MOKE setup.

Taking into account the applied magnetic field which is oriented parallel to the sample normal either in “+B” or in the opposite direction “-B” the Kerr angle can be determined according to

$$\Theta_K = \frac{\Theta_{+B} - \Theta_{-B}}{2}. \quad (5.5)$$

The angle of incidence of the light is close to zero (1.3°) and the magnetic field strength applied during the measurements is 0.35 T. The sign of the MOKE spectra is defined as in reference [Herrmann06] following a sign convention which is often used in the literature.

The MCD spectra were obtained using a homebuilt instrument consisting of a JASCO J-715 spectropolarimeter and an Oxford Instruments SPECTROMAG magnetocryostat. The spectra were recorded for the organic films grown on quartz glass. The measurements were performed at the Max Planck Institute in Mülheim. The measuring procedure is analogous to the MOKE measurements whereas MCD measurements were performed in transmission.

5.3.2 Crystalline structure of H₂Pc and PTCDA

The Lewis and crystal structure of H₂Pc is shown in figure 5.5 [McKeown98]. The ability of H₂Pc to form crystals by vacuum sublimation enabled their thorough structural characterization by X-ray diffraction. Their studies [McKeown98] show that the β -form crystal is monoclinic and belongs to the $P2_1/a$ space group, with two H₂Pc molecules per unit cell. The H₂Pc stacks make an angle between 45° and 49° with the b-axis of the crystal. The H₂Pc molecules in neighboring stacks are roughly orthogonal, producing a herringbone like arrangement.

The α -phase also has a monoclinic crystal structure of the $C2/c$ space group, with four molecules per unit cell. The H₂Pc stacks make an angle between 27° and 30° with the b-axis of the crystal.

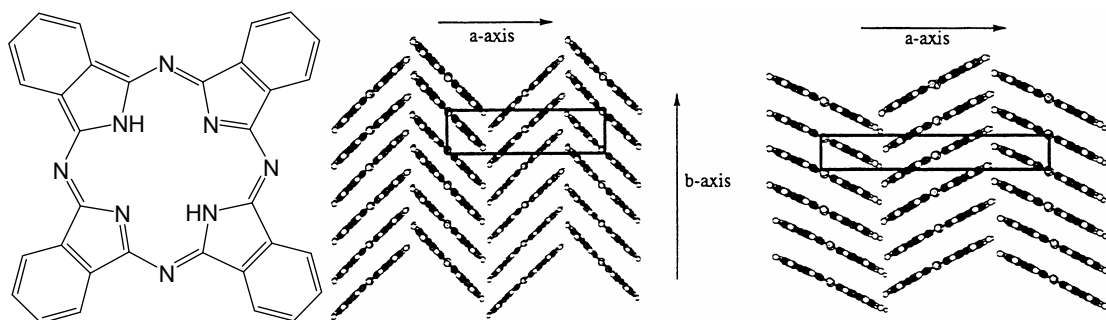


Figure 5.5. a) Lewis structure and b) crystal structure of β -type H₂Pc and c) α -type H₂Pc. [McKeown98].

The Lewis and crystal structure of 3,4,9,10-Perylenetetracarboxylic-dianhydride (PTCDA) is shown in figure 5.6 [Forrest97]. The α modification crystallizes in the space group $P2_1/c$ with lattice constants $a=0.372$, $b=1.196$, $c=1.734$ nm and $\beta=98.8^\circ$. The β modification is found to crystallize in the same space group, but with different lattice parameters: $a=0.378$, $b=1.930$, $c=1.077$ nm and $\beta=83.6^\circ$ [Ogawa99]. The molecules are almost parallelly oriented with respect to each other.

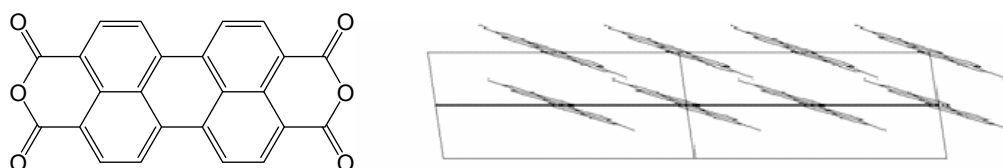


Figure 5.6. a) Lewis structure and b) crystal structure of PTCDA.

The crystal structure of molecules can be influenced by various parameters such as temperature, pressure, or even the substrate on which the molecules are grown. The latter effect was studied for H₂Pc grown on top of PTCDA. Since PTCDA lies flat on the substrate it can induce a change in the molecular orientation shown in figure 5.7 for the H₂Pc molecules on top of it [Gordan06a, Sakurai06, Gordan06b]. One reason might be a strong electronic interaction between the π electron systems of the H₂Pc and the PTCDA molecules decreasing the tilt angle α , *i.e.* the angle between the substrate and the molecule plane, see figure 5.7. Furthermore, it was proposed [Sakurai06] that this enforced growth mode relaxes gradually with increasing distance to the H₂Pc/PTCDA interface.

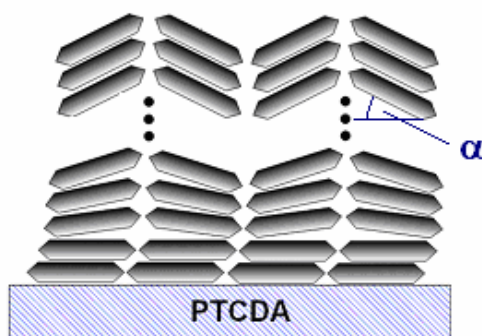


Figure 5.7. Schematic model of the H₂Pc growth on PTCDA including the tilt angle α .

5.3.3 Sample preparation

The organic layers were produced by organic molecular beam deposition under high vacuum conditions. The organic films were deposited on Si covered with native oxide and on quartz substrates simultaneously. For sample S1 the H₂Pc was directly grown on SiO₂ and for sample S2 the SiO₂ was covered with 3 nm of PTCDA and afterwards the H₂Pc was deposited on top, see figure 5.8. H₂Pc and PTCDA was deposited with a rate of 0.5 nm/min at a base pressure of $8 \cdot 10^{-7}$ mbar. The films grown on silicon substrates were investigated by means of spectroscopic MOKE and SE while the layers grown on quartz were used for MCD investigations.

Thin films of **21** for magneto-optical investigations were prepared according to the described procedure in chapter 4. The magneto-optical measurements in transmission were performed in 10^{-5} molar butyronitril solutions.

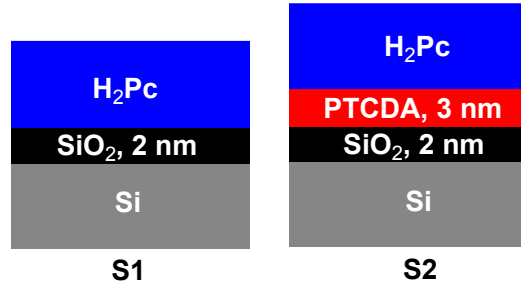


Figure 5.8. Schematic of the investigated samples.

5.4 Results and discussion

5.4.1 Spectroscopic ellipsometry investigations

Figures 5.10 and 5.11 show the Kramers-Kronig consistent dielectric functions of H₂Pc grown on Si/SiO₂ (S1) and Si/SiO₂/PTCDA (S2), respectively. They were derived from the VASE spectra, recorded for three angles of incidence ($\phi = 65^\circ, 70^\circ$, and 75°) and are shown in the appendix figure 5.a1. The dielectric function can be significantly influenced by the molecular orientation. Due to the strong correlation between the dielectric function and the film thickness in the modeling of the VASE data, it is useful to investigate several samples with the same dielectric function and different thickness and fit their experimental spectra simultaneously.

Therefore two samples having different thicknesses, namely 45 nm (S1-45 and S2-45) and 97 nm (S1-97 and S2-97) were prepared for each system. The dielectric functions are described by the Cauchy equation in the range from 1.0 to 1.4 eV, *cf.* table 5.1, and by a sum of Gauss oscillators in the absorbing spectral range from 1.4 to 4.4 eV, *cf.* table 5.2. Some Cauchy parameters had to be fixed to avoid negative values.

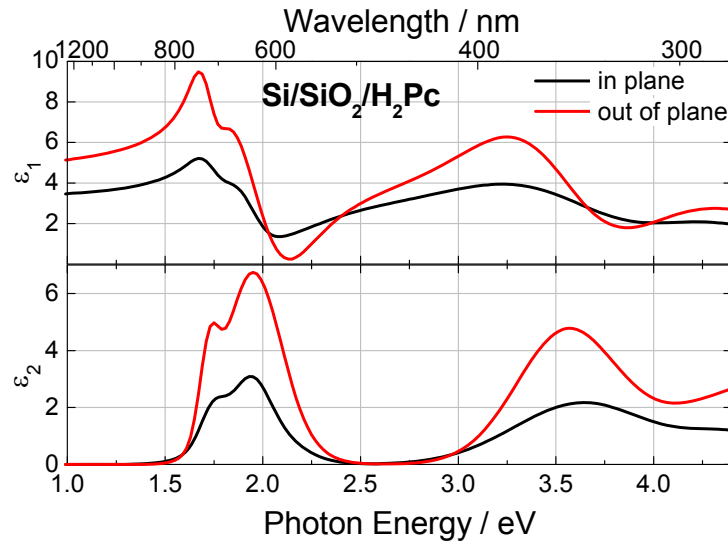
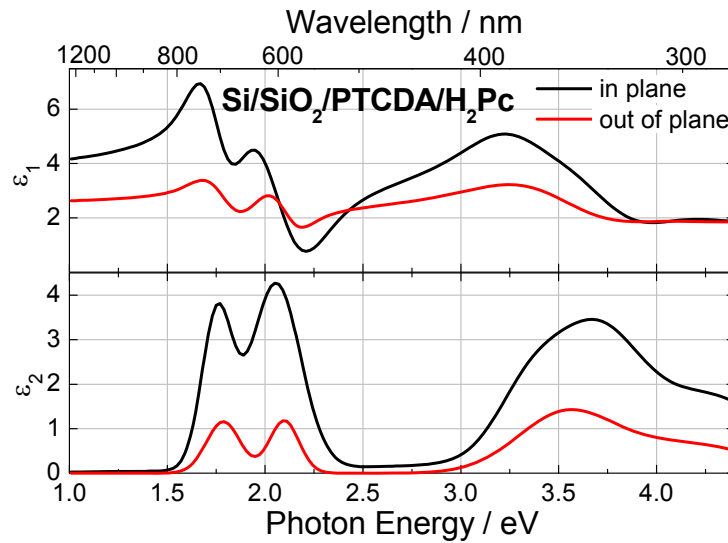
Table 5.1. Film thickness and surface roughness values determined by applying the Cauchy model (left). Cauchy parameters using a coupled model of the 45 and 97 nm thick films (right).

Sample	$\alpha^a)$	thickness	roughness	light plane ^{b)}	Cauchy parameters		
	/ °	/ nm	/ nm		A_n	B_n	C_n
S1-45	> 45	44.7±0.4	5.3±0.6	S1 oop	2.23±0.01	0 fixed	0.118±0.003
S1-97	> 45	84.1±0.2	17.0±0.3	$\alpha > 45^\circ$ ip	1.83±0.01	0 fixed	0.096±0.001
S2-45	< 45	44.6±0.3	0	S2 oop	1.57±0.02	0.05±0.04	0.11±0.02
S2-97	< 45	88.1±0.6	0	$\alpha < 45^\circ$ ip	1.94±0.02	0.07±0.05	0.003±0.025
S2-45	> 45	6.4±0.4	0	S2 oop	2.23 fixed	0 fixed	0.118 fixed
S2-97	> 45	17.7±0.9	0	$\alpha > 45^\circ$ ip	1.83 fixed	0 fixed	0.0958 fixed

^{a)} tilt angle α of the molecules, compare figure 5.7; ^{b)} coupled model, ip: in plane, *i.e.* parallel to the sample plane; oop: out of plane, *i.e.* perpendicular to the sample plane; MSE(S1)=0.9, MSE(S2)=0.7.

Table 5.2. Summary of the Gaussian oscillators employed by the oscillator model.

Gauss. oscillat.		S1 and S2 (for $\alpha > 45^\circ$) ^{a)}			S2 (for $\alpha < 45^\circ$) ^{b)}		
		energy	amplitude	broadening	energy	amplitude	broadening
1	ip	1.742±0.004	1.14±0.06	0.147±0.00	1.756±0.03	3.52±0.09	0.184±0.004
	oop	1.725±0.011	2.8±0.7	0.11±0.02	1.789±0.00	1.20±0.08	0.199±0.014
2	ip	1.941±0.003	1.44±0.08	0.207±0.00	2.054±0.03	4.2±0.6	0.296±0.004
	oop	1.945±0.016	6.5±1.2	0.33±0.03	2.096±0.00	1.19±0.03	0.181±0.006
3	ip	1.938±0.004	1.65±0.02	0.439±0.00	3.3±0.7	1.3±1.2	0.40±0.05
	oop	2.1±0.3	0.5±1.2	0.37±0.16	3.57±0.09	1.5±0.2	0.62±0.10
4	ip	3.637±0.001	2.16±0.01	0.824±0.00	3.69±0.05	2.8±0.9	3.69±0.05
	oop	3.5±0.2	4.4±0.5	0.6±0.2	4.23±0.18	0.6±0.2	0.6±0.6
5	ip	4.42±0.02	0.99±0.03	0.58±0.03	4.2±0.2	1.1±0.4	0.7±0.4
	oop	4.70±0.04	3.04±0.07	1.33±0.06	5.0±0.5	2+6/-2	0.4+1.3/-0.4
6	ip	6.3±0.4	3.5±1.5	1.2±0.7	9.6±0.4	3.75±0.11	6.5±0.4

^{a)} MSE: 4; ^{b)} MSE: 7**Figure 5.9.** Dielectric function of H₂Pc grown on SiO₂.**Figure 5.10.** Dielectric function of H₂Pc grown on PTCDA, in the region close to the interface.

Additionally, the surface roughness was included in the model, described as a mixture of 50 % material and 50 % void. Modeling the samples with H₂Pc on a PTCDA thin film required a more sophisticated model because of the template effect of PTCDA on phthalocyanine films grown on top, *cf.* section 5.3.2.

The complete relaxation towards small tilt angles of the H₂Pc in a distance of more than about 30 nm was assumed. The outermost part of the H₂Pc film was consequently modeled using an uniaxial anisotropic dielectric function of H₂Pc plus surface roughness, as obtained from the layers grown directly on SiO₂. Below, for the transition region, a graded layer with Bruggeman effective medium approximation in 10 steps was used. At the interface to PTCDA an uniaxial anisotropic mathematical model for the unknown dielectric function, as described above, was applied.

The resulting dielectric function of H₂Pc on SiO₂ implies a large tilt angle α of the molecules, as the out-of-plane component is stronger than the in-plane component, *cf.* figure 5.9, and the transition dipole lies within the molecular plane. Reverse behavior could be observed for H₂Pc grown on PTCDA. The H₂Pc is strongly tilted, *i.e.* small α , which can be derived from the strongly pronounced in-plane component compared to a weak out-of-plane component of the dielectric function, *cf.* figure 5.10. This model is strictly valid only for the first nanometers near the H₂Pc/PTCDA. For higher film thicknesses the molecules orient back into their crystal structure imposed alignment.

It was previously shown [Gordan04] that the orientation of the molecules with respect to the substrate plane can be estimated from the ratio of the out-of-plane and the in-plane component of k in the spectral range of the optical transition between 1.5 eV and 2.4 eV (Q band). There it was assumed that the absorbance is proportional to the \cos^2 of the transition dipole moment and that the molecular orientation can be considered as isotropic in the azimuthal plane. This leads to the formula

$$\alpha = \arccos \sqrt{\frac{2A_{\text{in}} - A_{\text{out}}}{2A_{\text{in}} + A_{\text{out}}}}. \quad (5.6)$$

Assuming that the Q band originates from two nearly degenerated optical transitions with transition dipoles lying in the molecular plane, the single molecule can be considered to have disk symmetry in absorption. Using

equation 5.6 the angles 82° and 29° were determined for H_2Pc grown on Si/SiO_2 (S1-45) and $\text{Si}/\text{SiO}_2/\text{PTCDA}$ (S2-45), respectively.

5.4.2 Magneto-optical Kerr effect investigations

The MOKE spectra shown in figure 5.11 are measured on the samples with PTCDA (S2-45 and S2-97) and without PTCDA (S12-45 and S1-97). The main spectral features shift towards lower energies with increasing film thickness, an indication that they are strongly influenced by interference effects.

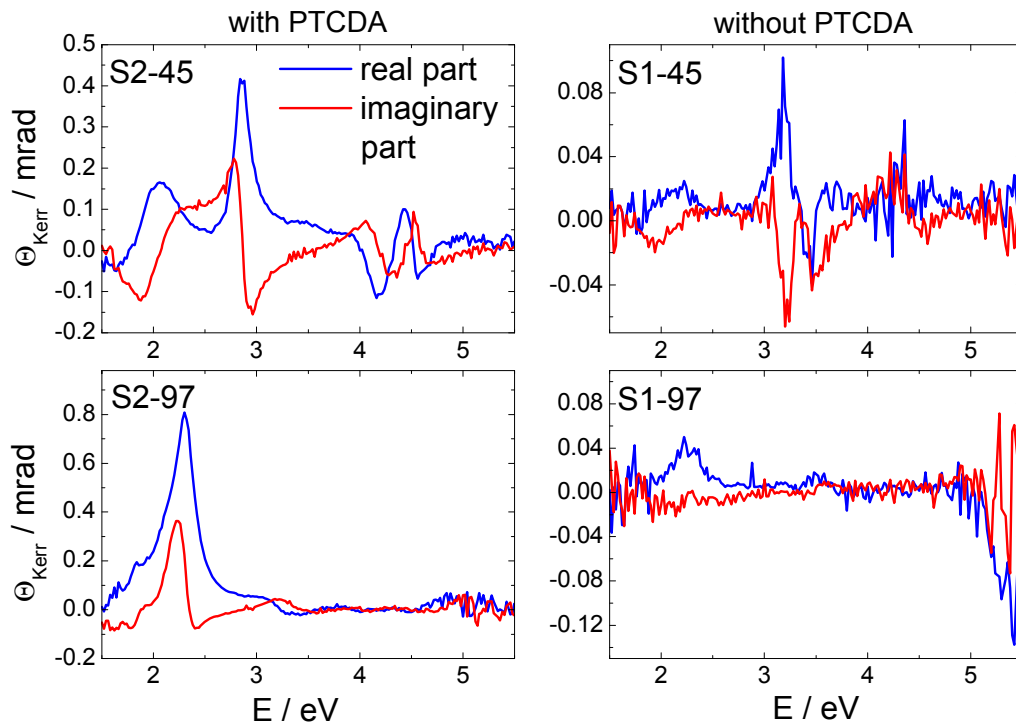


Figure 5.11. MOKE spectra of four different H_2Pc samples with different film thicknesses and with or without PTCDA.

The Voigt spectra, *i.e.* the Q values, of S1-45 and S2-45 are shown in figure 5.12. The interference effects are removed in the Voigt spectra, a fact that provides the first evidence of the model outlined in section 5.2.2. The model was further checked by inserting the calculated Q values and the optical constants into equation 5.2 to obtain the MCD spectrum. In figure 5.13 the calculated MCD ellipticity is compared with the experimental results obtained for a 46 nm thick sample at $B = 0.35$ T. A good agreement in the shape and the magnitude of the calculated and experimental MCD spectra is found which provides an independent proof of the proposed model. However, some minor

differences in the signal height and small spectral shifts are apparent. This can be due to slight structural differences in the organic films grown on the quartz and silicon substrates for MCD and MOKE investigations, respectively.

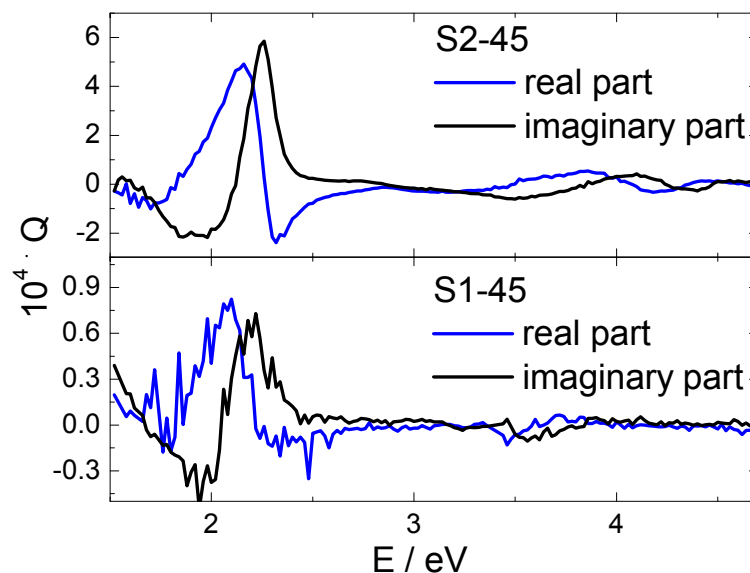


Figure 5.12. Voigt spectrum of H_2Pc grown on Si/SiO_2 with and without PTCDA as interlayer.

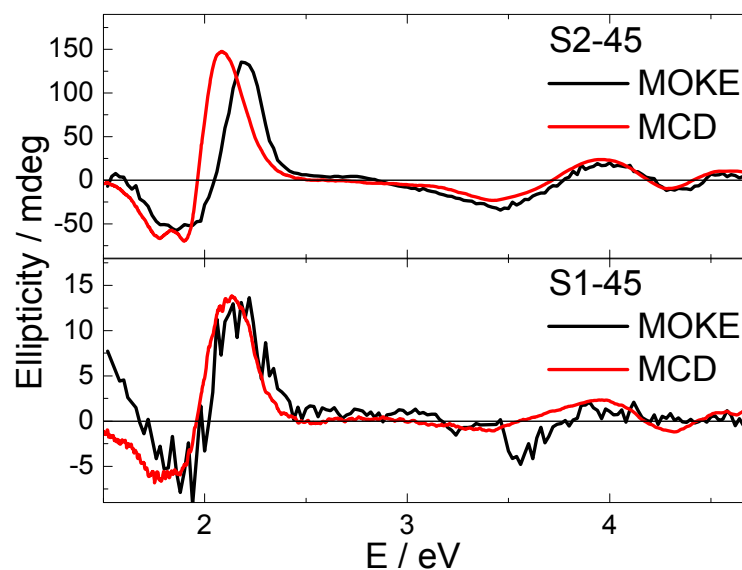


Figure 5.13. Ellipticity derived from MOKE and MCD spectra for H_2Pc grown on Si/SiO_2 with (S2-45) and without PTCDA (S1-45) as interlayer.

The spectrum of the Q parameter in figure 5.13 of the sample S1-45 shows significantly less intensity (almost by a factor of 10) than that of the sample S2-45, *cf. e.g.* the value for Q at 2.23 eV. The same trend was observed for the ellipticity. Assuming a cosine dependence of the magnitude of Q on the

molecular tilt angle α , the Voigt spectra of the samples S1-45 and S2-45 imply rather small tilt angles of $\alpha < 30^\circ$ if PTCDA is used as a template.

The influence of the molecular orientation on the magneto-optical response has already been used in [McInnes02] to explain MCD results. There it was suggested that 2D transitions polarised in the molecular plane, such as the almost degenerated Q band transitions of the phthalocyanines, produce a maximum MCD signal for light incident normal to the molecular plane and zero signal for light propagating in the molecular plane. Thus for light incident normal to the sample surface perfectly lying molecules would yield a maximum MCD signal while standing molecules would give no signal. This hypothesis also holds for the Voigt constant, though the exact angular dependence may differ from the case of MCD signal because of the fact that the refractive index \tilde{n} , which is angular dependent, enters as a factor between Q and the MCD ellipticity, *cf.* equation 5.2.

A small tilt angle implies that the field vector of the nearly normal incident light interacts more strongly with the molecules inducing a MOKE signal with higher intensity. The tilt angles compare well with those extracted from the SE measurements, *cf.* table 5.3, and were found to be within the error limits of SE. The absolute error value in determining the molecular tilt angle from SE especially for small α is higher than for the MOKE investigations, since equation 5.6 is only a rough guesstimate for the determination of α by means of SE when the angle becomes small. Therefore the MOKE measurements may provide a more accurate tool to determine the molecular orientation.

Table 5.3: Values of the angle between the molecular plane of H₂Pc and the substrate plane estimated from SE investigations. The magnitude of the Q constant was determined at 2.23 eV. The normalisation was done with respect to S2-45. The angle in the last column was calculated from $\arccos(Q)$.

H ₂ Pc layers	angle $\alpha / ^\circ$ from SE	$\cos(\alpha)$	Normalised cosine	Normalised Q- magnitude	angle $\alpha / ^\circ$ from MOKE
S1-45	82±4	0.14±0.07	0.16±0.08	0.12±0.03	81±2
S2-45	29±4	0.87±0.03	1.00±0.03	1.00±0.03	29±4

5.4.3 Magneto-optical Kerr effect studies of *bis*(oxamato) complexes

The magneto-optical spectrum of **21** measured in reflection at room temperature compared to the spectra measured in transmission at different temperatures is shown in figure 5.14. The former shows two very weak yet

measurable MOKE signals at 3.5 and 4.5 eV. The low signal intensity is most probably due to the high degree of roughness of the spin-coated film. Further improvement of the film quality should therefore lead to reliable magneto-optical measurements in reflection on opaque substrates. The different energetic positions of the magneto-optical features in solution and on thin films might be due to interactions of the molecules with the solvent as well as interference effects in the films. Unfortunately, the quality of the MOKE spectrum did not allow to extract the Voigt constant and thus the corresponding MCD spectrum. MCD measurements were performed at 298 K in liquid and at 25 as well as 2 K in frozen butyronitrile solutions. The magneto-optical behaviour of **21**, shown in the lower panel of figure 5.14, is strongly temperature dependent. This is due to the different measuring conditions in liquid and frozen solutions, as well as the strongly increasing magnetic super-exchange interaction within the molecules at low temperatures, *cf.* section 3, which leads to a higher ellipticity, compare *e.g.* the band at 4 eV at 2 and 25 K, respectively.

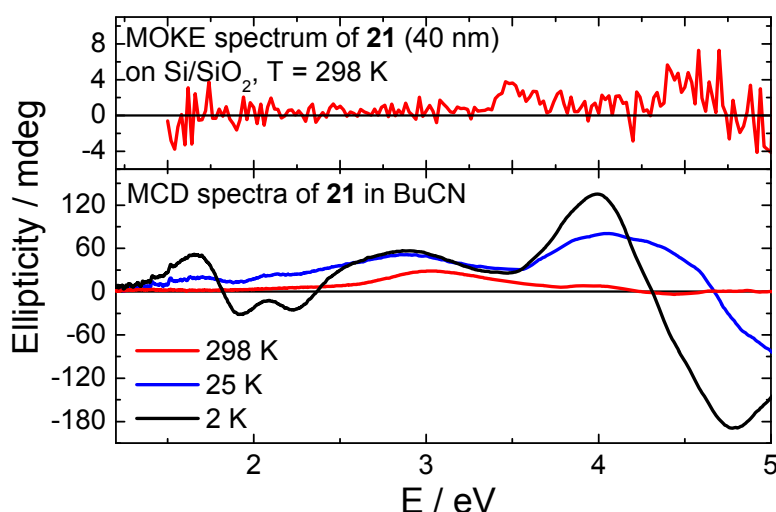


Figure 5.14. Magneto-optical spectrum measured in reflection at room temperature (MOKE spectrum) compared to the spectra at different temperatures measured in transmission (MCD spectra).

5.5 Summary and Conclusions

MOKE spectroscopy in the energy range from 1.5 eV to 5 eV was demonstrated for the first time to be a highly sensitive tool for the detection of the molecular orientation of diamagnetic organic semiconductors with layer thicknesses in the range of tens of nanometres deposited onto opaque substrates. The growth

mode and thus the intensity of the MOKE signal of H₂Pc was shown to be strongly influenced by the templating effect of 3,4,9,10-perylene-tetracarboxylic-dianhydride (PTCDA) leading to a small tilt angle of the H₂Pc molecules.

Using a three-layers model, the Voigt constant of the organic film was extracted. For that purpose the MOKE spectra, the optical constants of the film as well as of the substrate and the film thickness are required. On the example of H₂Pc it was shown that the magnitude of the Voigt constant in the visible spectral range can be exploited to estimate the tilt angle of the molecular plane with respect to the substrate plane. The highest intensity of the Voigt constant was observed in the spectral range of the π - π^* transitions and in case when the H₂Pc molecules possess a small tilt angle with respect to the substrate.

The MOKE spectroscopy was shown to be more sensitive regarding the orientation of the molecules with respect to the substrate than SE. This provides an important contribution to the field of organic semiconductor physics in which the molecular orientation is of great importance. The prerequisite for using MOKE spectroscopy when investigating a system of samples with differently oriented molecules is, however, that the orientation of one sample must be known.

Magneto-optical investigations on spin coated thin films of *bis*(oxamato) complexes were successfully performed. The low signal intensity can be due to a still present inhomogeneity and non-preferential alignment of the molecules, as derived from the SE measurements. Nevertheless, the obtained results are a promising basis for forthcoming investigations on soluble transition metal complexes. MCD measurements on solution have shown a strong enhancement of the MCD signal when going to low temperatures related to an increase in magnetization, *cf.* magnetic susceptibility measurements of the trinuclear *bis*(oxamato) complexes in chapter 3.

6 Electronic and magnetic properties of Ni nanoparticles in organic matrices

6.1 Introduction

Nanosized particles of ferromagnetic metals such as Fe, Co, and Ni are subject to growing interest thanks to a variety of interesting physical properties and potential applications like catalysts, high density magnetic recording media, ferrofluids, and medical diagnostics [Schultz90, Lu00, Ozaki89, Gleiter92]. Recently, an enhancement of quantum efficiency of organic light emitting devices by doping with magnetic nanoparticles was reported [Sun07].

When decreasing the size of the particles to several nanometers, they behave like a single magnetic domain, leading to a super paramagnetic state for temperatures above the blocking temperature [Stoner48]. Furthermore, the chemical and structural properties of the interface between the particles and the surrounding medium play an important role in determining their magnetic properties. Isolated Ni nanoparticles embedded in an inert nonmagnetic matrix can be obtained by evaporation [Hayashi77], sputtering [Gavrin93], high energy ball milling [Gonzalez98], ion exchange [Jung99], and sol-gel procedures [Estourne97, Leite02]. The preparation of Ni nanoparticles dispersed in porous matrices exhibits difficulties in controlling the size and the oxidation of the particle surface. The resulting particles have a shell-core morphology with an antiferromagnetic oxide layer surrounding the ferromagnetic core, a fact which can complicate the interpretation of the magnetic data.

The reason for the complex magnetic behaviour of oxidized particles is the appearance of the exchange bias (EB) phenomenon which was discovered by Meiklejohn and Bean in Co/CoO core/shell nanoparticles in 1956 [Meiklejohn56]. Since that time the EB phenomenon has been used for controlling the magnetization in devices such as spin valves in magnetic reading heads and for magnetic random access memories as well as for ultrahigh density recording

media [Skumryev03, Nogúes99]. The EB is characterized by an enhanced coercivity and a field shift in the hysteresis loop when the system is cooled down in an external magnetic field below the Néel temperature (T_N) of the antiferromagnet. The EB depends among others on the magnetization, the anisotropy, the thicknesses of both layers, the roughness, and the atomic intermixing at the interface [Makhlouf08]. Hysteresis effects accompanied with large EB were also observed in single-phase antiferromagnetic nanoparticles, such as NiO, originating from uncompensated surface spins [Makhlouf08].

This chapter focuses on the formation of Ni nanoparticles in organic matrices when Ni and the organic molecules, shown in figure 6.1, are co-deposited in ultra-high vacuum onto substrates kept at room temperature. Organic molecules were chosen to understand how the broad variety of carbon chemistry helps tailoring the physical properties of the particles. The particle size, their magnetic, and electronic properties are assessed by a variety of methods: photoelectron spectroscopy (PES), Raman spectroscopy, high resolution transmission electron microscopy (HR-TEM), and temperature dependent magnetic measurements.

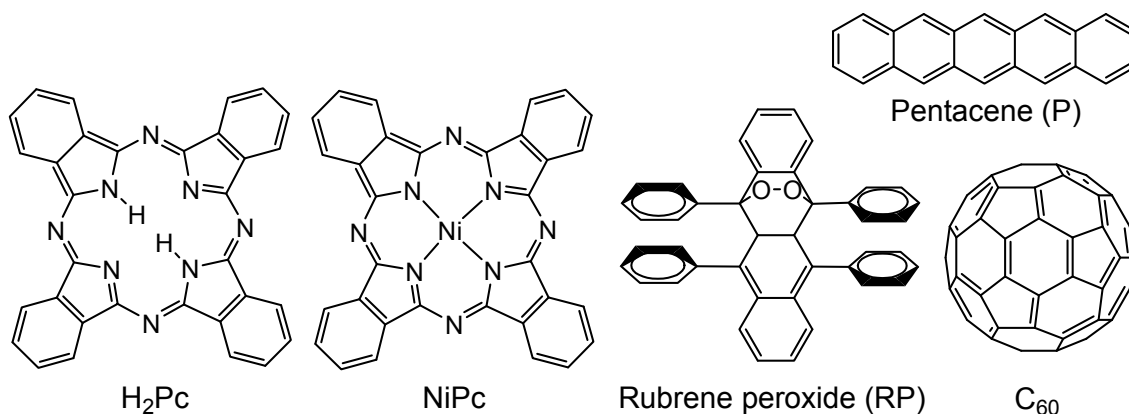


Figure 6.1. Molecules codeposited with Ni.

6.2 Theoretical background

6.2.1 Photoelectron spectroscopy

When an energetic photon beam irradiates matter, ionization can occur and electrons, so-called photoelectrons, are ejected. Ultraviolet photoelectron spectroscopy (UPS) and x-ray photoelectron spectroscopy (XPS) can be distinguished depending on the energy of the incoming light. The former

technique excites a valence electron and the latter an electron from the core level to the continuum as shown in figure 6.2 (a) and (b), respectively. During the primary photoionization process other electrons can be excited to higher-lying bound states (shake-up process, *cf.* figure 6.2 (c) left) and the corresponding lines in the photoemission spectrum, appearing at higher binding energies, are called shake-up satellites. If the excitation occurs into free continuum states, leaving the atom in a doubly ionized state, the effect is denoted as shake-off process, *cf.* figure 6.2 (c) right).

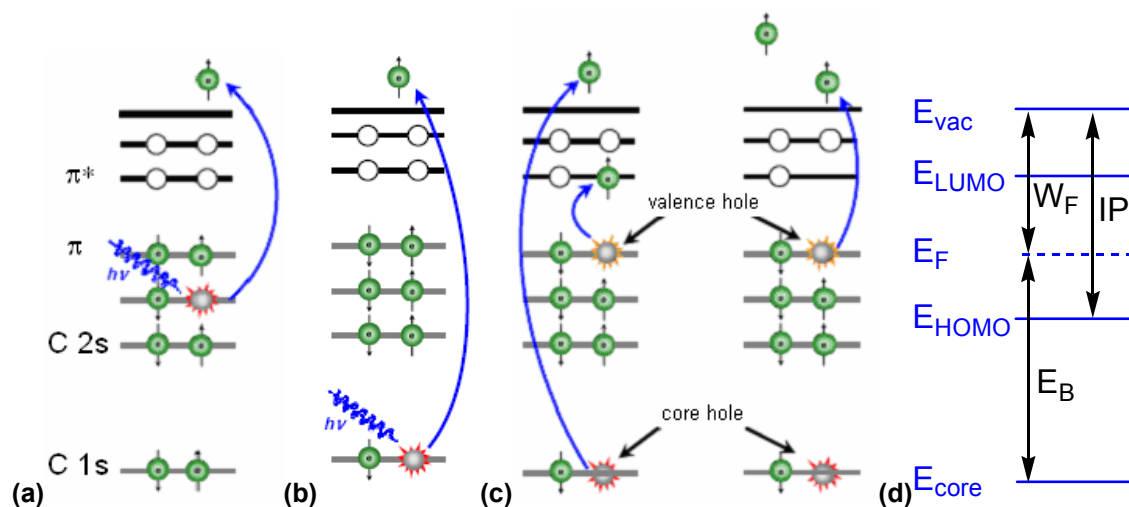


Figure 6.2. Schematic of radiation absorption of a molecule as probed in this work by (a) UPS and (b) XPS. In (c) multielectronic processes during photoemission are shown: shake-up process (left) and shake-off process (right). (d) Schematic energy level diagram of an organic semiconductor with the vacuum (E_{vac}), LUMO (E_{LUMO}), Fermi (E_F), HOMO (E_{HOMO}), and the core level (E_{core}).

Since the positively charged species (S^+) relaxes very quickly ($<10^{-12}$ s) back to the neutral species (S) the ionization process of the neutral species can be studied without mixing with S^+ , S^{2+} , *etc.* This relaxation occurs by Auger or fluorescence decay. For an ionization to take place, the energy of the incoming photon ($h\nu$) has to be larger than the ionization potential (IP) of the bound valence electrons or the binding energy (E_B) of the core electrons and the work function (W_F). The photon energy is transferred completely to the electron and $h\nu$ is partitioned between E_B , W_F , and the kinetic energy (E_{Kin}) of the ejected electron, as given by Einstein's photoelectric equation:

$$E_{Kin} = h\nu - E_B - W_F \quad (6.1)$$

The E_{kin} can be measured very accurately with an electrostatic analyzer. Since the photon energy is known, equation 6.1 enables the determination of the E_{B} of valence, inner valence, and core electrons. A photoelectron spectrum consists of a plot of intensity, which is proportional to the number of electrons with a given IP versus the binding energy. The spectra are conventionally plotted with E_{kin} increasing from left to right and E_{B} increasing from right to left. For solids, the binding energy E_{B} is measured with respect to the Fermi energy E_{F} since the sample and the analyzer are grounded and thus on the same potential. Next to the main peak also satellite peaks related to shake-up and shake-off electrons can appear.

6.2.2 Magnetic nanoparticles

In 1946 Kittel established by energy considerations, that a single magnetic domain would be more stable for particles below a certain critical size. This critical size lies in the range of several nanometers for Ni. Néel [Néel49] pointed out that for such small particles thermal agitation will prevent the existence of stable magnetization, leading to a superparamagnetic state. Stoner provided a model of magnetization reversal in single domain particles, based on a coherent rotation of the magnetic moment [Stoner48]. The transition between the magnetic state and the superparamagnetic state is assisted by thermal phonons and characterized by the so-called blocking temperature T_{B} .

6.3 Experimental details

6.3.1 Sample preparation

The co-evaporation of the metal and the organic material took place in high vacuum conditions ($5 \cdot 10^{-9}$ mbar base pressure). For the magnetic and the Raman spectroscopic measurements Si (111) substrates covered with native oxide were used, while the samples for HR-TEM investigations were grown on freshly cleaved NaCl substrates. In all cases the substrates were kept at room temperature during the deposition. The organic source material was thermally evaporated from a Knudsen cell and the Ni was evaporated using an electron beam evaporator. The deposition rates were around 0.2 nm/min for the organic material and 0.15 nm/min for nickel. The ratio of Ni atoms to the number of

organic molecules was estimated to 10:1. The films were grown to a nominal thickness of 50 nm on Si and NaCl substrates for magnetic and TEM studies, respectively. The films for the PES investigations were grown to a thickness of 7 nm on passivated n-Si(111) ($7.5 \Omega \text{ cm}$) substrates, *i. e.* the native oxide of the Si substrates was removed by keeping them in 5 % HF for 5 min. All characterization techniques were employed *ex situ*.

6.3.2 Experimental techniques

The high resolution transmission electron microscopy (HR-TEM) and electron diffraction investigations of the NiPc+Ni samples were performed using a Philips CM 20 FEG electron microscope.

The Raman spectra presented in this work were recorded in a macro-configuration at 300 K unless specified otherwise. The Raman spectra were excited with the 15454 cm^{-1} (647.1 nm) line of a Kr^+ laser, which lies in the lower energy tail of the Q band optical transition of the phthalocyanines. The spectral resolution was $\sim 4 \text{ cm}^{-1}$ as determined from the full-width at half-maximum (FWHM) of the laser line. Typical values of the incident laser power were in the range from 5 to 10 mW. The polarization of the scattered light was not analyzed. A more detailed description of the setup is given in chapter 4.

The UPS studies were performed using the He I (21.22 eV) and He II (40.8 eV) photon lines of a He-discharge lamp. The photoelectrons are counted with a double-pass cylindrical mirror analyzer. The total energy resolution of the measurement is 0.2 eV, as determined from the width of the Fermi step measured on a clean poly-crystalline Au substrate. The ionization energy of the film is defined here as the energy difference between the vacuum level, determined in a standard way from the position of the onset of photoemission spectrum, and the extrapolated leading edge of the highest occupied molecular orbital (HOMO) [Cahen03]. The XPS studies were performed with an Al $K\alpha$ (1486.6 eV) emission line with a total energy resolution of $\sim 0.9 \text{ eV}$. A schematic of the setup is shown in figure 6.3.

The magnetic hysteresis curves and the measurement of the magnetization upon cooling in a magnetic field of 5 mT and in zero magnetic field were performed with a Cryogenic S600 SQUID magnetometer. A more detailed description of the method is given in chapter 3.

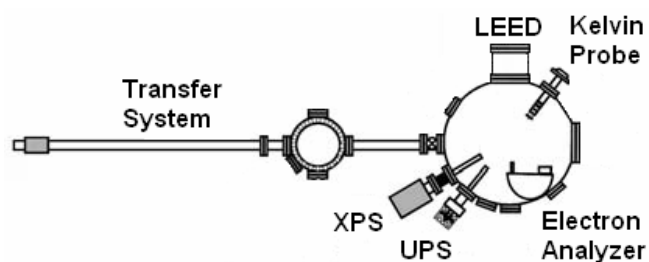


Figure 6.3. Schematic of the PES system.

6.4 Results and discussion

6.4.1 HR-TEM investigations

Typical HR-TEM images for the Ni/H₂Pc system displayed in figure 6.4 (a) show dark regions representing the metal particles surrounded by bright regions representing the organic matrix. The statistic size distribution calculated for more than 100 particles is shown in figure 6.4 (b). Most of the particles have a size of 3 to 4 nm. However, since the information from particles throughout the whole thickness of the films is superimposed in a two-dimensional TEM image the true size distribution is expected to be shifted towards smaller particle size. Measurements of the electron diffraction pattern are shown in the inset of figure 6.4 (a). The well defined diffraction rings indicate the presence of nanoparticles having crystalline character but random orientation with respect to the substrate. Similar results were also obtained for the other Ni/organic systems.

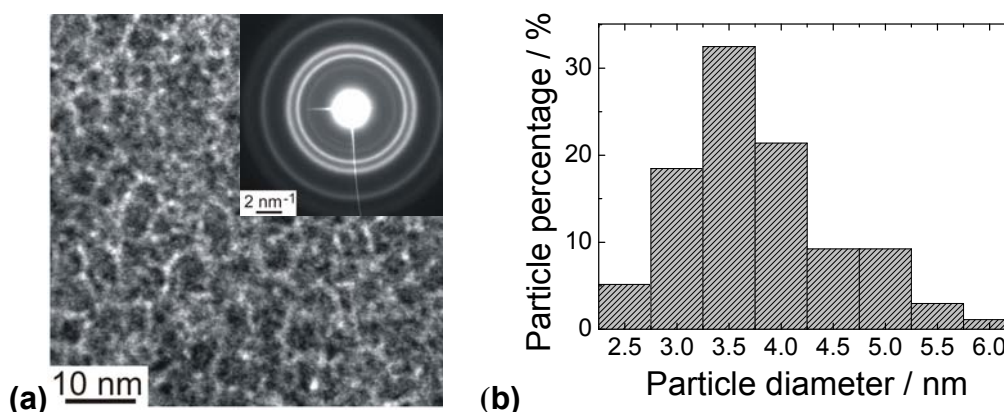


Figure 6.4. (a) Phase-contrasts in a typical bright-field TEM image recorded for a Ni/H₂Pc film and (b) the statistic size distribution calculated for more than 100 particles.

6.4.2 Raman spectroscopic investigations

Raman spectroscopy was used to identify the chemical composition of the mixed films, by comparing the Raman spectra of the powder source materials with the spectra of the thin films.

The Raman spectra of the mixed films obtained by the co-deposition of Ni and H₂Pc (a), and of Ni and NiPc (c) are compared in figure 6.5 to the spectra of films (40 nm) of the pure organic materials (H₂Pc (d) and NiPc (b)).

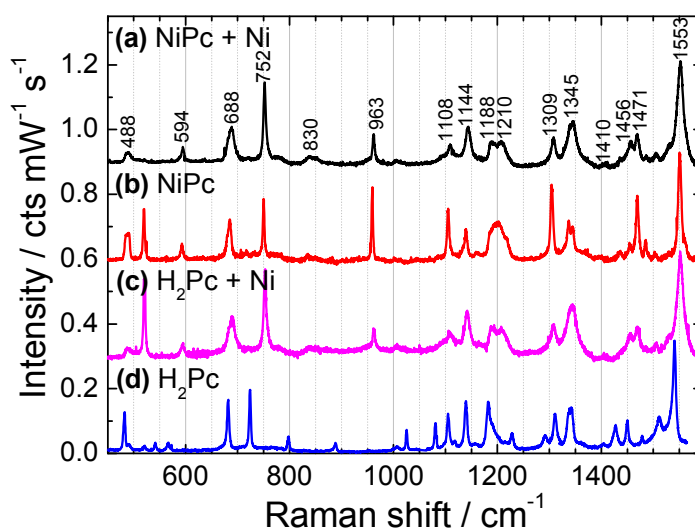


Figure 6.5. Raman spectra of thin films of a) co-deposited NiPc+Ni in comparison with b) NiPc, c) H₂Pc+Ni, and d) H₂Pc. The spectra were normalized to the band at 1553 cm⁻¹.

A comparison of the spectrum c) with d) in figure 6.5 possess many differences in the Raman shift and the intensity of the bands, indicating that the molecular structure in the mixed H₂Pc+Ni films differs from that of the H₂Pc. On the other hand, the spectra of NiPc+Ni films (a) and H₂Pc+Ni films (c) are almost identical, suggesting a similar chemical composition of the two mixed films. This can only happen, if during the deposition process, a reaction between the H₂Pc molecules and Ni takes place, leading to the formation of NiPc molecules and Ni aggregates. To prove this finding, PES investigations will be employed in the next section. It should be noted that the band observed at 521 cm⁻¹ in the spectra (b) and (c) stems from the optical phonon mode of the Si substrate.

Slight differences are observable also between the spectra of NiPc+Ni (a) and NiPc (b). Some bands are enhanced in the spectra of the mixed films, *cf. e.g.* the out-of-plane deformation vibration $\delta(\text{CH})$ at 752 cm⁻¹. A more pronounced difference is the increase in the FWHM of the bands if nanoparticles are

embedded, *cf.* e.g. the deformation vibration of $\delta(\text{CNC})$ of the isoindole fragment at 688 cm^{-1} and the stretching vibration $\nu(\text{NiN})$ at 1309 cm^{-1} . Such an effect can be caused by deformations of the NiPc molecular geometry induced by and/or charge transfer from/to the Ni particles formed in the mixed films. The latter band is also shifted towards higher frequencies in the spectra of the mixed films, possibly reflecting a charge transfer from the NiPc to the Ni nanoparticles which will be discussed in detail later. A detailed assignment of the Raman bands for NiPc can be found in [Liu07].

For the $\text{C}_{60}+\text{Ni}$ systems literature studies suggest the preservation of the C_{60} molecule structure but the presence of a charge transfer [Zheng00]. In the time constraints of this work it was not possible to meet favourable experimental conditions for the detection of the Raman signal from the RP+Ni and P+Ni mixed films. Therefore only photoemission studies will be employed for the elucidation of the chemical composition of these films.

6.4.3 Photoelectron spectroscopy studies

The UPS spectra of Ni in NiPc are shown in figure 6.6. The He I and II spectra for the Ni layer and the Ni nanoparticles embedded in NiPc are very similar because of the high ratio of Ni. The work function W_F , see equation 6.1, of NiPc ($4.10\pm0.05\text{ eV}$) is larger compared to that of the Ni film ($3.85\pm0.05\text{ eV}$) and that of the mixed NiPc+Ni film ($3.80\pm0.05\text{ eV}$), while the latter two are similar within the experimental error.

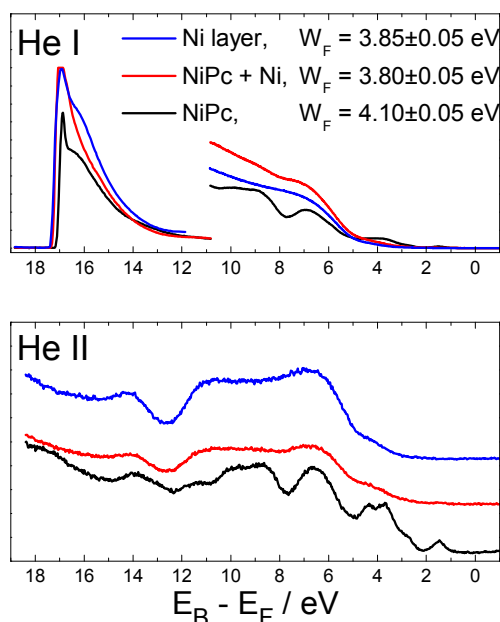


Figure 6.6. Filled states of Ni containing layers measured with UPS.

In figure 6.7 the XPS spectra corresponding to the Ni 2p core level of the thin films under investigation are shown. The peak decomposition of the Ni 2p core level assumes a spin-orbit splitting ($2p_{1/2}$ and $2p_{3/2}$) of 17.5 eV and a statistical 1:2 branching ratio for p-levels. The Ni 2 $p_{3/2}$ spectra were fitted in order to determine the ratio of Ni to NiO_x in the samples in analogy to literature [Oliveira06]. Selected fitting parameters are summarized in table 6.1. The bands at 853.4 eV and 856.8 eV are assigned as Ni and NiO_x , respectively. From the total area ratio of the bands assigned as Ni and NiO_x the relative amount of NiO_x was estimated. In the range from 862 eV to 865 eV a complex multiplet structure occurs.

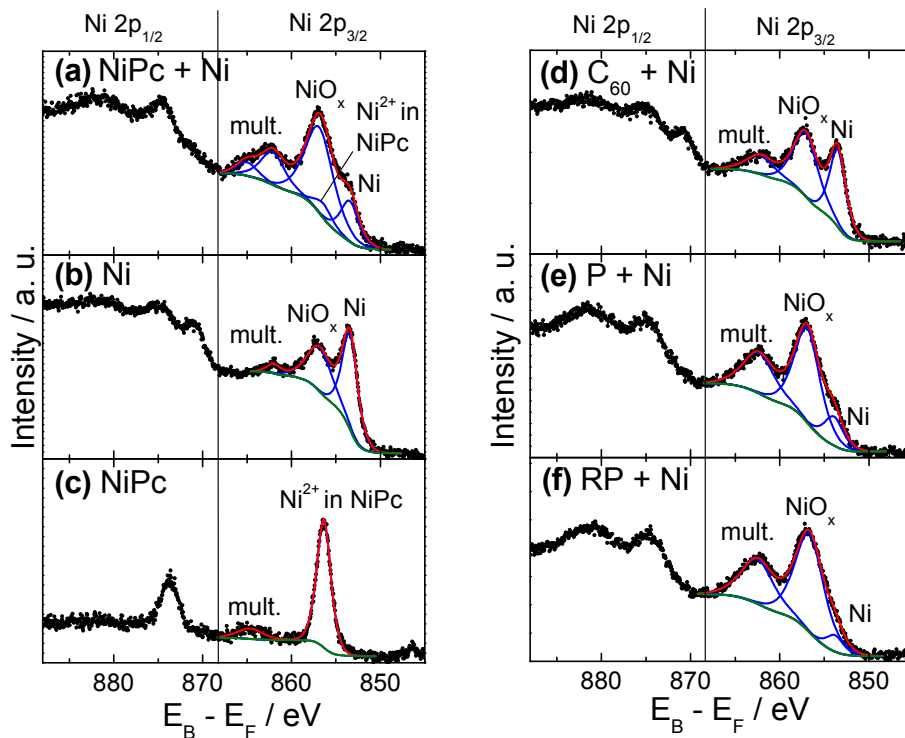


Figure 6.7. XPS spectra of the Ni 2p core levels of (a) co-deposited NiPc with Ni, (b) oxidized Ni, (c) NiPc, (d) co-deposited C_{60} with Ni, (e) co-deposited pentacene with Ni, and (f) co-deposited rubrene peroxide with Ni. All films were prepared on n-Si and exposed to air for 10 days.

All the investigated samples were exposed to air for 10 days before the PES investigations. The intensity of the NiO_x band at around 857 eV varies with respect to the intensity of the Ni band depending on the structure of the organic matrix in which the nanoparticles are embedded. For instance it can be derived that in the mixed NiPc+Ni films almost 75 % of Ni is in a oxidized state, *cf.* table 6.1 (a) and figure 6.7 (a). The lowest ratio of NiO_x was found for the oxidized Ni layer, *cf.* table 6.1 (b) and figure 6.7 (b), which could be due to a fast saturation

in the Ni oxidation. In the case of the nanoparticles, however, the surface to volume ratio is very high favouring a stronger oxidation. The lowest ratio of NiO_x was detected for Ni nanoparticles embedded in C₆₀ and the highest ratio for rubrene peroxide as organic matrix, *cf.* table 6.1 (d) and (f) and figure 6.7 (d) and (f), respectively. The low amount of oxidized Ni in C₆₀ should be due to the spherical structure of C₆₀ which can enclose the particles more densely than the other molecules studied. The rubrene peroxide, which is formed from rubrene after exposure to air, is highly disordered after the oxidation process leading to a less densely packed matrix which allows the oxygen to react with nickel. For the planar molecules NiPc and pentacene the concentration of NiO_x lies in between the two extreme cases.

Table 6.1. XPS fit parameters for the Ni 2p core levels. All films were prepared on n-Si and exposed to air for 10 days.

band	E/eV	rel. area	band	E/eV	rel. area
<i>(a) NiPc + Ni</i>			<i>(d) C₆₀ + Ni</i>		
Ni	853.4	1	Ni	853.5	1
Ni ²⁺ in NiPc	856.4	0.36	NiO _x	857.1	1.25
NiO _x	856.8	3.27	multiplet	862.2	0.41
multiplet	862.0	1.07	<i>(e) P + Ni</i>		
multiplet	865.0	0.38	Ni	853.9	1
<i>(b) Ni</i>			NiO _x	856.9	4.29
Ni	853.4	1	multiplet	862.3	2.26
NiO _x	856.8	0.74	<i>(f) RP + Ni</i>		
multiplet	862.0	0.08	Ni	853.8	1
<i>(c) NiPc</i>			NiO _x	856.7	9.81
Ni ²⁺ in NiPc	856.4	1	multiplet	862.5	4.98
multiplet	864.7	0.14			

In figure 6.8 the C 1s core level XPS spectra of the thin films under investigation are shown. Selected fitting parameters are summarized in table 6.2. Depending on the organic matrix the XPS peaks were fitted with a different number of oscillators. Since the spectral resolution is limited to 0.9 eV not all components of the C 1s core level can be fitted separately. To account for that, several atoms with similar chemical shifts were grouped in the same class. For NiPc the C 1s peak was resolved into three components. The obtained binding energies are 284.9 eV for the aromatic carbon of benzene rings, 286.3 eV for the pyrole carbon linked to nitrogen, and 287.9 eV for the shake-up satellites of the pyrole carbon in good agreement with the literature [Petraki07]. The co-deposition of Ni and NiPc induces a shift of the XPS signal of NiPc to higher binding energies. The two main peaks are shifted by around 0.3-0.5 eV. The satellite peak cannot

be resolved since a new peak at 288.8 eV appears which superimposes the satellite peak. Due to its high intensity, the new peak is assumed to arise from partial oxidation of a certain amount of NiPc molecules. This behaviour can be attributed to a partial charge transfer from the NiPc to the oxidized Ni nanoparticles.

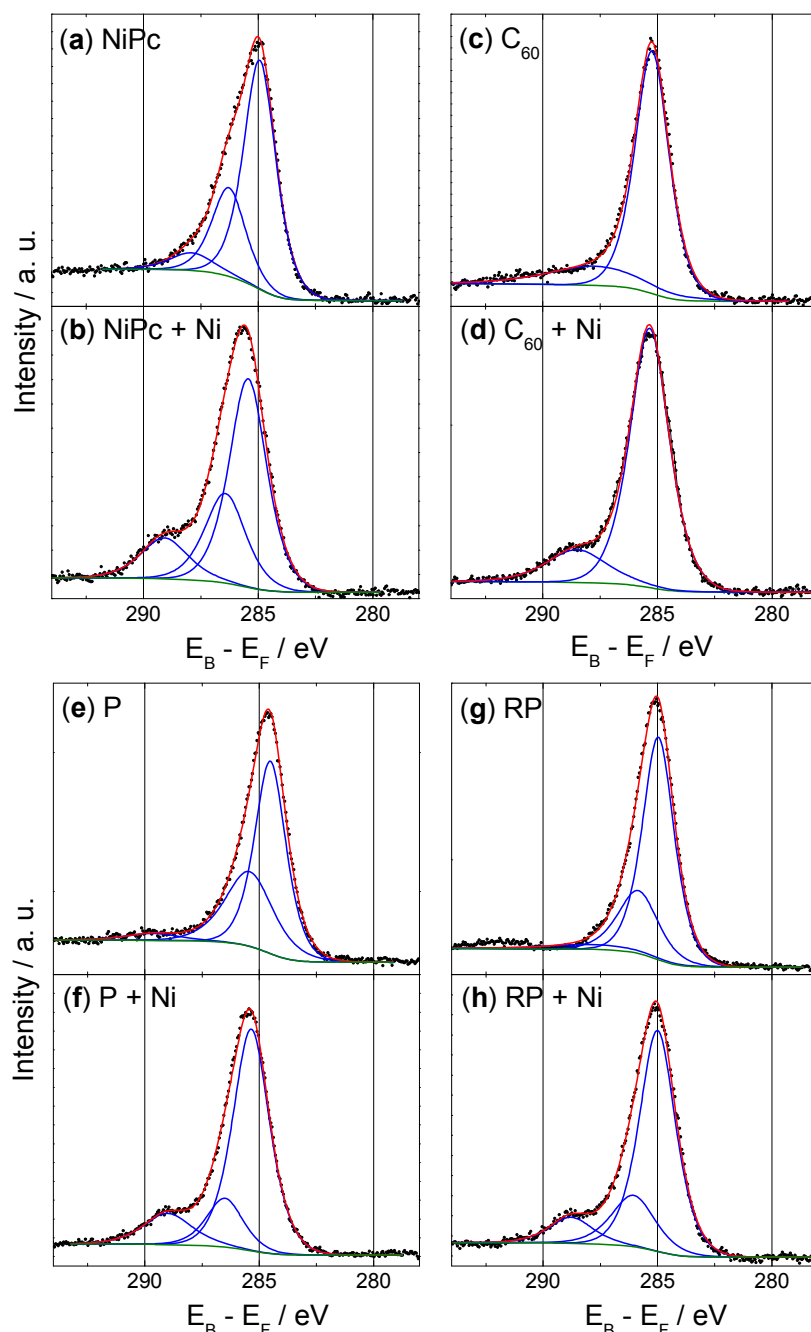


Figure 6.8. XPS spectra of the C 1s core levels of (a) NiPc, (b) co-deposited NiPc with Ni, (c) C₆₀, (d) co-deposited C₆₀ with Ni, (e) P, (f) co-deposited P with Ni, (g) RP, and (h) co-deposited RP with Ni. All films were prepared on n-Si and exposed to air for 10 days.

For C₆₀, the shift of the C 1s peak is much less pronounced than for NiPc. This fact can be explained considering the higher ionisation potential of C₆₀ which

prevents an effective charge transfer from C_{60} to the Ni. However, a part of the C_{60} molecules appears to interact more strongly with the Ni nanoparticles leading to an intense peak at 288.5 eV due to a partial charge transfer from the C_{60} to the oxidized Ni nanoparticles.

Table 6.2. XPS fit parameters for the C 1s core levels shown in figure 6.8. All films were prepared on n-Si and exposed to air for 10 days.

E/eV	rel. area	E/eV	rel. area
<i>a) NiPc</i>		<i>b) NiPc + Ni</i>	
284.9	1	285.4	1
286.3	0.4	286.5	0.4
287.9	0.1	288.8	0.3
<i>c) C₆₀</i>		<i>d) C₆₀ + Ni</i>	
285.2	1	285.3	1
287.7	0.2	288.5	0.2
<i>e) P</i>		<i>f) P + Ni</i>	
284.5	1	285.4	1
285.4	0.5	286.5	0.2
289.6	0.06	289.0	0.2
<i>g) RP</i>		<i>h) RP + Ni</i>	
285.0	1	285.0	1
285.8	0.4	286.0	0.3
287.9	0.1	288.8	0.2

For pentacene the XPS spectrum was fitted using two main peaks and a shake-up satellite peak. Shifts of approximately 1 eV were observed for the main peaks in the mixed compared to the pure pentacene film. In addition, a new peak arises at 289.0 eV in the spectrum of the mixed P+Ni film. Similar results were obtained for RP+Ni, with a new peak at 288.8 eV. The appearance of the new peak around 289 eV might be due to a partial charge transfer from some of the organic molecules to the nanoparticles.

6.4.4 Magnetic susceptibility studies

The magnetization vs. temperature behaviour of a freshly prepared co-deposited NiPc+Ni sample using the zero magnetic field cooled (ZFC) and the magnetic field (5 mT) cooled (FC) procedure is shown in figure 6.9 (a). This measurement method has been demonstrated to be particularly useful for the determination of the T_B in ensembles of nanoparticles [Sappey97]. The magnetisation behaviour is typical for particles with a size of several nanometers. Below the blocking temperature ($T_B = 17$ K) the different behaviour of the ZFC and FC curves indicates a ferromagnetic or blocked behaviour, *i.e.* the freezing of the magnetic moments. This behaviour is often observed in nanoparticle systems when the applied field, here 5 mT, is not enough to

overcome the anisotropy field of the system. Above T_B the nanoparticles behave superparamagnetically. The sharpness of the ZFC peak, *cf.* figure 6.9 (a), reflects according to Poddar *et al.* [Poddar04] the highly monodisperse nature of the Ni nanoparticles embedded in NiPc.

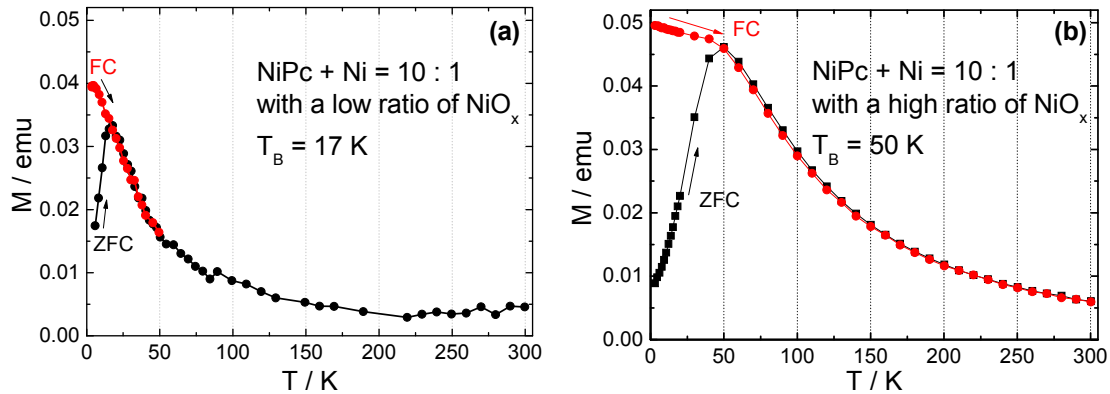


Figure 6.9. Temperature dependence of the magnetization for a ZFC and FC (5 mT) experiment performed on (a) a freshly prepared sample and (b) an air exposed sample of NiPc + Ni.

In figure 6.9 (b) the FC and ZFC magnetization is shown for a co-deposited NiPc+Ni sample which was exposed to air for ten days. The magnetic behaviour deviates significantly from that of the freshly prepared sample in figure 6.9 (a). The blocking temperature shifts from 17 to 50 K in the fresh and the oxidized sample, respectively. At the same time, the ZFC peak becomes broader. Recalling that the amount of NiO_x determined by XPS investigations is 3 to 4 times higher than the amount of Ni in the sample exposed for ten days to air, the different magnetic behaviour of the two samples must be caused by the oxidation of the nanoparticles. The oxidation of the nanoparticles implies the formation of a NiO_x shell with the reduction of the Ni particle volume. The reduction of the Ni volume should lead to a reduction of the blocking temperature with aging, contrary to the experimental observation.

To clarify whether the EB mechanism is responsible for the observed shift to higher blocking temperatures, hysteresis measurements, shown in figure 6.10 (a), were performed at 3 K for the fresh and oxidized NiPc+Ni samples. The coercive field was found to increase with aging from 26 mT to 50 mT, respectively. Defining H_{C+} and H_{C-} as the coercive field with decreasing and increasing applied magnetic fields, respectively, $\Delta H_C = (H_{C+} - H_{C-})/2$ is a measure for the magnitude of the EB effect [Meiklejohn56]. Previously reported

values of ΔH_C in Ni/NiO systems range from 8 mT in Ni/NiO nanowires [Fraune01] to 70 mT in partially oxidized Ni nanoparticles [Yao96]. The hysteresis curves in figure 6.10 (a) show ΔH_C of (2.0 ± 0.5) mT for the freshly prepared, and therefore less oxidized, and (2.5 ± 0.5) mT for the 10 days old sample, respectively. Therefore it can be concluded the EB effect has a rather small influence on the magnetic properties of the nanoparticles discussed herein.

Since the intensity of the NiO_x component in the PES spectra of the nanoparticle is 3 to 4 times higher than that of the metallic component, the increase of the coercive field observed with aging could be due to uncompensated surface spins of the antiferromagnetic NiO_x in the nanoparticles [Makhlouf08]. This hypothesis implies that the larger the amount of the NiO_x in the system, the thicker the NiO_x shell of the particles is and hence the larger the amount of uncompensated spins and the larger the coercive field.

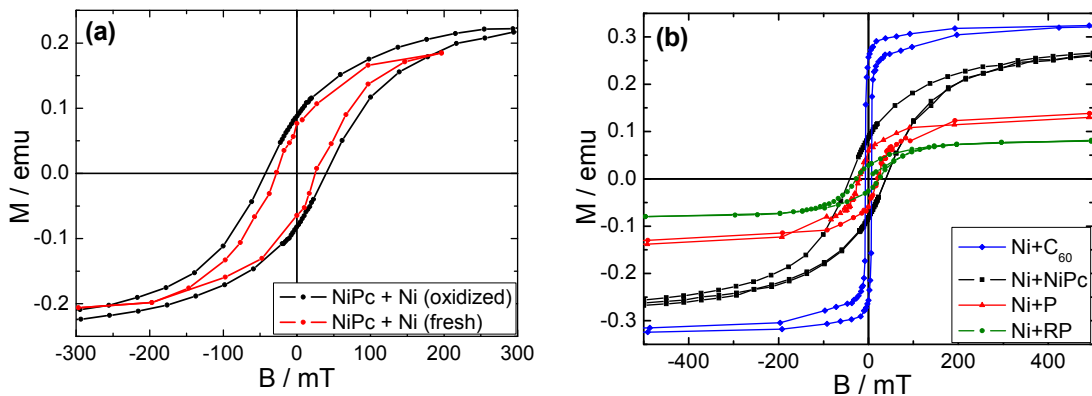


Figure 6.10. Magnetisation versus magnetic field curve at 3 K for (a) freshly prepared and oxidized NiPc+Ni and (b) Ni in different organic matrices.

Indeed this trend is experimentally confirmed when comparing the Ni+C₆₀ and Ni+NiPc systems. In figure 6.10 (b) the hysteresis curves of the Ni nanoparticles are shown. The smallest coercive field was found for Ni+C₆₀ ($B_C = 7$ mT) system which has the smallest concentration of NiO_x . The coercive fields of Ni+NiPc, Ni+P, and Ni+RP systems amount to 40 mT, 20 mT, and 21 mT, respectively. The PES results in section 6.4.3 showed that the NiO_x ratio is higher for the last mentioned systems than for Ni+C₆₀. The coercive fields of Ni+P and Ni+RP are, however, smaller than for Ni+NiPc although the NiO_x ratio is lower in the latter case. This could be due to different particle sizes which can also vary due to diffusion after a certain amount of time.

6.4.5 Magneto-optical studies

In figure 6.11 (a) the Kerr rotation spectra for Ni/organic heterostructures are compared. The samples show a signal which can be clearly measured resulting from inter- and intraband transitions of Ni. Their spectral features are red-shifted compared to the spectrum of the bare Ni film. The lower intensity is probably due to the smaller amount of Ni in the mixed films. The line shape of the MOKE rotation angle spectra in the measured region is similar to that reported by Amekura *et al.* [Amekura04] for Ni nanoparticles in quartz glasses with a zero-crossing point around 4 eV. The similarity in the line shape between the MOKE spectra of Ni nanoparticles in different matrices could indicate similar electronic processes at the interface of the Ni particles with the organic compounds and the quartz glass, respectively. This hypothesis might be supported by the presence of the NiO_x shell around the Ni nanoparticles demonstrated by PES. A second hypothesis would be that the nanoparticles, participating in the Kerr rotation are large enough to feel almost no influence from the electronic processes at the interface.

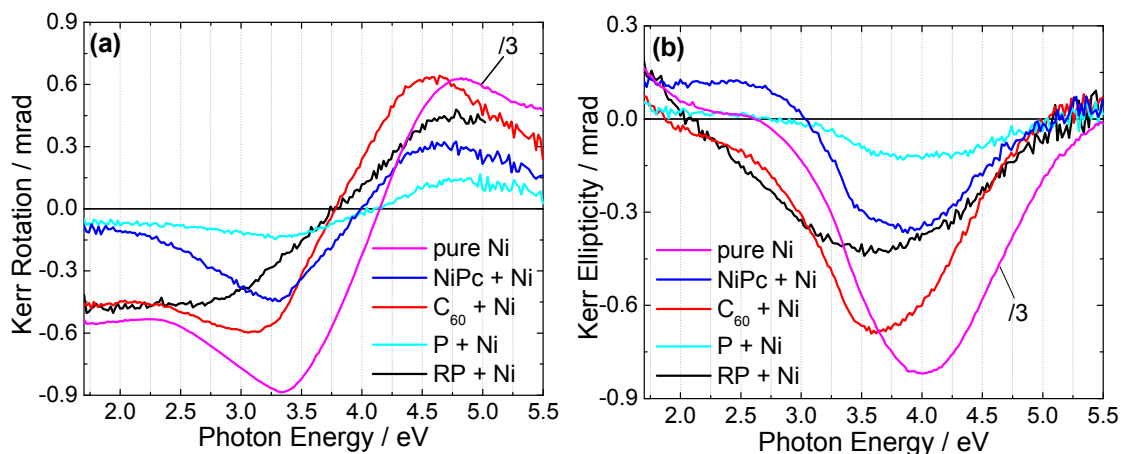


Figure 6.11. (a) Kerr rotation and (b) Kerr ellipticity spectra of Ni/organic heterostructures with a thickness of around 40 nm recorded at RT in a magnetic field of 0.35 T. For reason of comparison the MOKE spectrum of the pure Ni sample was divided by 3.

The differences in the line shape of the Kerr rotation and ellipticity for the different matrices in figure 6.11 are additional indications for the existence of a charge transfer at the interface between Ni and the organic matrices. However, the size of the charge transfer effect cannot be derived in a quantitative way since both the size of the particles and its size distribution contribute to the line shape of the MOKE spectrum. The largest magnitude of the MOKE signal for

the mixed films was observed for the C₆₀+Ni sample which is in agreement with the high magnetization of this sample in comparison to the others, *cf.* figure 6.10.

In comparison to the MOKE spectra of metal free phthalocyanine in section 5.4 the bands are broader for the Ni nanoparticle films. This arises from the fact that discrete optical transitions govern the spectra of molecules while intraband and interband transitions are responsible for the MOKE features of Ni nanoparticles. Possibly, the contribution of the organic matrices to the MOKE spectra leads to a further increase of the broadening.

6.5 Summary and Conclusions

The formation of Ni nanoparticles in several organic matrices produced by co-deposition of the Ni and organic material was demonstrated. When co-evaporated, Ni and H₂Pc react leading to the formation of NiPc and Ni nanoparticles as shown by Raman spectroscopy and PES results.

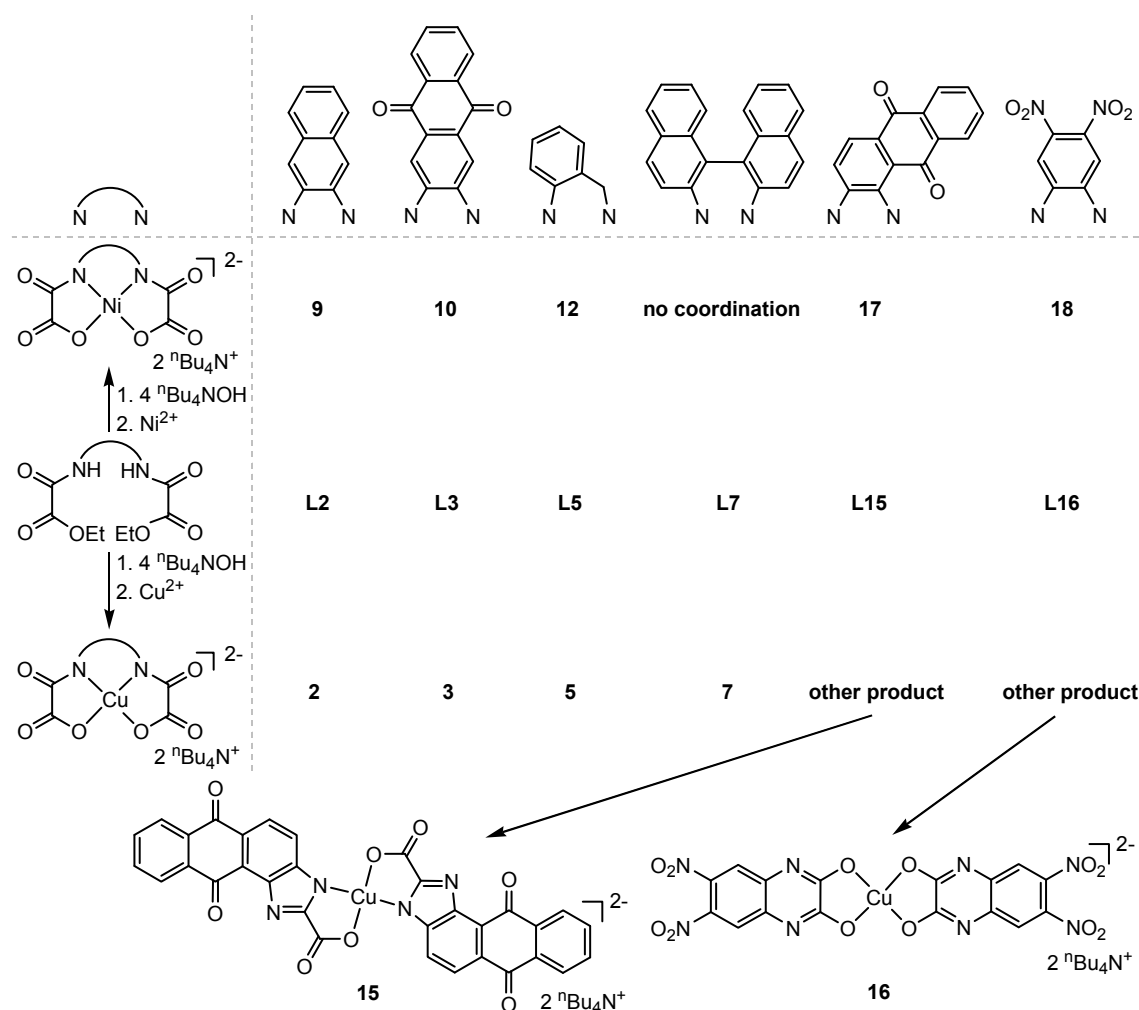
Ni nanoparticles embedded in different organic matrices, grown on Si, were exposed to air for several days. The influence of oxidation was investigated by means of PES. The formation of Ni oxide occurs in all cases but its amount depends strongly on the organic matrix. C₆₀ was found to prevent the nanoparticles from oxygen most effectively. Due to the oxide shell the nanoparticles can accept electrons from the organic matrix. The oxidation of nanoparticles has a strong influence on the magnetic properties leading to higher blocking temperatures and coercive fields.

The magnetization of the less oxidized Ni nanoparticles, *i.e.* C₆₀+Ni, is higher than for the other matrices, as shown by MOKE and SQUID measurements.

7 Summary and Conclusions

Mononuclear Cu(II)- and Ni(II)-*bis*(oxamato) complexes were synthesized and structurally characterized. They were investigated by means of electron paramagnetic resonance (EPR), pulse electron nuclear double resonance (ENDOR), and Raman spectroscopy. The experimental parameters were compared to those predicted by density functional theory (DFT) calculations. The following results were achieved.

- 1 The identity of the synthesized mononuclear Cu(II) and Ni(II) complexes shown in scheme 7.1 was proved by elemental analysis and X-ray crystallography.



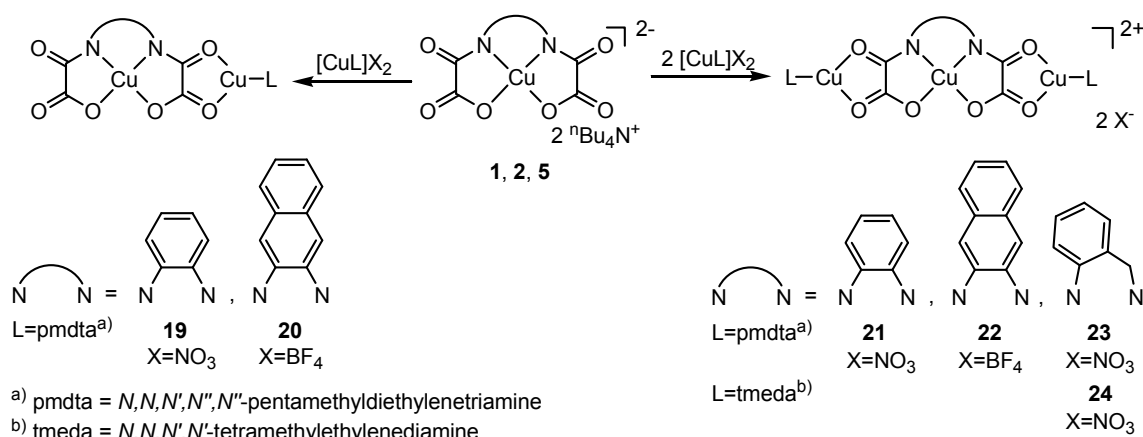
Scheme 7.1. Synthesized mononuclear Ni(II)- and Cu(II)-*bis*(oxamato) complexes.

- 2 Exceptions from the general reaction behaviour, *i.e.* deviations from the $\eta^4(\kappa^2N:\kappa^2O)$ coordination were observed for the reaction of **L7** with a base and a Ni(II) salt. Due to the strong deviation from the square planar coordination geometry of **L7** resulting in a distorted tetrahedral one the chelating effect is too weak for coordinating Ni(II). The treatment of **L15** and **L16** with a base and a transition metal salt leads to the expected product for Ni(II) which is then almost ideal square planar coordinated. In contrast, the addition of a Cu(II) salt leads to the transition metal induced formation of **15** (${}^n\text{Bu}_4\text{N})_2[\text{Cu}(\text{niqo})_2]^{2-}$, niqo = 7,8-dinitro-2,3-quinoxaline-dionato), and **16** (${}^n\text{Bu}_4\text{N})_2[\text{Cu}(\text{aibo})_2]^{2-}$, aibo = anthra[1,2-d]-(imidazole-2-carboxylato)-6,11-dione.
- 3 With **7** the first enantiopure Cu(II)-*bis*(oxamato) complex has been synthesized. Due to the extremely high tetrahedral distortion induced by the *N,N'*-bridge, **7** is a valuable system for bench-marking theoretical studies.
- 4 From the EPR as well as the pulse ENDOR studies for diamagnetically diluted powders of the investigated Cu(II) complexes the *g*, *A*, and *Q* tensor was determined. From these values the distribution of the spin population was derived. The ability to induce various type of structural distortion in the complexes and to determine their EPR parameters allowed the extraction of correlations between the geometry and these parameters. The principal values of the *g* tensor are smaller for the almost ideal square planar compounds, *e.g.* **2** in comparison to the tetrahedral distorted complex **7**, while the opposite case holds for the *A* tensor principal values. This effect arises from the decrease in the energy separation of the electronic levels when going from square-planar to tetrahedral distorted structures. A linear dependence of the spin population on *N* versus the N–Cu–N angle in Cu(II)-*bis*(oxamato) complexes was experimentally shown.
- 5 It was shown that the trends in the EPR parameters can be predicted correctly using DFT with B3LYP, def2-TZVP methods, and the COSMO model.

- 6 A detailed assignment based on DFT calculations of vibrational bands of **1** and **2** was carried out for the Raman and IR spectroscopic investigations.

Di- and trinuclear Cu(II)-*bis*(oxamato) complexes were synthesized and structurally characterized and their magnetic susceptibility was studied as a function of temperature. Thin films of these complexes were prepared by means of spin coating and were analyzed using spectroscopic ellipsometry. The following results were achieved.

- 1 The identity of the synthesized di- and trinuclear Cu(II)-*bis*(oxamato) complexes (**19-24**), shown in scheme 7.2 was proved by elemental analysis and X-ray crystallography.



Scheme 7.2. Di- and trinuclear Cu(II)-*bis*(oxamato) complexes.

- 2 The magnetic superexchange coupling parameters J were determined from the magnetic susceptibility measurements. The interaction between two neighbouring Cu(II) centers was found to be antiferromagnetic, with its strength depending strongly on the coordination geometry of the terminal and the central Cu(II) ions. Quantitative dependencies of the J parameter on the geometry and the spin population on the N atoms were derived. It was shown that packing effects strongly influence the J parameter. DFT calculations of the J -parameter using the broken symmetry approach were found to give reliable predictions of the experimental trends.

- 3 Spin coating was shown to be a promising method for the preparation of several tens of nanometer thick films of **21** and **22** on Si/SiO₂. The optical constants of the films were determined from spectroscopic ellipsometry studies. The assignment of the optical transitions was done by means of time dependent DFT.
- 4 A detailed assignment based on DFT calculations of vibrational bands of **21** and **22** was done for the Raman and IR spectra. Temperature dependent Raman spectroscopy investigations show that the onset of super-exchange interactions at low temperatures does not involve a modification of the structural parameters.

Magneto-optical measurements in reflection were performed for the first time on metal free phthalocyanines (H₂Pc) and spin coated trinuclear Cu(II)-*bis*-(oxamato) complexes. The model for extracting the Voigt constant Q was successfully used for thin films of H₂Pc. The good ordering of the H₂Pc films allowed showing that Q depends strongly on the tilt angle of the H₂Pc with respect to the substrate and can thus be used as a valuable parameter for precise measurements of the molecular orientation on surfaces.

Recording a magneto-optical Kerr effect signal from a spin coated film of a trinuclear Cu(II)-*bis*(oxamato) complex can already be seen as an important starting step in magneto-optical investigations of such complexes on opaque substrates. The signal intensity at room temperature and in the range of magnetic fields available during this work was, however, very small. Following strategies can be applied in the future to increase the magneto-optical response in the polar reflection geometry:

- 1 Applying high magnetic fields.
- 2 Performing the experiments at low temperatures.
- 3 Compounds that exhibit a high magnetization.
- 4 Using molecules with strongly absorbing functional groups.
- 5 Forcing the molecules to orient parallel with their optical transition dipole moment to the substrate.
- 6 Transition metal complexes with a high solubility in polar solvents which is a prerequisite for a higher homogeneity of spin coated films.

Besides the investigations on transition metal complexes, an important issue of this work was to understand the formation of transition metal nanoparticles embedded in organic matrices, when prepared by the co-deposition of various organic molecules and the transition metal. These studies were performed on the example of Ni co-deposited with either diamagnetic or paramagnetic molecules. The following results were achieved.

- 1 The co-deposition of Ni and H₂Pc leads to the formation of NiPc.
- 2 Exposed to air for several days the Ni nanoparticles were oxidized and the amount of the formed NiO_x depends strongly on the organic matrix. C₆₀ was found to prevent the oxidation of the Ni nanoparticles in the best way.
- 3 An electron transfer from the organic matrix to the oxide shell of the nanoparticles was detected by means of photoelectron spectroscopy.
- 4 The oxidation of the nanoparticles has a strong influence on the magnetic properties leading to higher blocking temperatures and coercive fields.
- 5 Magneto-optical measurements show that the magnetization of the less oxidized Ni nanoparticles, *i.e.* Ni nanoparticles embedded in C₆₀, is higher than for the other materials.

Appendix

Appendix of chapter 2

Experimental

All starting chemicals and solvents were purchased from commercial sources. For crystallisation, the powdered substances were dissolved in $\text{CH}_2\text{Cl}_2:\text{MeCN}$ (1:1) and crystallized under aerobic conditions in closed systems by slow condensation of Et_2O . The diamines 4,5-Dinitro-*o*-phenylenediamine and 2,3-Diaminoanthrachinone were prepared according to published procedures [Kleineweischede06] and [Scholl04], respectively. Elemental analyses for C, H and N were performed on a Thermo FlashEA 1112 series Elemental Analyzer. FT-IR spectra were recorded in the range of $400 - 4000 \text{ cm}^{-1}$ on Perkin-Elmer Spectrum 1000 FT-IR spectrophotometer from the materials embedded in KBr pellets. NMR spectra were recorded at room temperature with a Bruker Avance 250 spectrometer (^1H at 250.130 MHz and $^{13}\text{C}\{^1\text{H}\}$ at 62.86 MHz) in the Fourier transform mode. Chemical shifts are reported in δ (ppm) vs. SiMe_4 with the solvent as the reference signal ($[\text{D}_6]\text{-DMSO}$: ^1H NMR, $\delta = 2.54$; and $^{13}\text{C}\{^1\text{H}\}$ NMR, $\delta = 40.45$). The numbering schemes for the NMR signal assignments for the compounds under investigation are given in figure 2.a1.

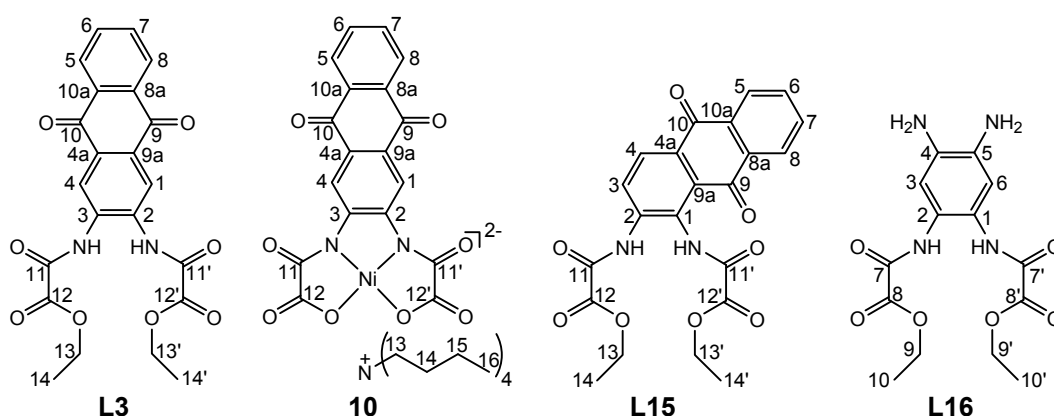


Figure 2.a1. The atomic numbering scheme for L3, 10, L15, and L16.

Synthesis of mononuclear Cu(II)- and Ni(II)-bis(oxamato) complexes

Synthesis of 2,3-naboH₂Et₂ (L2): To a solution of 2,3-diaminonaphthalene (1.5 g, 9.49 mmol) in THF (50 ml), ethyloxalyl chloride (2.59 g, 19 mmol) was

added drop-wise via a dropping funnel within 20 min. The resulting mixture was refluxed for 30 min, filtrated and concentrated to about one third on a rotary evaporator. The careful addition of water resulted in the precipitation of a solid which was filtered off and washed with water to give a grey powder. According to elemental analysis and NMR measurements, this solid was sufficiently pure **L2**. Yield: 2.3 g (68 %). Anal. Calc. for $C_{18}H_{18}N_2O_6$ (358.36 g/mol): C 60.33, H 5.06, N 7.82; found: C 60.61, H 4.98, N 7.72 %. 1H NMR ($[D_6]$ -acetone): δ = 1.43 (t, 6H, CH_3), 4.42 (q, 4H, CH_2), 7.57/7.96/8.34 (dd/dd/s, 2H/2H/2H, aromatic H), 10.14 (s, 2H, NH).

Synthesis of $(nBu_4N)_2[M(nabo)]$ M = Ni (9**), Cu (**2**):** To a solution of **L2** (3.60 g, 10 mmol) in an ethanol/water mixture (1:1, 100 mL) $(nBu_4N)OH$ (26.2 g, 40 mmol, 40% in H_2O) was added. The resulting mixture was refluxed under stirring for 30 min. After cooling to room temperature, aqueous solutions (50 mL) of $[Ni(H_2O)_6]Cl_2$ (2.38 g, 10 mmol) and $[Cu(NO_3)_2(H_2O)_3]$ (2.40 g, 10 mmol), respectively, were then added drop-wise under stirring. The obtained solutions were extracted with CH_2Cl_2 ($3 \cdot 100$ mL) and the combined organic phases were washed with H_2O ($3 \cdot 200$ mL). The organic phases were dried with Na_2SO_4 , concentrated to approximately 25 mL. **9** and **2** were then precipitated by addition of Et_2O (200 mL). The obtained orange **9** and purple **2** solids were then filtered off, washed with Et_2O , and dried in air. Crystals of **9** and **2**, suitable for X-ray crystallography, were obtained from CH_2Cl_2 solutions by slow condensation of Et_2O . Yields: **9** (5.72 g, 68%), **2** (6.26 g, 74%). Anal. calc. for $C_{46}H_{78}N_4O_6Ni$ (**9**, 841.83 g/mol): C 65.63, H 9.34, N 6.66; found: C 65.48, H 9.22, N 6.53 %. Anal. calc. for $C_{46}H_{78}N_4O_6Cu$ (**2**, 846.66 g/mol): C 65.26, H 9.29, N 6.62; found: C 65.16, H 9.18, N 6.53 %.

Synthesis of 2,3-acboH₂Et₂ (L3**):** In THF (30 mL) 2,3-Diaminoanthrachinone (476 mg, 2 mmol) and NEt_3 (445 mg, 4.4 mmol) to be used as an acid scavenger were dissolved under stirring. After five minutes ethoxyalylchloride (613 mg, 0.51 mL, 98 %, 4.4 mmol) in THF (20 mL) was added drop-wise. The suspension was refluxed for 30 minutes. The resulting mixture was then filtered and concentrated to about one third on a rotary evaporator. After addition of Et_2O (100 mL) **L3** precipitated as a brown powder. Yield: 526 mg (60 %). Anal.

calc. for $C_{22}H_{18}N_2O_8$ (438.2 g/mol): C 60.27, H 4.15, N 6.39; found: C 60.50, H 4.05, N 6.43 %. 1H NMR: δ = 1.32 (s, 6H, $H^{14,14'}$), 4.32 (s, 4H, $H^{13,13'}$), 7.91 (dd, 2H, $H^{6,7}$), 8.17 (dd, 2H, $H^{5,8}$), 8.43 (s, 2H, $H^{1,4}$), 10.76 (s, 2H, NH). $^{13}C\{^1H\}$ NMR: δ = 14.1 ($C^{14,14'}$), 63.0 ($C^{13,13'}$), 123.7 ($C^{1,4}$), 126.9 ($C^{5,8}$), 130.7 ($C^{4a,9a}$), 133.2 ($C^{8a,10a}$), 134.7 ($C^{2,3,6,7}$), 156.1 ($C^{11,11'}$), 159.9 ($C^{12,12'}$), 181.6 ($C^{9,10}$). The atomic numbering scheme for **L3** is given in figure 2.a1.

Synthesis of (nBu_4N) $_2$ [M(2,3-acbo)] for M = Ni (10**), Cu (**3**):** **10** and **3** were synthesized in analogy to the procedure described for $[Cu(opba)]^{2-}$ [Stumpf93]. To a suspension of **L3** (250 mg, 0.57 mmol) in water/ethanol (150 mL, 1:1) nBu_4NOH (1.49 g of a 40 % aqueous solution, 2.3 mmol) was added drop-wise and stirred for 20 min at 60 °C resulting in an orange/brown solution. After cooling to room temperature aqueous solutions (50 mL) of $[Ni(H_2O)_6]Cl_2$ (0.14 g, 0.57 mmol) and $[Cu(NO_3)_2(H_2O)_3]$ (0.1 g, 0.57 mmol), respectively, were then added drop-wise under stirring. The obtained solutions were then extracted with CH_2Cl_2 (3 \times 50 mL), concentrated to 30 mL and dried with Na_2SO_4 . After filtration the solutions were further concentrated to 5 mL and were then precipitated by addition of Et_2O (200 mL). The obtained dark red (**3**) and red-brown (**10**) solids were then filtered off, washed with Et_2O , and dried on air. Yield **10**: 284 mg, 54 %; Yield **3**: 338 mg (64 %). Anal. calc. for $NiC_{50}H_{78}N_4O_8$ (**10**) (921.9 g/mol): C 64.79, H 8.55, N 6.05; found: C 64.25, H 8.38, N 6.01 %. IR (in cm^{-1}): 1638s, 1657s, 1673s. 1H NMR: δ = 1.00 (t, 12H, H^{16}), 1.36 (m, 8H, H^{15}), 1.6 (t, 8H, H^{14}), 3.2 (t, 8H, H^{13}), 8.14 (dd, 2H, $H^{6,7}$), 7.86 (2H, $H^{5,8}$), 8.55 (s, 2H, $H^{1,4}$). $^{13}C\{^1H\}$ NMR: δ = 14.4 (C^{16}), 20.1 (C^{15}), 24.0 (C^{14}), 58.5 (C^{13}), 116.4 ($C^{1,4}$), 127.2 ($C^{5,8}$), 128.4 ($C^{4a,9a}$), 134.3 ($C^{6,7}$), 134.7 ($C^{8a,10a}$), 149.2 ($C^{2,3}$), 163.0/169.5 ($C^{12,12'}/C^{11,11'}$), 182.9 ($C^{9,10}$). The atomic numbering scheme for **10** is given in figure 2.a1. Anal. calc. for $CuC_{50}H_{78}N_4O_8$ (**3**) (926.8 g/mol): C 64.79, H 8.50, N 6.05; found C 64.09, H 8.47, N 5.80 %. IR (ν_{CO} / cm^{-1}): 1630s, 1654s, 1678s.

Synthesis of obboH $_2$ Et $_2$ (L5**):** To a solution of 2-aminobenzylamine (1.5 g, 12.03 mmol) in THF (50 mL), ethyloxalyl chloride (3.35 g, 24.06 mmol) was added drop-wise via a dropping funnel within 20 min. The resulting mixture was refluxed for 30 min, filtrated and concentrated to about one third on a rotary

evaporator. The careful addition of water resulted in the precipitation of a solid, which was filtered off and washed with water to give a grey powder. According to elemental analysis and NMR measurements, this solid was sufficiently pure **L5**. Yield: 2.57 g (65%). Anal. calc. for $C_{15}H_{18}N_2O_6$ (322.32 g/mol) (**L5**): C 55.90, H 5.63, N 8.69; found: C 55.71, H, 5.75, N 8.49 %. 1H NMR: δ = 1.31/1.37 (t/t, 3H/3H, OCH_2CH_3 / OCH_2CH_3), 4.25/4.35 (q/q, 4H/4H, OCH_2CH_3 / OCH_2CH_3), 4.34 (d, 2H, $NHCH_2$), 7.35 (m, 4H, C_6H_4), 9.48 (t, $NHCH_2$), 10.67 (s, 1H, NH).

Synthesis of $(^nBu_4N)_2[M(obbo)]$ for M = Ni (12**), Cu (**5**):** To a solution of **L5** (3.22 g, 10 mmol) in an ethanol/water mixture (1:1, 100 mL) (nBu_4N)OH (25.9 g, 40 mmol, 40 % in H_2O) was added. The resulting mixture was refluxed under stirring for 30 min. After cooling to room temperature, an aqueous solution (50 mL) of $[Ni(H_2O)_6]Cl_2$ (2.38 g, 10 mmol) and $[Cu(NO_3)_2(H_2O)_3]$ (2.40 g, 10 mmol), respectively, were then added drop-wise under stirring. The obtained solution was then extracted with CH_2Cl_2 (3 · 100 mL) and the combined organic phases were washed with H_2O (3 · 200 mL). After drying with Na_2SO_4 and concentrating to approximately 25 mL, **12** and **5** was precipitated by the addition of Et_2O (200 mL). The obtained purple (**5**) and brown (**12**) solid was filtered off, washed with Et_2O , and air-dried. Yield: 4.45 g, 55%. Anal. calc. $C_{43}H_{78}N_4O_6Cu$ (**5**, 810.65 g/mol): C 63.71, H 9.70, N 6.91; found: C 63.66, H 9.52, N 6.73 %. $C_{43}H_{78}N_4O_6Ni$ (**5**, 805.8 g/mol), C 64.09, H 9.78, N 6.95; found: C 63.86, H 9.57, N 6.68 %.

Synthesis of $R\text{-}bnboH_2Et_2$ (L5**):** (R)-(+)-2,2'-diamino-1,1'-binaphthalene (284 mg, 1 mmol) was dissolved in THF (100 ml) under stirring. After five minutes ethoxyalychloride (278 mg, 98 %, 2 mmol) in THF (50 ml) was added drop-wise. The suspension was refluxed for 60 minutes. The resulting mixture was then filtrated and concentrated. The remaining oil was dissolved in CH_2Cl_2 (5 ml). After addition of hexane/ Et_2O (4:1, 100 ml) **L5** was precipitated as a white powder. Yield: 360 mg, 74 %. Anal. calc. for $C_{28}H_{24}N_2O_6$ (484,5 g/mol): C 69.40, H 5.00, N 5.78; found C 69.71, H 5.01, N 5.81. 1H -NMR: δ = 1.13 (t, 6H, CH_2CH_3), 4.08 (q, 4H, CH_2CH_3), 7.20/7.35/7.51/8.11/8.28/8.64 (m, 12 H, arom. H), 9.17 (s, 2H, NH).

Synthesis of $(^n\text{Bu}_4\text{N})_2[\text{Cu}(\text{R-bnbo})]\cdot 2\text{H}_2\text{O}$ (7**):** To a solution of **L7** (241 mg, 0.5 mmol) in MeOH (60 mL) $(^n\text{Bu}_4\text{N})\text{OH}$ (1.31 g of a 40 % solution in MeOH, 2 mmol) was added. After 20 minutes of stirring a solution of $[\text{CuCl}_2(\text{H}_2\text{O})_2]$ (85 mg, 0.5 mmol) in MeOH (10 mL) was added drop-wise. The resulting mixture was stirred for 120 minutes and afterwards the solvent was completely evaporated. The residue was solved in H_2O (100 mL) and extracted in CH_2Cl_2 (3 x 50 mL). The organic phase was dried with Na_2SO_4 and then the solvent was evaporated. The obtained green solid was then dried in air. Suitable crystals of **7** for X-ray crystallography were obtained from CH_2Cl_2 solutions by slow condensation of Et_2O . Yield: 235 mg (48 %) of **7**. Anal. calc. for $\text{CuC}_{56}\text{H}_{84}\text{N}_4\text{O}_6\cdot 2\text{H}_2\text{O}$ (991.0 g/mol): C 67.73, H 8.95, N 5.64; found C 67.77, H 9.01, N 5.37.

Synthesis of 1,2-acboH₂Et₂ (L15**):** In THF (100 mL) 1,2-diaminoanthrachinone (4.76 g, 20 mmol) was dissolved under stirring. After five minutes ethoxyalylchloride (613 mg, 0.5 mL, 98 %, 4.4 mmol) in THF (20 mL) was added drop-wise. The suspension was refluxed for 30 minutes. The resulting mixture was then filtered and concentrated to about one third on a rotary evaporator. After addition of Et_2O (200 mL) **L15** was precipitated as a yellow powder. Yield: 5.26 mg, 60 %. Anal. calc. for $\text{C}_{22}\text{H}_{18}\text{N}_2\text{O}_8$ (438,2 g/mol): C 60.27, H 4.15, N 6.39; Found C 60.01, H 4.33, N 6.22 %. ^1H NMR: $\delta = 1.36/1.41$ (s, 6H, $\text{H}^{14,14'}$), 4.32/4.42 (s, 4H, $\text{H}^{14,14'}$), 7.95/7.96 (m, 2H, $\text{H}^{6,7}$), 8.17/8.19 (m, 2H, $\text{H}^{5,8}$), 8.32 (m, 2H, $\text{H}^{3,4}$), 10.38/11.32 (s, 1H/1H, NH). The atomic numbering scheme for **L15** is given in figure 2.a1.

Synthesis of $(^n\text{Bu}_4\text{N})_2[\text{Cu}(\text{aibo})_2]$ (15**):** To a suspension of **L15** (250 mg, 0.57 mmol) in methanol (150 mL) $(^n\text{Bu}_4\text{N})\text{OH}$ (1.49 g of a 40 % methanol solution, 2.3 mmol) was added and then stirred for 20 min at 25 °C. $[\text{CuCl}_2(\text{H}_2\text{O})_2]$ (0.05 g, 0.28 mmol), dissolved in methanol (50 mL), was added drop-wise and then stirred for 20 minutes at 25 °C. The dark red suspension was filtered, the filtrate was concentrated to 20 mL, and Et_2O was added. After filtration and crystallisation in methanol the dark brown solid **15** was obtained. Yield: 286 mg (25 %). Anal. calc. for $\text{CuC}_{64}\text{H}_{84}\text{N}_6\text{O}_8$ (1129,1 g/mol), C 68.08, H 7.51, N 7.44; found: C 68.28, H 7.31, N 7.29 %.

In the case of **15** very tiny needles with dimensions of $0.15 \times 0.02 \times 0.02$ mm suitable for single-crystal X-ray measurements were used at measurement temperatures of 100 K. After measurement times of approximately two days, the mounted crystals were broken into pieces during the measurement with the remaining part connected to the fiber loop used for fixing. Due to repeated measurements data could be collected to a completeness of 89.2 % up to $\theta = 63.95^\circ$. All non-hydrogen atoms could be refined anisotropically and no unrefined electron density remains (max./min. electron density = $2.141/-0.556$ eÅ⁻³), although final *R* values ($R_1 = 0.1409$, $wR_2 = 0.3951$) exceed acceptable limits, most probably due to the low completeness. Therefore, bond lengths and angles cannot be discussed here. The identity of **15** and the chemical connectivity is, however, verified without doubt by X-ray measurements.

Synthesis of (ⁿBu₄N)₂[Ni(1,2-acbo)] (17): To a suspension of **L15** (250 mg, 0.57 mmol) in methanol (150 mL) (ⁿBu₄N)OH (1.49 g of a 40 % methanol solution, 2.3 mmol) was added. After further stirring for 20 min at 25 °C [Ni(H₂O)₆]Cl₂ (0.14 g, 0.57 mmol), solved in methanol (50 mL), was added drop-wise. The dark brown suspension was concentrated to 20 mL, Et₂O (200 mL) was added, and filtered off. The obtained brown powder was recrystallised from methanol and identified as **17**. Yield: 286 mg (54 %). Anal. calc. for NiC₅₀H₇₈N₄O₈ (921.9 g/mol): C 65.14, H 8.55, N 6.08; Found C 65.40, H 8.27, N 6.18 %.

Synthesis of niboH₂Et₂ (L16): To a solution of 4,5-dinitro-o-phenylenediamine (2.0 g, 10 mmol) in THF (50 mL) ethyloxalyl chloride (2.81 g, 2.31 mL, 98 %, 20 mmol) in THF (100 mL) was added drop-wise within 20 min. The resulting mixture was refluxed for 30 min, filtrated and concentrated to 50 mL on a rotary evaporator. After addition of Et₂O (200 mL) **L16** was precipitated as a grey yellow powder. Yield: 3 g (75%). Anal. calc. for C₁₄H₁₄N₄O₁₀ (398.28 g/mol): C 42.22, H 3.54, N 14.07; Found: C 42.24, H 3.17, N 14.69 %. ¹H NMR: δ = 1.37 (t, 6H, H^{10,10'}), 4.39 (q, 4H, H^{9,9'}), 8.51 (s, 2H, H^{3,6}), 11.00 (s, 2H, NH). The atomic numbering scheme for **L16** is given in figure 2.a1.

Synthesis of (ⁿBu₄N)₂[Cu(niqo)] (16): To a solution of **L16** (0.4 g, 1 mmol) in methanol (50 mL) was added a solution of (ⁿBu₄N)OH (2.61 g of 40 % methanol solution, 4 mmol) in methanol (25 mL). The resulting mixture was refluxed under stirring for 30 min. After cooling to room temperature [CuCl₂(H₂O)₂] (89 mg, 0.5 mmol) dissolved in methanol was added drop-wise under stirring. The obtained solution was then extracted with CH₂Cl₂ (100 mL) and washed with H₂O (3 × 25 mL). After drying with Na₂SO₄, filtering and concentrating to approximately 25 mL, **16** was precipitated by the addition of Et₂O (200 mL). The obtained brown-black solid was filtered off, washed with Et₂O, and air-dried. Yield: (0.4 g, 38 %). Anal. calc. for CuC₄₈H₇₆N₁₀O₁₂ (1048.32 g/mol): C 54.95, H 7.32, N 13.35; found: C 54.66, H 7.09, N 13.58 %.

Synthesis of (ⁿBu₄N)₂[Ni(nibo)] (18): To a solution of **L16** (0.4 g, 1 mmol) in ethanol (50 mL) (ⁿBu₄N)OH (2.61 g of a 40 % aqueous solution, 4 mmol) in H₂O (25 mL) was added. The resulting mixture was refluxed under stirring for 30 min. After cooling to room temperature an aqueous solution (25 mL) of [Ni(H₂O)₆](Cl)₂ (0.24 g, 1 mmol) was added drop-wise under stirring. The obtained solution was then extracted with CH₂Cl₂ (100 mL) and washed with H₂O (3 × 25 mL). After drying with Na₂SO₄, filtering, and concentrating to approximately 25 mL, **18** was precipitated by the addition of Et₂O (200 mL). The obtained brown-black solid was filtered off, washed with Et₂O, air-dried, and identified as **18**. Yield: (0.6 g, 66 %). Anal. calc. for NiC₄₂H₇₄N₆O₁₀ (881.80 g/mol): C 57.20, H 8.48, N 9.53; found: C 57.43, H 8.49, N 8.68 %.

Synthesis of dinuclear Cu(II)-bis(oxamato) complexes

Synthesis of [Cu₂(opba)(pmdta)(MeOH)]·½MeOH·dmf (19) and [Cu₂(nabo)-(pmdta)(MeOH)] (20): To a solution of **1** (100 mg, 0.126 mmol) or **2** (106.7 mg, 0.126 mmol), respectively, in MeCN (30 mL) was added a solution of [Cu(pmdta)(NO₃)₂] (45.5 mg, 0.126 mmol) in MeCN (30 mL) drop-wise under stirring within one hour. After stirring for additional two hours, the resulting reaction mixtures were concentrated to approximately 10 mL and Et₂O (100 mL) was added to give green precipitates. The overlaying solvent mixture was removed and dmf (5 mL) was added to resolve the green precipitates. Thf (10 mL) and Et₂O (100 mL) were then successively added to precipitate green

powders which were washed three times with Et₂O (3 x 30 mL). After removal of the supernatant the remaining solids were dried in vacuum (10⁻¹ mbar) resulting in the formation of green powders. As proved by elemental analysis, the obtained green powders were in no case analytically pure [Cu₂(opba)(pmdta)] or [Cu₂(nabo)(pmdta)], respectively, or any definite solvate of it. From dmf:MeOH (1:1, **19**) or dmf:MeOH (4:1, **20**) solvent mixtures of the respected green powders, **19** and **20**, respectively, were crystallized in form of crystals suitable for X-ray crystallography studies by slow diffusion of Et₂O. Yield of **19**: ca. 80 mg (ca. 95 %). Anal. calc. for C_{23.50}H₄₀Cu₂N₆O_{8.50} (669.70 g/mol): C 42.15, H 6.02, N 12.55; found: C 41.87, H 5.77, N 12.28 %. Yield of **20**: ca. 75 mg (ca. 95 %). Anal. calc. for C₂₄H₃₃Cu₂N₅O₇ (630.63 g/mol): C 45.71, H 5.27, N 11.11; found: C 45.77, H 5.15, N 11.07.

Synthesis of trinuclear Cu(II)-bis(oxamato) complexes

Synthesis of [Cu₃(opba)(pmdta)₂(NO₃)](NO₃)·2CH₃CN (21**):** To a solution of **1** (1.59 g, 1.88 mmol) in MeCN (50 mL) was added a solution of [Cu(pmdta)(NO₃)₂] (1.36 g, 3.77 mmol) in MeCN (25 mL) drop-wise under stirring within one hour. After stirring for additional two hours, the resulting reaction mixture was concentrated to approximately 5 mL and Et₂O (100 mL) was added to give a blue precipitate. The overlaying solvent mixture was removed and MeCN (5 mL) was added to resolve the blue precipitate. Again Et₂O (100 mL) was added to precipitate a blue powder. After removal of the supernatant the remaining solid was dried in vacuum (10⁻¹ mbar). From a MeCN solution of the blue powder, complex **19** was isolated in form of crystals suitable for X-ray crystallography by slow diffusion of Et₂O. Yield: 1.12 g (30 %). C₃₂H₅₆Cu₃N₁₂O₁₂ (991.51 g/mol). Anal. calc. for C 38.76, H 5.70, N 16.95; found C 38.49, H 5.52, N 16.71.

Synthesis of [Cu₃(1,2-nabo)(pmdta)₂(BF₄)](BF₄)·MeCN·Et₂O (22**):** To a solution of **2** (1.68 g, 2 mmol) in MeCN (50 mL) was added a solution of [Cu(pmdta)(BF₄)₄] (1.64 g, 4 mmol) in MeCN (25 mL) drop-wise under stirring within one hour. After stirring for additional two hours, the resulting reaction mixture was concentrated to approximately 5 mL and Et₂O (100 mL) was added to give a blue precipitate. The overlaying solvent mixture was removed and

MeCN (5 mL) was added to resolve the blue precipitate. Again Et₂O (100 mL) was added to precipitate a blue powder. After removal of the supernatant the remaining solid was dried in vacuum (10⁻¹ mbar). From a MeCN solution of the blue powder, complex **22** was isolated in form of crystals suitable for X-ray crystallography by slow diffusion of Et₂O. Yield: 0.92 g (41 %). Anal. calc. for C₃₂H₅₆B₂Cu₃F₈N₉O₇ (1124.23 g/mol): C 34.19, H 5.02, N 11.22; found C 33.91, H 4.83, N 10.95.

Synthesis of [Cu₃(obbo)(pmdta)₂](NO₃)₂ (23): To a solution of **5** (1.22 g, 1.50 mmol) in MeCN (50 mL) was added a solution of [Cu(pmdta)(NO₃)₂] (1.08 g, 3.00 mmol) in MeCN (25 mL) drop-wise under stirring within one h. After stirring for additional two h, the resulting reaction mixture was concentrated to approximately 5 mL and Et₂O (100 mL) was added to give a blue precipitate. The overlaying solvent mixture was removed and MeCN (5 mL) was added to resolve the blue precipitate. Again Et₂O (100 mL) was added to precipitate a blue powder. After removal of the supernatant the remaining solid was dried in vacuum (10⁻¹ mbar). The solid was determined by elemental analysis to be pure **23**. Yield: 0.48 g, 35%. Anal. calc. for C₂₉H₅₂Cu₃N₁₀O₁₂ (923.44 g/mol): C 37.72, H 5.68, N 15.17; found: C 37.49, H 5.72, N 15.01 %. From a CH₂Cl₂ solution of the blue powder using non-dried CH₂Cl₂, **23** was crystallized in the form of crystals suitable for X-ray crystallography studies by slow diffusion of Et₂O.

Synthesis of [Cu₃(obbo)(tmeda)₂](NO₃)₂ (24): To a solution of **5** (1.62 g, 2.0 mmol) in MeCN (50 mL) was added a solution of [Cu(tmeda)(NO₃)₂] (1.10 g, 4 mmol) in MeCN (25 mL) drop-wise under stirring within 1 h. After stirring for additional 2 h, the resulting reaction mixture was concentrated to approximately 5 mL and Et₂O (100 mL) was added to give a blue precipitate. The overlaying solvent mixture was removed and MeCN (5 mL) was added to resolve the blue precipitate. Again Et₂O (100 mL) was added to precipitate a blue powder. After removal of the supernatant the remaining solid was dried in vacuum (10⁻¹ mbar). The solid was proofed by elemental analysis to be pure **24**. Yield: 0.70 g, 43 %. Anal. calc. for C₂₃H₃₈Cu₃N₈O₁₂ (809.25 g/mol): C 34.14, H 4.73, N 13.85; found: C 33.94, H 4.85, N 13.65 %. From a MeCN/dmf (4:1) solution of the blue

powder, **24** was isolated in the form of crystals suitable for X-ray crystallography by slow diffusion of Et₂O.

Table 2.a1. Crystallographic data.

Complex	3	7·2H₂O	L7	10
Formula	C ₅₀ H ₇₈ CuN ₄ O ₈	C ₅₆ H ₈₈ N ₄ O ₈ Cu	C ₅₇ H ₅₀ Cl ₂ N ₄ O ₁₂	C ₅₀ H ₇₈ NiN ₄ O ₈
M / g mol ⁻¹	926.70	1008.84	526.96	921.87
Crystal system	Monoclinic	tetragonal	monoclinic	Monoclinic
Space group	C2/c	P4 ₁ 2 ₁ 2	P2 ₁	C2/c
a / Å	20.0668(9)	12.0818(4)	10.9379(5)	19.751(9)
b / Å	17.5601(8)	12.0818(4)	17.0703(11)	17.612(8)
c / Å	14.2159(7)	37.624(2)	14.0946(9)	14.656(6)
α / °	90.0	90.00	90.00	90.0
β / °	94.3730(10)	90.00	99.366(4)	94.174(9)
γ / °	90.0	90.00	90.00	90.0
V / Å ³	4994.7(4)	5492.0(4)	2596.6(3)Å ₃	5085(4)
Z	4	4	2	4
Temperature / K	298	100	100	298
Radiation, λ / Å	Mo-K _α , 0.71073	Mo-K _α , 0.71073	Mo-K _α , 0.71073	Mo-K _α , 0.71073
ρ _{calcd} / g cm ⁻³	1.232	1.220	1.348 g/cm ₃	1.204
μ / mm ⁻¹	0.492	0.453	0.453	0.435
Reflect. measured	22131	30601	30565	13492
Independent reflect.	4921	4987	8549	4462
R _{int}	0.0319	0.0437	0.0417	0.0407
Parameters	285	312	319	285
scan range / °	1.54 - 26.00	1.54 - 26.00	1.54 - 52.12	1.55 - 25.19
Compl. to θ _{max} / %	100.0	99.8	99.7	97.5
Flack x _[Flack83]	-	-0.045(17)	-	-
R (F, F ² > 2σ)	0.0343	0.0437	0.0296	0.0711
R _w (F ² , all data)	0.0885	0.0711	0.0411	0.1855
Goodness of fit F ²	1.080	0.900	0.980	1.091
Max., min. electron	0.304, -0.459	0.518, -0.317	0.224, -0.263	0.504, -0.616

Table 2.a2. Crystallographic data.

Complex	15	16	17	18
Formula	C ₆₄ H ₈₄ CuN ₆ O ₈	C ₄₈ H ₇₆ CuN ₁₀ O ₁₂	C _{50.25} H _{78.5} Cl _{0.5} N ₄ NiO ₈	C ₄₂ H ₇₄ NiN ₆ O ₁₀
M / g mol ⁻¹	1128.91	1048.73	943.11	881.78
Crystal system	Triclinic	Triclinic	Monoclinic	Triclinic
Space group	P-1	P-1	P2(1)/c	P1
a / Å	8.6448(3)	9.5075(8)	12.5924(12)	10.6560(9)
b / Å	12.2959(5)	12.4277(11)	14.7415(14)	11.098(1)
c / Å	27.5630(12)	12.7321(13)	28.920(3)	11.793(1)
α / °	86.336(4)	63.886(9)	90.0	115.967(8)
β / °	88.039(3)	88.994(7)	98.768(2)	107.976(11)
γ / °	89.983(3)	78.688(7)	90.0	94.790(7)
V / Å ³	2922.1(2)	1320.5(2)	5305.8(9)	1153.01(17)
Z	2	1	4	1
Temperature / K	100	100	178	298
Radiation, λ / Å	Cu-K _α , 1.54184	Mo-K _α , 0.71073	Mo-K _α , 0.71073	Mo-K _α , 0.71073
ρ _{calcd} / g cm ⁻³	1.283	1.319	1.181	1.270
μ / mm ⁻¹	1.009	0.482	0.443	0.481
Reflect. measured	14881	13149	58021	5785
Independent reflect.	8643	5201	10318	5495
R _{int}	0.0362	0.0275	0.0530	0.0164
Parameters	755	322	875	532
scan range / °	3.85 - 63.95	3.10 - 26.07	1.55 - 25.91	3.32 - 26.06
Compl. to θ _{max} / %	89.2	99.3	99.8	97.1
Flack x _[Flack83]	-	-	-	0.118(14)
R (F, F ² > 2σ)	0.1409	0.0299	0.0770	0.0481
R _w (F ² , all data)	0.3951	0.0711	0.2570	0.1267
Goodness of fit F ²	1.132	0.962	1.098	1.018
Max., min. electron	2.141, -0.556	0.291, -0.356	1.281, -0.511	0.770, -0.529

Table 2.a3. Crystallographic data.

	2	9	21	22
Empirical Formula	C ₄₆ H ₇₈ N ₄ O ₆ Cu	C ₄₆ H ₇₈ N ₄ O ₆ Ni	C ₃₂ H ₅₆ Cu ₃ N ₁₂ O ₁₂	C ₃₂ H ₅₆ B ₂ Cu ₃ F ₈ N ₉ O ₇
M / g mol ⁻¹	846.66	841.83	991.51	1124.23
Crystal system	monoclinic	monoclinic	monoclinic	monoclinic
Space group	C2/c	C2/c	P2(1)/n	P2(1)/c
a [Å]	18.884(2)	18.5813(18)	15.700(2)	17.1300(11)
b [Å]	16.8271(18)	16.6748(16)	8.6710(12)	20.0771(13)
c [Å]	15.2379(15)	15.4806(15)	31.722(4)	15.3340(10)
α / °	90.0	90.00	90.0	
β / °	91.836(2)	92.083(2)	92.271(3)	106.9740(10)
γ / °	90.0	90.00	90.0	
V [Å ³]	4839.5(9)	4793.3(8)	4315.1(10)	5043.9(6)
Z	4	4	4	4
D _{calcd.} / g cm ⁻³	1.162	1.167	1.526	1.480
μ / mm ⁻¹	0.498	0.452	1.536	1.336
$\theta_{\min.}/\theta_{\max.}$ / °	1.62/25.15	1.64/24.64	2.26/27.13	2.34/26.42
Reflections collected	22601	21481	39298	54438
Reflections unique	4334	4051	8755	10667
Reflections observed	2455	2803	6227	8111
No. of parameters	305	296	544	757
R(F)	0.0555	0.0427	0.0662	0.0554
Rw(F ²)	0.1348	0.1183	0.2022	0.1381
S (GOF) on F ²	0.988	1.050	1.080	1.072
$\Delta\rho_{\max.}/\Delta\rho_{\min.}$ / e Å ⁻³	0.16/−0.29	0.33/−0.23	1.64/−0.70	1.17/−0.72

Table 2.a4. Crystallographic data.

	19	20
Empirical Formula	C _{23.5} H ₄₀ Cu ₂ N ₆ O _{8.5}	C ₂₄ H ₃₃ Cu ₂ N ₅ O ₇
M / g mol ⁻¹	669.70	630.65
Crystal system	monoclinic	monoclinic
Space group	P2(1)/n	P2(1)/c
a [Å]	8.55383(16)	9.0029(4)
b [Å]	22.1938(4)	13.5570(4)
c [Å]	15.8405(3)	21.4343(7)
β [°]	98.3957(19)	100.621(3)
V [Å ³]	2974.96(10)	2571.29(16)
Z	4	4
D _{calcd.} [g/cm ³]	1.495	1.629
μ [mm ⁻¹]	1.486	1.708
$\theta_{\min.}/\theta_{\max.}$ [°]	3.03/26.00	3.01/26.00
Reflections collected	26846	24232
Reflections unique	5801	5026
Reflections observed	4428	3525
No. of parameters	381	347
R(F)	0.0610	0.0292
Rw(F ²)	0.1841	0.0630
S (GOF) on F ²	1.102	0.880
$\Delta\rho_{\max.}/\Delta\rho_{\min.}$ [e/ Å ³]	1.69/−0.92	0.46/−0.34

Table 2.a5. Crystallographic data.

	5	23	24
Empirical Formula	C ₄₃ H ₇₈ N ₄ O ₆ Cu	C ₃₀ H ₅₆ Cl ₂ N ₁₀ O ₁₃ Cu ₃	C ₂₆ H ₄₅ Cu ₃ N ₉ O ₁₃
M / g mol ⁻¹	810.63	1026.37	882.33
Crystal system	monoclinic	monoclinic	monoclinic
Space group	C2/c	C2/c	P2(1)/n
a [Å]	18.677(2)	26.853(2)	7.7191(8)
b [Å]	17.341(2)	18.9180(15)	33.012(4)
c [Å]	14.8443(17)	17.0949(14)	14.7572(16)
β [°]	90.352(2)	95.6300(10)	97.445(2)
V [Å ³]	4807.7(10)	8642.5(12)	3728.8(7)
Z	4	8	4
D _{calcd.} [g/cm ³]	1.120	1.578	1.572
μ [mm ⁻¹]	0.499	1.656	1.766
θ _{min.} /θ _{max.} [°]	1.60/26.51	1.52/26.0	1.52/26.0
Reflections collected	21011	38010	27346
Reflections unique	5108	8414	7352
Reflections observed	2280	6332	3775
No. of parameters	346	581	525
R(F)	0.0748	0.0980	0.0631
Rw(F ²)	0.2154	0.2048	0.1697
S (GOF) on F ²	1.058	1.131	0.937
Δρ _{max} /Δρ _{min.} [e/ Å ³]	0.37/−0.35	1.04/−1.21	0.51/−0.95

Appendix of chapter 4 and 5

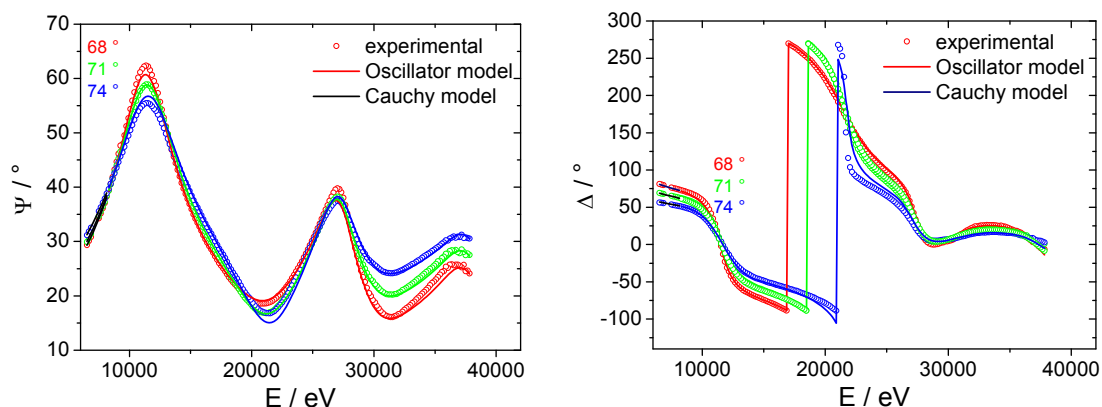


Figure 4.a1. Ψ and Δ of compound 22.

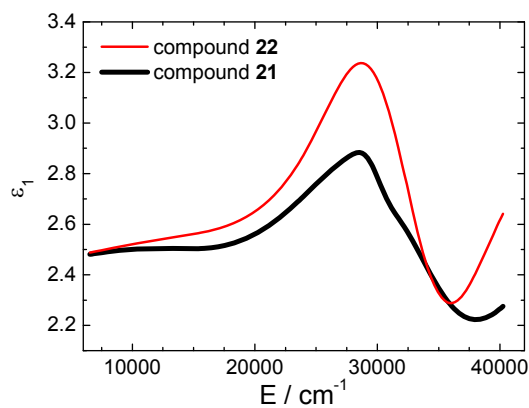


Figure 4.a2. ϵ_1 of compound 21 and 22.

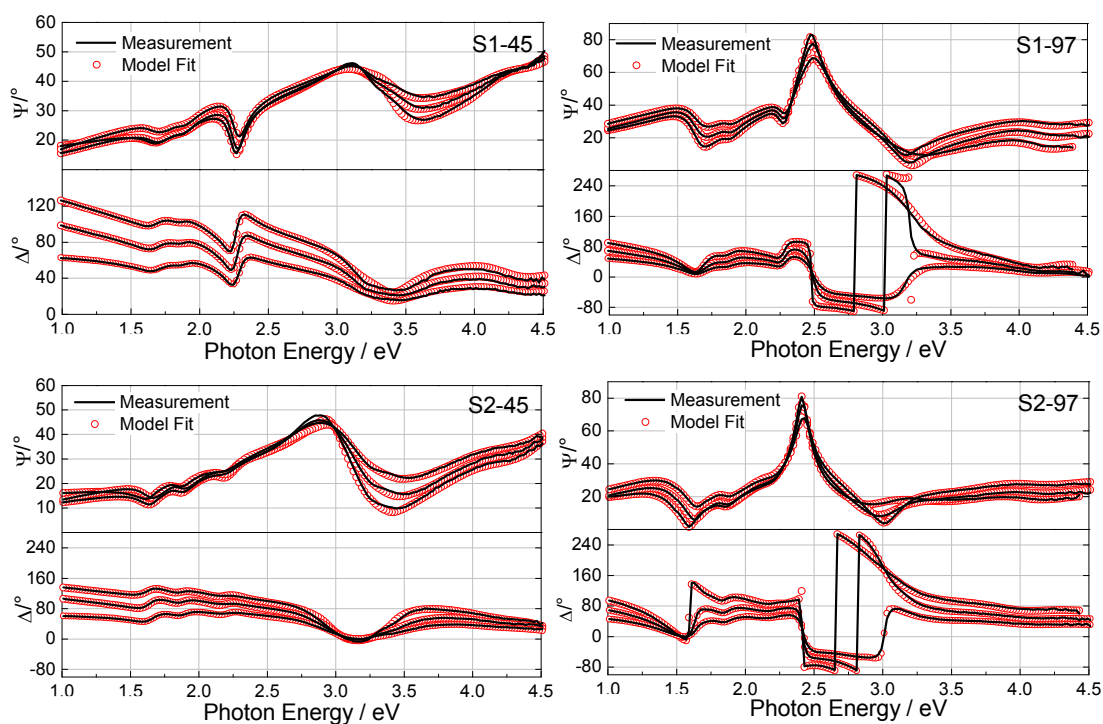


Figure 5.a1. Ellipsometric angles (Ψ and Δ) for 65°, 70°, and 75° angles of incidence.

References

Chapter 1

- [Ahlrichs89] R. Ahlrichs, M. Bär, M. Häser, H. Horn, C. Kölmel, *Chem. Phys. Lett.*, **1989**, 162, 165.
- [Allwood02] D.A. Allwood, G. Xiong, M.D. Cooke, C.C. Faulkner, *et al.*, *Science*, **2002**, 296, 2003.
- [Antonov01] V. N. Antonov, L. Uba, S. Uba, A. N. Yaresko, *et al.*, *Low Temp. Phys.*, **2001**, 27, 6, 425.
- [Chen06] Z. Chen, F. Huang, Y. Wu, D. Gu, F. Gan, *Inorg. Chem. Commun.*, **2006**, 9, 21.
- [Costa93] R. Costa, A. Garcia, J. Ribas, T. Mallah, Y. Journaux, J. Sletten, X. Solans, V. Rodriguez, *Inorg. Chem.*, **1993**, 32, 3733.
- [Cowburn00] R. P. Cowburn, M.E. Welland, *Science*, **2000**, 287, 1466.
- [Dormann97] J. L. Dormann, D. Fiorani, and E. Tronc, *Adv. Chem. Phys.*, **1997**, 98, 283.
- [Gatteschi03] D. Gatteschi and R. Sessoli, *Angew. Chem. Int. Ed. Eng.*, **2003**, 42, 268.
- [Gatteschi06] D. Gatteschi, R. Sessoli, J. Villain, *Molecular Nanomagnets*, Oxford University Press, **2006**.
- [Gütlich01] P. Gütlich, Y. Garcia, and T. Woike, *Coord. Chem. Rev.*, **2001**, 219, 839.
- [Iikawa02] F. Iikawa, P.V. Santos, M. Kästner, F. Schippan, L. Däweritz, *Phys. Rev. B*, **2002**, 65, 205328.
- [Jenkins03] D. Jenkins, W. Clegg, J. Windmill, S. Edmund, P. Davey, D. Newman, C. D. Wright, M. Loze, M. Armand, R. Atkinson, B. Hendren, P. Nutter, *Microsyst. Technol.*, **2003**, 10, 66.
- [Keneko00] M. Kaneko, *Magneto-Optics*, ed. S. Sugano, N. Kojima, Springer-Verlag, Berlin, **2000**, 271.
- [Lafuente99] C. Lafuente, C. Mingotaud, P. Delhaes, *Chem. Phys. Lett.*, **1999**, 302, 523.
- [Milster04] T. D. Milster, *Handbook of Laser Technology and Applications*, edited by Colin E. Webb and Julian D. C. Jones, Vol. III, Chapter D5.1: Optical data storage, **2004**.
- [Neese03] a) F. Neese, *J. Chem. Phys.*, **2003**, 119, 9428. b) F. Neese, *Int. J. Quantum Chem.*, **2001**, 83, 104.
- [Ohkoshi00] S. Ohkoshi, M. Mizuno, G. Hung, K. Hashimoto, *J. Phys. Chem. B*, **2000**, 104, 40, 9366.
- [Ohkoshi01] S. Ohkoshi, K. Hashimoto, *J. Photochem. Photobiol. C, Photochem. Rev.*, **2001**, 2, 71.
- [Ohkoshi01] S. Ohkoshi, K. Hashimoto, *J. Photochem. Photobiol. C: Photochem. Rev.*, **2001**, 2, 71.
- [Pankhurst03] Q. A. Pankhurst, J. Connolly, S. K. Jones, and J. Dobson, *J. Phys. D: Appl. Phys.*, **2003**, 36, 167.
- [Rasing97] T. Rasing, *J. Magn. Magn. Mater.*, **1997**, 175, 35.
- [Seip97] C. T. Seip, G.E. Granroth, M.W. Meisel, D.R. Talham, *J. Am. Chem. Soc.*, **1997**, 119, 7084.
- [Shir03] F. Shir, L. Yanik, L. H. Bennett, E. Della Torre, and R. D. Shull, *J. Appl. Phys.*, **2003**, 93, 8295.
- [Soyer99] H. Soyer, E. Dupart, C.J. Gomez-Garcia, C. Mingotaud, P. Delhaes, *Adv. Mater.*, **1999**, 11, 5, 382.

- [Tejada01] J. Tejada, *Polyhedron*, **2001**, 20, 1751.
- [Terris05] B. D. Terris and T. Thomson, *J. Phys. D: Appl. Phys.*, **2005**, 38, 199.
- [Tozawa03] M. Tozawa, S. Ohkoshi, N. Kojima, K. Hashimoto, *Chem. Commun.* **2003**, 1204.
- [Wahl03] M. Wahl, T. Herrmann, N. Esser, W. Richter, *Phys. Stat. Sol. C*, **2003**, 8, 3002.
- [Wernsdorfer01] W. Wernsdorfer, *Adv. Chem. Phys.*, **2001**, 118, 99.
- [You05] C. Y. You, S. C. Shin, *Thin Solid Films*, **2005**, 493, 226.

Chapter 2

- [Adachi05] K. Adachi, Y. Sugiyama, K. Yoneda, K. Yamada, K. Nozaki, A. Fuyuhira, S. Kawata *Chem. Eur. J.*, **2005**, 11, 6616.
- [Addison84] A. W. Addison, T. N. Rao, J. Reedijk, J. v. Rijn, G. C. Verschoor, *J. Chem. Soc., Dalton Trans.*, **1984**, 1349.
- [Aukauloo00] A. Aukauloo, X. Ottenwaelder, R. Ruiz, Y. Journaux, Y. Pei, E. Revière, M. Munoz, *Eur. J. Inorg. Chem.*, **2000**, 951.
- [Aukauloo99] A. Aukauloo, X. Ottenwaelder, R. Ruiz, S. Poussereau, Y. Pei, Y. Journaux, P. Fleurat, F. Volatron, B. Cervera, M. C. Munoz, *Eur. J. Inorg. Chem.*, **1999**, 1067.
- [Berg02] K. E. Berg, Y. Pellegrin, G. Blondin, X. Ottenwaelder, Y. Journaux, M. M. Canovas, T. Mallah, S. Parsons, A. Aukauloo, *Eur. J. Inorg. Chem.*, **2002**, 323.
- [Cervera98] B. Cervera, J. L. Sanz, M. J. Ibanez, G. Vila, F. Lloret, M. Julve, R. Ruiz, X. Ottenwaelder, A. Aukauloo, S. Poussereau, Y. Journaux, M. C. Munoz, *J. Chem. Soc., Dalton Trans.*, **1998**, 781.
- [Costa93] a) R. Costa, A. Garcia, J. Ribas, T. Mallah, Y. Journaux, J. Sletten, X. Solans, V. Rodriguez, *Inorg. Chem.*, **1993**, 32, 3733. b) R. Costa, A. Garcia, R. Sanchez, J. Ribas, X. Solans, V. Rodriguez, *Polyhedron*, **1993**, 12, 2697.
- [Crys06] CrysAlis CCD, Oxford Diffraction Ltd., Version 1.171.29.2, **2006**.
- [Dias01] A. C. Dias, M. Knobel, H. O. Stumpf, *J. Magn. Magn. Mater*, **2001**, 226, 1961.
- [Fettouhi96] M. Fettouhi, L. Quahab, A. Boukhari, O. Cador, C. Mathoniere, O. Kahn, *Inorg. Chem.*, **1996**, 35, 4932.
- [Flack83] H. D. Flack, *Acta Cryst. A*, **1983**, 39, 876.
- [Francese98] G. Francese, A. Neels, H. Stoeckli-Evans, and S. Decurtins, *Acta Cryst. E*, **1998**, 54, 1858.
- [Gaade36] W. Gaade, *Recl. Trav. Chim. Pays-Bas*, **1936**, 55, 324.
- [Galy79] J. Galy, J.-J. Bonnet, S. Anderson, *Acta Chem. Scand. A*, **1979**, A33, 383.
- [Gao01] a) E. Q. Gao, Q. H. Zhao, J. K. Tang, D. Z. Liao, Z. H. Jiang, S. P. Yan, *J. Chem. Soc., Dalton Trans.*, **2001**, 1537. b) E. Q. Gao, J. K. Tang, D. Z. Liao, Z. H. Jiang, S. P. Yan, G. L. Wang, *Inorg. Chem.*, **2001**, 40, 3134.
- [Huheey93] J. E. Huheey, E. A. Keiter, and R. L. Keiter, *Inorganic Chemistry, Principles of Structure and Reactivity*, 4th ed., **1993**, Harper Collins College Publ., New York.
- [Kahn93] O. Kahn, *Molecular Magnetism*, VCH Weinheim, **1993**.
- [Kahn95] O. Kahn, *Adv. Inorg. Chem.*, **1995**, 43, 179.
- [Kahn96] O. Kahn, *Magnetism: a supramolecular function*, NATO ASI Series C, Kluwer (Academic Publishers), Dordrecht, The Netherlands, **1996**, 484.

- [Kleineweischede06] A. Kleineweischede, J. Mattay, *Eur. J. Org. Chem.*, **2006**, 947.
- [Kubicki96] M. Kubicki, T. W. Kindopp, M. C. Capparelli, P. W. Coddington, *Acta Cryst. B*, **1996**, 52, 587.
- [Martin02] S. Martin, J. I. Beitia, M. Ugalde, P. Vitoria, and R. Cortes, *Acta Cryst. E*, **2002**, 58, 913.
- [Miyashita80] A. Miyashita, A. Yasuda, H. Takaya, K. Toriumi, T. Ito, T. Souchi, and R. Noyori, *J. Am. Chem. Soc.*, **1980**, 102, 7932.
- [Munoz98] M. C. Munoz, R. Ruiz, M. Traianidis, A. Aukauloo, J. Cano, Y. Journaux, I. Fernandez, J. R. Pedro, *Angew. Chem. Int. Ed.*, **1998**, 37, 1834.
- [Nonoyama76] K. Nonoyama, H. Ojima, M. Nonoyama, *Inorg. Chim. Acta*, **1976**, 20, 127.
- [Noyori02] R. Noyori, *Angew. Chem., Int. Ed. Engl.*, **2002**, 41, 2008.
- [Pereira03] C. L. M. Pereira, E. F. Pedroso, M. A. Novak, A. L. Brandl, M. Knobel, H. O. Stumpf, *Polyhedron*, **2003**, 22, 2387.
- [Ribas91] J. Ribas, A. Garcia, R. Costa, M. Monfort, S. Alvarez, Z. Zanchini, X. Solans, M. V. Domenech, *Inorg. Chem.*, **1991**, 30, 841.
- [Ribas97] J. Ribas, C. Diaz, X. Solans, M. Font-Bardia, *J. Chem. Soc., Dalton Trans.*, **1997**, 35.
- [Rüffer06] T. Rüffer, B. Bräuer, B. Walfort, *Inorg. Chem. Comm.*, **2006**, 9, 1111.
- [Rüffer07] T. Rüffer, B. Bräuer, *Analytical Sciences*, **2007**, 23.
- [Ruiz87] R. Ruiz, M. Triannidis, A. Aukauloo, Y. Journeaux, I. Fernandez, *Chem. Comm.*, **1987**, 2283.
- [Scholl04] R. Scholl, *Chem. Ber.*, **1904**, 37, 4427.
- [Sheldrick96] G. M. Sheldrick, *SHELXTL, Version 5.03*, Siemens Energy & Automation, Inc., Analytical Instrumentation, Madison, WI, USA, **1996**.
- [Stumpf93] H. O. Stumpf, Y. Pei, O. Kahn, J. Sletten, J. P. Renard, *J. Am. Chem. Soc.*, **1993**, 6738.
- [Stumpf93a] H. O. Stumpf, L. Ouahab, Y. Pei, D. Grandjean, O. Kahn, *Science*, **1993**, 261, 447.
- [Svensson76] C. Svensson, *Acta Chem. Scand. B*, **1976**, 30, 581.
- [Takaya86] H. Takaya, K. Mashima, K. Koyano, M. Yagi, H. Kumobayashi, T. Taketoni, S. Akutagawa, R. Noyori, *J. Org. Chem.*, **1986**, 51, 629.
- [Tapodi06] B. Tapodi, G. Speier, M. Giorgi, M. Reglier, T. Funabiki, L. Korecz, A. Rockenbauer, *Inorg. Chem. Commun.*, **2006**, 9, 367.
- [Tercero01] J. Tercero, C. Diaz, M. S. El Fallah, J. Ribas, X. Solans, M. A. Maestro, J. Mahia, *Inorg. Chem.*, **2001**, 40, 3077.
- [Tercero02] J. Tercero, C. Diaz, J. Ribas, A. Mahia, *J. Chem. Soc., Dalton Trans.*, **2002**, 2040.
- [Tuner95] S. S. Tuner, C. Michaut, O. Kahn, L. Quahab, A. Lecos, *New J. Chem.*, **1995**, 19, 773.
- [Wang02] Q. L. Wang, D. Z. Liao, S. P. Yan, Z. H. Jiang, P. Cheng, *Chin. J. Chem.*, **2002**, 20, 1249.
- [Zhu00] Z. C. Zhu, X. P. Mao, Z. Xu, X. Y. Huang, *Chin. J. Struct. Chem.*, **2000**, 19, 322.

Chapter 3

- [Ahlrichs89] R. Ahlrichs, M. Bär, M. Häser, H. Horn, C. Kölmel, *Chem. Phys. Lett.*, **1989**, 162, 165.
- [Arbuznikov02] A. V. Arbuznikov, M. Kaupp, M. Malkin, R. Reviakine, O. L. Malkina, *Phys. Chem. Chem. Phys.*, **2002**, 4, 5467.
- [Atanasov06] M. Atanasov, C. A. Daul, M.-M. Rohmer, T. Venkatachalam, *Chem. Phys. Lett.*, **2006**, 427, 449.
- [Autschbach03] J. Autschbach, F. E. Jorge, T. Ziegler, *Inorg. Chem.*, **2003**, 42, 2867.
- [Baron97] V. Baron, B. Gillon, A. Cousson, C. Mathoniere, O. Kahn, A. Grand, L. Ohrstrom, B. Delley, M. Bonnet, J. X. Boucherle, *J. Am. Chem. Soc.*, **1997**, 119, 3500.
- [Barone95] V. Barone, *Recent Advances in Density Functional Methods, Part I*, D. P. Chong (ed.), World Scientific, Singapore, **1995**.
- [Becke88] A. D. Becke, *J. Chem. Phys.*, **1988**, 88, 2547.
- [Becke93] A. D. Becke, *J. Chem. Phys.*, **1993**, 98, 5648.
- [Bencini05] a) A. Bencini, F. Totti, *Int. J. Quantum. Chem.*, **2005**, 101, 819. b) C. Adamo, V. Barone, A. Bencini, F. Totti, I. Ciofini, *Inorg. Chem.*, **1999**, 38, 1996.
- [Bencini83] A. Bencini, D. Gatteschi, *J. Am. Chem. Soc.*, **1983**, 105, 17, 5535.
- [Casida98] M. E. Casida, C. Jamorski, K. C. Casida, D. R. Salahub, *J. Chem. Phys.*, **1998**, 108, 4439.
- [Cervera98] B. Cervera, J. L. Sanz, M. J. Ibanez, G. Vila, F. Lloret, M. Julve, R. Ruiz, X. Ottenwaelde, A. Aukauloo, S. Poussereau, Y. Journaux, M. C. Munoz, *J. Chem. Soc., Dalton Trans.*, **1998**, 781.
- [Costa93] a) R. Costa, A. Garcia, J. Ribas, T. Mallah, Y. Journaux, *Inorg. Chem.*, **1993**, 32, 3733. b) R. Costa, A. Garcia, R. Sanchez, J. Ribas, X. Solans, V. Rodriguez, *Polyhedron*, **1993**, 12, 2697.
- [Davies74] E. R. Davies, *Phys. Lett. A*, **1974**, 47, 1.
- [Deeth01] R. J. Deeth, *J. Chem. Soc., Dalton Trans.*, **2001**, 664.
- [Eriksson94] L. A. Eriksson, O. L. Malkina, V. G. Malkin, D. R. Salahub, *J. Chem. Phys.*, **1994**, 100, 5066.
- [Finazzo06] C. Finazzo, C. Calle, S. Stoll, S. V. Doorslaer, A. Schweiger, *Phys. Chem. Chem. Phys.*, **2006**, 8, 1942.
- [Gauld97] J. W. Gauld, L. A. Eriksson, L. Radom, *J. Phys. Chem. A*, **1997**, 101, 1352.
- [Hohenberg64] P. Hohenberg, W. Kohn, *Phys. Rev. B*, **1964**, 136, 864.
- [Huheey93] J. E. Huheey, E. A. Keiter, and R. L. Keiter, *"Inorganic Chemistry, Principles of Structure and Reactivity"*, 4th ed., **1993**, Harper Collins College Publ., New York.
- [Kahn93] O. Kahn, *Molecular Magnetism*, VCH Weinheim, **1993**.
- [Kirmse85] R. Kirmse, J. Stach, *ESR-Spektroskopie*, Akademie-Verlag, Berlin, **1985**.
- [Kivelson61] D. Kivelson, R. Neiman, *J. Chem. Phys.*, **1961**, 35, 149.
- [Klamt93] A. Klamt, G. Schüürmann, *J. Chem. Soc. Perkin Trans.*, **1993**, 2, 799.
- [Kobitski03] Y. A. Kobitski, R. Scholz, D. R. T. Zahn, *THEOCHEM*, **2003**, 625, 39.
- [Kohn65] W. Kohn, L. J. Sham, *Phys. Rev.*, **1965**, 140, A1133.
- [Lee88] C. Lee, W. Yang, R. G. Parr, *Phys. Rev. B*, **1988**, 37, 785.
- [Lenthe97] E. Lenthe, P.E.S. Wormer, A. Avid, *J. Phys. Chem.*, **1997**, 107, 7, 2488.
- [Marques04] M. A. L. Marques, E. K. U. Gross, *Annu. Rev. Phys. Chem.*, **2004**, 55, 427.
- [Morton78] J. R. Morton, K. F. Preston, *J. Magn. Reson.*, **1978**, 30, 577.

- [Mulliken55] R. S. Mulliken, *J. Chem. Phys.*, **1955**, 23, 1833.
- [Neese01] F. Neese, *J. Chem. Phys.*, **2001**, 115, 11080.
- [Neese03] a) F. Neese, *J. Chem. Phys.*, **2003**, 119, 9428. b) F. Neese, *Int. J. Quantum Chem.*, **2001**, 83, 104.
- [Noodleman81] a) L. Noodleman, J. G. Norman, *J. Chem. Phys.*, **1979**, 70, 4903. b) L. Noodleman, *J. Chem. Phys.*, **1981**, 74, 5737.
- [Ong99] K. K. Ong, J. O. Jensen, H. F. Hameka, *J. Mol. Struct. (Theochem)*, **1999**, 459, 131.
- [Pillet04] S. Pillet, M. Souhassou, C. Mathonière, C. Lecomte, *J. Am. Chem. Soc.*, **2004**, 126, 1219.
- [Reed85] A. E. Reed, R. B. Weinstock, F. Weinhold, *J. Chem. Phys.*, **1985**, 83, 735.
- [Ruiz05] E. Ruiz, A. Rodríguez-Forteza, J. Tercero, T. Cauchy, C. Massobrio, *J. Chem. Phys.*, **2005**, 123, 074102.
- [Schaefer92] H. Schaefer, R. Horn, R. Ahlrichs, *J. Chem. Phys.*, **1992**, 97, 2571.
- [Schreckenbach97] G. Schreckenbach, T. Ziegler, *J. Phys. Chem. A*, **1997**, 101, 3388.
- [Schweiger01] A. Schweiger, G. Jeschke, *Principles of pulse electron paramagnetic resonance*, Oxford university press, Oxford, **2001**.
- [Slater30] J. C. Slater, *Phys. Rev. B*, **1930**, 36, 57.
- [Stoll06] S. Stoll, A. Schweiger, *J. Magn. Reson.*, **2006**, 178, 42.
- [Stumpf93] H. O. Stumpf, Y. Pei, O. Kahn, J. Sletten, J. P. Renard, *J. Am. Chem. Soc.*, **1993**, 115, 6738.
- [Sun05] Y. Sun, C. Liu, Z. Qi, D. Zhang, *J. Mol. Struct. Theochem.*, **2005**, 718, 49.
- [Szabo89] A. Szabo, N. S. Ostlund, *Modern quantum chemistry*, Dover Publications, **1989**.
- [Szilagyi02] R. K. Szilagyi, M. Metz, E. I. Solomon, *J. Phys. Chem. A*, **2002**, 106, 2994.
- [Turbo05] TURBOMOLE V5-8, **2005**, University of Karlsruhe.
- [Unamuno98] I. Unamuno, J. M. Gutiérrez-Zorrilla, A. Luque, P. Román, L. Lezama, R. Calvo, T. Rojo, *Inorg. Chem.*, **1998**, 37, 6452.
- [Vosko80] S. H. Vosko, L. Wilk, M. Nusair, *Can. J. Phys.*, **1980**, 58, 1200.
- [Wang03] Q. L. Wang, B. Zhao, D. Z. Liao, S. P. Yan, P. Cheng, *Trans. Met. Chem.*, **2003**, 28, 326.
- [Wang95] D. Wang, G. R. Hanson, *J. Magn. Reson.*, **1995**, A117, 1.
- [Weigend05] F. Weigend, R. Ahlrichs, *Phys. Chem. Chem. Phys.*, **2005**, 7, 3297.
- [Wilson66] R. Wilson, D. Kivelson, *J. Chem. Phys.*, **1966**, 44, 1.
- [Zimmer05] C. Zimmermann, C. E. Anson, F. Weigend, R. Clerac, S. Dehnen, *Inorg. Chem.*, **2005**, 44, 5686.

Chapter 4

- [Azzam92] R. M. A. Azzam, N. M. Bashara, *Ellipsometry and Polarized Light*, Elsevier, North-Holland, **1992**.
- [Azzam99] R. M. A. Azzam, N. M. Bashara, *Ellipsometry and Polarized Light*, North Holland, Amsterdam, **1999**.
- [Bauer00] A. Bauer, *Far-Field and Near-Field Magneto-Optical Microscopy of Ultrathin Films*, Habilitationsschrift, FU Berlin, **2000**.
- [Becke88] (a) Becke, A. D. *Phys. Rev. A: At., Mol., Opt. Phys.*, **1988**, 38, 3098. (b) A. D. Becke, *J. Chem. Phys.*, **1993**, 98, 1372. (c) A. D. Becke, *J. Chem. Phys.*,

- 1993**, 98, 5648.
- [Creighton86] a) J. A. Creighton, *Surf. Sci.*, **1986**, 173, 665. b) J. A. Creighton, *Spectroscopy of Surfaces*, R. J. H. Clark, R. E. Hester, Wiley, **1988**, 37.
- [Eichkorn95] K. Eichkorn, O. Treutler, H. Öhm, M. Häser, R. Ahlrichs, *Chem. Phys. Lett.*, **1995**, 240, 283.
- [Frisch04] M. J. Frisch, G. W. Trucks, H. B. Schlegel, G. E. Scuseria, M. A. Robb, J. R. Cheeseman, J. A. Montgomery, T. Vreven, K. N. Kudin, J. C. Burant, J. M. Millam, S. S. Iyengar, J. Tomasi, V. Barone, B. Mennucci, M. Cossi, G. Scalmani, N. Rega, G. A. Petersson, H. Nakatsuji, M. Hada, M. Ehara, K. Toyota, R. Fukuda, J. Hasegawa, M. Ishida, T. Nakajima, Y. Honda, O. Kitao, H. Nakai, M. Klene, X. Li, J. E. Knox, H. P. Hratchian, J. B. Cross, V. Bakken, C. Adamo, J. Jaramillo, R. Gomperts, R. E. Stratmann, O. Yazyev, A. J. Austin, R. Cammi, C. Pomelli, J. W. Ochterski, P. Y. Ayala, K. Morokuma, G. A. Voth, P. Salvador, J. J. Dannenberg, V. G. Zakrzewski, S. Dapprich, A. D. Daniels, M. C. Strain, O. Farkas, D. K. Malick, A. D. Rabuck, K. Raghavachari, J. B. Foresman, J. V. Ortiz, Q. Cui, A. G. Baboul, S. Clifford, J. Cioslowski, B. B. Stefanov, G. Liu, A. Liashenko, P. Piskorz, I. Komaromi, R. L. Martin, D. J. Fox, T. Keith, M. A. Al-Laham, C. Y. Peng, A. Nanayakkara, M. Challacombe, P. M. W. Gill, B. Johnson, W. Chen, M. W. Wong, C. Gonzalez, J. A. Pople, *Gaussian 03*, revision C.02; Gaussian, Inc.: Wallingford, CT, **2004**.
- [Hamagucchi77] H. Hamagucchi, *J. Chem. Phys.*, **1977**, 66, 5, 5757.
- [Klamt93] A. Klamt, G. Schürmann, *J. Chem. Soc. Perkin Trans.*, **1993**, 2, 799.
- [Lee88] C. Lee, W. Yang, R. G. Parr, *Phys. Rev. B*, **1988**, 37, 785.
- [Miles05] R. W. Miles, K. M. Hynes, I. Forbes, *Progress in Crystal Growth and Characterization of Materials*, **2005**, 51, 1.
- [Mingardi75] M. Mingardi, W. Siebrand, *J. Chem. Phys.*, **1975**, 62, 3, 1074.
- [Moskovits85] M. Moskovits, *Rev. Mod. Phys.*, **1985**, 57, 783.
- [Neese01] F. Neese, *Int. J. Quantum Chem.*, **2001**, 83, 104.
- [Neese03] F. Neese, *J. Chem. Phys.*, **2003**, 119, 9428.
- [Ong99] K. K. Ong, J. O. Jensen, H. F. Hameka, *J. Mol. Struct. (Theochem)*, **1999**, 459, 131.
- [Oppeneer92] P. M. Oppeneer, J. Sticht, T. Maurer, J. Kübler, *Z. Phys. B – Cond. Mat.*, **1992**, 8, 309.
- [Salvan03] G. Salvan, *Metal/organic/inorganic semiconductor heterostructures characterized by vibrational spectroscopies*, Dissertation, TU Chemnitz, **2003**.
- [Silaghi05] S. D. Silaghi, *Optical characterization of DNA bases on silicon surfaces*, Dissertation, TU Chemnitz, **2005**.
- [Turbomole05] a) TURBOMOLE V5-8, **2005**, University of Karlsruhe. b) H. Horn, H. Weiss, M. Häser, M. Ehrig, R. Ahlrichs, *J. Comput. Chem.*, **1991**, 12, 1058. c) M. Häser, R. Ahlrichs, H. P. Baron, P. Weis, H. Horn, *Theor. Chim. Acta*, **1992**, 83, 455. d) A. Schäfer, H. Horn, R. Ahlrichs, *J. Chem. Phys.*, **1992**, 97, 2571. e) A. Schäfer, C. Huber, R. Ahlrichs, *J. Chem. Phys.*, **1994**, 100, 5829. f) R. Ahlrichs, M. Bär, M. Häser, H. Horn, C. Kölmel, *Chem. Phys. Lett.*, **1989**, 162, 165.
- [Weigend05] F. Weigend, R. Ahlrichs, *Phys. Chem. Chem. Phys.*, **2005**, 7, 3297.
- [Weigend06] F. Weigend, *Phys. Chem. Chem. Phys.*, **2006**, 8, 1057.
- [Woollam99] a) J. A. Woollam, B. Johs, C. M. Herzinger, J. Hilfiker, R. Synowicki, C. L. Bungay, Overview of Variable Angle Spectroscopic Ellipsometry (VASE), Critical Reviews of Optical Science and Technology, **1999**, CR72. b) J. A. Woollam Co., Inc., Guide to Using WVASE32™, Software for VASE and M-44 Ellipsometers, **1999**.
- [Zak91] J. Zak, E. R. Moog, C. Liu, S. D. Bader, *Phys. Rev. B*, **1991**, 43, 6423.

- [Zimmer05] C. Zimmermann, C. E. Anson, F. Weigend, R. Clerac, S. Dehnen, *Inorg. Chem.*, **2005**, 44, 5686.

Chapter 5

- [Azzam99] R. M. A. Azzam, N. M. Bashara, *Ellipsometry and Polarized Light*, North Holland, Amsterdam, **1999**.
- [Dietrich94] W. Dietrich, *Diplomarbeit*, TU Chemnitz–Zwickau, **1994**.
- [Forrest97] S. R. Forrest, *Chem. Rev.*, **1997**, 97, 1793.
- [Fronk08] M. Fronk, B. Bräuer, G. Salvan, to be submitted.
- [Gordan04] a) O. Gordan, M. Friedrich, D. R. T. Zahn, *Thin Solid Films*, **2004**, 551, 455. b) O. D. Gordan, M. Friedrich, D. R. T. Zahn, *Organic Electronics*, **2004**, 5, 291.
- [Gordan06] O. D. Gordan, *Molecular Orientation and Electronic Interactions in Organic Thin Films Studied by Spectroscopic Ellipsometry*, Dissertation, TU Chemnitz, **2006**.
- [Gordan06a] O. D. Gordan, T. Sakurai, M. Friedrich, K. Akimoto, D. R. T. Zahn, *Org. Electron.*, **2006**, 7, 521.
- [Herrmann06] T. Herrmann, K. Lüdge, W. Richter, K. G. Georgarakis, P. Pouloupoulos, R. Nünthel, J. Lindner, M. Wahl, N. Esser, *Phys. Rev. B*, **2006**, 73, 134408.
- [McInnes02] E. J. L. McInnes, E. Pidcock, V. S. Oganessian, M. R. Cheesman, A. K. Powell, A. J. Thomson, *J. Am. Chem. Soc.*, **2002**, 124, 9220.
- [McKeown98] N. B. McKeown, *Phthalocyanine materials*, Cambridge University Press, **1998**.
- [Ogawa99] T. Ogawa, K. Kuwamoto, S. Isoda, T. Kobayashi, N. Karl, *Acta Cryst.*, **1999**, B 55, 123.
- [Pope99] M. Pope, C. Swenberg, *Electronic processes in organic crystals and polymers*, 2nd edition, Oxford University Press, New York, **1999**.
- [Sakurai06] T. Sakurai, R. Fukasawa, and K. Akimoto, *Jpn. J. Appl. Phys.*, **2006**, 45, 255.
- [Sugano00] S. Sugano, N. Kojima, *Magneto–Optics*, Springer, *Solid State Sciences*, **2000**.
- [Zahn07] D. R. T. Zahn, G. N. Gavrila, G. Salvan, *Chem. Rev.*, **2007**, 107, 1161.
- [Zvezdin97] A. K. Zvezdin, V. A. Kotov, *Modern Magnetooptics and Magneto-optical Materials*, IOP Publishing Ltd, Studies in Condensed Matter Physics, **1997**.

Chapter 6

- [Amekura04] H. Amekura, Y. Takeda, N. Kishimoto, *Thin Solid Films*, **2004**, 464, 268.
- [Cahen03] D. Cahen, A. Kahn, *Adv. Mat.*, **2003**, 15, 271.
- [Estournès97] C. Estournès, T. Lutz, J. Happich, T. Quaranta, P. Wissler, J. L. Guille, *J. Magn. Magn. Mater.*, **1997**, 173, 83.
- [Fonseca02] F. C. Fonseca, G. F. Goya, R. F. Jardim, R. Muccillo, N. L. V. Carreno, E. Longo, E. R. Leite, *Phys. Rev. B*, **2002**, 66, 104406.
- [Fraune01] M. Fraune, U. Rudiger, G. Guntherodt, S. Cardoso, P. Freitas, *Appl. Phys. Lett.*, **2001**, 77, 3815.

- [Gavrila05] G. N. Gavrila, *Electronic Properties and Chemistry of Metal/ Organic Semiconductor/S-GaAs(100) Heterostructures*, Dissertation, TU Chemnitz, **2005**.
- [Gavrin93] A. Gavrin and C. L. Chen, *J. Appl. Phys.*, **1993**, 73, 6949.
- [Gleiter92] H. Gleiter, *Nanostruct. Mater.*, **1992**, 1, 1.
- [Gonzalez98] E. M. González, M. I. Montero, F. Cebollada, C. de Julián, J. L. Vicent, J. M. González, *Europhys. Lett.*, **1998**, 42, 91.
- [Hayashi77] T. Hayashi, T. Ohno, S. Yatsuya, R. Ueda, *Jpn. J. Appl. Phys.*, **1977**, 16, 705.
- [Jung99] J. S. Jung, W. S. Chae, R. A. McIntyre, C. T. Seip, J. B. Wiley, C. J. O'Connor, *Mater. Res. Bull.*, **1999**, 34, 1353.
- [Leite02] E. R. Leite, N. L. V. Carreno, E. Longo, A. Valentini, L. F. D. Probst, *J. Nanosci. Nanotechnol.*, **2002**, 2, 89.
- [Liu07] Z. Liu, X. Zhang, Y. Zhang, J. Jiang, *Spectrochimica Acta A*, **2007**, 67, 1232.
- [Lu00] L. Lu, M. L. Sui, K. Lu, *Science*, **2000**, 287, 1463.
- [Makhlouf08] Salah A. Makhlouf, H. Al-Attar, R. H. Kodama, *Solid State Commun.*, **2008**, 145, 1.
- [Meiklejohn56] W. H. Meiklejohn, C. P. Bean, *Phys. Rev.*, **1956**, 102, 1413.
- [Néel49] L. Néel, *Ann. Geophys.*, **1949**, 5, 99.
- [Oliveira06] M. C. Oliveira, A. M. B. Rego, *J. Alloys Compounds*, **2006**, 425, 64.
- [Ozaki89] M. Ozaki, *Mater. Res. Bull.*, **1989**, XIV, 35.
- [Petraki07] F. Petraki, V. Papaefthimiou, S. Kennou, *Organic Electronics*, **2007**, 8, 522.
- [Poddar04] P. Poddar, J. L. Wilson, H. Srikanth, S. A. Morrison, E. E. Carpenter, *Nanotechnology*, **2004**, 15, 570.
- [Rubinstein01] M. Rubinstein, R. H. Kodama, S. A. Makhlouf, *J. Magn. Magn. Mater.*, **2001**, 234, 289.
- [Sappey97] R. Sappey, E. Vincent, N. Hadacek, F. Chaput, J. P. Boilot, D. Zins, *Phys. Rev. B*, **1997**, 56, 22, 14551.
- [Schultz90] L. Schultz, K. Schitzke, J. Wecker, *Appl. Phys. Lett.*, **1990**, 56, 868.
- [Stoner48] E. C. Stoner, E. P. Wohlfarth, *Philos. Trans. R. Soc. London, Ser. A*, **1948**, 240, 599.
- [Sun07] C.-J. Sun, Y. Wu, Z. Xu, B. Hu, J. Bai, J.-P. Wang, J. Shen, *Appl. Phys. Lett.*, **2007**, 90, 232110.
- [Yao96] Y. D. Yao, Y. Y. Chen, M. F. Tai, D. H. Wang, H. M. Lin, *Mater. Sci. Eng. A*, **1996**, 217, 837.
- [Zheng00] L. A. Zheng, B. M. Lairson, E. V. Barrera, *Appl. Phys. Lett.*, **2000**, 70, 3110.

Ich erkläre, dass ich die vorliegende Arbeit selbständig und nur unter Verwendung der angegebenen Literatur und Hilfsmittel angefertigt habe.

14. April 2008

Dipl.-Chem. Dipl.-Phys. Björn Bräuer

Curriculum Vitae

Personal data

Name	Björn Bräuer
Date of birth	14 th January 1981
Place of birth	Marienberg, Germany
Nationality	German

Education

5/2006 to 4/2008	Doctoral work in Natural Sciences with Prof. Dr. H. Lang (Inorganic Chemistry) and Juniorprof. Dr. G. Salvan (Organic Semiconductors), in cooperation with Prof. Dr. Dr. h. c. D.R.T. Zahn and Dr. T. Rüffer.
8/2005 to 5/2006	Diplom in Physics (Organic Semiconductors) with Juniorprof. Dr. G. Salvan and Prof. Dr. Dr. h. c. D.R.T. Zahn, " <i>Magnetic and optical investigations on transition metal complexes</i> "
10/2004 to 7/2005	Diplom in Chemistry (Inorganic Chemistry) with Prof. Dr. H. Lang and Dr. T. Rüffer, " <i>Synthesis and characterisation of Cu(II)- and Ni(II)-Bis(oxamato) complexes</i> "
10/2000 to 9/2004	Studies in Chemistry and Physics at Chemnitz University on Technology
8/1999 to 8/2000	Military service, study in Economic Science at FernUniversität Hagen.
8/1992 to 7/1999	Gymnasium Marienberg, Abitur

Grants and prizes

10/2006	University prize of the Chemnitz University of Technology for the best Diplom in Chemistry and the best Diplom in Physics.
9/2006 to 12/2006	Marie Curie Scholarship (4 months).
4/2006 to 7/2008	Scholarship of the Fonds der Chemischen Industrie (24 months).

Research stays

- 10/2007 to 11/2007 Research stay in the group of Prof. Dr. A. Kahn, Department of Electrical Engineering, Surface/Interface Science Laboratory, Princeton (NJ), USA.
"Photoelectron Spectroscopy investigations of magnetic nanoparticles in organic matrices"
- 9/2006 to 12/2006 and 6/2007 to 7/2007 Research stays in the group of Prof. Dr. D. Gatteschi, Department of Chemistry, Laboratory of Molecular Magnetism, Florence, Italy.
"Electron paramagnetic resonance and magnetic susceptibility studies on exchange coupled systems"
- 05/2007 Research visit in the group of Prof. Dr. R. Ahlrichs (Dr. F. Weigend), Research centre Karlsruhe, Germany.
"DFT studies of magnetic super-exchange interactions in trinuclear Cu(II) complexes "
- 05/2007 Research visit in the group of Prof. Dr. W. Lubitz (Dr. E. Reijerse), Max Planck Institute of Bioinorganic Chemistry, Mülheim, Germany.
"ENDOR investigations of Cu(II)-Bis(oxamato)-complexes"
- 10/2005 Research visit at Bessy (Berlin Synchrotron), Berlin, Germany.
"Visible and Ultraviolet Ellipsometry investigations on thin films of trinuclear transition metal complexes using Synchrotron Radiation"
- 7/2006 Research visit in the group of Prof. Dr. A. Powell, Institute for Inorganic Chemistry, Chair for Supramolecular Chemistry, Karlsruhe, Germany.
"SQUID measurements on trinuclear transition metal complexes"
- 11/2004 Research visit in the group of Prof. Dr. R. Kirmse, Institute for Inorganic Chemistry, University Leipzig, Germany.
"EPR spectroscopy on Cu(II) complexes"

List of publications

Publications related to the content to this thesis (supervised by Dr. G. Salvan)

- [15] **B. Bräuer**, Y. Vaynzof, W. Zhao, A. Kahn, W. Li, C. J. Fernández, C. Sangregorio, G. Salvan, *Electronic and magnetic properties of Ni nanoparticles embedded in Phthalocyanines*, submitted
- [14] M. Fronk, **B. Bräuer**, G. Salvan, *Room temperature magneto-optical Kerr effect in organic semiconductors*, submitted
- [13] **B. Bräuer**, F. Weigend, M. Fittipaldi, D. Gatteschi, A. Guerri, S. Ciattini, E. J. Reijerse, G. Salvan, T. Rüffer, *EPR and DFT studies on Cu(II)-bis(oxamato) building blocks for molecule based magnetic materials*, Inorg. Chem., DOI: 10.1021/ic702460t.
- [12] **B. Bräuer**, F. Weigend, F. Totti, D. R. T. Zahn, T. Rüffer, G. Salvan, *Magnetic Cu(II)-bis(oxamato) complexes: Combined quantum chemical DFT and vibrational spectroscopy studies*, J. Phys. Chem. B., 2008, 112, 5585-5593.
- [11] **B. Bräuer**, D. R. T. Zahn, T. Rüffer, G. Salvan, *Deposition of thin films of a transition metal complex by spin coating*, Chem. Phys. Lett., 2006, 432, 226-229.
- [10] **B. Bräuer**, T. Rüffer, R. Kirmse, J. Griebel, F. Weigend, G. Salvan, *Spin density distribution in oxamato-type transition metal complexes*, Polyhedron, 2007, 26, 1773-1775.

Publications related to the content to this thesis (supervised by Dr. T. Rüffer)

- [9] T. Rüffer, **B. Bräuer**, F. E. Meva, B. Walfort, *Transition metal induced novel coordination behaviour of bis(oxamato) ligands*, Dalton Trans., accepted.
- [8] T. Rüffer, **B. Bräuer**, F. E. Meva, L. Sorace, *Synthesis, characterization, and magnetic properties of new binuclear Cu^{II}Cu^{II} bis(oxamato) complexes*, Inorg. Chim. Acta, DOI: 10.1016/j.ica.2008.05.005.
- [7] T. Rüffer, **B. Bräuer**, F. E. Meva, B. Walfort, G. Salvan, A. K. Powell, I. J. Hewitt, L. Sorace, A. Caneschi, *Synthesis, characterization, and magnetic properties of new homotrinuclear copper(II) complexes with an asymmetric N,N'-bridge*, Inorg. Chim. Acta, 2007, 360, 12, 3777-3784.
- [6] T. Rüffer, **B. Bräuer**, A. K. Powell, I. J. Hewitt, G. Salvan, *Synthesis, characterization, and magnetic properties of new homotrinuclear copper(II) complexes*, Inorg. Chim. Acta, 2007, 360, 11, 3475-3483.
- [5] T. Rüffer, **B. Bräuer**, *Crystal Structure of (R)-Diethyl N,N'-[1,1'-Binaphthalene]-2,2'-bis(oxamate)*, Analytical Sciences, 2007, 23-25.

- [4] T. Rüffer, **B. Bräuer**, B. Walfort, *A novel coordination behaviour of bis-oxamato ligands*, Inorg. Chem. Commun., 9, 2006, 1111-1113.

Publications not related to this thesis

- [3] R. Packheiser, P. Ecorchard, T. Rüffer, M. Lohan, **B. Bräuer**, F. Justaud, C. Lapinte, H. Lang, *Heterotrimetallic M-M'-M'' transition metal complexes based on 1,3,5-Triethynyl-benzene: synthesis, solid state structure and electrochemical characterization*, submitted.
- [2] M. Fronk, **B. Bräuer**, D. R. T. Zahn, and Georgeta Salvan, *Temperature dependent reflection anisotropy spectroscopy investigations of vanadyl phthalocyanine films*, Thin Solid Films, DOI: 10.1016/j.tsf.2008.04.094.
- [1] G. Salvan, R. Pacurariu, W. Li, M. Fronk, **B. Bräuer**, S. Schubert, G. Radons, D. M. Rosu, D. R. T. Zahn, S. Schulze, M. Hietschold, J. Bachmann, K. Nielsch, C. Sangregorio, *Nickel nanoparticles embedded in fullerene matrix: structural, magnetic and magneto-optical properties*, submitted.

Attended international conferences and meetings

16/02 to 21/02/08	Klosters, Switzerland Invited Talk	19th Edgar-Lüscher-Seminar , "Magneto-optical spectroscopies applied to organic semiconductors", <u>B. Bräuer</u> , M. Fronk, G. Salvan.
12/11/07	Princeton, USA Talk	Research seminar , "Magnetic nanomaterials - from molecules to particles", <u>B. Bräuer</u> .
28/05 to 01/05/07	Strassburg, France Poster	Conference of the European Materials Research Society , "EPR, magnetic susceptibility and optical investigations on thin films of Cu(II)-bis(oxamato) complexes", <u>B. Bräuer</u> , T. Rüffer, D.R.T. Zahn, G. Salvan, D. Gatteschi, A. Caneschi, M. Fittipaldi, F. Totti.
25/03 to 29/03/07	Oxford, England Poster	40th meeting of the Electron Spin Resonance group , "ESR spectroscopy on Cu(II)-bis(oxamato) building blocks for molecule based magnetic materials", <u>B. Bräuer</u> , T. Rüffer, G. Salvan, M. Fittipaldi, D. Gatteschi, A. Caneschi, F. Totti, A. Powell, I. Hewitt, F. Weigend, R. Kirmse, J. Griebel.
13/08 to 17/08/06	Victoria, Canada Poster	10th International Conference on Molecule-Based Magnets , "Magnetic interaction and spin density distribution in oxamato-type transition metal complexes", <u>B. Bräuer</u> , T. Rüffer, D.R.T. Zahn, G. Salvan, A. Powell, I. Hewitt, R. Kirmse, J. Griebel.

20/07 to 26/07/06	Erice, Italy Poster	International School of Solid State Physics, EPIOPTICS-9 , "Magnetic interaction and spin density distribution in oxamato-type transition metal complexes", <u>B. Bräuer</u> , T. Rüffer, D. R. T. Zahn, A. Powell, I. Hewitt, R. Kirmse, J. Griebel, F. Weigend, G. Salvan.
02/07 to 07/07/06	Dublin, Ireland Talk	The International Conference on Synthetic Metals , "Magnetic exchange interactions and spin density distribution in oxamato-type single molecule magnets", <u>B. Bräuer</u> , T. Rüffer, D. R. T. Zahn, G. Salvan.

Attended national conferences and meetings

25/02 to 29/02/08	Berlin, Germany Talk	DPG Spring meeting , "Coordination geometry induced changes on magnetic parameters of Cu(II) complexes", <u>B. Bräuer</u> , T. Rüffer, D. Gatteschi, M. Fittipaldi, A. Caneschi, F. Weigend, G. Salvan.
25/02/08	Berlin, Germany Talk	Stipendiatentreffen des Fonds der chemischen Industrie , "Einfluss der Koordinationsgeometrie auf die magnetischen Eigenschaften von Cu(II)-bis(oxamato)-Komplexen", <u>B. Bräuer</u> , T. Rüffer, D. Gatteschi, M. Fittipaldi, A. Caneschi, F. Weigend, G. Salvan.
16/09 to 19/09/07	Ulm, Germany Poster	Wissenschaftsforum Chemie 2007 , "ESR-Spektroskopie an Cu(II)-bis(oxamato)-Bausteinen für molekülbasierte magnetische Materialien", <u>B. Bräuer</u> , T. Rüffer, G. Salvan, H. Lang, M. Fittipaldi, A. Caneschi, D. Gatteschi.
22/05 to 25/05/07	Mülheim, Germany Talk	Research seminar , "ESR and DFT studies on Cu(II)-bis(oxamato) building blocks for molecule based magnetic materials", <u>B. Bräuer</u> .
25/03 to 29/03/07	Regensburg, Germany Poster	DPG Spring meeting , "EPR and magnetic susceptibility investigations on Cu(II)-bis(oxamato) complexes", <u>B. Bräuer</u> , T. Rüffer, D.R.T. Zahn, G. Salvan, D. Gatteschi, A. Caneschi, M. Fittipaldi, F. Totti.
18/02 to 20/02/07	Berlin, Germany Talk	3rd Coordination chemistry meeting , "Synthesis, magnetic resonance, and susceptibility investigations of Cu(II)-bis(oxamato) complexes", <u>B. Bräuer</u> , T. Rüffer, D.R.T. Zahn, G. Salvan, D. Gatteschi, A. Caneschi, M. Fittipaldi, F. Totti.

12/05/06	Chemnitz, Germany Talk	Soft Matter Symposium , “Magnetic and optical properties of oxamato-type single molecule magnets“, <u>B. Bräuer</u> , T. Rüffer, D. R. T. Zahn, G. Salvan.
26/03 to 31/03/06	Dresden, Germany Talk	DPG Spring meeting , “Magnetic and optical properties of oxamato bridged Cu(II) complexes“, <u>B. Bräuer</u> , T. Rüffer, D. R. T. Zahn, G. Salvan.
20/02 to 22/02/06	Berlin, Germany Poster	4th Workshop Ellipsometry , “Ellipsometry investigations on magnetic active oxamato bridged Cu(II) complexes“, <u>B. Bräuer</u> , T. Rüffer, D. Lehmann, O. Gordan, D. R. T. Zahn, W. Braun, A. Powell, G. Salvan.
20/9/05	Leipzig, Germany Talk	Mitteldeutsches Anorganiker-Symposium , “Synthesis and Characterisation of novel Bis-oxamato Complexes“, <u>B. Bräuer</u> .
03/04 to 05/04/05	Kaisers- lautern Germany Talk	1st Coordination chemistry meeting , „Design mehrkerniger Übergangsmetallkomplexe bezüglich ihres materialwissenschaftlichen Anwendungspotentials“, <u>B. Bräuer</u> .

Acknowledgements

I want to thank my supervisor in the department of Physics Juniorprof. Dr. Georgeta Salvan for many interesting scientific discussions, training in English scientific writing, for her support in my applications, and for a very friendly working atmosphere. In the department of Chemistry I thank Dr. Tobias Rüffer for performing many of the single crystal x-ray analysis investigations, for introducing me in this field, and all his motivating and interesting discussions.

My special thanks go to Prof. Dr. Heinrich Lang for his support in all my applications, the opportunity to work out a part of my PhD thesis in his labs, and the discussions with him and his working group. I want to thank Prof. Dr. Dr. h. c. Dietrich R. T. Zahn for a great cooperation, his many important comments and fruitful discussions during our weekly meetings.

I thank Prof. Dr. Annie Powell for refereeing my dissertation, for her help in my applications, and a very interesting research stay in her group.

Furthermore, I thank all the respective working group members, among others: Daniel for offering his great abilities in fixing Computer problems, working out complicated spectroscopic ellipsometry models, and entrusting me to use his vacuum chamber; Michael for his enthusiasm in improving the magneto-optical setup and in modelling the data; Wen for the preparation of the Ni nanoparticles in organic matrices; François for growing large amounts of single crystals especially for the magnetic measurements. I also want to thank Dr. Steffen Schulz for the electron microscopy measurements.

For a research stay of five months I gratefully acknowledge Prof. Dr. Dante Gatteschi and Prof. Dr. Andrea Caneschi in Florence. It was an honour and great pleasure to work out a part of my thesis in this famous research group. I thank all the researchers there for their great hospitality and fruitful scientific discussions. Among others I thank Maria, Lorenzo, Claudio, César, Federico, and Fabrice for the great research training in the field of molecular magnetism.

I wish to express my appreciation to Prof. Dr. Antoine Kahn and his very nice working group in Princeton where I did a research stay of one month, especially Yana and Wei for the photoelectron spectroscopy studies.

I thank Prof. Dr. Wolfgang Lubitz in Mülheim for the great opportunity to do a research training in his regarded EPR group and thank especially Edward for the measurements and discussions.

From the research centre in Karlsruhe I thank Dr. Florian Weigend (group of Prof. Dr. Reinhart Ahlrichs) for guiding me through the field of DFT.

I thank Emma Scales from Manchester for her patience in reading my thesis before submission and her suggestions regarding the English grammar.

For financial support I would like to thank the *Fonds der chemischen Industrie* and the *Marie Curie* program for two PhD fellowships and the *Molmag* project, MEST-CT-2004-504204 for covering the costs of some of my measurements.

Finally I would like to express my gratefulness to my parents who were always a source of spiritual support, wisdom, and patience.